

Faculty of Mathematics and Physics  
CHARLES UNIVERSITY in PRAGUE

Institute of Theoretical Physics  
&  
Astronomical Institute



## Radiation of accretion discs in strong gravity

Thesis submitted for the degree of Doctor Philosophiae

Michal Dovčiak

Supervisor: doc. RNDr. Vladimír Karas, DrSc.

---

Prague, June 2004

**Referees:**

Professor Annalisa Celotti  
Astrophysics sector  
International School for Advanced  
Studies in Trieste  
Italy

Professor Andrew Fabian  
Institute of Astronomy  
University of Cambridge  
United Kingdom

Professor Zdeněk Stuchlík  
Institute of Physics  
Faculty of Philosophy and Science  
Silesian University at Opava  
Czech Republic

## Acknowledgements

Firstly I would like to thank my supervisor, Vladimír Karas, for all of his helpful advice, useful ideas and pertinent comments on this text and my research from which it has germinated. I wish to thank Andrea Martocchia and Giorgio Matt for discussing the lamp-post model and polarization. Many thanks go to my colleague, Ladislav Šubr, with whom I had many long discussions and who initiated me into the great open world of Linux. I also want to thank Adela Kawka for reading the manuscript and filling in all the missing (mostly definite) articles.

I thank everyone whom I worked with at my *Alma Mater*, Charles University in Prague, and at the Institute of Astronomy in Ondřejov for their friendship. I gratefully acknowledge the support from the Czech Science Foundation grants 202/02/0735 and 205/03/0902, and from the Charles University grant GAUK 299/2004.

Last but not least, I would like to thank my parents, who supported me during the whole period of my PhD studies.



# Contents

<b>Preface</b>	<b>1</b>
<b>Introduction</b>	<b>2</b>
On black holes and accretion discs . . . . .	2
Linking theory with observation . . . . .	3
This thesis . . . . .	4
<b>1 Transfer functions for a thin disc in Kerr space-time</b>	<b>6</b>
1.1 Gravitational and Doppler shift . . . . .	8
1.2 Emission angle . . . . .	10
1.3 Gravitational lensing . . . . .	11
1.4 Relative time delay . . . . .	12
1.5 Change of polarization angle . . . . .	13
1.6 Azimuthal emission angle . . . . .	14
<b>2 Radiation of accretion discs in strong gravity</b>	<b>15</b>
2.1 Basic spectral components of X-ray sources . . . . .	16
2.2 Photon flux from an accretion disc . . . . .	18
2.3 Stokes parameters in a strong gravity regime . . . . .	21
2.4 Local emission in lamp-post models . . . . .	21
<b>3 New models for XSPEC</b>	<b>24</b>
3.1 Models for a relativistic spectral line . . . . .	27
3.1.1 Non-axisymmetric Gaussian line model KYG1LINE . . . . .	27
3.1.2 Axisymmetric Gaussian line model KYGLINE . . . . .	30
3.1.3 Non-axisymmetric fluorescent lamp-post line model KYF1LL . . . . .	32
3.2 Compton reflection models . . . . .	34
3.2.1 Non-axisymmetric lamp-post Compton reflection model KYL1CR . . . . .	34
3.2.2 Non-axisymmetric Compton reflection model KYH1REFL . . . . .	37
3.3 General relativistic convolution models . . . . .	39
3.3.1 Non-axisymmetric convolution model KYC1ONV . . . . .	39
3.3.2 Axisymmetric convolution model KYCONV . . . . .	41
3.4 Non-stationary model KYSPOT . . . . .	41
3.5 Summary of the new model . . . . .	44
<b>4 Applications</b>	<b>47</b>
4.1 Seyfert galaxy MCG-6-30-15 . . . . .	47
4.2 Relativistic spectral features from X-ray illuminated spots . . . . .	53
4.3 Polarization signatures of strong gravity in AGN accretion discs . . . . .	62

<b>Summary and future prospects</b>	<b>68</b>
<b>A Kerr space-time</b>	<b>69</b>
A.1 Kerr metric . . . . .	69
A.2 Light rays in Kerr space-time . . . . .	70
A.3 Keplerian disc in Kerr space-time . . . . .	71
A.4 Initial conditions of integration . . . . .	72
A.5 Christoffel symbols . . . . .	73
<b>B Description of FITS files</b>	<b>78</b>
B.1 Transfer functions in KBHtablesNN.fits . . . . .	78
B.2 Tables in KBHlineNN.fits . . . . .	80
B.3 Lamp-post tables in lamp.fits . . . . .	81
B.4 Coefficient of reflection in fluorescent_line.fits . . . . .	82
B.5 Tables in refspectra.fits . . . . .	83
<b>C Description of the integration routines</b>	<b>84</b>
C.1 Non-axisymmetric integration routine ide . . . . .	84
C.2 Axisymmetric integration routine idre . . . . .	86
<b>D Atlas of transfer functions</b>	<b>88</b>
g-factor . . . . .	89
Inclination $0.1^\circ$ . . . . .	89
Inclination $45^\circ$ . . . . .	90
Inclination $85^\circ$ . . . . .	91
Emission angle . . . . .	92
Inclination $0.1^\circ$ . . . . .	92
Inclination $45^\circ$ . . . . .	93
Inclination $85^\circ$ . . . . .	94
Lensing . . . . .	95
Inclination $0.1^\circ$ . . . . .	95
Inclination $45^\circ$ . . . . .	96
Inclination $85^\circ$ . . . . .	97
Relative time delay . . . . .	98
Inclination $0.1^\circ$ . . . . .	98
Inclination $45^\circ$ . . . . .	99
Inclination $85^\circ$ . . . . .	100
Change of polarization angle . . . . .	101
Inclination $0.1^\circ$ . . . . .	101
Inclination $45^\circ$ . . . . .	102
Inclination $85^\circ$ . . . . .	103
Azimuthal emission angle . . . . .	104
Inclination $0.1^\circ$ . . . . .	104
Inclination $45^\circ$ . . . . .	105
Inclination $85^\circ$ . . . . .	106
Overall transfer function . . . . .	107
Inclination $0.1^\circ$ . . . . .	107
Inclination $45^\circ$ . . . . .	108
Inclination $85^\circ$ . . . . .	109

---

Scale 1000x1000 . . . . .	110
g-factor, emission angle and lensing . . . . .	110
Rel. time delay, change of polar. angle and azimuthal emission angle . . . .	111
<b>Bibliography</b>	<b>112</b>



# Preface

Einstein's general relativity remains, after almost a century, our best theory of gravitation. Its mathematical formalism and quantitative predictions will most likely play a crucial role also in future, especially on temporal and spatial scales that are relevant for astronomical purposes. This concerns mainly the description of stellar-mass compact objects as well as dark supermassive bodies in galactic nuclei. In spite of many evident successes, the general theory of relativity has not been tested yet with sufficient accuracy in the regime of strong gravity. Nevertheless, partial observational tests have been obtained, mainly by employing the methods of X-ray spectroscopy. Some questions have been answered, while others have emerged. In the near future, improved technology will allow to perform high-throughput high-resolution spectroscopy and polarimetry in X-rays with capabilities for detailed mapping of the close neighbourhood of compact objects. In this way, physical parameters of the central compact bodies will be measured and properties of accretion flows will be studied, including the innermost regions near the black-hole horizon. The aim of the present thesis is to contribute to the effort by developing an advanced computational tool for X-ray spectro-polarimetry in a strong gravity regime.

We will turn our attention to nuclei of galaxies that harbour very massive objects, attracting a gaseous environment from their imminent surroundings. It appears beyond all reasonable doubt that these are black holes. The case for black holes residing in hearts of galaxies is not based on any single type of evidence. Instead, it is a mosaic of various observations that strongly supports the aforementioned interpretation. A similar situation arises on a vastly different scale of masses, namely in compact binary stars containing a stellar-mass accreting black hole as one of its components.

This thesis concentrates on a fragment of the whole picture. Our main goal is to discuss and improve the procedures and computational packages that are appropriate for spectroscopical studies of accreting black holes, including timing and polarimetry. The aim of this research is to discriminate between objects containing black holes from those containing other forms of compact bodies and to assess the possibility of determining physical parameters of these systems via the spectroscopy of accretion discs. We study the effects of curved space-time on light rays and specific spectral features which should arise when the gaseous environment emits radiation while falling onto the black-hole horizon. We thus develop an extended tool to fit X-ray data of real sources within a full general relativistic context.

Prague, June 2004

# Introduction

It has been established observationally that significant amounts of glowing gas is often present in the cores of galaxies. This is particularly true in the case of very bright active galactic nuclei (AGN) and also in Galactic black-hole candidates (BHC). In spite of the big scale difference between the two types of cosmic objects, we can be rather confident that the accretion of gas proceeds in disc-like configurations in both cases. However, the sizes of the discs and their geometries are often quite uncertain.

## On black holes and accretion discs

It is not so long ago that the general theory of relativity was brought to life by Albert Einstein (1916). Black holes belong to the first of its offspring, the static ones being described as early as in 1916 by Karl Schwarzschild. These objects are characterized by strong gravity and an imaginary horizon that enwraps a region from which nothing can escape, not even the light. Black holes have their ancestors in the ideas of John Michell (1784) and Pierre Simon Laplace (1796; 1799), who defined similar objects more than one century before – stars with such large masses that the escape velocity from their surface is larger than the speed of light. But this would be a different story, a Newtonian one. Soon the family of black holes grew bigger, several new types were classified – black holes with a non-zero angular momentum (Kerr 1963), with an electric charge or with a hypothetic magnetic monopole (Reissner 1916; Nordström 1918; Newman *et al.* 1965).

However, electrically charged non-rotating black holes are not of direct astrophysical interest since, if the hole is immersed in a cloud of ionized or partially ionized plasma, which is a typical situation in cosmic environments and we assume it hereafter in this work, then any excess charge becomes rapidly neutralized by selective accretion. Nevertheless, charged black holes have a role as a model for the realistic black holes formed in a spinning collapse, see Wald (1974); Blandford & Znajek (1977); Damour *et al.* (1978); Damour (1980); Price & Thorne (1986); Karas & Vokrouhlický (1991). The properties of black holes have been studied by numerous authors in various contexts; see e.g. Thorne, Price & MacDonald (1986); Kormendy & Richstone (1995); Wald (1998) for a survey of the problems and the general discussion of astrophysical connotations of black holes. As far as the Kerr (rotating) black holes are concerned, the possibility to extract its rotational energy either in the ergosphere by Penrose process (Penrose & Floyd 1971) or by Blandford-Znajek process, when the black hole is embedded in the electromagnetic field (Blandford & Znajek 1977), are really intriguing.

The problem of the origin of black holes is very exciting as well. Oppenheimer considered black holes as the last stage in the evolution of massive stars when after having burnt all their fuel neither the pressure of electrons (Chandrasekhar 1931) nor the pressure of neutrons (Oppenheimer & Volkoff 1939; Rhoades & Ruffini 1974) can stop them from collapsing. There are theories that the black holes may be nearly as old as the universe itself.

These primordial black holes (Hawking 1971) may have been the seeds for the formation of galaxies.

From the astrophysical point of view the motion of matter and the propagation of light near black holes has a special significance because the matter can emit light that can be observed and thus we can deduce what is going on out there. The emission from the stellar-mass and supermassive black holes themselves is rather low (Hawking 1975a). Many authors investigated these issues and calculated either the time-like and null geodesics in the black-hole space-times (Sharp 1979; Chandrasekhar 1983; Bičák, Semerák & Hadrava 1993) or even the more complex hydrodynamical models for the accreting matter or the outflowing wind. The spherical accretion onto the black hole was firstly considered as early as in 1944 by Bondi and Hoyle. The disc-like accretion (Lynden-Bell 1969; Pringle & Rees 1972; Novikov & Thorne 1973; Shakura & Sunyaev 1973; Shapiro, Lightman & Eardley 1976) is potentially much more efficient in converting the gravitational energy into the thermal energy which can be radiated away. It is also a more realistic configuration when we consider that the accreting matter has a non-zero angular momentum.

The family of accretion discs is quite large. Let us just mention the Shakura-Sunyaev or standard discs (SS), the advection dominated accretion flow (ADAF), the convection dominated accretion flows (CDAF), the advection dominated inflows-outflows solution (ADIOS), the Shapiro-Lightman-Eardley discs (SLE) and the slim discs. Their behaviour depends mainly on the density, pressure, viscosity and opacity of the matter that they consist of as well as on the equation of state and their accretion rate. For a basic review on accretion disc theories see e.g. Kato, Fukue & Mineshige (1998) or Frank, King & Raine (2002).

The interaction between an accretion disc and the matter above and below the disc may also play an important role in the accretion process and therefore the configuration of the black hole, accretion disc and corona seems to be more appropriate (Paczynski 1978b; Haardt & Maraschi 1993).

As can be seen from the multitude of the disc models, some of the processes involved in the accretion are quite well understood. Nevertheless, there are still many open issues, one of them being the origin of viscosity in accretion discs. Turbulence and magnetic fields may play an important role here. Another important phenomenon is the existence of jets emerging from the vicinity of the central black hole, which may be due to the interaction between the black hole and the accretion disc. To tackle these problems much more complex three dimensional numerical models of accretion discs in curved space-time with magnetic field present have to be investigated (e.g. Hawley, Gammie & Balbus 1995; Nishikawa *et al.* 2001; de Villiers & Hawley 2003).

If the disc is thick and/or dense, its own gravity, in particular farther away from the central black hole, cannot be neglected. These self-gravitating discs were investigated by various authors in various approximations, starting with Ostriker (1964), Bardeen (1973), Fishbone & Moncrief (1976), Paczynski (1978a) and Karas, Lanza & Vokrouhlický (1995). A very useful and pertinent review of this subject was recently written by Karas, Huré & Semerák (2004).

## Linking theory with observation

Last century was rich in discovering highly energetic and violent objects in astronomy. In 1918 Curtis discovered a long jet of material coming out from elliptical galaxy M87. Later, galaxies with particularly bright and compact nuclei were observed (Seyfert 1943)

and they were classified as a new type of galaxies, the so-called Seyfert galaxies. But truly amazing discoveries came when radio astronomy fully developed. When quasars were observed for the first time in 1960s, they were called radio stars (Matthews *et al.* 1960; Matthews & Sandage 1962) because their emission in the radio part of the spectrum was enormous and they appeared like point sources. It was three years later that Schmidt (1963) realized that these objects were not hosted by our Galaxy but that they were rather distant extragalactic objects with highly redshifted spectral lines. Since then many strange radio sources with jets and lobes of various shapes and sizes have been discovered, mostly associated with optical extragalactic objects – centres of distant galaxies. The luminosity, size and variability of these sources indicate that highly energetic processes were once at work there. Because of their huge activity they are called active galactic nuclei. In 1960s it was realized that the only reasonable way of explaining the production of such large amounts of energy was to be sought in the gravitational energy conversion by means of an accreting massive black hole (Salpeter 1964; Zeldovich & Novikov 1964).

A new branch of astronomy has emerged, in which many novel discoveries were made: it was the X-ray astronomy and it developed quickly. The first observations were made by Geiger counters carried by rockets in 1950s and balloons in 1960s and later by specially designed X-ray astronomy satellites that have been orbiting the Earth since 1970s. The first Galactic X-ray source was discovered in 1962 – a neutron star Sco X-1 (Giacconi *et al.* 1962). Soon more discoveries followed, X-ray binary source Cygnus X-1 (Bowyer *et al.* 1965) being one of them. The fact that this object is a strong X-ray emitter and that the optical and X-ray emission varies on very short time scales (as short as one thousandth of a second) suggests that the companion might be a black hole. Many Galactic objects (most of them binaries containing neutron stars) and active galactic nuclei emitting X-rays have been observed since then. It is believed that AGN sources host a supermassive black hole with a mass of approximately  $10^6 - 10^8 M_\odot$  and that some of the Galactic X-ray binaries contain a black hole with the mass equal to several solar masses.

A breakthrough has come with the two most recent X-ray satellites, *Chandra* and *XMM-Newton*, which provide us with the most detailed images and spectra with an unprecedented resolution. Some of the observed objects exhibit redshifted, broad or narrow features in their spectra, thus suggesting that the emission is coming from the very close vicinity of a black hole. But still, the data acquired by the instruments on board these satellites are not as complete and detailed as would be necessary for an unambiguous interpretation and comparison with the theoretical models. New X-ray missions are being planned – *Astro-E2* (already being assembled), *Constellation-X* and *Xeus*. Hopefully, with the data measured by the satellites involved in these observations, it will be possible not only to decide whether there is a black hole in the observed system but also to determine its properties, its mass and angular momentum, as well as the properties of the surrounding accretion disc.

## This thesis

Nowadays both the theory describing accreting black-hole systems and the instruments for observing such objects are quite advanced. Computational tools for comparing acquired data with theories have been developed to such an advanced state that we are able now to find out properties of particular observed systems on the one hand and check if our models are good enough for describing these systems on the other. One of the tools used for processing X-ray data, which also implements the possibility to fit the data

within a certain set of models,<sup>1</sup> is XSPEC. This X-ray spectral fitting package contains various models for explaining the measured spectra but it lacks fully general relativistic models. One of the aims of this thesis has been to help to fill this gap and provide new general relativistic models that would be fast and flexible enough and would be able to fit parameters describing a black hole, mainly its mass and angular momentum. Although it is not possible to fit time resolved data within XSPEC and polarimetric data have not been available for X-ray sources yet (though they may become available when future X-ray missions materialize), we developed new models able to deal also with these issues.

Our objective is to model X-ray spectra from accretion discs near compact objects. The observed spectrum depends not only on the local radiation emitted from the disc but it is also affected by strong gravitation on its way to the observer. Emission from different parts of the disc may be either amplified or reduced by gravitational effects. We will focus our attention on these effects in Chapter 1, where we deal with calculations of six functions that are needed for the integration of the total spectra of the accretion disc (including time varying spectra and polarimetric information). These functions include the Doppler and gravitational shifts, gravitational lensing, relative time delay, two emission angles and change of the polarization angle.

The basic types of local emission coming from an accretion disc are summarized in Chapter 2, where also the equations for the observed flux and polarization at infinity are derived.

In Chapter 3 we describe new KY models that we have developed and that can be used either inside XSPEC or as standalone programs for studying the non-stationary emission from accretion discs or for studying polarimetry. These are models for a general relativistic line and Compton reflection continuum, general convolution models and a model for an orbiting spot. We also compare these models with some of the models already present in XSPEC.

Some applications of the new models are summarized in Chapter 4. Firstly, we employ the models to high-quality X-ray data that are currently available for the Seyfert galaxy MCG-6-30-15. Then we calculate the flux from X-ray illuminated orbiting spot and polarization from an accretion disc illuminated from a primary source located above the black hole.

There are several appendixes in this thesis. There is a summary of the basic equations for Kerr space-time in Appendix A. Appendix B describes the layout of data files used in this thesis. A detailed description of the integration routines that we have developed and that can be used inside the XSPEC framework for general relativistic computations is included in Appendix C. In Appendix D an atlas of contour figures of all transfer functions is shown.

This thesis describes my original work except where references are given to the results of other authors. Parts of the research were carried out in collaboration and published in papers, as indicated in the text. In particular, various features and usage of the newly developed code have been described in Dovčiak, Karas & Yaqoob (2004) and Dovčiak *et al.* (2004b). Chapter 4 is based on papers Dovčiak, Karas & Matt (2004); Dovčiak, Karas & Yaqoob (2004) and Dovčiak *et al.* (2004a). Another application to random emitting spots in the accretion disc can be found in Czerny *et al.* (2004) but it is not included in the present thesis.

---

<sup>1</sup>Notice that, in accordance with traditional terminology, we use the term ‘model’ in two slightly different connotations: first, it can mean a physical model of an astronomical system or a process that is under discussion; other possible meaning of the word is more technical, referring to a computational representation, or a routine that is employed in order to compare actual observational data with the theory.

# Chapter 1

## Transfer functions for a thin disc in Kerr space-time

Photons emitted from an accretion disc are affected by gravitation in several ways. They change their energy due to the gravitational and Doppler shifts because photons are emitted by matter moving close to the source of strong gravitation. The cross-section of light tube changes as the photons propagate in the curved space-time. This effect is strongest for high inclinations of the observer when trajectories of photons coming from behind the black hole are bent very much. Bending of light also influences the effective area from which photons arrive due to different emission angles. Here, aberration caused by motion of the disc matter plays its role as well. All three of these effects, the  $g$ -factor, lensing and emission angle, influence the intensity of light that the observer at infinity measures.

If the local emission from the disc is non-stationary one must take into account the relative delay with which photons from different parts of the disc arrive to the observer. A part of the local emission may be due to the reflection of the light incident on the disc from the corona above. In this case the disc radiation may be partially polarized. The polarization vector changes as the light propagates through the curved space-time. The change of polarization angle that occurs between the emission of light at the disc and its reception by the observer at infinity is needed for calculation of the overall polarization that the observer measures. When calculating the local polarization we need to know the geometry of incident and emitted light rays. Therefore we need to know also the azimuthal emission angle of the emitted photons. Thus six functions are necessary to transfer the local flux to the observer at infinity. The exact definitions for all of them will be given in next sections. For simplicity we will refer to them as transfer functions.

Various authors have computed radiation from matter moving around a black hole in different approximations and in different parameter space. De Felice, Nobili & Calvani (1974) computed the effects of gravitational dragging on the electromagnetic radiation emitted by particles moving on bound orbits around a Kerr black hole. Cunningham (1975) studied the combined effects of the gravitational and Doppler shifts together with the gravitational lensing effect on the X-ray radiation from an accretion disc in the strong gravitational field of a black hole. He introduced a concept of a transfer function where he includes all of the above-mentioned effects into a single function that describes the overall influence of the gravitational field on light rays emerging from the disc. He also studied self-irradiation of the disc and its impact on the disc emission (Cunningham 1976). Since then numerous authors have investigated emission from disc (line,

blackbody, reflected, etc.) in strong gravity – Gerbal & Pelat (1981); Asaoka (1989); Fabian *et al.* (1989); Kojima (1991); Laor (1991); Karas, Vokrouhlický & Polnarev (1992); Viergutz (1993); Bao, Hadrava & Østgaard (1994); Hameury, Marck & Pelat (1994); Zakharov (1994); Speith, Riffert & Ruder (1995); Bromley, Chen & Miller (1997); Martocchia, Karas & Matt (2000); Čadež, Calvani & Fanton (2003); Beckwith & Done (2004). In the situation when full spectral resolution is not available, power spectra of light curves provide us with partial information on the emission from accretion discs (see e.g. Abramowicz *et al.* 1991; Schnittman & Bertschinger 2004). Other works also included the studies of net polarization from accretion discs, here we should mention Connors, Piran & Stark (1980); Laor, Netzer & Piran (1990); Chen & Eardley (1991); Matt (1993); Matt, Fabian & Ross (1993); Agol (1997); Bao *et al.* (1997); Ogura, Ohuo & Kojima (2000). All of the above-mentioned authors used various methods for computing the transfer of photons from the accretion disc to the observer far away from the central black hole. Some of them assumed the black hole to be non-rotating, others performed their calculations for a rotating Kerr black hole. Karas, Lanza & Vokrouhlický (1995) and Usui, Nishida & Eriguchi (1998) explored a substantially more complex case when self-gravity of the disc is not neglected and photons move in a space-time, the metric of which is itself derived from a numerical solution of Einstein’s equations. Similar approach is appropriate also for ray-tracing in the field of a fast rotating neutron star, and in this way these techniques are pertinent to the study of sources of quasi-periodic oscillations in X-ray binaries.

Our numerical codes for computing the emission from accretion discs (see Chapter 3) have to be fast, so that they are suitable for fitting data. That is the reason for which we have decided to pre-calculate the transfer functions and store them in the form of tables in a FITS<sup>1</sup> file (see Appendix B). We have chosen to compute the transfer of photons from the infinity (represented by setting the initial radius  $r_i = 10^{11}$  in our numerical calculations) to the disc numerically by solving the equation of the geodesic. For this purpose the Bulirsch-Stoer method of integration has been used (alternatively, the semi-analytical method of elliptical integrals could be used, see e.g. Rauch & Blandford 1994). An optically thick and geometrically thin flat disc has been assumed. Only null geodesics starting at the observer at infinity and ending at the equatorial plane of the black hole, without crossing this plane, has been taken into account (higher order images of the disc have not been computed). The Kerr space-time has been assumed and the medium between the disc and the observer has been supposed to be optically thin for the wavelengths that we are interested in (X-rays in our case). Special Kerr ingoing coordinates, which are non-singular on the horizon and bring spatial infinity to a finite value (to zero), have been used (see Appendix A). This has enabled us to calculate the transfer functions with a high precision even very close to the horizon of the black hole. By using these coordinates the Boyer-Lindquist azimuthal coordinate  $\varphi$  has been unfolded to the Kerr coordinate  $\varphi_K$ , which is more precise when interpolating between the computed values on the disc. Some of the transfer functions depend on the motion of the matter in the disc, which has been assumed to be Keplerian above the marginally stable orbit  $r_{ms}$  and freely falling below it, where it has the same energy and angular momentum as the matter which is on the marginally stable orbit. All of the transfer functions except lensing have been actually calculated analytically (see formulae in the next sections) but with the numerical mapping of the impact parameters  $\alpha$  and  $\beta$  to the disc coordinates  $r$  and  $\varphi_K$ . The lensing has

---

<sup>1</sup>Flexible Image Transport System. See e.g. Hanisch *et al.* (2001) or <http://fits.gsfc.nasa.gov/> for specifications.

been computed by numerical integration of the equation of the geodesic deviation by the same method as described above. The initial conditions for the numerical integration are summarized in Appendix A.4. In numerical computations, approximately  $10^5$  geodesics have been integrated. They have covered the disc from the horizon to an outer radius of  $r_{\text{out}} \sim 1000$  in such a way that the region closest to the horizon has been most densely covered. Thus we have obtained values of transfer functions on a non-regular grid over the disc which have been interpolated to a regular grid in  $r$  and  $\varphi_K$  coordinates using Delaunay triangulation. Graphical representation of the transfer functions can be seen in Appendix D.

In the following sections we summarize the equations used for the evaluation of particular transfer functions over the disc. In this chapter as well as everywhere else in the thesis we use units where  $GM_\bullet = c = 1$  with  $M_\bullet$  being the mass of the central black hole.

## 1.1 Gravitational and Doppler shift

The four-momentum of the photons emitted from the disc is given by (see e.g. Carter 1968 and Misner, Thorne & Wheeler 1973)

$$p_e^t = [a(l - a) + (r^2 + a^2)(r^2 + a^2 - al)/\Delta]/r^2, \quad (1.1)$$

$$p_e^r = R_{\text{sgn}}\{(r^2 + a^2 - al)^2 - \Delta[(l - a)^2 + q^2]\}^{1/2}/r^2, \quad (1.2)$$

$$p_e^\theta = -q/r^2, \quad (1.3)$$

$$p_e^\varphi = [l - a + a(r^2 + a^2 - al)/\Delta]/r^2, \quad (1.4)$$

where  $a$  is the dimensionless angular momentum of the black hole ( $0 \leq a \leq 1$ ). In eqs. (1.1)–(1.4) we employed usual notation (see Appendix A for the exact meaning of the quantities).

The combined gravitational and Doppler shift ( $g$ -factor) is defined as the ratio of the energy of a photon received by an observer at infinity to the local energy of the same photon when emitted from an accretion disc

$$g = \frac{\nu_o}{\nu_e} = \frac{p_{ot}}{p_{e\mu}U^\mu} = -\frac{1}{p_{e\mu}U^\mu}. \quad (1.5)$$

Here  $\nu_o$  and  $\nu_e$  denote the frequency of the observed and emitted photons respectively, and  $U^\mu$  is a four-velocity of the matter in the disc.

Contour graphs of the  $g$ -factor in Appendix D show that the effect of rotation of the black hole is visible only in its vicinity ( $r \lesssim 10$ ). Near the horizon the  $g$ -factor decreases down to zero due to the gravitational redshift, whereas far from the black hole the Doppler shift prevails. Very far from the black hole, where matter of the disc rotates slowly, the  $g$ -factor goes to unity.

Preliminary considerations on the line emission (its energy shift and its width) can be based on the extremal values of the energy shift,  $g_+$  and  $g_-$ , which photons experience when arriving at the observer's location from different parts of the disc. This is particularly relevant for some narrow lines whose redshift can be determined more accurately than if the line is broad (e.g. Turner *et al.* 2002; Guainazzi 2003; Yaqoob *et al.* 2003). Careful discussion of  $g_\pm$  can, in principle, circumvent the uncertainties which are introduced by the uncertain form of the intrinsic emissivity of the disc and yet still constrain some of parameters. Advantages of this technique were pointed out already by Cunningham (1975) and it was further developed by Pariev, Bromley & Miller (2001).

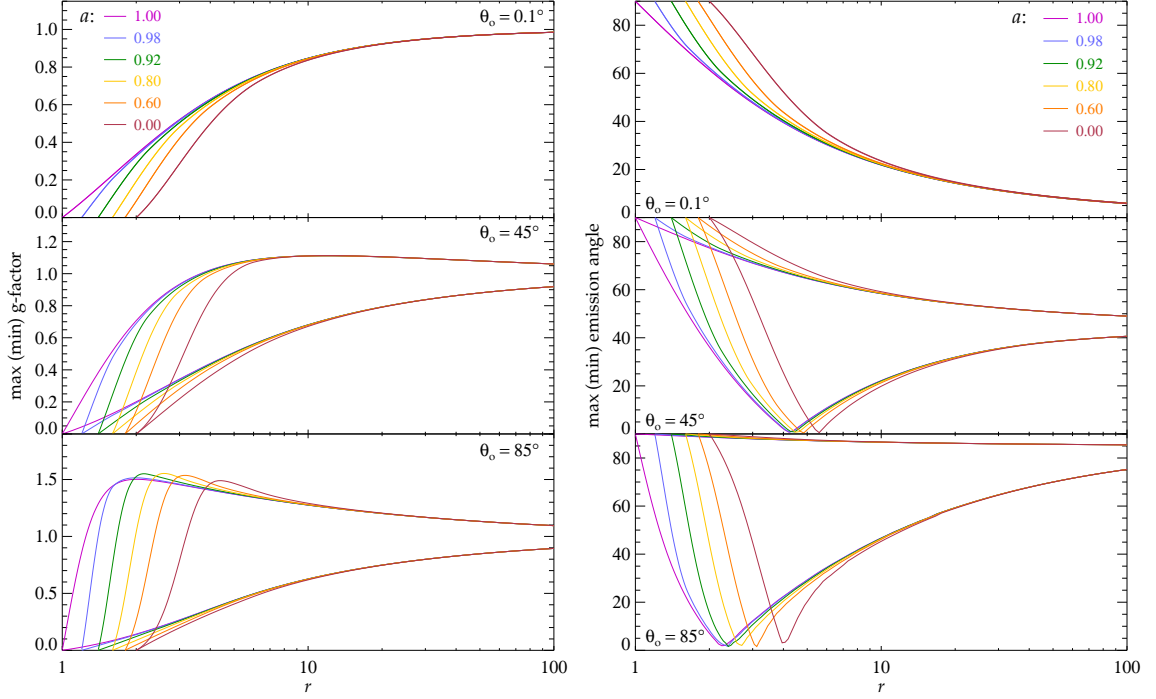


Figure 1.1: Maximum and minimum values of energy shift (left) and emission angle (right) of photons originating from different radii in the disc. The dependence on the black-hole angular momentum,  $a$ , is shown for three different inclination angles,  $\theta_o = 0.1^\circ$ ,  $45^\circ$  and  $85^\circ$ . Each curve corresponds to a fixed value of  $a$  in the range  $(0, 1)$ , encoded by line colours.

Fig. 1.1 shows the extremal values of the redshift factor for the observer inclinations  $\theta_o = 0.1^\circ, 45^\circ$  and  $85^\circ$ . These were computed along circles with radius  $r$  in the disc plane. Corresponding contour lines of constant values of  $g_\pm$  in the plane  $a$  versus  $r$  can be seen in Fig. 1.2. In other words, radiation is supposed to originate from radius  $r$  in the disc, but it experiences a different redshift depending on the polar angle. Contours of the redshift factor provide a very useful and straightforward technique to determine the position of a flare or a spot, provided that a narrow spectral line is produced and measured with sufficient accuracy. The most direct use of extremal  $g$ -values would be if one were able to measure variations of the line profile from its lowest-energy excursion (for  $g_-$ ) to its highest-energy excursion (for  $g_+$ ), i.e. over a complete cycle. Even partial information can help to constrain models (for example, the count rate is expected to dominate the observed line at the time that  $g = g_+$ , and so the high-energy peak is easier to detect). While it is very difficult to achieve sufficient precision on the highly shifted and damped red wing of a broad line, prospects for using narrow lines are indeed interesting, provided that they originate close enough to the black hole and that sufficient resolution is achieved both in the energy and time domains.

Fig. 1.2 also makes it clear that it is possible in principle (but intricate in practice) to deduce the  $a$ -parameter value from spectra. It can be seen from the redshift factor that the dependence on  $a$  is rather small and it quickly becomes negligible if the light from the source is dominated by contributions from  $r \gtrsim 10$ .

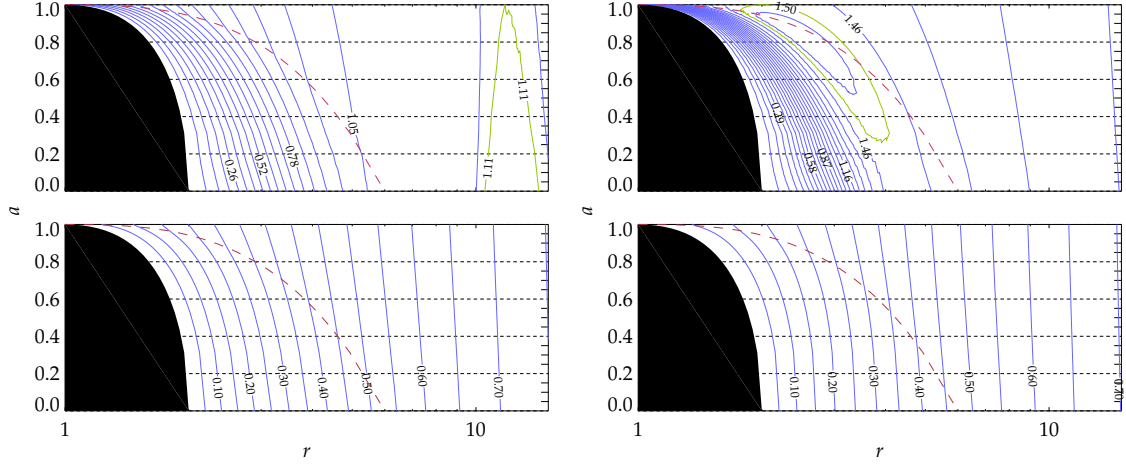


Figure 1.2: Contour lines of extremal energy shift factors in the plane of the rotation parameter  $a$  versus radius  $r$  for observer inclination  $\theta_o = 45^\circ$  (left) and  $85^\circ$  (right). Maximum  $g$ -factor is shown at the top, minimum  $g$ -factor at the bottom. Radius is in units of  $GM/c^2$ . The horizon is shown in black. The curve  $a(r)|_{r=r_{\text{ms}}}$  (dashed) is also plotted across the contour lines. Notice that, in the traditional disc-line scheme, no radiation is supposed to originate from radii below marginally stable orbit  $r_{\text{ms}}$ . If this is the case then one must assume that all photons originate outside the dashed curve and so the effect of frame-dragging is further reduced.

## 1.2 Emission angle

Here we examine the angle of emission with respect to the disc normal. We assume the local frame co-moving with the medium of the disc. The cosine of the local emission angle is

$$\mu_e = \cos \delta_e = -\frac{p_{e\alpha} n^\alpha}{p_{e\mu} U^\mu}, \quad (1.6)$$

where  $n^\alpha = -e_{(\theta)}^\alpha$  are components of the disc normal.

One can see from contours of  $\mu_e$  plotted in the disc plane (Appendix D) and from graphs of its maximum and minimum values (Fig. 1.1) that gravitation influences visibly only those light rays that pass close to the black hole on their way to the observer, and especially for large inclination angles. Due to the effect of light bending and aberration there exists a point on the disc where the emission angle is zero, i.e. the local direction of the emission is perpendicular to the disc surface. On the other hand, near the horizon only the light rays emitted almost parallel to the disc plane can reach the observer. Very far from the black hole, where matter rotates slowly, the emission angle is determined mainly by special-relativistic aberration and it gradually approaches the value of the observer inclination.

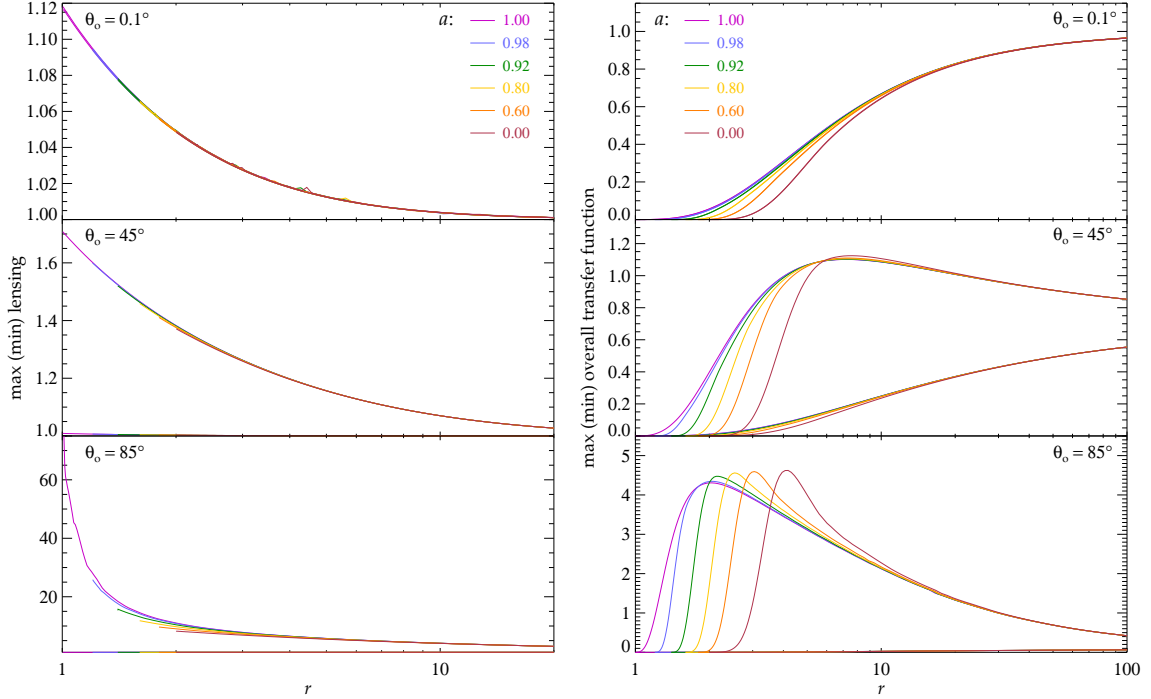


Figure 1.3: Same as in Fig. 1.1 but for lensing (left) and overall transfer function (right).

### 1.3 Gravitational lensing

We define lensing as the ratio of the cross-section  $dS_f$  of the light tube at infinity to the cross-section  $dS_\perp$  of the same light tube at the disc:

$$l = \frac{dS_f}{dS_\perp} = \frac{1}{\sqrt{\|Y_{e1}\|^2 \|Y_{e2}\|^2 - \langle Y_{e1}, Y_{e2} \rangle^2}}. \quad (1.7)$$

The four-vectors  $Y_{e1}$  and  $Y_{e2}$  are transported along the geodesic according to the equation of the geodesic deviation from infinity where they are unit, space-like and perpendicular to each other and to the four-momentum of light (for the exact definition of these vectors very far from the black hole see Appendix A.4). In eq. (1.7) we have denoted the magnitude of a four-vector by  $\| \cdot \|$  and scalar product of two four-vectors by  $\langle \cdot, \cdot \rangle$ . The cross section of light tube is constant for all observers (see Schneider, Ehlers & Falco 1992).

Lensing can significantly amplify the emission from some parts of the disc (located behind the black hole from the point of view of the observer and in Kerr ingoing coordinates). This is true mainly for observers with large inclination angles (see figures in Appendix D and Fig. 1.3).

When one wants to estimate the total effect that gravitation has on the intensity of light coming from different parts of the disc, one has to take into account all the three effects – the  $g$ -factor, the emission angle and the lensing. These effects combine into a single function defined by (see eq. (2.11))

$$F = g^2 \mu_e l. \quad (1.8)$$

We call it the overall transfer function. See contour graphs in Appendix D and plots in Fig. 1.3 for the total gravitational amplification of photon flux emitted from a Keplerian accretion disc.

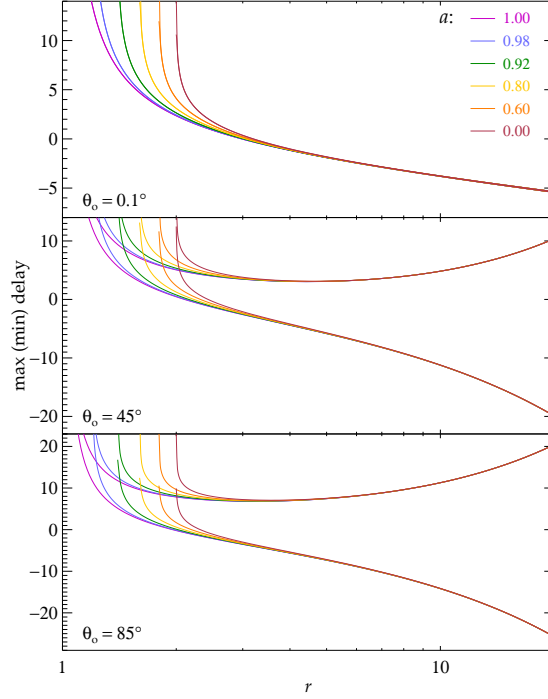


Figure 1.4: Same as in Fig. 1.1 but for maximum and minimum relative time delay.

## 1.4 Relative time delay

The relative time delay  $\Delta t$  is the Boyer-Lindquist time which elapses between the emission of a photon from the disc and its reception by an observer (plus a certain constant so that the delay is finite close to the black hole but not too close). We integrate the equation of the geodesic in Kerr ingoing coordinates and thus we calculate the delay in the Kerr ingoing time coordinate  $\Delta t_K$ . The Boyer-Lindquist time can be obtained from  $\Delta t_K$  using the following equation:

$$dt = dt_K - \left[ 1 + \frac{2r}{(r - r_+)(r - r_-)} \right] dr, \quad (1.9)$$

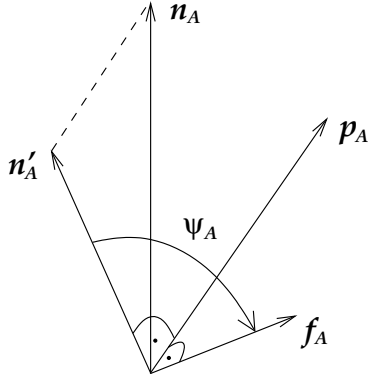
with  $r_{\pm} = 1 \pm \sqrt{1 - a^2}$  being inner  $(-)$  and outer  $(+)$  horizon of the black hole. Then we integrate the above equation and define the time delay as

$$\Delta t = \Delta t_K - \left[ r + \frac{2}{r_+ - r_-} \ln \frac{r - r_+}{r - r_-} + \ln [(r - r_+)(r - r_-)] \right] \quad \text{for } a < 1, \quad (1.10)$$

$$\Delta t = \Delta t_K - \left[ r - \frac{2}{r - 1} + 2 \ln (r - 1) \right] \quad \text{for } a = 1. \quad (1.11)$$

There is a minus sign in front of the brackets because the direction of integration is from infinity to the disc.

For contour graphs of the relative time delay see figures in Appendix D and for plots of maximum and minimum delay at a constant radius see Fig. 1.4.



- (i) Let three-vectors  $\mathbf{p}_A$ ,  $\mathbf{n}_A$ ,  $\mathbf{n}'_A$  and  $\mathbf{f}_A$  be the momentum of a photon, normal to the disc, projection of the normal to the plane perpendicular to the momentum and a vector which is parallelly transported along the geodesic (as four-vector), respectively;
- (ii) let  $\Psi_A$  be an angle between  $\mathbf{n}'_A$  and  $\mathbf{f}_A$ ;
- (iii) let the quantities in (i) and (ii) be evaluated at the disc for  $A = 1$  with respect to the local rest frame co-moving with the disc, and at infinity for  $A = 2$  with respect to the stationary observer at the same light geodesic;
- (iv) then the change of polarization angle is defined as  $\Psi = \Psi_2 - \Psi_1$ .

Figure 1.5: Definition of the change of polarization angle  $\Psi$ .

## 1.5 Change of polarization angle

Various physical effects can influence polarization of light as it propagates towards an observer. Here we examine only the influence of the gravitational field represented by the vacuum Kerr space-time. The change of the polarization angle is defined as the angle by which a vector parallelly transported along the light geodesic rotates with respect to some chosen frame. We define it in this way because in vacuum the polarization vector is parallelly transported along the light geodesic. This angle depends on the choice of the local frame at the disc and at infinity. See Fig. 1.5 for an exact definition.

The change of polarization angle is (see Connors & Stark 1977; Connors, Piran & Stark 1980)

$$\tan \Psi = \frac{Y}{X}, \quad (1.12)$$

where

$$X = -(\alpha - a \sin \theta_o) \kappa_1 - \beta \kappa_2, \quad (1.13)$$

$$Y = (\alpha - a \sin \theta_o) \kappa_2 - \beta \kappa_1, \quad (1.14)$$

with  $\kappa_1$  and  $\kappa_2$  being components of the complex constant of motion  $\kappa_{\text{pw}}$  (see Walker & Penrose 1970)

$$\kappa_1 = ar p_e^\theta f^t - r [a p_e^t - (r^2 + a^2) p_e^\varphi] f^\theta - r(r^2 + a^2) p_e^\theta f^\varphi, \quad (1.15)$$

$$\kappa_2 = -r p_e^r f^t + r [p_e^t - a p_e^\varphi] f^r + ar p_e^r f^\varphi. \quad (1.16)$$

Here the polarization vector  $f^\mu$  is a four-vector corresponding to the three-vector  $\mathbf{f}_1$  from Fig. 1.5 which is chosen in such a way that it is a unit vector parallel with  $\mathbf{n}'_1$  (i.e.  $\Psi_1 = 0$ )

$$f^\mu = \frac{n^\mu - \mu_e (g p_e^\mu - U^\mu)}{\sqrt{1 - \mu_e^2}}. \quad (1.17)$$

For contour graphs of the change of the polarization angle see figures in Appendix D.

## 1.6 Azimuthal emission angle

We define the azimuthal emission angle as the angle between the projection of the three-momentum of the emitted photon into the equatorial plane (in the local rest frame co-moving with the disc) and the radial tetrad vector:

$$\Phi_e = \arctan \frac{p_e^\alpha e_{(\varphi)\alpha}}{p_e^\mu e_{(r)\mu}} = \arctan \left( g \frac{\Delta}{r} \frac{-p_e^t U^\varphi + p_e^\varphi U^t}{g p_e^r - U^r} \right). \quad (1.18)$$

The explicit formula for this angle is not necessary for computations of light curves and spectral profiles, but it appears in discussions of polarimetry. This is also the reason why we have computed  $\Phi_e$ . Like the quantities discussed previously, the resulting values of the azimuthal angle depend on the adopted geometry of the source and the rotation law of the medium. They are determined by mutual interplay of special- and general-relativistic effects. Therefore, we remind the reader that our analysis applies to geometrically thin Keplerian discs residing in the equatorial plane, although generalization to more complicated situations should be fairly straightforward. For contour graphs of the change of the azimuthal emission angle see figures in Appendix D.

## Chapter 2

# Radiation of accretion discs in strong gravity

There is now plausible evidence that the emission in some active galactic nuclei and some Galactic X-ray binary black-hole candidates originates, at least in part, from an accretion disc in a strong gravitational field. A lively debate is aimed at addressing the question of what the spectral line profiles and the associated continuum can tell us about the central black hole, and whether they can be used to constrain parameters of the accretion disc in a nearby zone, about ten gravitational radii or less from the centre. For a recent review of AGNs see Fabian *et al.* (2000); Reynolds & Nowak (2003), and references cited therein. For BHCs see Miller *et al.* (2002); McClintock & Remillard (2003) and references therein. In several sources there is indication of iron  $K\alpha$  line emission from within the last stable orbit of a Schwarzschild black hole, e.g. in the Seyfert galaxy MCG-6-30-15 (see Iwasawa *et al.* 1996; Fabian *et al.* 2000; Wilms *et al.* 2001; Martocchia, Matt & Karas 2002) or from the region near above the marginally stable orbit, as in the case of the X-ray transient source XTE J1650-500 (Miniutti, Fabian & Miller 2004) that has been identified with a Galactic black-hole candidate. In other cases the emission appears to arise farther from the black hole (e.g. in the microquasar GRS 1915+105, see Martocchia *et al.* 2002; for AGNs see Yaqoob & Padmanabhan 2004 and references therein). Often, the results from X-ray line spectroscopy are inconclusive, especially in the case of low spectral resolution data. For example, a spinning black hole is allowed but not required by the line model of the microquasar V4641 Sgr (Miller *et al.* 2002). The debate still remains open, but there are good prospects for future X-ray astronomy missions to be able to use the iron  $K\alpha$  line to probe the space-time in the vicinity of a black hole, and in particular to measure the angular momentum, or the spin, associated with the metric.

One may also be able to study the ‘plunge region’ (about which very little is known), between the event horizon and the last stable orbit, and to determine if any appreciable contribution to the iron  $K\alpha$  line emission originates from there (Reynolds & Begelman 1997; Krolik & Hawley 2002). In addition to the Fe K lines, there is some evidence for relativistic soft X-ray emission lines due to the  $Ly\alpha$  transitions of oxygen, nitrogen, and carbon (Mason *et al.* 2003), although the observational support for this interpretation is still controversial (Lee *et al.* 2001).

With the greatly enhanced spectral resolution and throughput of future X-ray astronomy missions, the need arises for realistic theoretical models of the disc emission and computational tools that are powerful enough to deal with complex models and to allow

Model	Effects that are taken into account					
	Energy shift/ Lensing effect	$a$	Non-axisymmetric emission region	Emission from plunge region	Timing	Polarization
DISKLINE	yes/no	0	no	no	no	no
LAOR	yes/yes	0.998	no	no	no	no
KERRSPEC	yes/yes	$\langle 0, 1 \rangle^\dagger$	yes	no	no	no
KY	yes/yes	$\langle 0, 1 \rangle$	yes <sup>‡</sup>	yes	yes	yes

<sup>†</sup> The value of the dimensionless  $a$  parameter is kept frozen.

<sup>‡</sup> A one-dimensional version is available for the case of an axisymmetric disc. In this axisymmetric mode, KY still allows  $a$  and other relevant parameters to be fitted (in which case the computational speed of KY is then comparable to LAOR). The results can be more accurate than those obtained with other routines because of the ability to tune the grid resolution.

Table 2.1: Basic features of the new model in comparison with other black-hole disc-line models. For references see Fabian *et al.* (1989), Laor (1991), Martocchia, Karas & Matt (2000) and Dovčiak *et al.* (2004b), respectively.

actual fitting of theoretical models to observational data. It is worth noting that some of the current data have been used to address the issue of distinguishing between different space-time metrics around a black hole, however, the current models available for fitting X-ray data are subject to various restrictions.

In this chapter and the next one we describe a generalized scheme and a code which can be used with the standard X-ray spectral fitting package XSPEC (Arnaud 1996). We have in mind general relativity models for black-hole accretion discs. Apart from a better numerical resolution, the principal innovations compared to the currently available schemes (see Tab. 2.1) are that the new model allows one to (i) fit for the black-hole spin, (ii) study the emission from the plunge region, and (iii) specify a more general form of emissivity as a function of the polar coordinates in the disc plane (both for the line and for the continuum). Furthermore, it is also possible to (iv) study time variability of the observed signal and (v) compute Stokes parameters of a polarized signal. Items (i)–(iii) are immediately applicable to current data and modelling, while the last two mentioned features are still mainly of theoretical interest at the present time. Time-resolved analysis and polarimetry of accretion discs are directed towards future applications when the necessary resolution and the ability to do polarimetry are available in X-rays. Thus our code has the advantage that it can be used with time-resolved data for reverberation studies of relativistic accretion discs (Stella 1990; Reynolds *et al.* 1999; Ruszkowski 2000; Goyder & Lasenby 2004). Also polarimetric analysis can be performed, and this will be extremely useful because it can add very specific information on strong-gravitational field effects (Connors, Piran & Stark 1980; Matt, Fabian & Ross 1993; Bao *et al.* 1997). Theoretical spectra with temporal and polarimetric information can be analysed with the current version of our code and such analysis should provide tighter constraints on future models than is currently possible.

## 2.1 Basic spectral components of X-ray sources

There are several components in the spectra of X-ray sources. Not all of them are always present and some of them are more prominent in certain objects than the others.

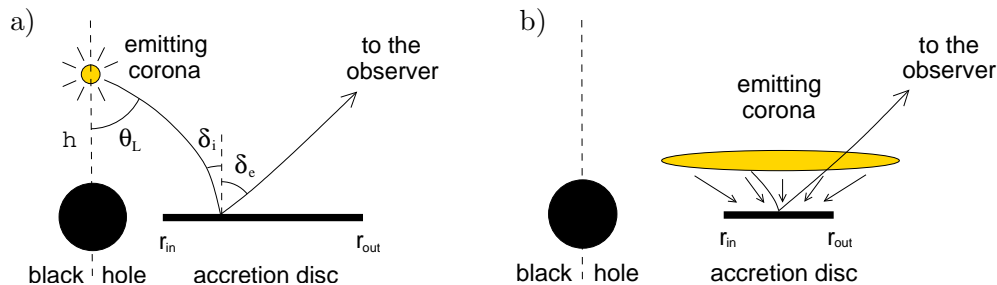


Figure 2.1: Reflection models: a) lamp-post model; b) diffuse corona model.

One of the characteristic spectral features that is almost always present is a power-law component. It is assumed that this feature results from inverse Compton scattering of thermal photons in a hot corona above the accretion disc. Usually two different configurations are considered. The first one assumes a patch of hot corona placed on the rotational axis of the central black hole at some height above it (lamp-post model). It is usually supposed to be an isotropic and point-like source of stationary primary power-law emission. The second configuration is a diffuse optically thin hot corona near above the accretion disc. For simple sketches of both configurations see Fig. 2.1. In both cases the shape of this primary power-law continuum (in the rest frame of the corona) is not affected by the relativistic effects acting on photons during their journey to the observer at infinity. These effects change only the normalization of the spectra. This component extends up to a cut-off energy of some tenths or a few hundreds keV.

Often, mainly in the spectra of active galactic nuclei, additional continuum emission, a “hump”, is added to the primary component. It is assumed that this is due to the reflection of the primary emission from the illuminated disc. The shape of the reflected continuum in the local rest frame co-moving with the accretion disc depends mainly on photoelectric absorption and Compton scattering of photons hitting the disc. The local emission is then smeared by relativistic effects – this concerns mainly its sharp features (e.g. iron edge). The shape of the observed spectra also depends on the illumination of the disc. This differs for the lamp-post model and the diffuse corona model. In the former case the radial dependence of illumination is determined by the height at which the patch of corona is placed. In the latter case the illumination of the disc depends on the emissivity of the diffuse corona near above the disc which may have quite a complicated radial dependence (but usually is assumed to be decreasing with radius as a power law).

Spectral lines are an important feature observed in X-ray spectra. We assume that the origin of lines is the same as in the previous case – the illumination of the cold disc by primary (power-law) emission and reflection, in this case, by fluorescence. Originally narrow spectral lines are blurred by relativistic effects and thus they become broad, their width being as large as several keV in several sources. The most prominent examples are the iron lines  $K\alpha$  and  $K\beta$ .

In the present thesis we are concerned with the spectral components described above but here, we should not omit to mention other two important components – the thermal emission and the warm absorber. The thermal emission is more noticeable in the spectra of X-ray binaries with the black-hole candidate as the central object. This is due to the fact that in these sources the temperature of the accretion disc is much higher and therefore the black body emission extends as far as the soft X-ray energy band. This type of emission

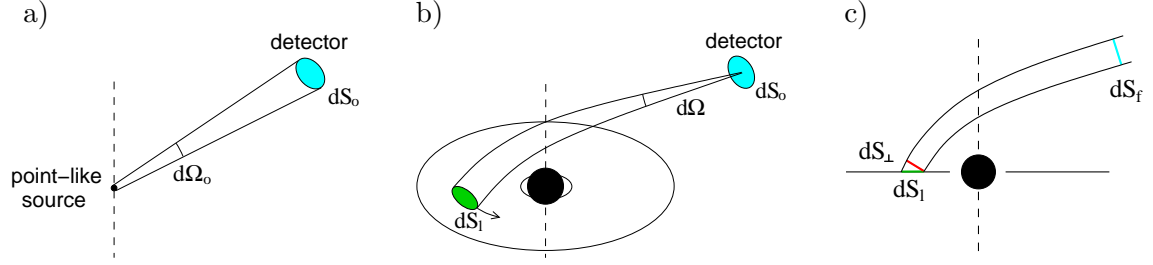


Figure 2.2: Denomination of various elements of solid angles and areas defined in the text: a) the light source appears to the observer to be point-like; b) the light rays received by the detector are coming from different parts of the disc (closer view of the disc than in previous figure); c) area of a light tube changes as the light rays travel close to the black hole (the disc is edge on).

manifests itself in the spectra of active galactic nuclei as a “big blue bump” in the optical and UV frequencies.

If there is ionized matter, a warm absorber, in the line of sight of the observer then the absorption spectral features are present in the observed spectra. These can include edges or resonant absorption lines due to oxygen and other ions.

## 2.2 Photon flux from an accretion disc

Properties of radiation are described in terms of photon numbers. The source appears as a point-like object for a distant observer, so that the observer measures the flux entering the solid angle  $d\Omega_o$ , which is associated with the detector area  $dS_o \equiv D^2 d\Omega_o$  (see Fig. 2.2a). This relation defines the distance  $D$  between the observer and the source. We denote the total photon flux received by a detector,

$$N_o^S(E) \equiv \frac{dn(E)}{dt dS_o} = \int d\Omega N_1(E/g) g^2, \quad (2.1)$$

where

$$N_1(E_1) \equiv \frac{dn_1(E_1)}{d\tau dS_1 d\Omega_1} \quad (2.2)$$

is a local photon flux emitted from the surface of the disc,  $dn(E)$  is the number of photons with energy in the interval  $\langle E, E + dE \rangle$  and  $g = E/E_1$  is the redshift factor. The local flux,  $N_1(E_1)$ , may vary over the disc as well as in time, and it can also depend on the local emission angle. This dependency is emphasized explicitly only in the final formula (2.11), otherwise it is omitted for brevity.

The emission arriving at the detector within the solid angle  $d\Omega$  (see Fig. 2.2b) originates from the proper area  $dS_1$  on the disc (as measured in the rest frame co-moving with the disc). Hence, in our computations we want to integrate the flux contributions over a fine mesh on the disc surface. To achieve this aim, we adjust eq. (2.1) to the form

$$N_o^S(E) = \frac{1}{D^2} \int dS \frac{D^2 d\Omega}{dS} N_1(E/g) g^2 = \frac{1}{D^2} \int dS \frac{dS_\perp}{dS} \frac{dS_f}{dS_\perp} N_1(E/g) g^2. \quad (2.3)$$

Here  $dS_f$  stands for an element of area perpendicular to light rays corresponding to the solid angle  $d\Omega$  at a distance  $D$ ,  $dS_\perp$  is the proper area measured in the local frame of

the disc and perpendicular to the rays, and  $dS$  is the coordinate area for integration. We integrate in a two-dimensional slice of a four-dimensional space-time, which is specified by coordinates  $\theta = \pi/2$  and  $t = t_o - \Delta t$  with  $\Delta t$  being a time delay with which photons from different parts of the disc (that lies in the equatorial plane) arrive to the observer (at the same coordinate time  $t_o$ ). Therefore, let us define the coordinate area by (we employ coordinates  $t', \theta, r, \varphi$  with  $t' = t - \Delta t$  and  $\Delta t = \Delta t(r, \theta, \varphi)$ )

$$dS \equiv |d^2 S_{t'\theta}| = \left| \frac{\partial x^\mu}{\partial t'} d^2 S_{\mu\theta} \right| = |d^2 S_t^\theta| = |g^{\theta\mu} d^2 S_{t\mu}|. \quad (2.4)$$

We define the tensor  $d^2 S_{\alpha\beta}$  by two four-vector elements  $dx_1^\mu \equiv (dt_1, dr, 0, 0)$  and  $dx_2^\mu \equiv (dt_2, 0, 0, d\varphi)$  and by Levi-Civita tensor  $\varepsilon_{\alpha\beta\gamma\delta}$ . The time components of these vectors,  $dt_1$  and  $dt_2$ , are such that the vectors  $dx_1^\mu$  and  $dx_2^\mu$  lie in the tangent space to the above defined space-time slice. Then we obtain

$$dS = |g^{\theta\theta} \varepsilon_{t\theta\alpha\beta} dx_1^{[\alpha} dx_2^{\beta]}| = g^{\theta\theta} \sqrt{-\|g_{\mu\nu}\|} dr d\varphi = dr d\varphi, \quad (2.5)$$

where  $g_{\mu\nu}$  is the metric tensor and  $\|g_{\mu\nu}\|$  is the determinant of the metric. The proper area,  $dS_\perp$ , perpendicular to the light ray can be expressed covariantly in the following way:

$$dS_\perp = -\frac{U^\alpha p^\beta d^2 S_{\alpha\beta}}{U^\mu p_\mu}. \quad (2.6)$$

Here,  $dS_\perp$  is the projection of an element of area, defined by  $d^2 S_{\alpha\beta}$ , on a spatial slice of an observer with velocity  $U^\alpha$  and perpendicular to light rays.  $U^\alpha$  is four-velocity of an observer measuring the area  $dS_\perp$ , and  $p^\beta$  is four-momentum of the photon. The proper area  $dS_\perp$  corresponding to the same flux tube is identical for all observers (see Schneider, Ehlers & Falco 1992). This means that the last equation holds true for any four-velocity  $U^\alpha$ , and we can express it as

$$p^\beta d^2 S_{\alpha\beta} + p_\alpha dS_\perp = 0, \quad \alpha = t, r, \theta, \varphi. \quad (2.7)$$

For  $\alpha = t$  (note that  $d^2 S_{tr} = d^2 S_{t\varphi} = 0$ ) we get

$$\frac{dS_\perp}{dS} = \left| \frac{1}{g^{\theta\theta}} \frac{dS_\perp}{d^2 S_{t\theta}} \right| = \left| -\frac{p_\theta}{p_t} \right| = \frac{r\mu_e}{g}. \quad (2.8)$$

In the last equation we used the formula for the cosine of local emission angle  $\mu_e$ , see eq. (1.6), and the fact that we have chosen such an affine parameter of the light geodesic that  $p_t = -1$ . From eqs. (2.3), (2.4) and (2.8) we get for the observed flux per unit solid angle

$$N_o^\Omega(E) \equiv \frac{dn(E)}{dt d\Omega_o} = N_0 \int_{r_{in}}^{r_{out}} dr \int_\phi^{\phi+\Delta\phi} d\varphi N_l(E/g) g l \mu_e r, \quad (2.9)$$

where  $N_0$  is a normalization constant and

$$l = \frac{dS_f}{dS_\perp} \quad (2.10)$$

is the lensing factor in the limit  $D \rightarrow \infty$  (keeping  $D^2 d\Omega$  constant, see Fig. 2.2c).

For the line emission, the normalization constant  $N_0$  is chosen in such a way that the total flux from the disc is unity. In the case of a continuum model, the flux is normalized

to unity at a certain value of the observed energy (typically at  $E = 1$  keV, as in other XSPEC models).

Finally, the integrated flux per energy bin,  $\Delta E$ , is

$$\begin{aligned} \Delta N_o^\Omega(E, \Delta E, t) &= \int_E^{E+\Delta E} d\bar{E} N_o^\Omega(\bar{E}, t) = \\ &= N_0 \int_{r_{\text{in}}}^{r_{\text{out}}} dr \int_{\phi}^{\phi+\Delta\phi} d\varphi \int_{E/g}^{(E+\Delta E)/g} dE_1 N_1(E_1, r, \varphi, \mu_e, t - \Delta t) g^2 l \mu_e r, \end{aligned} \quad (2.11)$$

where  $\Delta t$  is the relative time delay with which photons arrive to the observer from different parts of the disc. The transfer functions  $g$ ,  $l$ ,  $\mu_e$  and  $\Delta t$  are read from the FITS file `KBHtablesNN.fits` described in Appendix B.1. This equation is numerically integrated for a given local flux  $N_1(E_1, r, \varphi, \mu_e, t - \Delta t)$  in all hereby described new general relativistic *non-axisymmetric models*.

Let us assume that the local emission is stationary and the dependence on the axial coordinate is only through the prescribed dependence on the local emission angle  $f(\mu_e)$  (limb darkening/brightening law) together with an arbitrary radial dependence  $R(r)$ , i.e.

$$N_1(E_1, r, \varphi, \mu_e, t - \Delta t) \equiv N_1(E_1) R(r) f(\mu_e). \quad (2.12)$$

The observed flux  $N_o^\Omega(E)$  is in this case given by

$$N_o^\Omega(E) = \int_{-\infty}^{\infty} dE_1 N_1(E_1) G(E, E_1), \quad (2.13)$$

where

$$G(E, E_1) = N_0 \int_{r_{\text{in}}}^{r_{\text{out}}} dr R(r) \int_0^{2\pi} d\varphi f(\mu_e) g^2 l \mu_e r \delta(E - gE_1). \quad (2.14)$$

In this case, the integrated flux can be expressed in the following way:

$$\begin{aligned} \Delta N_o^\Omega(E, \Delta E) &= \int_E^{E+\Delta E} d\bar{E} N_o^\Omega(\bar{E}) = \\ &= \int_E^{E+\Delta E} d\bar{E} N_0 \int_{r_{\text{in}}}^{r_{\text{out}}} dr R(r) \int_0^{2\pi} d\varphi f(\mu_e) N_1(\bar{E}/g) g l \mu_e r \int_{-\infty}^{\infty} dE_1 \delta(E_1 - \bar{E}/g) = \\ &= N_0 \int_{r_{\text{in}}}^{r_{\text{out}}} dr R(r) \int_{-\infty}^{\infty} dE_1 N_1(E_1) \int_{E/E_1}^{(E+\Delta E)/E_1} d\bar{g} F(\bar{g}), \end{aligned} \quad (2.15)$$

where we substituted  $\bar{g} = \bar{E}/E_1$  and

$$F(\bar{g}) = \int_0^{2\pi} d\varphi f(\mu_e) g^2 l \mu_e r \delta(\bar{g} - g). \quad (2.16)$$

Eq. (2.15) is numerically integrated in all *axially symmetric models*. The function  $dF(\bar{g}) \equiv d\bar{g} F(\bar{g})$  has been pre-calculated for several limb darkening/brightening laws  $f(\mu_e)$  and stored in separate files, `KBHlineNN.fits` (see Appendix B.2).

## 2.3 Stokes parameters in a strong gravity regime

For polarization studies, Stokes parameters are used. Let us define specific Stokes parameters in the following way:

$$i_\nu \equiv \frac{I_\nu}{E}, \quad q_\nu \equiv \frac{Q_\nu}{E}, \quad u_\nu \equiv \frac{U_\nu}{E}, \quad v_\nu \equiv \frac{V_\nu}{E}, \quad (2.17)$$

where  $I_\nu$ ,  $Q_\nu$ ,  $U_\nu$  and  $V_\nu$  are Stokes parameters for light with frequency  $\nu$ ,  $E$  is the energy of a photon at this frequency. Further on, we drop the index  $\nu$  but we will always consider these quantities for light of a given frequency. We can calculate the integrated specific Stokes parameters (per energy bin), i.e.  $\Delta i_o$ ,  $\Delta q_o$ ,  $\Delta u_o$  and  $\Delta v_o$ . These are the quantities that the observer determines from the local specific Stokes parameters  $i_l$ ,  $q_l$ ,  $u_l$  and  $v_l$  on the disc in the following way:

$$\Delta i_o(E, \Delta E) = N_0 \int dS \int dE_l i_l(E_l) Fr, \quad (2.18)$$

$$\Delta q_o(E, \Delta E) = N_0 \int dS \int dE_l [q_l(E_l) \cos 2\Psi - u_l(E_l) \sin 2\Psi] Fr, \quad (2.19)$$

$$\Delta u_o(E, \Delta E) = N_0 \int dS \int dE_l [q_l(E_l) \sin 2\Psi + u_l(E_l) \cos 2\Psi] Fr, \quad (2.20)$$

$$\Delta v_o(E, \Delta E) = N_0 \int dS \int dE_l v_l(E_l) Fr. \quad (2.21)$$

Here,  $F \equiv F(r, \varphi) = g^2 l \mu_e$  is a transfer function,  $\Psi$  is the angle by which a vector parallelly transported along the light geodesic rotates. We refer to this angle also as a change of the polarization angle, because the polarization vector is parallelly transported along light geodesics. See Fig. 1.5 for an exact definition of the angle  $\Psi$ . The integration boundaries are the same as in eq. (2.11). As can be seen from the definition, the first specific Stokes parameter is equal to the photon flux, therefore, eqs. (2.11) and (2.18) are identical. The local specific Stokes parameters may depend on  $r$ ,  $\varphi$ ,  $\mu_e$  and  $t - \Delta t$ , which we did not state in the eqs. (2.18)–(2.21) explicitly for simplicity.

The specific Stokes parameters that the observer measures may vary in time in the case when the local parameters also depend on time. In eqs. (2.18)–(2.21) we used a law of transformation of the Stokes parameters by the rotation of axes (eqs. (I.185) and (I.186) in Chandrasekhar 1960).

An alternative way for expressing polarization of light is by using the degree of polarization  $P_o$  and two polarization angles  $\chi_o$  and  $\xi_o$ , defined by

$$P_o = \sqrt{q_o^2 + u_o^2 + v_o^2} / i_o, \quad (2.22)$$

$$\tan 2\chi_o = u_o / q_o, \quad (2.23)$$

$$\sin 2\xi_o = v_o / \sqrt{q_o^2 + u_o^2 + v_o^2}. \quad (2.24)$$

## 2.4 Local emission in lamp-post models

The local emission from a disc is proportional to the incident illumination from a power-law primary source placed on the axis at height  $h$  above the black hole. To calculate the incident illumination we need to integrate the geodesics from the source to the disc.

The four-momentum of the incident photons which were emitted by a primary source and which are striking the disc at radius  $r$  is (see eqs. (A.8)–(A.11) with  $l = 0$  and  $\theta = \pi/2$  or also Carter 1968 and Misner, Thorne & Wheeler 1973)

$$p_i^t = 1 + 2/r + 4/\Delta, \quad (2.25)$$

$$p_i^r = R'_{\text{sgn}}[(r^2 + a^2)^2 - \Delta(a^2 + q_L^2)]^{1/2}/r^2, \quad (2.26)$$

$$p_i^\theta = q_L/r^2, \quad (2.27)$$

$$p_i^\varphi = 2a/(r\Delta), \quad (2.28)$$

where  $q_L^2 = \sin^2\theta_L (h^2 + a^2)^2/\Delta_L - a^2$  is Carter's constant of motion with  $\Delta_L = h^2 - 2h + a^2$ , and with the angle of emission  $\theta_L$  being the local angle under which the photon is emitted from a primary source (it is measured in the rest frame of the source). We define this angle by  $\tan\theta_L = -p_L^{(\theta)}/p_L^{(r)}$ , where  $p_L^{(r)} = p_L^\mu e_{L\mu}^{(r)}$  and  $p_L^{(\theta)} = p_L^\mu e_{L\mu}^{(\theta)}$  with  $p_L^\mu$  and  $e_{L\mu}^{(a)}$  being the four-momentum of emitted photons and the local tetrad connected with a primary source, respectively. The angle is  $0^\circ$  when the photon is emitted downwards and  $180^\circ$  if the photon is emitted upwards.

We denoted the sign of the radial component of the momentum by  $R'_{\text{sgn}}$ . We have chosen such an affine parameter for the light geodesic that the conserved energy of the light is  $-p_{it} = -p_{Lt} = 1$ . The conserved angular momentum of incident photons is zero ( $l_L = 0$ ).

The gravitational and Doppler shift of the photons striking the disc which were emitted by a primary source is

$$g_L = \frac{\nu_i}{\nu_L} = \frac{p_{i\mu}U^\mu}{p_{L\alpha}U_L^\alpha} = -\frac{p_{i\mu}U^\mu}{U_L^t}. \quad (2.29)$$

Here  $\nu_i$  and  $\nu_L$  denote the frequency of the incident and emitted photons, respectively and  $U_L^\alpha$  is a four-velocity of the primary source with the only non-zero component  $U_L^t = \sqrt{\frac{h^2 + a^2}{\Delta_L}}$ .

Cosine of the local incident angle is

$$\mu_i = |\cos\delta_i| = \frac{p_{i\alpha}n^\alpha}{p_{i\mu}U^\mu}, \quad (2.30)$$

where  $n^\alpha = -e_{(\theta)}^\alpha$  is normal to the disc with respect to the observer co-moving with the matter in the disc.

We further define the azimuthal incident angle as the angle between the projection of the three-momentum of the incident photon into the disc (in the local rest frame co-moving with the disc) and the radial tetrad vector,

$$\Phi_i = -R_{\text{sgn}}^i \arccos\left(\frac{-1}{\sqrt{1 - \mu_i^2}} \frac{p_{i\alpha}e_{(\varphi)}^\alpha}{p_{i\mu}U^\mu}\right) + \frac{\pi}{2}, \quad (2.31)$$

where  $R_{\text{sgn}}^i$  is positive if the incident photon travels outwards ( $p_i^{(r)} > 0$ ) and negative if it travels inwards ( $p_i^{(r)} < 0$ ) in the local rest frame of the disc.

In lamp-post models the emission of the disc will be proportional to the incident radiation  $N_i^S(E_i)$  which comes from a primary source

$$N_i^S(E_i) = N_L^\Omega(E_L) \frac{d\Omega_L}{dS_i}. \quad (2.32)$$

Here  $N_L^\Omega(E_L) = N_{0L} E_L^{-\Gamma}$  is an isotropic and stationary power-law emission from a primary source which is emitted into a solid angle  $d\Omega_L$  and which illuminates local area  $dS_1$  on the disc. The energy of the photon striking the disc (measured in the local frame co-moving with the disc) will be redshifted

$$E_1 = g_L E_L. \quad (2.33)$$

The ratio  $d\Omega_L/dS_1$  is

$$\frac{d\Omega_L}{dS_1} = \frac{d\Omega_L}{dS} \frac{dS}{dS_1} = \frac{\sin \theta_L d\theta_L d\varphi}{dr d\varphi} \frac{dS}{dS_1}, \quad (2.34)$$

where (see eqs. (2.5) and (2.7))

$$dS = dr d\varphi = |d^2 S_t^\theta| = -g^{\theta\theta} \frac{p_{it}}{p_i^\theta} dS_\perp = \frac{g^{\theta\theta}}{p_i^\theta} dS_\perp. \quad (2.35)$$

Here we used the same space-time slice as in the discussion above eq. (2.4) and thus the element  $d^2 S_{\alpha\beta}$  is defined as before, see eq. (2.5). Note that here the area  $dS_\perp$  is defined by the incident flux tube as opposed to  $dS_\perp$  in eq. (2.8) where it was defined by the emitted flux tube. The coordinate area  $dS$  corresponds to the proper area  $dS_\perp$  which is perpendicular to the incident light ray (in the local rest frame co-moving with the disc). The corresponding proper area (measured in the same local frame) lying in the equatorial plane will be

$$\begin{aligned} dS_1 &= |d^2 S_{(t)}^{(\theta)}| = |e_{(t)}^\mu e^{(\theta)\nu} d^2 S_{\mu\nu}| = |g_{\theta\theta}^{-1/2} U^\mu d^2 S_{\mu\theta}| = \\ &= -g_{\theta\theta}^{-1/2} \frac{p_{i\mu} U^\mu}{p_i^\theta} dS_\perp = g_{\theta\theta}^{-1/2} \frac{U_L^t}{p_i^\theta} g_L dS_\perp. \end{aligned} \quad (2.36)$$

Here we have used eq. (2.4) for the tetrad components of the element  $d^2 S_{\alpha\beta}$ , eqs. (2.6) and (2.29).

It follows from eqs. (2.32)–(2.36) that the incident radiation will be again a power law with the same photon index  $\Gamma$  as in primary emission

$$N_i^S(E_1) = N_{0i} E_1^{-\Gamma}, \quad (2.37)$$

with the normalization factor

$$N_{0i} = N_{0L} g_L^{\Gamma-1} \sqrt{1 - \frac{2h}{h^2 + a^2}} \frac{\sin \theta_L d\theta_L}{r dr}. \quad (2.38)$$

The emission of the disc due to illumination will be proportional to this factor.

## Chapter 3

# New models for XSPEC

We have developed several general relativistic models for line emission and Compton reflection continuum. The line models are supposed to be more accurate and versatile than the LAOR model (Laor 1991), and substantially faster than the KERRSPEC model (Martocchia, Karas & Matt 2000). Several models of intrinsic emissivity were employed, including the lamp-post model (Matt *et al.* 1992). Among other features, these models allow various parameters to be fitted such as the black-hole angular momentum, observer inclination, accretion disc size and some of the parameters characterizing disc emissivity and primary illumination properties. They also allow a change in the grid resolution and, hence, to control accuracy and computational speed. Furthermore, we developed very general convolution models. All these models are based on pre-calculated tables described in Chapter 1 and thus the geodesics do not need to be calculated each time one integrates the disc emission. These tables are calculated for the vacuum Kerr space-time and for a Keplerian co-rotating disc plus matter that is freely falling below the marginally stable orbit. The falling matter has the energy and angular momentum of the matter at the marginally stable orbit. It is possible to use different pre-calculated tables if they are stored in a specific FITS file (see Appendix B.1 for its detailed description).

There are two types of new models. The first type of model integrates the local disc emission in both of the polar coordinates on the disc and thus enables one to choose non-axisymmetric area of integration (emission from spots or partially obscured discs). One can also choose the resolution of integration and thus control the precision and speed of the computation. The second type of model is axisymmetric – the axially dependent part of the emission from rings is pre-calculated and stored in a FITS file (the function  $dF(\bar{g}) = d\bar{g} F(\bar{g})$  from eq. (2.16) is integrated for different radii with the angular grid having 20 000 points). These models have less parameters that can be fitted and thus are less flexible even though more suited to the standard analysis approach. On the other hand they are fast because the emission is integrated only in one dimension (in the radial coordinate of the disc). It may be worth emphasizing that the assumption about axial symmetry concerns only the form of intrinsic emissivity of the disc, which cannot depend on the polar angle in this case, not the shape of individual light rays, which is always complicated near a rotating black hole.

There are several parameters and switches that are common for all new models (see Tab. 3.1):

$a/M$  – specific angular momentum of the Kerr black hole in units of  $GM/c$  ( $M$  is the mass of the central black hole),

parameter	unit	default value	minimum value	maximum value
<b>a/M</b>	$GM/c$	0.9982	0.	1.
<b>theta_o</b>	deg	30.	0.	89.
<b>rin-rh</b>	$GM/c^2$	0.	0.	999.
<b>ms</b>	–	1.	0.	1.
<b>rout-rh</b>	$GM/c^2$	400.	0.	999.
<b>zshift</b>	–	0.	-0.999.	10.
<b>ntable</b>	–	0.	0.	99.

Table 3.1: Common parameters for all models.

parameter	unit	default value	minimum value	maximum value
<b>phi</b>	deg	0.	-180.	180.
<b>dphi</b>	deg	360.	0.	360.
<b>nrad</b>	–	200.	1.	10000.
<b>division</b>	–	1.	0.	1.
<b>nphi</b>	–	180.	1.	20000.
<b>smooth</b>	–	1.	0.	1.
<b>Stokes</b>	–	0.	0.	6.

Table 3.2: Common parameters for non-axisymmetric models.

**theta\_o** – inclination of the observer in degrees,

**rin-rh** – inner radius of the disc relative to the black-hole horizon in units of  $GM/c^2$ ,

**ms** – switch for the marginally stable orbit,

**rout-rh** – outer radius of the disc relative to the black-hole horizon in units of  $GM/c^2$ ,

**zshift** – overall redshift of the object,

**ntable** – number of the FITS file with pre-calculated tables to be used.

The inner and outer radii are given relative to the black-hole horizon and, therefore, their minimum value is zero. This becomes handy when one fits the **a/M** parameter, because the horizon of the black hole as well as the marginally stable orbit change with **a/M**, and so the lower limit for inner and outer disc edges cannot be set to constant values. The **ms** switch determines whether we also want to integrate emission below the marginally stable orbit. If its value is set to zero and the inner radius of the disc is below this orbit then the emission below the marginally stable orbit is taken into account, otherwise it is not.

The **ntable** switch determines which of the pre-calculated tables should be used for intrinsic emissivity. In particular, **ntable** = 0 for **KBHtables00.fits** (**KBHline00.fits**), **ntable** = 1 for **KBHtables01.fits** (**KBHline01.fits**), etc., corresponding to non-axisymmetric (axisymmetric) models.

The following set of parameters is relevant only for non-axisymmetric models (see Tab. 3.2):

**phi** – position angle of the axial sector of the disc in degrees,

**dphi** – inner angle of the axial sector of the disc in degrees,

**nrad** – radial resolution of the grid,

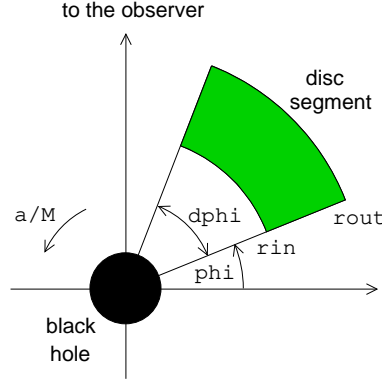


Figure 3.1: Segment of a disc from which emission comes (view from above).

value	photon flux array <b>photar</b> contains <sup>†‡</sup>
0	$i = I/E$ , where $I$ is the first Stokes parameter (intensity)
1	$q = Q/E$ , where $Q$ is the second Stokes parameter
2	$u = U/E$ , where $U$ is the third Stokes parameter
3	$v = V/E$ , where $V$ is the fourth Stokes parameter
4	degree of polarization, $P = \sqrt{q^2 + u^2 + v^2}/i$
5	angle $\chi$ [deg] of polarization, $\tan 2\chi = u/q$
6	angle $\xi$ [deg] of polarization, $\sin 2\xi = v/\sqrt{q^2 + u^2 + v^2}$

<sup>†</sup> the **photar** array contains the values described in the table and multiplied by the width of the corresponding energy bin

<sup>‡</sup>  $E$  is the energy of the observed photons

Table 3.3: Definition of the **Stokes** parameter.

**division** – switch for spacing of radial grid (0 – equidistant, 1 – exponential),

**nphi** – axial resolution of the grid,

**smooth** – switch for performing simple smoothing (0 – no, 1 – yes),

**Stokes** – switch for computing polarization (see Tab. 3.3).

The **phi** and **dphi** parameters determine the axial sector of the disc from which emission comes (see Fig. 3.1). The **nrad** and **nphi** parameters determine the grid for numerical integration. If the **division** switch is zero, the radial grid is equidistant; if it is equal to unity then the radial grid is exponential (i.e. more points closer to the black hole).

If the **smooth** switch is set to unity then a simple smoothing is applied to the final spectrum. Here  $N_o^\Omega(E_j) = [N_o^\Omega(E_{j-1}) + 2N_o^\Omega(E_j) + N_o^\Omega(E_{j+1})]/4$ .

If the **Stokes** switch is different from zero, then the model also calculates polarization. Its value determines which of the Stokes parameters should be computed by XSPEC, i.e. what will be stored in the output array for the photon flux **photar**; see Tab. 3.3. (If **Stokes**  $\neq 0$  then a new **ascii** data file **stokes.dat** is created in the current directory, where values of energy  $E$  together with all Stokes parameters  $i$ ,  $q$ ,  $u$ ,  $v$ ,  $P$ ,  $\chi$ [deg] and  $\xi$ [deg] are stored, each in one column.)

A realistic model of polarization has been currently implemented only in the **KYL1CR** model (see Section 3.2.1 below). In other models, a simple assumption is made – the local

emission is assumed to be linearly polarized in the direction perpendicular to the disc (i.e.  $q_l = i_l = N_l$  and  $u_l = v_l = 0$ ). In all models (including KYL1CR) there is always no final circular polarization (i.e.  $v = \xi = 0$ ), which follows from the fact that the fourth local Stokes parameter is zero in each model.

### 3.1 Models for a relativistic spectral line

Three general relativistic line models are included in the new set of XSPEC routines – non-axisymmetric Gaussian line model KYG1LINE, axisymmetric Gaussian line model KYGLINE and fluorescent lamp-post line model KYF1LL.

#### 3.1.1 Non-axisymmetric Gaussian line model KYG1LINE

The KYG1LINE model computes the integrated flux from the disc according to eq. (2.11). It assumes that the local emission from the disc is

$$N_l(E_l) = \frac{1}{r^{\text{alpha}}} f(\mu_e) \exp \left[ - \left( 1000 \frac{E_l - E_{\text{rest}}}{\sqrt{2} \text{sigma}} \right)^2 \right] \quad \text{for } r \geq r_b, \quad (3.1)$$

$$N_l(E_l) = \text{jump} r_b^{\text{beta}-\text{alpha}} \frac{1}{r^{\text{beta}}} f(\mu_e) \exp \left[ - \left( 1000 \frac{E_l - E_{\text{rest}}}{\sqrt{2} \text{sigma}} \right)^2 \right] \quad \text{for } r < r_b. \quad (3.2)$$

The local emission is assumed to be a Gaussian line with its peak flux depending on the radius as a broken power law. The line is defined by nine points equally spaced with the central point at its maximum. The normalization constant  $N_0$  in eq. (2.11) is such that the total integrated flux of the line is unity. The parameters defining the Gaussian line are (see Tab. 3.4):

**Erest** – rest energy of the line in keV,

**sigma** – width of the line in eV,

**alpha** – radial power-law index for the outer region,

**beta** – radial power-law index for the inner region,

**rb** – parameter defining the border between regions with different power-law indices,

**jump** – ratio between flux in the inner and outer regions at the border radius,

**limb** – switch for different limb darkening/brightening laws.

There are two regions with different power-law dependences with indices **alpha** and **beta**. The power law changes at the border radius  $r_b$  where the local emissivity does not need to be continuous (for **jump**  $\neq 1$ ). The **rb** parameter defines this radius in the following way:

$$r_b = \text{rb} \times r_{\text{ms}} \quad \text{for } \text{rb} \geq 0, \quad (3.3)$$

$$r_b = -\text{rb} + r_h \quad \text{for } \text{rb} < 0, \quad (3.4)$$

where  $r_{\text{ms}}$  is the radius of the marginally stable orbit and  $r_h$  is the radius of the horizon of the black hole.

parameter	unit	default value	minimum value	maximum value
a/M	$GM/c$	0.9982	0.	1.
theta_o	deg	30.	0.	89.
rin-rh	$GM/c^2$	0.	0.	999.
ms	—	1.	0.	1.
rout-rh	$GM/c^2$	400.	0.	999.
phi	deg	0.	-180.	180.
dphi	deg	360.	0.	360.
nrad	—	200.	1.	10000.
division	—	1.	0.	1.
nphi	—	180.	1.	20000.
smooth	—	1.	0.	1.
zshift	—	0.	-0.999	10.
ntable	—	0.	0.	99.
*Erest	keV	6.4	1.	99.
*sigma	eV	2.	0.01	1000.
*alpha	—	3.	-20.	20.
*beta	—	4.	-20.	20.
*rb	$r_{\text{ms}}$	0.	0.	160.
*jump	—	1.	0.	1e6
*limb	—	-1.	-10.	10.
Stokes	—	0.	0.	6.

Table 3.4: Parameters of the non-axisymmetric Gaussian line model KYG1LINE. Model parameters that are not common for all non-axisymmetric models are denoted by asterisk.

The function  $f(\mu_e) = f(\cos \delta_e)$  in eqs. (3.1) and (3.2) describes the limb darkening/brightening law, i.e. the dependence of the local emission on the local emission angle. Several limb darkening/brightening laws are implemented:

$$f(\mu_e) = 1 \quad \text{for } \texttt{limb} = 0, \quad (3.5)$$

$$f(\mu_e) = 1 + 2.06\mu_e \quad \text{for } \texttt{limb} = -1, \quad (3.6)$$

$$f(\mu_e) = \ln(1 + \mu_e^{-1}) \quad \text{for } \texttt{limb} = -2, \quad (3.7)$$

$$f(\mu_e) = \mu_e^{\texttt{limb}} \quad \text{for } \texttt{limb} \neq 0, -1, -2. \quad (3.8)$$

Eq. (3.5) corresponds to the isotropic local emission, eq. (3.6) corresponds to limb darkening in an optically thick electron scattering atmosphere (used by Laor, see Phillips & Mészáros 1986; Laor, Netzer & Piran 1990; Laor 1991), and eq. (3.7) corresponds to limb brightening predicted by some models of a fluorescent line emitted by an accretion disc due to X-ray illumination (Haardt 1993; Ghisellini, Haardt & Matt 1994).

There is also a similar model KYG2LINE present among the new XSPEC models, which is useful when fitting two general relativistic lines simultaneously. The parameters are the same as in the KYG1LINE model except that there are two sets of those parameters describing the local Gaussian line emission. There is one more parameter present, **ratio21**, which is the ratio of the maximum of the second local line to the maximum of the first local line. Polarization computations are not included in this model.

Results of an elementary code test are shown in Figs. 3.2–3.4. The intrinsic emissivity was assumed to be a narrow Gaussian line (width  $\sigma \doteq 0.42 \text{ FWHM} = 2 \text{ eV}$ ) with the am-

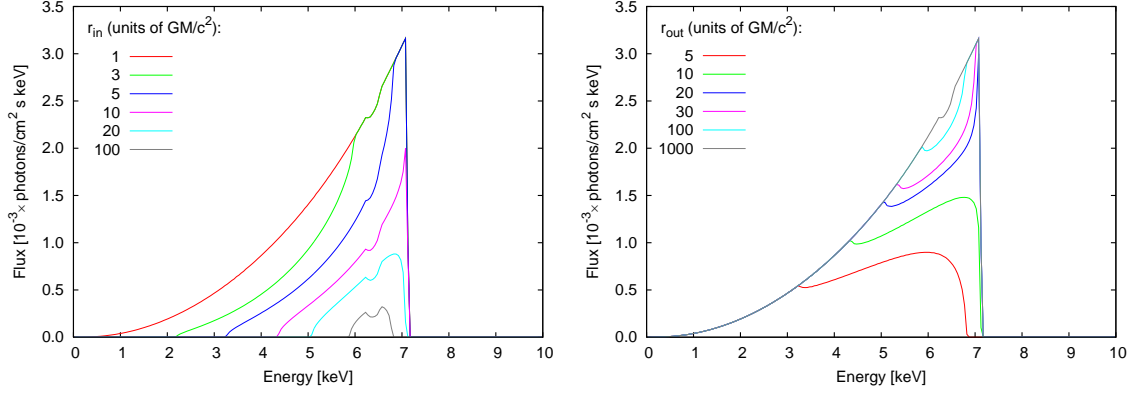


Figure 3.2: Comparative examples of simple line profiles, showing a theoretical line ( $E_{\text{rest}} = 6.4 \text{ keV}$ ) with relativistic effects originating from a black-hole accretion disc. Different sizes of the annular region (axially symmetric) have been considered, assuming that the intrinsic emissivity obeys a power law in the radial direction ( $\alpha = 3$ ). Resolution of the line-emitting region was  $n_r \times n_\phi = 3000 \times 1500$  with a non-equidistant layout of the grid in Kerr ingoing coordinates, as described in the text. Left: Dependence on the inner edge. Values of  $r_{\text{in}}$  are indicated in the plot (the outer edge has been fixed at the maximum radius covered by our tables,  $r_{\text{out}} = 10^3$ ). Right: Dependence on  $r_{\text{out}}$  (with the inner edge at horizon,  $r_{\text{in}} = r_{\text{h}}$ ). Other key parameters are:  $\theta_0 = 45^\circ$ ,  $a = 1.0$ . Locally isotropic emission was assumed in the disc co-rotating frame.

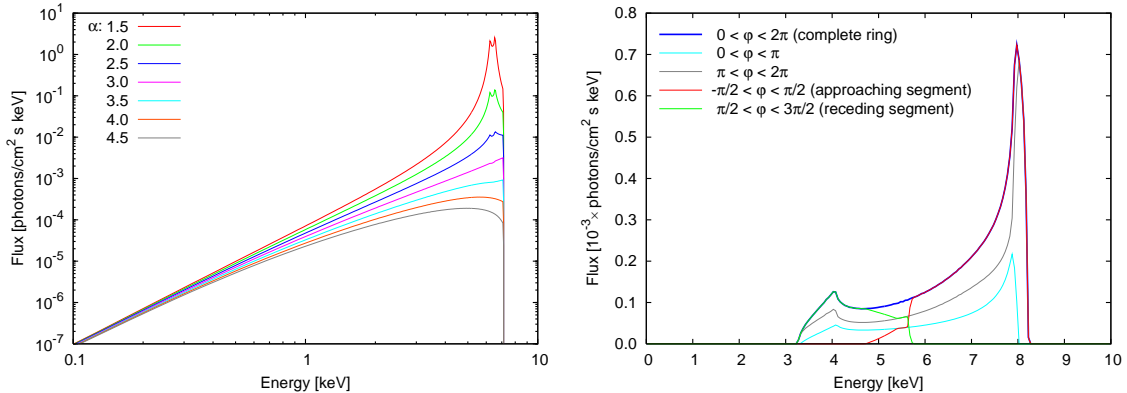


Figure 3.3: More calculated line profiles, as in the previous figure. Left: Line profiles for different values of  $\alpha$ . Notice the enhanced red tail of the line when the intrinsic emission is concentrated to the centre of the disc. Right: Line emission originating from four different azimuthal segments of the disc. This plot can serve as a toy model of non-axisymmetric emissivity or to illustrate the expected effects of disc obscuration. Obviously, the receding segment of the disc contributes mainly to the low-energy tail of the line while the approaching segment constitutes the prominent high-energy peak. These two plots illustrate a mutual interplay between the effect of changing  $\alpha$  and the impact of obscuration, which complicates interpretation of time-averaged spectra. The radial range is  $r_{\text{h}} < r < 10^3$  in both panels.

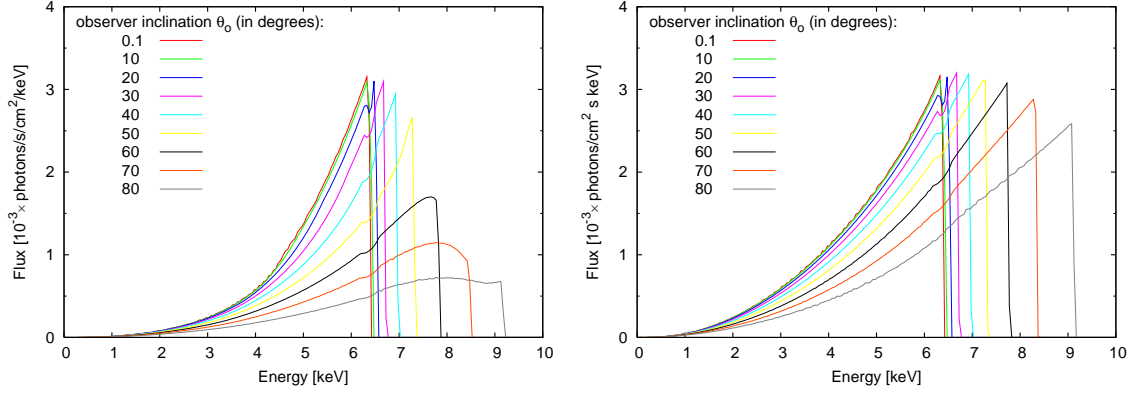


Figure 3.4: Dependence on the observer inclination,  $\theta_o$ , as given in the plot. Left: Non-rotating black hole,  $a = 0$ . Right: Maximally rotating black hole,  $a = 1$ . Other parameters as in Fig. 3.2 and 3.3.

plitude decreasing  $\propto r^{-\alpha}$  in the local frame co-moving with the disc medium. Typically, the slope of the low-energy wing is rather sensitive to the radial dependence of emissivity. No background continuum is included here, so these lines can be compared with similar pure disc-line profiles obtained in previous papers (Kojima 1991; Laor 1991) which also imposed the assumption of axially symmetric and steady emission from an irradiated thin disc. Again, the intrinsic width of the line is assumed to be much less than the effects of broadening due to bulk Keplerian motion and the central gravitational field.

Furthermore, Figs. 3.5–3.6 compare model spectra of widely used XSPEC models. In these examples one can see that the LAOR model gives zero contribution at energy below  $0.1E_{\text{rest}}$  (in the disc local frame). This is because its grid has only 35 radial points distributed in the whole range  $1.23 \leq r \leq 400$ . That is also why, in spite of a very efficient interpolation and smoothing of the final spectrum, the LAOR model does not accurately reproduce the line originating from a narrow ring. Also, the dependence on the limb darkening/brightening cannot be examined with this model, because the form of directionality of the intrinsic emission is hard-wired in the code, together with the position of the inner edge at  $r \geq r_{\text{ms}}$ . This affects especially the spectrum originating near the black hole, where radiation is expected to be very anisotropic and flow lines non-circular. The DISKLINE model has also been frequently used in the context of spectral fitting, assuming a disc around a non-rotating black hole. This model is analytical, and so it has clear advantages in XSPEC. Notice, however, that photons move along straight lines in this model and that the lensing effect is neglected.

### 3.1.2 Axisymmetric Gaussian line model KYGLINE

This model uses eq. (2.15) for computing the disc emission with local flux being

$$N_l(E_l) = \delta(E_l - E_{\text{rest}}), \quad (3.9)$$

$$R(r) = r^{-\alpha}. \quad (3.10)$$

The function  $dF(\bar{g}) \equiv d\bar{g} F(\bar{g})$  in eq. (2.16) was pre-calculated for three different limb darkening/brightening laws (see eqs. (3.5)–(3.7)) and stored in corresponding FITS files

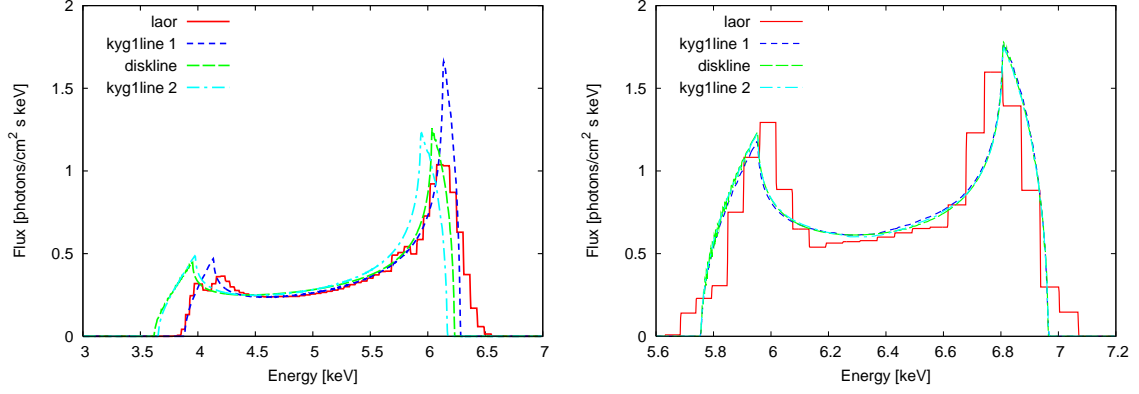


Figure 3.5: Comparison of the output from XSPEC models for the disc-line problem: LAOR, DISKLINE, and KYG1LINE (line 1 corresponds to the same limb darkening law and  $a = 0.9982$  as in LAOR; line 2 assumes locally isotropic emission and  $a = 0$  as in DISKLINE). Left panel:  $\theta_o = 30^\circ$ ,  $r_{\text{in}} = 6$ ,  $r_{\text{out}} = 7$ . Right panel:  $\theta_o = 70^\circ$ ,  $r_{\text{in}} = 100$ ,  $r_{\text{out}} = 200$ . Radial decay of intrinsic emissivity follows  $\alpha = 3$  power law.

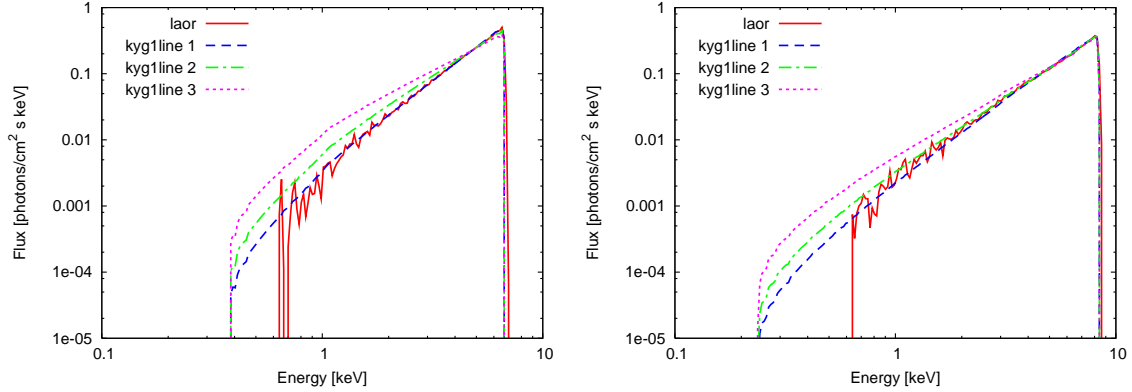


Figure 3.6: Similar to previous figure but in logarithmic scale and for three choices of the darkening law in KYG1LINE – (1)  $f(\mu_e) = 1 + 2.06\mu_e$ ; (2)  $f(\mu_e) = 1$ ; (3)  $f(\mu_e) = \log(1 + 1/\mu_e)$ . Left panel:  $\theta_o = 30^\circ$ ; Right panel:  $\theta_o = 70^\circ$ . In both panels,  $r_{\text{in}} = r_{\text{ms}}$ ,  $r_{\text{out}} = 400$ ,  $a = 0.9982$ .

**KBHline00.fits** – **KBHline02.fits**. The local emission is a delta function with its maximum depending on the radius as a power law with index **alpha** and also depending on the local emission angle. The normalization constant  $N_0$  in eq. (2.15) is such that the total integrated flux of the line is unity.

There are less parameters defining the line in this model than in the previous one (see Tab. 3.5):

**Erest** – rest energy of the line in keV,

**alpha** – radial power-law index.

Note that the limb darkening/brightening law can be chosen by means of the **ntable** switch.

This model is much faster than the non-axisymmetric KYG1LINE model. Although it is not possible to change the resolution grid on the disc, it is hardly needed because

parameter	unit	default value	minimum value	maximum value
<code>a/M</code>	$GM/c$	0.9982	0.	1.
<code>theta_o</code>	deg	30.	0.	89.
<code>rin-rh</code>	$GM/c^2$	0.	0.	999.
<code>ms</code>	–	1.	0.	1.
<code>rout-rh</code>	$GM/c^2$	400.	0.	999.
<code>zshift</code>	–	0.	-0.999	10.
<code>ntable</code>	–	1.	0.	99.
<code>*Erest</code>	keV	6.4	1.	99.
<code>*alpha</code>	–	3.	-20.	20.

Table 3.5: Parameters of the axisymmetric Gaussian line model KYGLINE. Model parameters that are not common for all axisymmetric models are denoted by asterisk.

the resolution is set to be very large, corresponding to `nrad` = 500, `division` = 1 and `nphi` = 20 000 in the KYG1LINE model, which is more than sufficient in most cases. (These values apply if the maximum range of radii is selected, i.e. `rin`=0, `ms`=0 and `rout`=999; in case of a smaller range the number of points decreases accordingly.) This means that the resolution of the KYGLINE model is much higher than what can be achieved with the `laor` model, and the performance is still very good.

### 3.1.3 Non-axisymmetric fluorescent lamp-post line model KYF1LL

The line in this model is induced by the illumination of the disc from the primary power-law source located on the axis at `height` above the black hole. This model computes the final spectrum according to eq. (2.11) with the local photon flux

$$\begin{aligned}
 N_l(E_l) = & g_L^{\text{PhoIndex}-1} \frac{\sin \theta_L d\theta_L}{r dr} \sqrt{1 - \frac{2\text{height}}{\text{height}^2 + (a/M)^2}} f(\mu_i, \mu_e) \\
 & \times \exp \left[ - \left( 1000 \frac{E_l - E_{\text{rest}}}{\sqrt{2} \text{sigma}} \right)^2 \right].
 \end{aligned} \tag{3.11}$$

Here,  $g_L$  is ratio of the energy of a photon received by the accretion disc to the energy of the same photon when emitted from a source on the axis,  $\theta_L$  is an angle under which the photon is emitted from the source (measured in the local frame of the source) and  $\mu_i \equiv \cos \delta_i$  is the cosine of the incident angle (measured in the local frame of the disc) – see Fig. 2.1. All of these functions depend on `height` above the black hole at which the source is located and on the rotational parameter `a/M` of the black hole. Values of  $g_L$ ,  $\theta_L$  and  $\mu_i$  for a given height and rotation are read from the lamp-post tables `lamp.fits` (see Appendix B.3). At present, only tables for `a/M` = 0.9987492 (i.e. for the horizon of the black hole  $r_h = 1.05$ ) and `height` = 2, 3, 4, 5, 6, 8, 10, 12, 15, 20, 30, 50, 75 and 100 are included in `lamp.fits`, therefore, the `a/M` parameter is used only for the negative values of `height` (see below).

The factor in front of the function  $f(\mu_i, \mu_e)$  gives the radial dependence of the disc emissivity, which is different from the assumed broken power law in the KYG1LINE model. For the derivation of this factor, which characterizes the illumination from a primary source on the axis see Section 2.4.

parameter	unit	default value	minimum value	maximum value
a/M	$GM/c$	0.9982	0.	1.
theta_o	deg	30.	0.	89.
rin-rh	$GM/c^2$	0.	0.	999.
ms	–	1.	0.	1.
rout-rh	$GM/c^2$	400.	0.	999.
phi	deg	0.	-180.	180.
dphi	deg	360.	0.	360.
nrad	–	200.	1.	10000.
division	–	1.	0.	1.
nphi	–	180.	1.	20000.
smooth	–	1.	0.	1.
zshift	–	0.	-0.999	10.
ntable	–	0.	0.	99.
*PhoIndex	–	2.	1.5	3.
*height	$GM/c^2$	3.	-20.	100.
*Erest	keV	6.4	1.	99.
*sigma	eV	2.	0.01	1000.
Stokes	–	0.	0.	6.

Table 3.6: Parameters of the fluorescent lamp-post line model KYF1LL. Model parameters that are not common for all non-axisymmetric models are denoted by asterisk.

The function  $f(\mu_i, \mu_e)$  is a coefficient of reflection. It depends on the incident and reflection angles. Although the normalization of this function also depends on the photon index of the power-law emission from a primary source, we do not need to take this into account because the final spectrum is always normalized to unity. Values of this function are read from a pre-calculated table which is stored in `fluorescent_line.fits` file (see Matt, Perola & Piro 1991 and Appendix B.4).

The local emission (3.11) is defined in nine points of local energy  $E_l$  that are equally spaced with the central point at its maximum. The normalization constant  $N_0$  in the formula (2.11) is such that the total integrated flux of the line is unity. The parameters defining local emission in this model are (see Tab. 3.6):

**PhoIndex** – photon index of primary power-law illumination,

**height** – height above the black hole where the primary source is located for **height** > 0,  
and radial power-law index for **height** ≤ 0,

**Erest** – rest energy of the line in keV,

**sigma** – width of the line in eV.

If positive, the **height** parameter works as a switch – the exact value present in the tables `lamp.fits` must be chosen. If the **height** parameter is negative, then this model assumes that the local emission is the same as in the KYG1LINE model with the parameters **alpha** = –**height**, **rb** = 0 and **limb** = –2 (**PhoIndex** parameter is unused in this case).

In Fig. 3.7 we demonstrate that the broad iron emission lines due to illumination from the source placed on the axis depend heavily on the height where the “lamp” is located (left), as well as on the photon index of the primary emission (right). These graphs correspond to the iron  $K\alpha$  line with the rest energy of 6.4 keV.

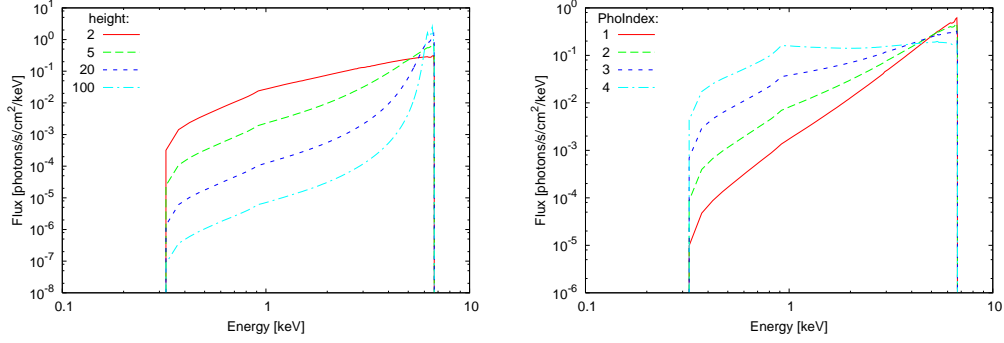


Figure 3.7: An example of a line profile originating from a disc in equatorial plane of a Kerr black hole ( $a = 0.9987$ , i.e.  $r_h = 1.05$ ) due to the illumination from a primary source on the axis. The KYF1LL model was used. Left: Dependence of the line profile on the height (in  $GM/c^2$ ) of a primary source with photon index  $\Gamma = 2$ . Right: Dependence of the line profile on the photon index of the primary emission with a source at height  $3 GM/c^2$  above the black hole.

## 3.2 Compton reflection models

We have developed two new relativistic continuum models – the lamp-post Compton reflection model KYL1CR and the KYH1REFL model which is a relativistically blurred HREFL model that is already present in XSPEC. Both of these models are non-axisymmetric.

### 3.2.1 Non-axisymmetric lamp-post Compton reflection model KYL1CR

The emission in this model is induced by the illumination of the disc from the primary power-law source located on the axis at `height` above the black hole. As in every non-axisymmetric model, the observed spectrum is computed according to eq. (2.11). The local emission is

$$N_l(E_l) = g_L^{\text{PhoIndex}-1} \frac{\sin \theta_L d\theta_L}{r dr} \sqrt{1 - \frac{2\text{height}}{\text{height}^2 + (a/M)^2}} f(E_l; \mu_i, \mu_e) \quad \text{for } \text{height} > 0, \quad (3.12)$$

$$N_l(E_l) = r^{\text{height}} \bar{f}(E_l; \mu_e) \quad \text{for } \text{height} \leq 0. \quad (3.13)$$

For the definition of  $g_L$ ,  $\theta_L$  and  $\mu_i$  see Section 3.1.3 and Appendix B.3, where pre-calculated tables of these functions in `lamp.fits` are described.

The function  $f(E_l; \mu_i, \mu_e)$  gives the dependence of the locally emitted spectrum on the angle of incidence and the angle of emission, assuming a power-law illumination. This function depends on the photon index `PhoIndex` of the power-law emission from a primary source. Values of this function for various photon indices of primary emission are read from the pre-calculated tables stored in `refspectra.fits` (see Appendix B.5). These tables were calculated by the Monte Carlo simulations of Compton scattering in Matt, Perola & Piro (1991). At present, tables for `PhoIndex` = 1.5, 1.6, ..., 2.9, 3.0 and for local energies in the range from 2 keV to 300 keV are available. The normalization constant  $N_0$  in eq. (2.11) is such that the final photon flux at an energy of 3 keV is equal to unity, which is different from what is usual for continuum models in XSPEC (where the

parameter	unit	default value	minimum value	maximum value
a/M	$GM/c$	0.9982	0.	1.
theta_o	deg	30.	0.	89.
rin-rh	$GM/c^2$	0.	0.	999.
ms	—	1.	0.	1.
rout-rh	$GM/c^2$	400.	0.	999.
phi	deg	0.	-180.	180.
dphi	deg	360.	0.	360.
nrad	—	200.	1.	10000.
division	—	1.	0.	1.
nphi	—	180.	1.	20000.
smooth	—	1.	0.	1.
zshift	—	0.	-0.999	10.
ntable	—	0.	0.	99.
*PhoIndex	—	2.	1.5	3.
*height	$GM/c^2$	3.	-20.	100.
*line	—	0.	0.	1.
*E_cut	keV	300.	1.	1000.
Stokes	—	0.	0.	6.

Table 3.7: Parameters of the lamp-post Compton reflection model KYL1CR. Model parameters that are not common for all non-axisymmetric models are denoted by asterisk.

photon flux is unity at 1 keV). The choice adopted is due to the fact that current tables in `refspectra.fits` do not extend below 2 keV.

The function  $\bar{f}(E_l; \mu_e)$ , which is used for negative **height**, is an averaged function  $f(E_l; \mu_i, \mu_e)$  over  $\mu_i$

$$\bar{f}(E_l; \mu_e) \equiv \int_0^1 d\mu_i f(E_l; \mu_i, \mu_e). \quad (3.14)$$

The local emission (3.13) can be interpreted as emission induced by illumination from clouds localized near above the disc rather than from a primary source on the axis (see Fig. 2.1). In this case photons strike the disc from all directions.

For positive values of **height** the KYL1CR model includes a physical model of polarization based on Rayleigh scattering in single scattering approximation. The specific local Stokes parameters describing local polarization of light are

$$i_l(E_l) = \frac{I_l + I_r}{\langle I_l + I_r \rangle} N_l(E_l), \quad (3.15)$$

$$q_l(E_l) = \frac{I_l - I_r}{\langle I_l + I_r \rangle} N_l(E_l), \quad (3.16)$$

$$u_l(E_l) = \frac{U}{\langle I_l + I_r \rangle} N_l(E_l), \quad (3.17)$$

$$v_l(E_l) = 0, \quad (3.18)$$

where the functions  $I_l$ ,  $I_r$  and  $U$  determine the angular dependence of the Stokes param-

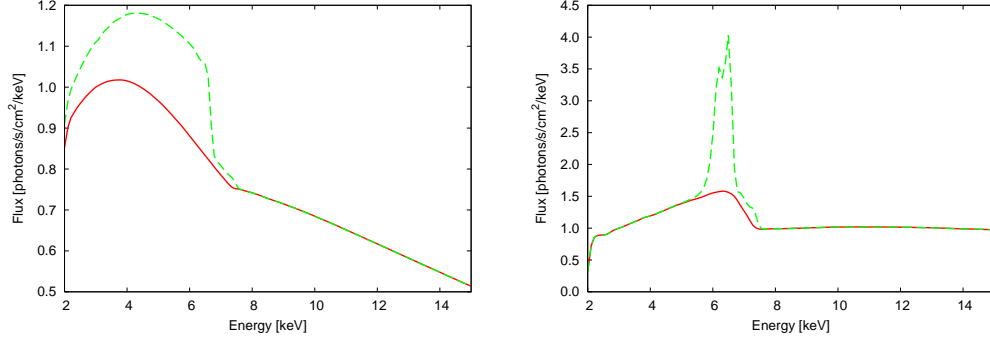


Figure 3.8: General relativistic lamp-post Compton reflection model KYL1CR with (dashed) and without (solid) iron lines  $K\alpha$  and  $K\beta$ . The emission from the disc is induced by illumination from a primary source placed  $2GM/c^2$  (left) and  $100GM/c^2$  (right) above the black hole.

eters in the following way

$$I_l = \mu_e^2(1 + \mu_i^2) + 2(1 - \mu_e^2)(1 - \mu_i^2) - 4\mu_e\mu_i\sqrt{(1 - \mu_e^2)(1 - \mu_i^2)} \cos(\Phi_e - \Phi_i) - \mu_e^2(1 - \mu_i^2) \cos[2(\Phi_e - \Phi_i)], \quad (3.19)$$

$$I_r = 1 + \mu_i^2 + (1 - \mu_i^2) \cos[2(\Phi_e - \Phi_i)], \quad (3.20)$$

$$U = -4\mu_i\sqrt{(1 - \mu_e^2)(1 - \mu_i^2)} \sin(\Phi_e - \Phi_i) - 2\mu_e(1 - \mu_i^2) \sin[2(\Phi_e - \Phi_i)]. \quad (3.21)$$

Here  $\Phi_e$  and  $\Phi_i$  are the azimuthal emission and the incident angles in the local rest frame co-moving with the accretion disc (see Sections 1.6 and 2.4 for their definition). For the derivation of these formulae see the definitions (I.147) and eqs. (X.172) in Chandrasekhar (1960). We have omitted a common multiplication factor, which would be cancelled anyway in eqs. (3.15)–(3.18). The symbol  $\langle \rangle$  in definitions of the local Stokes parameters means value averaged over the difference of the azimuthal angles  $\Phi_e - \Phi_i$ . We divide the parameters by  $\langle I_l + I_r \rangle$  because the function  $f(E_l; \mu_i, \mu_e)$ , and thus also the local photon flux  $N_l(E_l)$ , is averaged over the difference of the azimuthal angles.

The parameters defining local emission in this model are (see Tab. 3.7):

**PhoIndex** – photon index of primary power-law illumination,

**height** – height above the black hole where the primary source is located for **height**  $> 0$ ,  
and radial power-law index for **height**  $\leq 0$ ,

**line** – switch whether to include the iron lines (0 – no, 1 – yes),

**E\_cut** – exponential cut-off energy of the primary source in keV.

The tables **refspectra.fits** for the function  $f(E_l; \mu_i, \mu_e)$  also contain the emission in the iron lines  $K\alpha$  and  $K\beta$ . The two lines can be excluded from computations if the **line** switch is set to zero. The **E\_cut** parameter sets the upper boundary in energies where the emission from a primary source ceases to follow a power-law dependence. If the **E\_cut** parameter is lower than both the maximum energy of the considered dataset and the maximum energy in the tables for  $f(E_l; \mu_i, \mu_e)$  in **refspectra.fits** (300 keV), then this model is not valid.

parameter	unit	default value	minimum value	maximum value
a/M	$GM/c$	0.9982	0.	1.
theta_o	deg	30.	0.	89.
rin-rh	$GM/c^2$	0.	0.	999.
ms	—	1.	0.	1.
rout-rh	$GM/c^2$	400.	0.	999.
phi	deg	0.	-180.	180.
dphi	deg	360.	0.	360.
nrad	—	200.	1.	10000.
division	—	1.	0.	1.
nphi	—	180.	1.	20000.
smooth	—	1.	0.	1.
zshift	—	0.	-0.999	10.
ntable	—	0.	0.	99.
*PhoIndex	—	1.	0.	10.
*alpha	—	3.	-20.	20.
*beta	—	4.	-20.	20.
*rb	$r_{\text{ms}}$	0.	0.	160.
*jump	—	1.	0.	1e6
*Feabun	—	1.	0.	200.
*FeKedge	keV	7.11	7.0	10.
*Escfrac	—	1.	0.	1000.
*covfac	—	1.	0.	1000.
Stokes	—	0.	0.	6.

Table 3.8: Parameters of the reflection KYH1REFL model. Model parameters that are not common for all non-axisymmetric models are denoted by asterisk.

Examples of the Compton reflection emission component of the spectra with and without the fluorescent  $K\alpha$  and  $K\beta$  lines are shown in Fig. 3.8. It can be seen that originally narrow lines can contribute substantially to the continuum component.

### 3.2.2 Non-axisymmetric Compton reflection model KYH1REFL

This model is based on an existing multiplicative HREFL model in combination with the POWERLAW model, both of which are present in XSPEC. Local emission in eq. (2.11) is the same as the spectrum given by the model HREFL\*POWERLAW with the parameters `thetamin` = 0 and `thetamax` = 90 with a broken power-law radial dependence added:

$$N_1(E_1) = r^{-\text{alpha}}_{\text{HREFL*POWERLAW}} \quad \text{for } r \geq r_b, \quad (3.22)$$

$$N_1(E_1) = \text{jump } r_b^{\text{beta-alpha}} r^{-\text{beta}}_{\text{HREFL*POWERLAW}} \quad \text{for } r < r_b. \quad (3.23)$$

For a definition of the boundary radius  $r_b$  by the `rb` parameter see eqs. (3.3)–(3.4), and for a detailed description of the HREFL model see Dovčiak, Karas & Yaqoob (2004) and the XSPEC manual. The KYH1REFL model can be interpreted as a Compton-reflection model for which the source of primary irradiation is near above the disc, in contrast to the lamp-post scheme with the source on the axis (see Fig. 2.1). The approximations for Compton reflection used in HREFL (and therefore also in KYH1REFL) are valid below

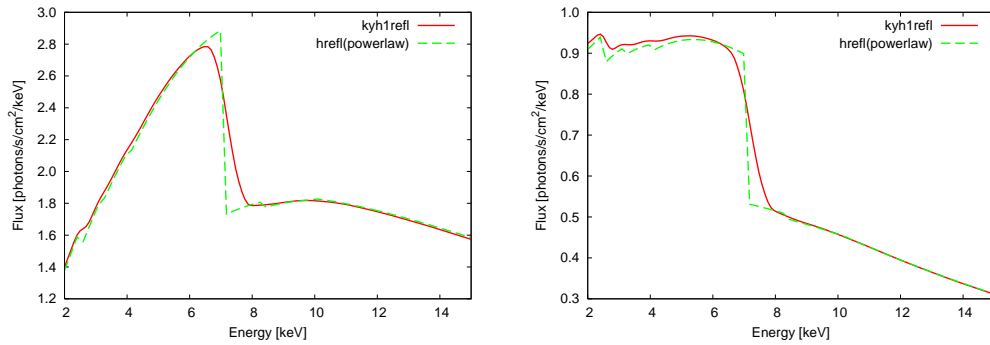


Figure 3.9: Comparison of the general relativistic KYH1REFL model with the non-relativistic HREFL(POWERLAW). The relativistic blurring of the iron edge is clearly visible. The power-law index of the primary source is `PhoIndex=2` (left) and `PhoIndex=2.6` (right).

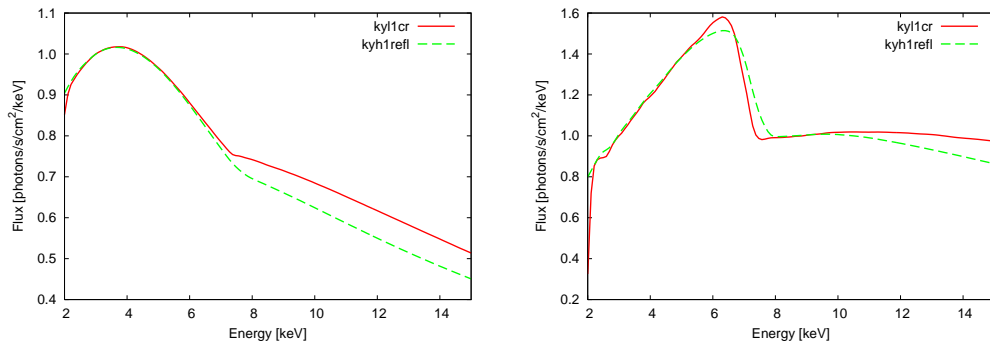


Figure 3.10: Comparison of the two new general relativistic Compton reflection models KYL1CR and KYH1REFL. The lamp-post KYL1CR model is characterized by the height  $h$  above the disc where a primary source of emission is placed, the reflection KYH1REFL model is characterized by the radial power-law index  $\alpha$ . Left:  $h = 2 GM/c^2$ ,  $\alpha = 3.4$ . Right:  $h = 100 GM/c^2$ ,  $\alpha = 1.5$ .

$\sim 15$  keV in the disc rest-frame. The normalization of the final spectrum in this model is the same as in other continuum models in XSPEC, i.e. photon flux is unity at the energy of 1 keV.

The parameters defining the local emission in KYH1REFL (see Tab. 3.8) are

`PhoIndex` – photon index of the primary power-law illumination,

`alpha` – radial power-law index for the outer region,

`beta` – radial power-law index for the inner region,

`rb` – parameter defining the border between regions with different power-law indices,

`jump` – ratio between flux in the inner and outer regions at the border radius,

`Feabun` – iron abundance relative to solar,

`FeKedge` – iron K-edge energy,

`Escfrac` – fraction of the direct flux from the power-law primary source seen by the observer,

`covfac` – normalization of the reflected continuum.

Smearing of sharp features in continuum (iron edge) by relativistic effects is demonstrated in Fig. 3.9, where non-relativistic reflection model `HREFL(POWERLAW)` is compared with our relativistic `KYH1REFL` model. Here, we set the radial power-law index  $\alpha = 1$  in `KYH1REFL`. Other parameters defining these models were set to their default values.

We compare the two new relativistic reflection models `KYL1CR` and `KYH1REFL` in Fig. 3.10. Note that the `KYL1CR` model is valid only above approximately 2 keV and the `KYH1REFL` model only below approximately 15 keV.

### 3.3 General relativistic convolution models

We have also produced two convolution-type models, `KY1CONV` and `KYCONV`, which can be applied to any existing `XSPEC` model for the intrinsic X-ray emission from a disc around a Kerr black hole. We must stress that these models are substantially more powerful than the usual convolution models in `XSPEC` (these are commonly defined in terms of one-dimensional integration over energy bins). Despite the fact that our convolution models still use the standard `XSPEC` syntax in evaluating the observed spectrum (e.g. `KYCONV(POWERLAW)`), our code accomplishes a more complex operation. It still performs ray-tracing across the disc surface so that the intrinsic model contributions are integrated from different radii and azimuths on the disc.

There are several restrictions that arise from the fact that we use existing `XSPEC` models:

- by local `XSPEC` models only the energy dependence of the photon flux can be defined,
- only a certain type of radial dependence of the local photon flux can be imposed – we have chosen to use a broken power-law radial dependence,
- there is no azimuthal dependence of the local photon flux, except through limb darkening law,
- local flux depends on the binning of the data because it is defined in the centre of each bin, a large number of bins is needed for highly varying local flux.

For emissivities that cannot be defined by existing `XSPEC` models, or where the limitations mentioned above are too restrictive, one has to add a new user-defined model to `XSPEC` (by adding a new subroutine to `XSPEC`). This method is more flexible and faster than convolution models (especially when compared with non-axisymmetric one), and hence it is recommended even for cases when these prefabricated models could be used. In any new model for `XSPEC` one can use the common ray-tracing driver for relativistic smearing of the local emission: `ide` for non-axisymmetric models and `idre` for axisymmetric ones. For a detailed description see Appendixes C.1 and C.2.

#### 3.3.1 Non-axisymmetric convolution model **KYC1ONV**

The local emission in this model is computed according to the eq. (2.11) with the local emissivity equal to

$$N_1(E_1) = r^{-\text{alpha}} f(\mu_e) \text{MODEL} \quad \text{for } r > r_b, \quad (3.24)$$

$$N_1(E_1) = \text{jump } r_b^{\text{beta-alpha}} r^{-\text{beta}} f(\mu_e) \text{MODEL} \quad \text{for } r \leq r_b. \quad (3.25)$$

parameter	unit	default value	minimum value	maximum value
a/M	$GM/c$	0.9982	0.	1.
theta_o	deg	30.	0.	89.
rin-rh	$GM/c^2$	0.	0.	999.
ms	—	1.	0.	1.
rout-rh	$GM/c^2$	400.	0.	999.
phi	deg	0.	-180.	180.
dphi	deg	360.	0.	360.
nrad	—	200.	1.	10000.
division	—	1.	0.	1.
nphi	—	180.	1.	20000.
smooth	—	1.	0.	1.
*normal	—	1.	-1.	100.
zshift	—	0.	-0.999	10.
ntable	—	0.	0.	99.
*ne_loc	—	100.	3.	5000.
*alpha	—	3.	-20.	20.
*beta	—	4.	-20.	20.
*rb	$r_{\text{ms}}$	0.	0.	160.
*jump	—	1.	0.	1e6
*limb	—	0.	-10.	10.
Stokes	—	0.	0.	6.

Table 3.9: Parameters of the non-axisymmetric convolution model KYC1ONV. Model parameters that are not common for all non-axisymmetric models are denoted by asterisk.

For a definition of the boundary radius  $r_b$  by the **rb** parameter see eqs. (3.3)–(3.4) and for the definition of different limb darkening laws  $f(\mu_e)$  see eqs. (3.5)–(3.8). The local emission is given by the MODEL in the centre of energy bins used in XSPEC with the broken power-law radial dependence and limb darkening law added. Apart from the parameters of the MODEL, the local emission is defined also by the following parameters (see Tab. 3.9):

- normal** – switch for the normalization of the final spectrum,  
 = 0 – total flux is unity (usually used for the line),  
 > 0 – flux is unity at the energy = **normal** keV (usually used for the continuum),  
 < 0 – flux is not normalized,
- ne\_loc** – number of points in the energy grid where the local photon flux is defined,
- alpha** – radial power-law index for the outer region,
- beta** – radial power-law index for the inner region,
- rb** – parameter defining the border between regions with different power-law indices,
- jump** – ratio between the flux in the inner and outer regions at the border radius,
- limb** – switch for different limb darkening/brightening laws.

The local emission in each KY model has to be defined either on equidistant or exponential (i.e. equidistant in logarithmic scale) energy grid. Because the energy grid used in the convolution model depends on the binning of the data, which may be arbitrary, the flux has to be rebinned. It is always rebinned into an exponentially spaced energy grid in KY

parameter	unit	default value	minimum value	maximum value
a/M	$GM/c$	0.9982	0.	1.
theta_o	deg	30.	0.	89.
rin-rh	$GM/c^2$	0.	0.	999.
ms	–	1.	0.	1.
rout-rh	$GM/c^2$	400.	0.	999.
zshift	–	0.	-0.999	10.
ntable	–	0.	0.	99.
*alpha	–	3.	-20.	20.
*ne_loc	–	100.	3.	5000.
*normal	–	1.	-1.	100.

Table 3.10: Parameters of the axisymmetric convolution model KYCONV. Model parameters that are not common for all axisymmetric models are denoted by asterisk.

convolution models. The `ne_loc` parameter defines the number of points in which the rebinned flux will be defined.

### 3.3.2 Axisymmetric convolution model KYCONV

The local emission in this model is computed according to eq. (2.15) with the local emissivity equal to

$$N_l(E_l) = \text{MODEL}, \quad (3.26)$$

$$R(r) = r^{-\text{alpha}}. \quad (3.27)$$

Except for the parameters of the MODEL, the local emission is defined also by the following parameters (see Tab. 3.10):

`alpha` – radial power-law index,

`ne_loc` – number of points in energy grid where local photon flux is defined,

`normal` – switch for the normalization of the final spectrum,

= 0 – total flux is unity (usually used for the line),

> 0 – flux is unity at the energy = `normal` keV (usually used for the continuum),

< 0 – flux is not normalized.

Note that the limb darkening/brightening law can be chosen through the `ntable` switch. This model is much faster than the non-axisymmetric convolution model KYC1ONV.

## 3.4 Non-stationary model KYSPOT

Emission in this model originates from a localized spot on the disc. The spot may either move along a stable circular orbit or fall from the vicinity of the marginally stable orbit down to the horizon. In the former case the spot is orbiting with a Keplerian velocity, in the latter it falls with energy and angular momentum of the matter on the marginally stable orbit. Because the emission changes in time this model cannot be included into XSPEC which cannot handle non-stationary problems. In spite of this we may include

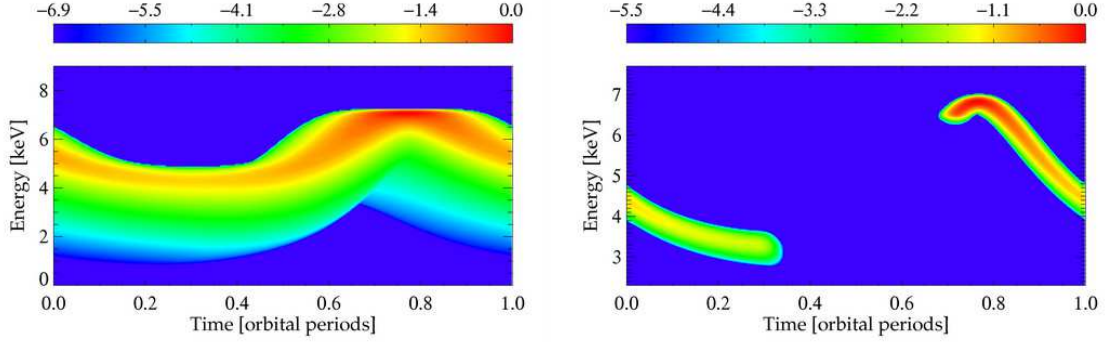


Figure 3.11: Dynamical profile of an iron line ( $E_{\text{rest}} = 6.4 \text{ keV}$ ) produced by an orbiting spot. Energy is on the ordinate, time on the abscissa. The horizontal range spans the interval of one orbital period. Time zero corresponds to the time when the observer receives photons from the spot at the closest approach to the observer. Left: Large spot ( $\beta = 0.1$ ) at the radius  $r_{\text{spot}} = 8GM/c^2$ . Right: Obscured small spot ( $\beta = 4$ ) at the radius  $r_{\text{spot}} = 5GM/c^2$ . Obscuration occurs between  $315^\circ - 540^\circ$  measured from the closest approach. In both cases the dimensionless angular momentum parameter of the black hole is  $a = 1$  and observer inclination is  $\theta_o = 45^\circ$ . The observed photon flux is colour-coded (logarithmic scale with arbitrary units).

integrated emission received by the observer in a certain time span (corresponding to a certain part of the orbit) in future.

In this model it is assumed that the corona above the disc is heated by a flare. Thus a hot cloud is formed, which illuminates the disc below it by X-rays. The disc reflects this radiation by Compton scattering and by fluorescence. In the current model we consider only the fluorescent part of the reflection.

The local emission from the disc is

$$N_l(E_l) = f(\mu_e) \exp \left[ - \left( \frac{E_l - E_{\text{rest}}}{\sqrt{2} \sigma} \right)^2 \right] \exp [-\text{beta} (\Delta r)^2] \quad \text{for } \text{beta} (\Delta r)^2 < 4, \quad (3.28)$$

$$N_l(E_l) = 0 \quad \text{for } \text{beta} (\Delta r)^2 \geq 4. \quad (3.29)$$

Here the function  $f(\mu_e)$  describes the limb darkening/brightening law (see Section 3.1.1 for more details),  $E_{\text{rest}}$  is the local energy of the fluorescent line,  $\sigma = 2 \text{ eV}$  is its width,  $\text{beta}$  determines the size of the spot and  $(\Delta r)^2 = r^2 + r_{\text{spot}}^2 - 2 r r_{\text{spot}} \cos(\varphi - \varphi_{\text{spot}})$  with  $r_{\text{spot}}$  and  $\varphi_{\text{spot}}$  being polar coordinates of the centre of the spot. The emission is largest at the centre of the spot and decreases towards its edge as is obvious from eq. (3.28). The Gaussian line in energies is defined by nine points equally spaced with the central point at its maximum.

The local emission is defined by the following parameters (see Tab. 3.11):

**Erest** – rest energy of the line in keV,

**sw** – switch for choosing the type of spot (1 – orbiting, 2 – falling),

**beta** – parameter defining the size of the spot,

**rsp** – radius (in  $GM/c^2$ ) at which the spot is orbiting or the initial radius in units of the marginally stable orbit  $r_{\text{ms}}$  if spot is in-falling,

parameter	unit	default value	minimum value	maximum value
a/M	$GM/c$	0.9982	0.	1.
theta_o	deg	30.	0.	89.
rin-rh	$GM/c^2$	0.	0.	999.
rout-rh	$GM/c^2$	20.	0.	999.
phi	deg	0.	-180.	180.
dphi	deg	360.	0.	360.
nrad	—	300.	1.	10000.
division	—	0.	0.	1.
nphi	—	750.	1.	20000.
smooth	—	1.	0.	1.
zshift	—	0.	-0.999	10.
ntable	—	0.	0.	99.
*Erest	keV	6.4	1.	99.
*sw	—	1.	1.	2.
*beta	—	0.1	0.001	1000.
*rsp	$GM/c^2$	8.	0.	1000.
*psp	deg	90.	-360.	360.
*Norbits	—	1.	0.	10
*nt	—	500.	1.	1e6
*limb	—	0.	-10.	10.
*polar	—	0.	0.	1.

Table 3.11: Parameters of the non-stationary model KYSPOT. Model parameters that are not common for all non-axisymmetric models are denoted by asterisk.

**psp** – azimuthal angle in degrees where the spot is initially located ( $90^\circ$  for the closest approach),

**Norbits** – number of orbits for an in-falling spot (not used for an orbiting spot),

**nt** – time resolution of the grid,

**limb** – switch for different limb darkening/brightening laws,

**polar** – switch for polarization calculations (0 – not performed, 1 – performed).

The KYSPOT model creates an `ascii` file `kyspot.dat`, where the dependence of the observed spectrum (columns) on time (rows) are stored. If the **polar** switch is set to unity then two other `ascii` files are created – `kyspot_poldeg.dat` and `kyspot_psi.dat`. Here, the dependence of the degree of polarization and the angle of polarization on time are stored. The polarization calculations in this model are based on the same assumptions as in the KYG1LINE model.

Examples of dynamical spectra of orbiting and in-falling spots can be seen in Figs. 3.11–3.12. The first figure represents an evolving spectral line in a dynamical diagram for an orbiting spot of two different sizes one of which is being obscured on part of its orbit around the black hole. The characteristic radius of the larger spot is  $\sim 6.3GM/c^2$  and the radius of the smaller spot is  $\sim 1GM/c^2$ . The second figure represents the dynamical spectra of the spot falling from the marginally stable orbit down towards the black-hole horizon. The characteristic radius of the spot is  $\sim 0.2GM/c^2$ . This figure reflects the effect of changing the energy shift along the spot trajectory. The in-spiral motion starts just below

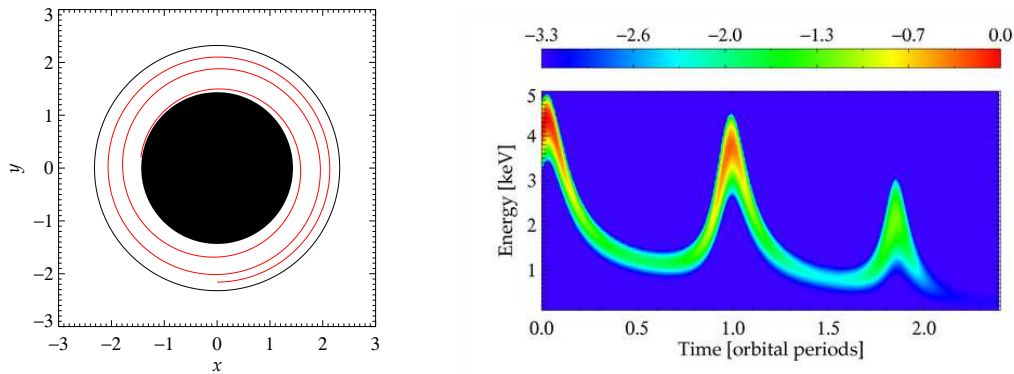


Figure 3.12: Dynamical profile of an iron line produced by an in-spiralling small spot ( $\beta = 100$ ) in free fall. Left: Trajectory (in the equatorial plane) of the spot, defined by a constant energy and angular momentum during the in-fall. The observer is located to the top of the figure. Right: Spectrum of the spot. Energy is on the ordinate, time on the abscissa. The horizontal range spans the interval of 2.4 orbital periods at the corresponding initial radius,  $r_{\text{spot}} = 0.93 r_{\text{ms}}(a)$ . Here, the dimensionless angular momentum parameter of the black hole is  $a = 0.9$ , observer inclination is  $\theta_o = 45^\circ$ . The observed photon flux is colour-coded (logarithmic scale with arbitrary units). Gradual decay of the signal and an increasing centroid redshift can be observed as the spot completes over two full revolutions and eventually plunges into the black hole.

the marginally stable orbit ( $\mathbf{rsp} = 0.93$ ) and it proceeds down to the horizon, maintaining the specific energy and angular momentum of its initial circular orbit at  $r_{\text{ms}}(a)$ . One can easily recognize that variations in the redshift could hardly be recovered from data if only time-averaged spectrum were available. In particular, the motion above  $r_{\text{ms}}(a)$  near a rapidly spinning black hole is difficult to distinguish from a descent below  $r_{\text{ms}}(0)$  in the non-rotating case.

### 3.5 Summary of the new model

The new KY model is suited for use with the XSPEC package (Arnaud 1996). Several mutations of KY were developed, with the aim to specifically provide different applications, and linked with a common ray-tracing subroutine, which therefore does not have to be modified when the intrinsic emissivity function in the model is changed.

When the relativistic line distortions are computed, the new model is more accurate than the LAOR model (Laor 1991) and faster than KERRSPEC (Martocchia, Karas & Matt 2000). These are the other two XSPEC models with a similar usage (see also Pariev & Bromley 1998; Gierliński, Maciolek-Niedźwiecki & Ebisawa 2001; Beckwith & Done 2004; Schnittman & Bertschinger 2004). It is also important to compare the results from fully independent relativistic codes since the calculations are sufficiently complex for significant differences to arise. Our code is more general than the currently available alternatives in XSPEC.

In our KY model it is possible to choose from various limb darkening/brightening laws and thus change the angular distribution of the local emission. The problem of directional distribution of the reflected radiation is quite complicated and the matter

Name	Type <sup>†</sup>	Symmetry	Usage
KYGline	additive	axisymmetric	spectral line from a black-hole disc
KYG1line		non-axisymmetric	
KYF1ll	additive	non-axisymmetric	lamp-post fluorescent line
KYL1cr	additive	non-axisymmetric	lamp-post Compton reflection model, physical model of polarization is included
KYH1refl	additive	non-axisymmetric	Compton reflection with an incident power-law (or a broken power-law) continuum
KYConv	convolution	axisymmetric	convolution of the relativistic kernel with
KYC1onv		non-axisymmetric	intrinsic emissivity across the disc
KYSpot	to be used as an independent code outside XSPEC		time-dependent spectrum of a pattern co-orbiting with the disc

<sup>†</sup> Different model types correspond to the XSPEC syntax and are defined by the way they act in the overall model and form the final spectrum. According to the usual convention in XSPEC, additive models represent individual *emission* spectral components, which may, for instance, originate in different regions of the source. Additive models are simply superposed in the total signal. Multiplicative components (e.g. HREFL) multiply the current model by an energy-dependent factor. Convolution models modify the model in a more non-trivial manner. See Arnaud (1996) for details.

Table 3.12: Different versions of the KY model.

has not been completely settled yet (e.g. George & Fabian 1991; Życki & Czerny 1994; Magdziarz & Zdziarski 1995, and references cited therein). A specific angular dependence is often assumed in models, such as limb darkening  $f(\mu_e) = 1 + 2.06\mu_e$  in the LAOR model. However, it has been argued that limb brightening may actually occur in the case of strong primary irradiation of the disc. This is relevant for accretion discs near black holes, where the effects of emission anisotropy are crucial (Beckwith & Done 2004; Czerny *et al.* 2004). We find that the spectrum of the inner disc turns out to be very sensitive to the adopted angular dependence of the emission, and so the possibility to modify this profile and examine the results using KY appears to be rather useful.

Among its useful features, the KY model allows one to fit various parameters such as the black-hole angular momentum ( $a$ ), the observer inclination angle relative to the disc axis ( $\theta_o$ ), and the size and shape of the emission area on the disc, which can be non-axisymmetric. A straightforward modification of a single subroutine suffices to alter the prescription for the disc emissivity, which is specified either by an analytical formula or in a tabular form. Our code allows one to change the mesh spacing and resolution for the (two-dimensional) polar grid that covers the disc plane, as well as the energy vector (the output resolution is eventually determined by the detector in use when the model is folded through the instrument response). Hence, there is sufficient control of the (improved) accuracy and computational speed.

Furthermore, KY can be run as a stand-alone program (detached from XSPEC). In this mode there is an option for time-variable sources such as orbiting spots, spiral waves or evolving flares (e.g. Czerny *et al.* 2004, who applied a similar approach to compute the predicted rms variability in a specific flare/spot model). The improved accuracy of the new model has been achieved in several ways: (i) photon rays are integrated in Kerr ingoing coordinates which follow principal photons, (ii) simultaneous integration of the geodesic

deviation equations ensures accurate evaluation of the lensing effect, and (iii) non-uniform and rather fine grids have been carefully selected.

Several versions of the routine have been prefabricated for different types of sources (Tab. 3.12): (i) an intrinsically narrow line produced by a disc, including the lamp-post fluorescent line model (Martocchia, Karas & Matt 2000), (ii) the Compton reflection model in two variants – a relativistically blurred Compton-reflection continuum including a primary power-law component and a lamp-post model (Martocchia, Karas & Matt 2000), (iii) general convolution models, and (iv) the time-dependent spectrum of an orbiting or a free-falling spot. Default parameter values for the line model correspond to those in the LAOR model, but numerous options have been added. For example, in the new model one is able to set the emission inner radius below the marginally stable orbit,  $r_{\text{in}} < r_{\text{ms}}(a)$ . One can also allow  $a$  to vary independently, in which case the horizon radius,  $r_{\text{h}}(a) \equiv 1 + \sqrt{1 - a^2}$ , has to be, and indeed is, updated at each step of the fit procedure. We thus define emission radii in terms of their offset from the horizon. Several arguments have been advocated in favour of having  $r_{\text{in}} \neq r_{\text{ms}}$  for the disc emission, but this possibility has never been tested rigorously against observational data. The set of KY-routines introduced above provide the tools to explore black-hole disc models and to actually fit for their key parameters, namely,  $a$ ,  $\theta_{\text{o}}$ , and  $r_{\text{in}}$ .

We have also produced a convolution-type model, KYCONV, which can be applied to any existing XSPEC model of intrinsic X-ray emission (naturally, a meaningful combination of the models is the responsibility of the user). We remind the reader that KYCONV is substantially more powerful than the usual convolution models in XSPEC, which are defined in terms of a one-dimensional integration over energy bins. Despite the fact that KYCONV still uses the standard XSPEC syntax in evaluating the observed spectrum (e.g. KYCONV(GAUSSIAN)), our code performs a more complex operation. It still performs ray-tracing across the disc surface so that the intrinsic model contributions are integrated from different radii. Thus the KYCONV(GAUSSIAN) model gives the same results as the KYGLINE model if corresponding parameters are set to the same values. The price that one has to pay for the enhanced functionality is a higher demand on computational power.

Other user-defined emissivities can be easily adopted. This can be achieved either by using the above mentioned convolution model or by adding a new user-defined model to XSPEC. The latter method is more flexible and faster, and hence recommended. In both approaches, the ray-tracing routine is linked and used for relativistic blurring.

## Chapter 4

# Applications

### 4.1 Seyfert galaxy MCG–6-30-15

The Seyfert 1 galaxy MCG–6-30-15 is a unique source in which the evidence of a broad and skewed Fe K $\alpha$  line has led to a wide acceptance of models with an accreting black hole in the nucleus (Tanaka *et al.* 1995; Iwasawa *et al.* 1996; Nandra *et al.* 1997; Guainazzi *et al.* 1999; Fabian & Vaughan 2003). Being a nearby AGN (the galaxy redshift is  $z = 0.0078$ ), this source offers an unprecedented opportunity to explore directly the pattern of the accretion flow onto the central hole. The Fe K line shape and photon redshifts indicate that a large fraction of the emission originates from  $r \lesssim 10$  ( $GM/c^2$ ). The mean line profile derived from *XMM-Newton* observations is similar to the one observed previously using *ASCA*. The X-ray continuum shape in the hard spectral band was well determined from *BeppoSAX* data (Guainazzi *et al.* 1999).

To illustrate the new KY model capabilities, we used our code to analyze the mean EPIC PN spectrum which we compiled from the long *XMM-Newton* 2001 campaign (e.g., as described in Fabian *et al.* 2002). The data were cleaned and reduced using standard data reduction routines, employing SAS version 5.4.1.<sup>1</sup> We summed the EPIC PN data from five observations made in the interval 11 July 2001 to 04 August 2001, obtaining a total good exposure time of  $\sim 290$  ks (see Fabian *et al.* 2002 for details of the observations). The energy range was restricted to 3 – 10 keV with 339 energy bins, unless otherwise stated, and models were fitted by minimizing the  $\chi^2$  statistic. Statistical errors quoted correspond to 90% confidence for one interesting parameter (i.e.  $\Delta\chi^2 = 2.706$ ), unless otherwise stated.

No absorber was taken into account; the assumption here is that any curvature in the spectrum above 3 keV is not due to absorption, and only due to the Fe K line. We remind the reader that the Fe K emission line dominates around the energy 6 – 7 keV, but it has been supposed to stretch down to  $\sim 3$  keV or even further. We emphasize that our aim here is to test the hypothesis that *if all of the curvature is entirely due to the broad Fe K feature, is it possible to constrain a of the black hole?* Obviously, if the answer to this is ‘no’, it will also be negative if some of the spectral curvature between  $\sim 3$  – 5 keV is due to processes other than the Fe K line emission.

We considered Fe K $\alpha$  and Fe K $\beta$  iron lines (with their rest-frame energy fixed at  $E_{\text{rest}} = 6.400$  and 7.056 keV, respectively), a narrow-line feature (observed at  $E_{\text{obs}} \sim 6.9$  keV) modelled as a Gaussian with the central energy, width, and intensity as free

---

<sup>1</sup>See <http://xmm.vilspa.esa.es/sas/>.

#	$a$	$\theta_o$	Continuum		$\chi^2$
			$\Gamma_c$	$\alpha_c$	(dof)
1	$0.35^{+0.57}_{-0.30}$	$31.8 \pm 0.3$	$2.01 \pm 0.02$	$1.0^{+9}_{-1}$	$\frac{368.8}{(329)}$
2a	$0.99 \pm 0.01$	$40.4 \pm 0.6$	$2.03 \pm 0.02$	$5.5^{+6}_{-2}$	$\frac{308.6}{(330)}$
2b	$0.72^{+0.12}_{-0.30}$	$28.5 \pm 0.5$	$2.01 \pm 0.01$	$0.1^{+2}_{-0.1}$	$\frac{313.5}{(330)}$
2c	$0.25 \pm 0.03$	$27.6 \pm 0.6$	$1.97 \pm 0.02$	$3.1^{+0.3}_{-0.1}$	$\frac{313.9}{(330)}$

#	Broad Fe K $\alpha$ line					
	$r_{in} - r_h$	$r_b - r_h$	$r_{out} - r_h$	$\alpha_{in}$	$\alpha_{out}$	EW
1	$5.1 \pm 0.2$	–	$11.4 \pm 0.8$	–	$3.9 \pm 0.6$	$258^{+26}_{-13}$
2a	$0.67 \pm 0.04$	$3.35 \pm 0.05$	$40^{+960}_{-33}$	$6.9^{+0.5}_{-0.4}$	$9.7^{+0.3}_{-0.8}$	$268 \pm 13$
2b	$0.65 \pm 0.35$	$2.1 \pm 0.2^{\dagger}$ $7.2 \pm 0.2$	$48^{+200}_{-25}$	$8.1^{+1.4}_{-0.9}$	$4.9^{+0.4}_{-0.3}$	$241^{+13}_{-10}$
2c	$1.23 \pm 0.06$	$4 \pm 0.02$	$109^{+20}_{-10}$	$9.2 \pm 0.2$	$3.1 \pm 0.1$	$267 \pm 10$

Best-fitting values of the important parameters and their statistical errors for models #1–2, described in the text. The models include broad Fe K $\alpha$  and Fe K $\beta$  emission lines, a narrow Gaussian line at  $\sim 6.9$  keV, and a Compton-reflection continuum from a relativistic disc. These models illustrate different assumptions about intrinsic emissivity of the disc (the radial emissivity law does not need to be a simple power law, but axial symmetry has been still imposed here). The inclination angle  $\theta_o$  is in degrees, relative to the rotation axis; radii are expressed as an offset from the horizon (in  $GM/c^2$ ); the equivalent width, EW, is in electron volts.

$^{\dagger}$  Two values of the transition radius define the interval  $\langle r_{b-}, r_{b+} \rangle$  where reflection is diminished.

Table 4.1: Spectral fitting results for MCG–6-30-15 using the KY model.

parameters, plus a power-law continuum. We used a superposition of two KYGLINE models to account for the broad relativistic K $\alpha$  and K $\beta$  lines, ZGAUSS for the narrow, high-energy line (which we find to be centred at 6.86 keV in the source frame, slightly redshifted relative to 6.966 keV, the rest-energy of Fe Ly $\alpha$ ), and KYH1REFL for the Comptonized continuum convolved with the relativistic kernel. We assumed that the high-energy narrow line is non-relativistic. Note that an alternative interpretation of the data (as pointed out by Fabian *et al.* 2002) is that there is not an emission line at  $\sim 6.9$  keV, but He-like resonance absorption at  $\sim 6.7$  keV. This would not affect our conclusions. The ratio of the intensities of the two relativistic lines was fixed at  $I_{K\beta}/I_{K\alpha} = 0.1133$  ( $= 17/150$ ), and the iron abundance for the Compton-reflection continuum was assumed to be three times the solar value (Fabian *et al.* 2002). We used the angles  $\theta_{min} = 0^\circ$  and  $\theta_{max} = 90^\circ$  for local illumination in KYH1REFL (these values are equivalent to a central illumination of an infinite disc). The normalization of the Compton-reflection continuum relative to the direct continuum is controlled by the effective reflection ‘covering factor’,  $R_c$ , which is the ratio of the actual reflection normalization to that expected from the illumination of an

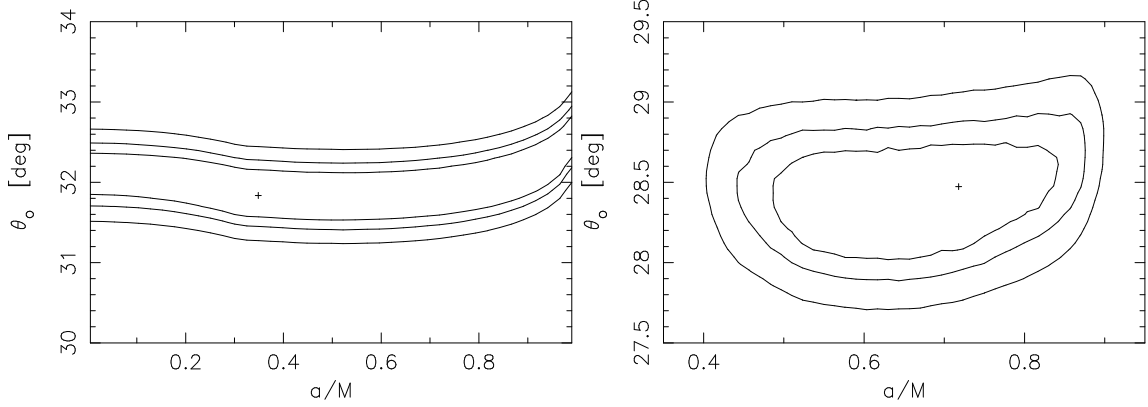


Figure 4.1: Confidence contours around the best-fitting parameter values (indicated by a cross). Left: the case of a single line-emitting region (model #1 with zero emissivity for  $r < r_{\text{ms}}$ ). Right: the case of a non-monotonic radial emissivity, model #2b. The joint two-parameter contour levels for  $a$  versus  $\theta_o$  correspond to 68%, 95% and 99% confidence.

infinite disc. Also  $r_{\text{out}}$  (outer radius of the disc),  $\alpha_c$  (slope of power-law continuum radial emissivity in the KYH1REFL model component), as well as  $R_c$ , were included among the free parameters, but we found them to be only very poorly constrained. Weak constraints on  $\alpha_c$  and  $R_c$  are actually expected in this model for two reasons. Firstly, in these data the continuum is indeed rather featureless. Secondly, the model continuum was blurred with the relativistic kernel of KYH1REFL, and so the dependence of the final spectrum on the exact form of the emissivity distribution over the disc must be quite weak.

*Model #1.* Using a model with a plain power-law radial emissivity on the disc, we obtained the best-fitting values for the following set of parameters:  $a$  of the black hole, disc inclination angle  $\theta_o$ , radii of the line-emitting region,  $r_{\text{in}} < r < r_{\text{out}}$ , the corresponding radial emissivity power-law index  $\alpha$  of the line emission, as well as the radial extent of the continuum-emitting region, its photon index  $\Gamma_c$ , and the corresponding  $\alpha_c$  for the continuum. Notice that  $\Gamma_c$  and  $\alpha_c$  refer to the continuum component *before* the relativistic kernel was applied to deduce the observed spectrum. As a result of the integration across the disc, the model weakly constrains these parameters.

There are two ways to interpret this. A model which is over-parameterized is undesirable from the point of view of deriving unique model parameters from modelling the data. However, another interpretation is that a model with a greater number of parameters may more faithfully reflect the real physics and it is the actual physical situation which leads to degeneracy in the model parameters. The latter implies that some model parameters can never be constrained uniquely, regardless of the quality of the data. In practice one must apply both interpretations and assess the approach case by case, taking into account the quality of the data, and which parameters can be constrained by the data and which cannot. If preliminary fitting shows that large changes in a parameter do not affect the fit, then that parameter can be fixed at some value obtained by invoking physically reasonable arguments pertaining to the situation.

We performed various fits with the inner edge tied to the marginally stable orbit and also fits where  $r_{\text{in}}$  was allowed to vary independently. Free-fall motion with constant angular momentum was assumed below  $r_{\text{ms}}$ , if the emitting region extended that far. Tab. 4.1 gives best-fitting values of the key relativistic line and continuum model parameters for

the case in which  $r_{\text{in}}$  and  $a$  were independent.

Next, we froze some of the parameters at their best-fit values and examined the  $\chi^2$  space by varying the remaining free parameters. That way we constructed joint confidence contours in the plane  $a$  versus  $\theta_o$  (see left panel of Fig. 4.1). These representative plots demonstrate that  $\theta_o$  appears to be tightly constrained, while  $a$  is allowed to vary over a large interval around the best fit, extending down to  $a = 0$ .

*Model #2.* We explored the possibility that the broad-line emission does not conform to a unique power-law radial emissivity but that, instead, the line is produced in two concentric rings (a ‘dual-ring’ model). This case can be considered as a toy model for a more complex (non-power law) radial dependence of the line emission than the standard monotonic decline, which we represent here by allowing for different values of  $\alpha$  in the inner and outer rings:  $\alpha_{\text{in}}$  and  $\alpha_{\text{out}}$ . Effectively, large values of the power-law index represent two separate rings. The two regions are matched at the transition radius,  $r = r_b$ , and so this is essentially a broken power law. We explored both cases of continuous and discontinuous line emissivity at  $r = r_b$ . Notice that the double power-law emissivity arises naturally in the lamp-post model (Martocchia, Karas & Matt 2000) in which the disc irradiation and the resulting Fe K $\alpha$  reflection are substantially anisotropic due to fast orbital motion in the inner ring. Although the lamp-post model is very simplified in several respects, namely the way in which the primary source is set up on the rotation axis, one can expect fairly similar irradiation to arise from more sophisticated schemes of coronal flares distributed above the disc plane. Also, in order to provide a physical picture of the steep emissivity found in *XMM-Newton* data of MCG-6-30-15, Wilms *et al.* (2001) invoked strong magnetic stresses acting in the innermost part of the system, assuming that they are able to dissipate a considerable amount of energy in the disc at very small radii. Intense self-irradiation of the inner disc may further contribute to the effect.

This more complex model is consistent with the findings of Fabian *et al.* (2002). Indeed, the fit is improved relative to models with a simple emissivity law because the enormous red wing and relatively sharp core of the line are better reproduced thanks to the contribution from a highly redshifted inner disc (see Tab. 4.1, model #2a). For the same reason that the more complex model reproduces the line core along with the red wing well, the model prefers higher values of  $a$  and  $\theta_o$  than what we found for case #1. Notice that  $a \rightarrow 1$  implies that all radiation is produced above  $r_{\text{ms}}$ . Maximum rotation is favoured with both  $a$  and  $\theta_o$  appearing to be tightly constrained near their best-fit values. Likewise for the continuum radial emissivity indices. There is a certain freedom in the parameter values that can be accommodated by this model. By scanning the remaining parameters, we checked that the reduced  $\chi^2 \sim 1$  can be achieved also for  $a$  going down to  $\sim 0.9$  and  $\theta_o \sim 37^\circ$ . This conclusion is also consistent with the case for large  $a$  in Dabrowski *et al.* (1997); however, we actually do not support the claim that the current data *require* a large value of  $a$ . As shown below, reasonable assumptions about the intrinsic emissivity can fit the data with small  $a$  equally well.

In model #2a, small residuals remain near  $E \sim 4.8$  keV (at about the  $\sim 1\%$  level), the origin of which cannot be easily clarified with the time-averaged data that we employ now. The excess is reminiscent of a Doppler horn typical of relativistic line emission from a disc, so it may also be due to Fe K $\alpha$  emission which is locally enhanced on some part of the disc. We were able to reproduce the peak by modifying the emissivity at the transition radius, where the broken power-law emissivity changes its slope (model #2b). We can even allow non-zero emissivity below  $r_{\text{ms}}$  (the inner ring) with a gap of zero emissivity between the outer edge of the inner ring and the inner edge of the outer one. The inner

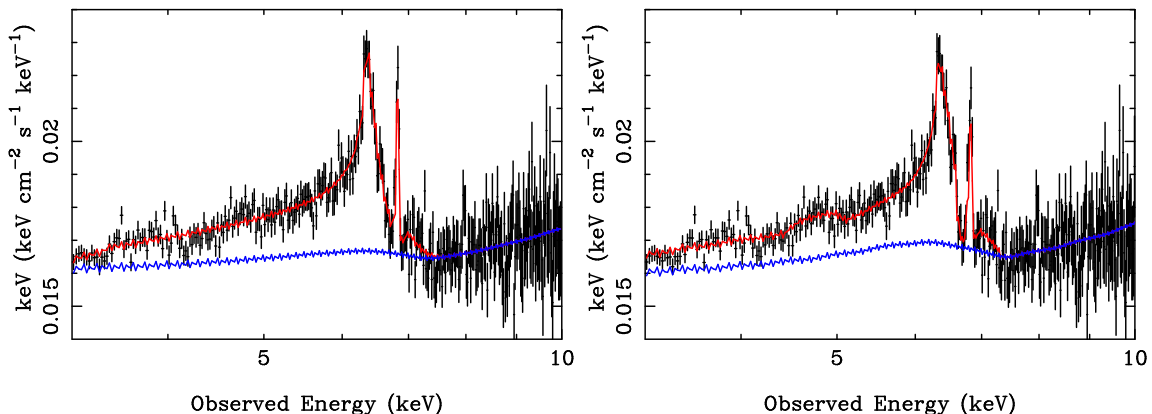


Figure 4.2: Spectrum and best-fitting model for the *XMM-Newton* data for MCG-6-30-15 in which the Fe K line originates in a dual-ring. The models 2a (left) and 2b (right) are shown in comparison. See Tab. 4.1 for the model parameters. The continuum component (KYH1REFL) is also plotted. The data points are not unfolded: the spectrum in these units was made by multiplying the ratio of measured counts to the counts predicted by the best-fitting model and then this ratio was multiplied by the best-fitting model and then by  $E^2$ .

ring,  $r_{\text{in}} \leq r \leq r_{\text{b-}}$ , contributes to the red tail of the line while the outer ring,  $r_{\text{b+}} \leq r \leq r_{\text{out}}$ , forms the main body of the broad line. The resulting plot of joint confidence contours of  $\theta_0$  versus  $a$  is shown in Fig. 4.1 (right panel). In order to construct the confidence contours we scanned a broad interval of parameters,  $0 < a < 1$  and  $0 < \theta_0 < 45^\circ$ ; here, detail is shown only around the minimum  $\chi^2$  region.

Two examples of the spectral profiles are shown in Fig. 4.2. It can be seen that the overall shapes are very similar and the changes concern mainly the red wing of the profile. For completeness we also fitted several modifications of the model #2 and found that with this type of disc emissivity (i.e. one which does not decrease monotonically with radius) we can still achieve comparably good fits which have small values of  $a$ . The case #2c in Tab. 4.1 gives another example. This shows that one cannot draw firm conclusions about  $a$  (and some of the other model parameters) based on the redshifted part of the line using current data. The data used here represent the highest signal-to-noise relativistically broadened Fe K line profile yet available for any AGN.

The differences in  $\chi^2$  between model #1 and models #2a, 2b, and 2c are very large ( $\sim 60$ ) for only one additional free parameter, so all variations of model 2 shown are better fits than the case #1. We note that formally, model #2a and #2c appear to constrain  $a$  much more tightly than model #1. The issue here is that the values of  $a$  can be completely different, with the statistical errors on  $a$  not overlapping (compare, for example, model #2a and #2c in Tab. 4.1). This demonstrates that, at least for the parameter  $a$ , it is not simply only the statistical error which determines whether a small  $a$  value is or is not allowed by the data. We confirmed this conclusion with more complicated models obtained in KY by relaxing the assumption of axial symmetry; additional degrees of freedom do not change the previous results.

One should bear in mind a well-known technical difficulty which is frequently encountered while scanning the parameter space of complex models and producing confidence contour plots similar to Fig. 4.1. That is, in a rich parameter space the procedure may

be caught in a local minimum which produces an acceptable statistical measure of the goodness of fit and appears to tightly constrain parameters near the best-fitting values. However, manual searching revealed equally acceptable results in rather remote parts of the parameter space. Indeed, as the results above show, we were able to find acceptable fits with the central black hole rotating either slowly or rapidly (in terms of the  $a$  parameter). This fact is not in contradiction with previous results (e.g. Fabian *et al.* 2002) because we assumed a different radial profile of intrinsic emissivity, but it indicates intricacy of unambiguous determination of model parameters. We therefore need more observational constraints on realistic physical mechanisms to be able to fit complicated models to actual data with sufficient confidence (Ballantyne, Ross & Fabian 2001; Nayakshin & Kazanas 2002; Róžańska *et al.* 2002).

We have seen that the models described above are able to constrain parameters with rather different degrees of uncertainty. It turns out that the more complex type #2 models (i.e. those that have radial emissivity profiles which are non-monotonic or even have an appreciable contribution from  $r < r_{\text{ms}}$ ) provide better fits to the data but a physical interpretation is not obvious. Ballantyne, Vaughan & Fabian (2003) also deduce a dual-reflector model from the same data and propose that the outer reflection is due to the disc being warped or flared with increasing radius.

## 4.2 Relativistic spectral features from X-ray illuminated spots

Relativistic iron line profiles may provide a powerful tool for measuring the mass of the black hole in active galactic nuclei and Galactic black-hole candidates. For this aim, Stella (1990) proposed to use temporal changes in the line profile following variations of the illuminating primary source (which at that time was assumed to be located on the disc axis for simplicity). Along the same line of thought, Matt & Perola (1992) proposed to employ, instead, variations of the integrated line properties such as equivalent width, centroid energy and line width. These methods are very similar conceptually to the classical reverberation mapping method, widely and successfully applied to optical broad lines in AGNs. Sufficiently long monitoring of the continuum and of the line emission is required, as well as large enough signal-to-noise ratio. However, the above-mentioned methods have not provided many results yet. Even in the best studied case of the Seyfert galaxy MCG-6-30-15, the mass estimate is hard to obtain due to the apparent lack of correlation between the line and continuum emission (Fabian *et al.* 2002). It was also suggested that these complications are possibly caused by an interplay of complex general relativistic effects (Miniutti *et al.* 2003). X-ray spectra from high throughput and high energy resolution detectors should resolve the problem of interpretation of observed spectral features. However, before such high quality data are available it is desirable to examine existing spectra and attempt to constrain physical parameters of the models.

A simple, direct and potentially robust way to measure the black-hole mass would be available if the line emission originates at a given radius and azimuth, as expected if the disc illumination is provided by a localized flare just above the disc (possibly due to magnetic reconnection), rather than a central illuminator or an extended corona. If a resulting ‘hot spot’ co-rotates with the disc and lives for at least a significant part of an orbit, by fitting the light curve and centroid energy of the line flux, the inclination angle  $\theta_o$  and the orbit radius could be derived (radius in units of the gravitational radius  $r_g$ ). Further, assuming Keplerian rotation, the orbital period is linked with radius in a well-known manner. The equation for the orbital period then contains the black-hole mass  $M_\bullet$  explicitly, and so this parameter can be determined, as discussed later.

Hot spots in AGN accretion discs were popular for a while, following the finding of apparent periodicity in the X-ray emission of the Seyfert 1 galaxy NGC 6814. They, however, were largely abandoned when this periodicity was demonstrated to be associated with an AM Herculis system in the field of view rather than the AGN itself (Madejski *et al.* 1993). Periodicities in AGNs were subsequently reported in a few sources (Iwasawa *et al.* 1998; Lee *et al.* 2000; Boller *et al.* 2001). The fact that they were not confirmed in different observations of the same sources is not surprising – quite on the contrary, it would be hard to imagine a hot spot surviving for several years.

Recently, the discovery of narrow emission features in the X-ray spectra of several AGNs (Turner *et al.* 2002; Guainazzi 2003; Yaqoob *et al.* 2003; Turner, Kraemer & Reeves 2004) has renewed interest in hot spots. There is a tentative explanation (even if not the only one) for these features, typically observed in the 5 – 6 keV energy range, in terms of iron emission produced in a small range of radii and distorted by joint action of Doppler and gravitational shift of photon energy. Iron lines would be produced by localized flares which illuminate the underlying disc surface, producing the line by fluorescence. Indeed, the formation of magnetic flares on the disc surface is one of the most promising scenarios for the X-ray emission of AGNs. A particularly strong flare, or one with a very large

anisotropic emission towards the disc, could give rise to the observed features. Small width of the observed spectral features implies that the emitting region must be small, and that it is seen for only a fraction of the entire orbit (either because the flare dies out, or because emission goes below detectability, see next section). If the flares co-rotate with the disc and if they last for a significant part of the orbit, it may be possible by observing their flux and energy variations with phase to determine the orbital parameters, and thence  $M_\bullet$ .

The basic properties of line emission from the innermost regions of an accretion disc around a black hole are well-known (see e.g. Fabian *et al.* 2000; Reynolds & Nowak 2003, for recent reviews). Let us here briefly summarize several formulae most relevant to our purposes.

If  $r$  is the orbital radius and  $a$  is the dimensionless black-hole angular momentum, the orbital period of matter co-rotating along a circular trajectory  $r = \text{const}$  around the black hole is given by (Bardeen, Press & Teukolsky 1972)

$$T_{\text{orb}} \doteq 310 \left( r^{\frac{3}{2}} + a \right) \frac{M_\bullet}{10^7 M_\odot} \quad [\text{sec}], \quad (4.1)$$

as measured by a distant observer. We express lengths in units of the gravitational radius  $r_g \equiv GM_\bullet/c^2 \doteq 1.48 \times 10^{12} M_7 \text{ cm}$ , where  $M_7$  is the mass of the black hole in units of  $10^7$  solar masses. Angular momentum  $a$  (per unit mass) is in geometrized units ( $0 \leq a \leq 1$ ). See e.g. Misner, Thorne & Wheeler (1973) for useful conversion formulae between geometrized and physical units.

The innermost stable orbit,  $r_{\text{ms}}$ , occurs for an equatorial disc at radius

$$r_{\text{ms}} = 3 + Z_2 - [(3 - Z_1)(3 + Z_1 + 2Z_2)]^{\frac{1}{2}}, \quad (4.2)$$

where  $Z_1 = 1 + (1 - a^2)^{\frac{1}{3}}[(1 + a)^{\frac{1}{3}} + (1 - a)^{\frac{1}{3}}]$  and  $Z_2 = (3a^2 + Z_1^2)^{\frac{1}{2}}$ ;  $r_{\text{ms}}$  spans the range of radii from  $r = 1$  ( $a = 1$ , i.e. the case of a maximally rotating black hole) to 6 ( $a = 0$ , a static black hole). Rotation of a black hole is believed to be limited by an equilibrium value  $a \doteq 0.998$  because of the capture of photons from the disc (Thorne 1974). This would imply  $r_{\text{ms}} \doteq 1.23$ . Different specific models of accretion can result in somewhat different limiting values of  $a$  and the corresponding  $r_{\text{ms}}$ . Notice that in the static case, the radial dependence  $T_{\text{orb}}(r)|_{a=0}$  is identical to that in purely Newtonian gravity.

In order to compute a synthetic profile of an observed spectral line one has to link the points of emission in the disc with corresponding pixels in the detector plane at spatial infinity. This can be achieved by solving the ray-tracing problem in curved space-time of the black hole. Appropriate methods were discussed by several authors; see Reynolds & Nowak (2003) for a recent review and for further references. This way one finds the redshift factor, which determines the energy shift of photons, the lensing effect (i.e. the change of solid angle due to strong gravity), and the effect of aberration (which influences the emission direction of photons from the disc; this must be taken into account if the intrinsic emissivity is non-isotropic). We consider these effects in our computations, assuming a rotating (Kerr) black-hole space-time (Misner, Thorne & Wheeler 1973). We also consider the time of arrival of photons originating at different regions of the disc plane. Variable travel time results in mutual time delay between different photons, which can be ignored when analyzing time-averaged data but it may be important for time-resolved data.

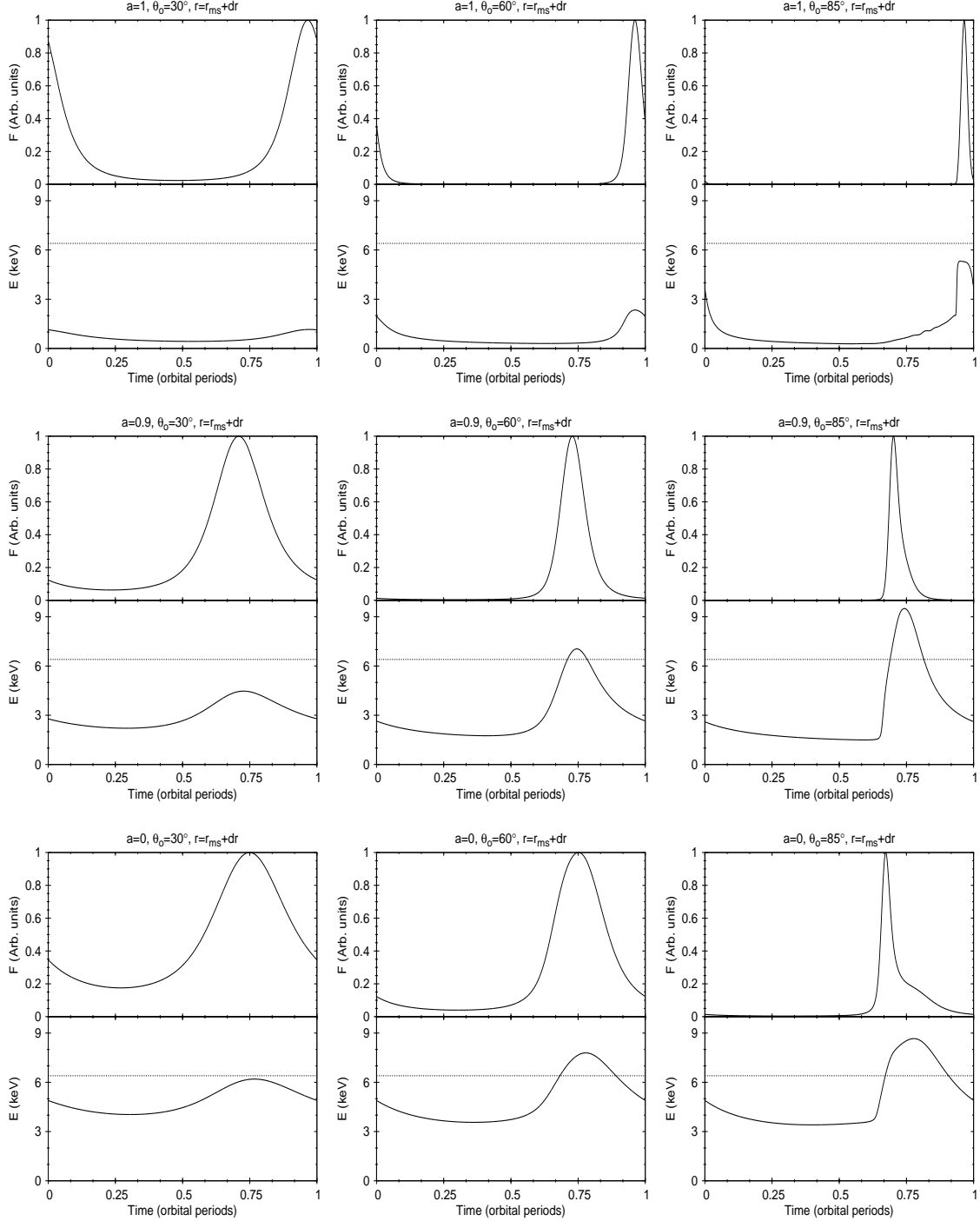


Figure 4.3: Line flux and centroid energy as functions of the orbital phase of a spot, for three values of angular momentum ( $a = 1, 0.9$ , and  $0$ ) and three inclination angles ( $\theta_o = 30^\circ, 60^\circ, 85^\circ$ ). The centre of the spot is located at radial distance  $r$ , which corresponds to the last stable orbit  $r_{\text{ms}}(a)$  for that angular momentum plus a small displacement given by the spot radius,  $dr$ . The intrinsic energy of the line emission is assumed to be at 6.4 keV (indicated by a dotted line). Prograde rotation is assumed. Time is expressed in orbital periods.

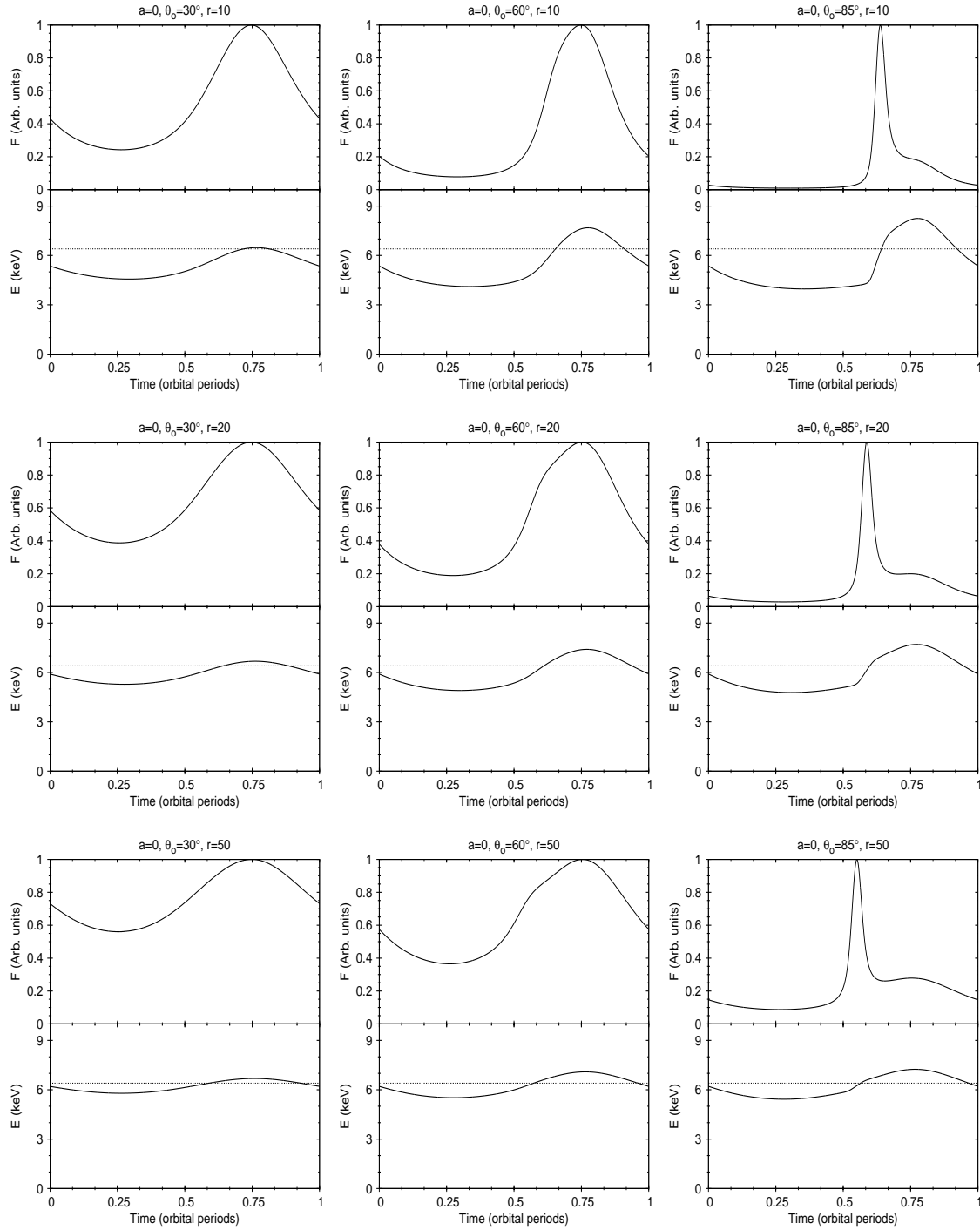


Figure 4.4: The same as the previous figure, but with  $a = 0$  and  $r = 10$  (top), 20 (middle), and 50 (bottom).

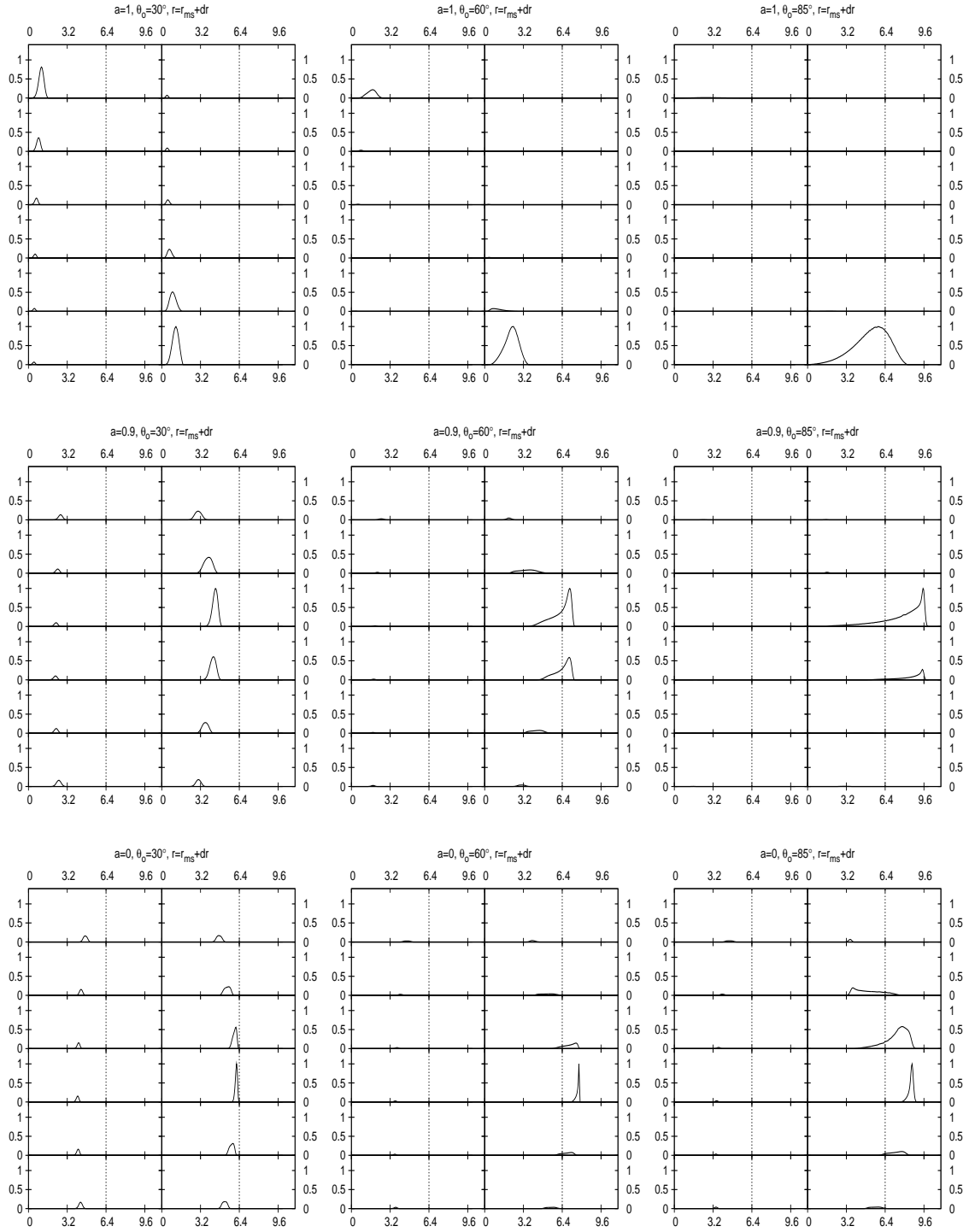


Figure 4.5: Line profiles integrated over twelve consecutive temporal intervals of equal duration. Each interval covers 1/12 of the orbital period at corresponding radius. As explained in the text, top-left frame of each panel corresponds to the spot being observed at the moment of passing through lower conjunction. Energy is on abscissa (in keV). Observed photon flux is on ordinate (arbitrary units, scaled to the maximum flux which is reached during the complete revolution of the spot). Notice the occurrences of narrow and prominent peaks which appear for relatively brief fraction of the total period.

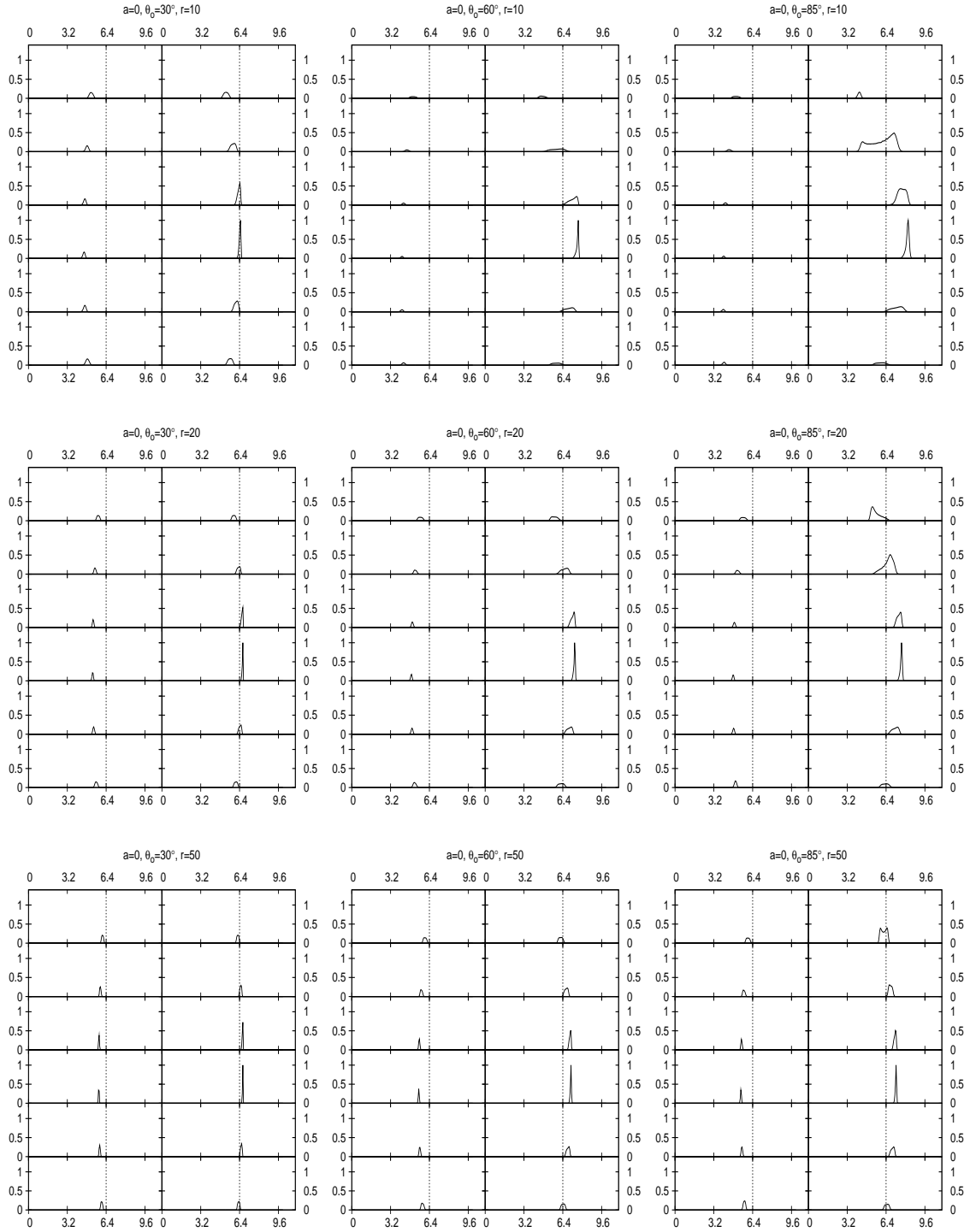


Figure 4.6: The same as in previous figure, but with  $r = 10$  (top), 20 (middle), and 50 (bottom). The black hole was assumed non-rotating,  $a = 0$  in this figure.

Assuming purely azimuthal Keplerian motion of a spot, one obtains for its orbital velocity (with respect to a locally non-rotating observer at corresponding radius  $r$ ):

$$v^{(\phi)} = \frac{r^2 - 2a\sqrt{r} + a^2}{\sqrt{\Delta}(r^{3/2} + a)}. \quad (4.3)$$

In order to derive time and frequency as measured by a distant observer, one needs to take into account the Lorentz factor associated with this orbital motion,

$$\Gamma = \frac{(r^{3/2} + a) \sqrt{\Delta}}{r^{1/4} \sqrt{r^{3/2} - 3r^{1/2} + 2a} \sqrt{r^3 + a^2r + 2a^2}}. \quad (4.4)$$

The corresponding angular velocity of orbital motion is  $\Omega = (r^{3/2} + a)^{-1}$ , which also determines the orbital period in eq. (4.1). The redshift factor  $g$  and the emission angle  $\vartheta$  (with respect to the normal direction to the disc) are then given by

$$g = \frac{\mathcal{C}}{\mathcal{B} - r^{-3/2}\xi}, \quad \vartheta = \arccos \frac{g\sqrt{\eta}}{r}, \quad (4.5)$$

where  $\mathcal{B} = 1 + ar^{-3/2}$ ,  $\mathcal{C} = 1 - 3r^{-1} + 2ar^{-3/2}$ ;  $\xi$  and  $\eta$  are constants of motion connected with the photon ray in an axially symmetric and stationary space-time.

For practical purposes formula (4.1) with  $a = 0$  is also accurate enough in the case of a spinning black hole, provided that  $r$  is not very small. For instance, even for  $r = 6$  (the last stable orbit in Schwarzschild metric),  $T_{\text{orb}}(r_{\text{ms}})$  calculated for a static and for a maximally rotating ( $a = 1$ ) black hole differ by about 6.8%. The relative difference decreases, roughly linearly, down to 1.1% at  $r = 20$ . This implies that eq. (4.1) can be used in most cases to estimate the black-hole mass even if the angular momentum is not known (deviations are relevant only for  $r < 6$ , when the radius itself can be used to constrain the allowed range of  $a$ ).

Various pseudo-Newtonian formulae have been devised for accreting black holes to model their observational properties, which are connected with the orbital motion of surrounding matter (e.g. Abramowicz *et al.* 1996; Artemova, Björnsson & Novikov 1996; Semerák & Karas 1999). Although this approach is often used and found to be practical, we do not employ it here because error estimates are not possible within the pseudo-Newtonian scheme.

Due to Doppler and gravitational energy shift the line shape changes along the orbit. Centroid energy is redshifted with respect to the rest energy of the line emission for most of the orbit. Furthermore, light aberration and bending cause the flux to be strongly phase-dependent. These effects are shown in Figs. 4.3–4.4. In these plots, the arrival time of photons is defined in orbital periods, i.e. scaled with  $T_{\text{orb}}(r; a)$ . The orbital phase of the spot is of course linked with the azimuthal angle in the disc, but the relation is made complex by time delays which cannot be neglected, given the large velocities of the orbiting matter and frame-dragging effects near the black hole. Here, zero time corresponds to the moment when the centre of the spot was at the nearest point on its orbit with respect to the observer (a lower conjunction). The plots in Fig. 4.3 refer to the case of a spot circulating at the innermost stable orbit  $r_{\text{ms}}(a)$  for  $a = 0, 0.9$  and  $1$ . The effect of black-hole rotation becomes prominent for almost extreme values of  $a$ ; one can check, for example, that the difference between cases  $a = 0$  and  $a = 0.5$  is very small.

Worth remarking is a large difference in the orbital phase of maximum emission between the extreme case,  $a \rightarrow 1$ , in contrast to the non-rotating case,  $a \rightarrow 0$ . The reason

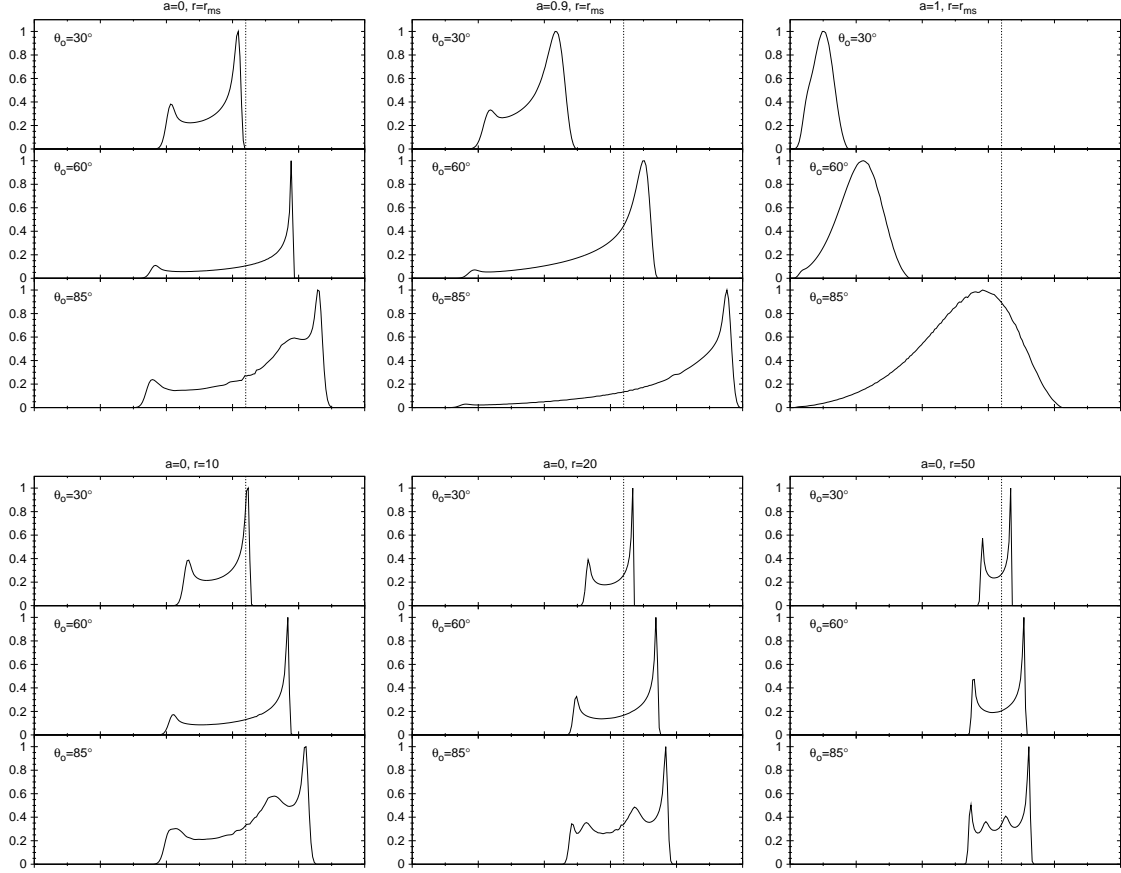


Figure 4.7: Time-averaged synthetic spectra in terms of photon flux (in arbitrary units) versus energy (in keV). These profiles represent the mean, background-subtracted spectra of the Fe  $K\alpha$  iron-line originating from spots at different radii. Top panels correspond to  $r = r_{\text{ms}}$  and  $a = 0$  (left),  $a = 0.9$  (middle), and  $a = 1$  (right). In bottom panels we fix  $a = 0$  and choose  $r = 10, 20$ , and  $50$ , respectively (other values of  $a$  give very similar profiles). Three consecutively increasing values of observer inclination  $\theta_o$  are shown, as indicated inside the frames.

is that for large  $a$  the time delay and the effect of frame-dragging on photons emitted behind the black hole are very substantial. It is also interesting to note that, for very high inclination angles, most of the flux comes from the far side of the disc, due to very strong light bending, as pointed out by Matt *et al.* (1992); Matt, Perola & Stella (1993) and examined further by many authors who performed detailed ray-tracing, necessary to determine the expected variations of the line flux and shape. A relatively simple fitting formula has also been derived (Karas 1996) and can be useful for practical computations.

Three more orbits (centred at  $r = 10, 20$  and  $50$ ) are shown for  $a = 0$  (Fig. 4.4). As said above, at these radii differences between spinning and static black holes are small. Indeed, it can be verified that the dependence on  $a$  is only marginal if  $r \gtrsim 20$ , and so it can be largely neglected for present-day measurements.

In Figs. 4.5–4.6 we show the actual form of the line profiles for the same sets of parameters as those explored in Figs. 4.3–4.4. The entire revolution was split into twelve different phase intervals. The intrinsic flux  $I$  is assumed to decrease exponentially with

the distance  $dr$  from the centre of the spot (i.e.  $\log I \propto -[\kappa dr/r]^2$ , where  $r$  is the location of the spot centre and  $\kappa \sim 10$  is a constant). The illumination is supposed to cease at  $dr = 0.2r$ , which also defines the illuminated area in the disc. Let us remark that we concentrate on a spectral line which is intrinsically narrow and unresolved in the rest frame of the emitting medium. Such a line can be produced by a spot which originates due to sharply localized illumination by flares, as proposed and discussed by various authors (e.g. Haardt, Maraschi & Ghisellini 1994; Poutanen & Fabian 1999; Merloni & Fabian 2001). Very recently, Czerny *et al.* (2004) have examined the induced rms variability in the flare/spot model with relativistic effects. In many cases, and especially for small radii and intermediate to large inclination angles, the line emission comes from a relatively minor fraction of the orbit. This implies in practice that for observations with *moderate signal-to-noise ratios, only a narrow blue horn can be visible, and only for a small part of the orbit*. These large and rapid changes of the line shape get averaged when integrating over the entire orbit, and so an important piece of information is missing in the mean spectra. The line profiles integrated over the whole revolution are shown in Fig. 4.7. Effectively, the mean profile of a spot is identical to the profile of an annulus whose radius is equal to the distance of the spot centre and the width is equal to the spot size.

We discussed the possibility that the narrow features in the 5 – 6 keV range, recently discovered in a few AGNs and usually interpreted as redshifted iron lines, could be due to illumination by localized orbiting spots just above the accretion disc. If this is indeed the case, these features may provide a powerful and direct way to measure the black-hole mass in active galactic nuclei. To achieve this aim, it is necessary to follow the line emission along the orbit. The orbital radius (in units of  $r_g$ ) and the disc inclination can be inferred from the variations of the line flux and centroid energy. Furthermore,  $M_\bullet$  can be estimated by comparing the measured orbital period with the value expected for the derived radius. We must point out, however, that present-day X-ray instruments do not have enough collecting area to perform this task accurately. This capability should be achieved by the planned high-performance X-ray missions such as *Constellation-X* and *Xeus*.

### 4.3 Polarization signatures of strong gravity in AGN accretion discs

Accretion discs in central regions of active galactic nuclei are subject to strong external illumination originating from some kind of corona and giving rise to specific spectral features in the X-ray band. In particular, the K-shell lines of iron are found to be prominent around 6–7 keV. It has been shown that the shape of the intrinsic spectra must be further modified by the strong gravitational field of the central mass, and so X-ray spectroscopy could allow us to explore the innermost regions of accretion flows near supermassive black holes (for recent reviews see Fabian *et al.* 2000; Reynolds & Nowak 2003). Similar mechanisms operate also in some Galactic black-hole candidates.

A rather surprising result from recent *XMM-Newton* observations is that relativistic iron lines are not as common as previously believed, see Bianchi *et al.* (2004) and references therein and also Yaqoob *et al.* (2003). This does not necessarily mean that the iron line is not produced in the innermost regions of accretion discs. The situation is likely to be more complex than in simple, steady scenarios, and indeed some evidence for line emission arising from orbiting spots is present in the time-resolved spectra of a few AGNs (Dovčiak *et al.* 2004a). Even when clearly observed, relativistic lines behave differently than expected. The best example is the puzzling lack of correlation between line and continuum emission in MCG–6-30-15 (Fabian *et al.* 2002), unexpected because the very broad line profile clearly indicates that the line originates in the innermost regions of the accretion disc, hence very close to the illuminating source. Miniutti *et al.* (2003) have proposed a solution to this problem in terms of an illuminating source moving along the black-hole rotation axis or very close to it.

In this section we show that polarimetric studies could provide additional information about accretion discs in a strong gravity regime, which may be essential to discriminate between different possible geometries of the source. The idea of using polarimetry to gain additional information about accreting compact objects is not a new one. In this context it was proposed by Rees (1975) that polarized X-rays are of high relevance. Pozdnyakov, Sobol’ & Sunyaev (1979) studied spectral profiles of iron X-ray lines that result from multiple Compton scattering. Later on, various influences affecting polarization (due to magnetic fields, absorption as well as strong gravity) were examined for black-hole accretion discs (Agol 1997). Temporal variations of polarization were also discussed, in particular the case of orbiting spots near a black hole (Connors, Piran & Stark 1980; Bao, Wiita & Hadrava 1996). With the promise of new polarimetric detectors (Costa *et al.* 2001), quantitative examination of specific models becomes timely.

Since the reflecting medium has a disc-like geometry, a substantial amount of linear polarization is expected in the resulting spectrum because of Compton scattering. Polarization properties of the disc emission are modified by the photon propagation in a gravitational field, providing additional information on its structure. Here we calculate the observed polarization of the reflected radiation assuming the lamp-post model for the stationary power-law illuminating source (Martocchia & Matt 1996; Petrucci & Henri 1997). We assume a rotating (Kerr) black hole as the only source of the gravitational field, having a common symmetry axis with an accretion disc. The disc is also assumed to be stationary and we restrict ourselves to the time-averaged analysis. In other words, we examine processes that vary at a much slower pace than the light-crossing time at the corresponding radius. Intrinsic polarization of the emerging light can be computed locally, assuming a plane-parallel scattering layer which is illuminated by light radiated

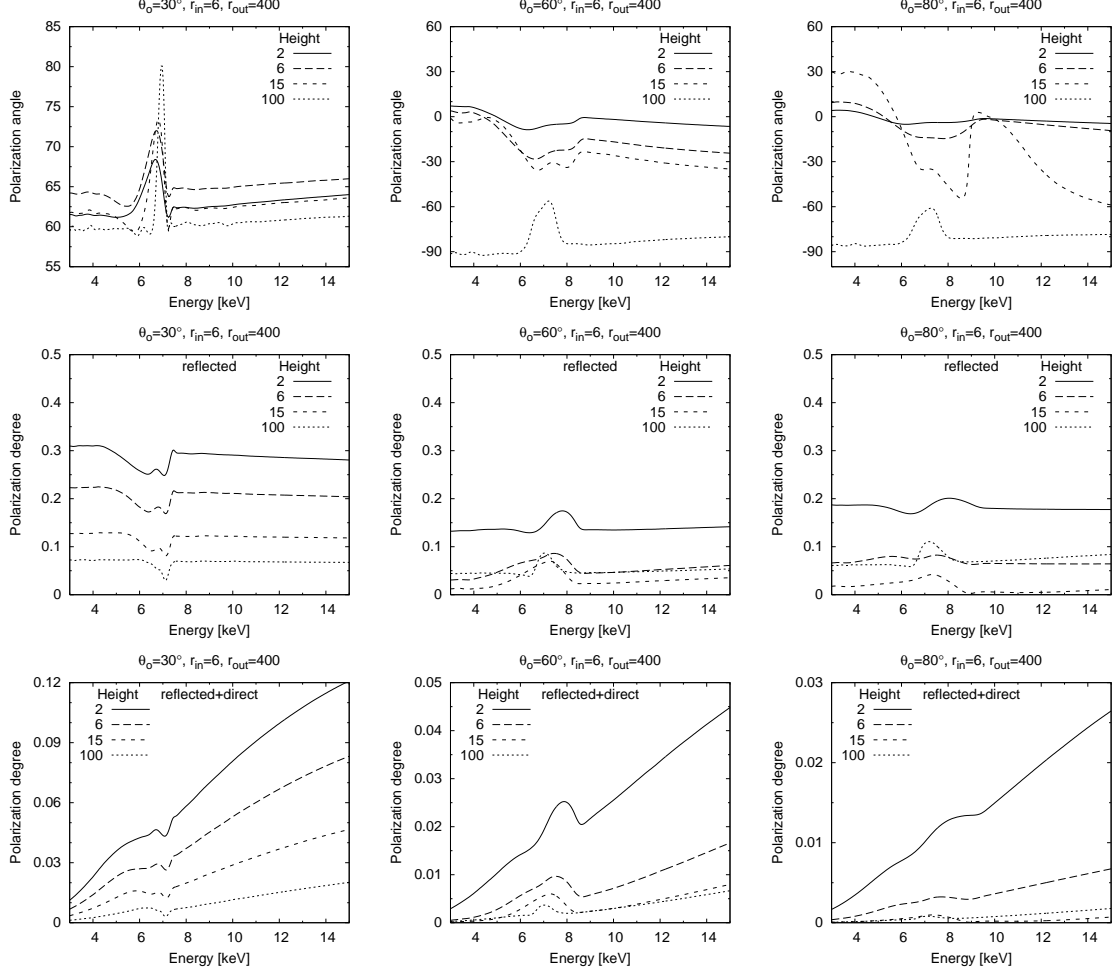


Figure 4.8: Energy dependence of polarization angle (top panels) and polarization degree (middle panels) due to reflected radiation for different observer's inclination angles ( $\theta_o = 30^\circ$ ,  $60^\circ$  and  $80^\circ$ ) and for different heights of the primary source ( $h = 2, 6, 15$  and  $100$ ). Polarization degree for reflected plus direct radiation is also plotted (bottom panels). The emission comes from a disc within  $r_{\text{in}} = 6$  and  $r_{\text{out}} = 400$ . Isotropic primary radiation with photon index  $\Gamma = 2$  and angular momentum of the central black hole  $a = 0.9987$  were assumed.

from the primary source. This problem was studied extensively in various approximations (e.g. Chandrasekhar 1960; Sunyaev & Titarchuk 1985). Here we employ the Monte Carlo computations (Matt, Perola & Piro 1991; Matt 1993) and thus we find the intrinsic emissivity of an illuminated disc. Then we integrate contributions to the total signal across the disc emitting region using a general relativistic ray-tracing technique described in previous chapters and we compute the polarization angle and degree as measured by a distant observer (see Section 2.3 and equations therein). We show the polarization properties of scattered light as a function of model parameters, namely, the height  $z = h$  of the primary source on the symmetry axis, the dimensionless angular momentum  $a$  of the black hole, and the viewing angle  $\theta_o$  of the observer.

In the first set of figures (Figs. 4.8–4.9) we show the energy dependence of polarization

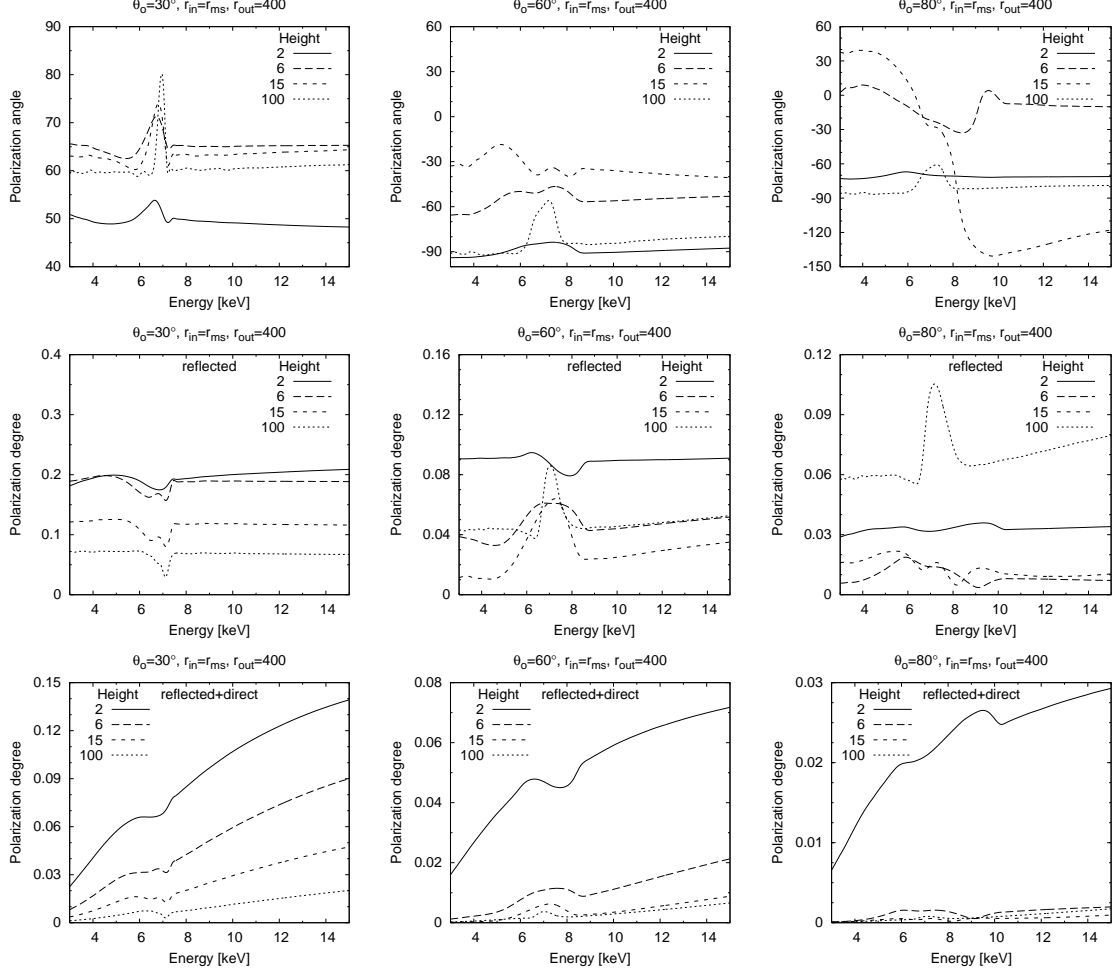


Figure 4.9: Same as in the previous figure but for disc starting at  $r_{\text{in}} = 1.20$ .

angle and degree due to reflected and reflected plus direct radiation for different inclination angles and different heights of the primary source. One can see that the polarization of reflected radiation can be as high as thirty percent or even more for small inclinations and small heights. Polarization of the reflected radiation does not depend on energy very much except for the region close to the iron edge at approximately 7.2 keV, where it either decreases for small inclinations or increases for large ones.

In order to compute observable characteristics one has to combine the primary power-law continuum with the reflected component. The polarization degree of the resulting signal depends on the mutual proportion of the two components and also on the energy range of an observation. The overall degree of polarization increases with energy (see bottom panels in Figs. 4.8–4.9) due to the fact that the intensity of radiation from the primary source decreases exponentially, the intensity of the reflected radiation increases with energy (in the energy range 3–15 keV) and the polarization of the reflected light alone is more or less constant. In our computations we assumed that the irradiating source emits isotropically and its light is affected only by gravitational redshift and lensing, according to the source location at  $z = h$  on axis. This results in a dilution of primary light by factor

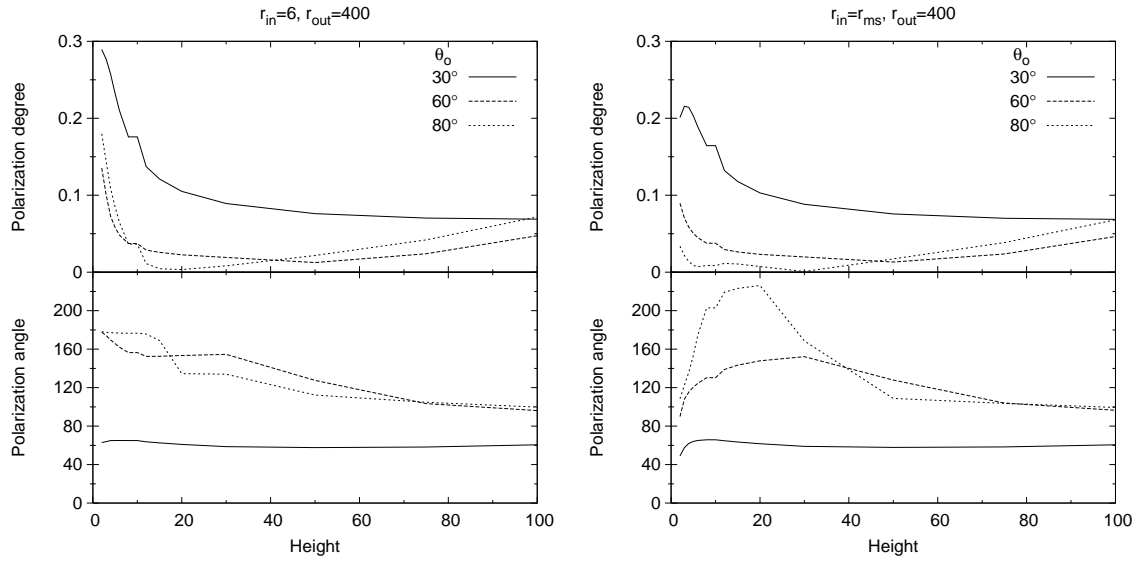


Figure 4.10: Polarization degree and angle due to reflected radiation integrated over the whole surface of the disc and propagated to the point of observation. Dependence on height  $h$  is plotted. Left panel:  $r_{\text{in}} = 6$ ; right panel:  $r_{\text{in}} = 1.20$ . In both the panels the energy range was assumed 9 – 12 keV, the photon index of incident radiation  $\Gamma = 2$ , the angular momentum  $a = 0.9987$ .

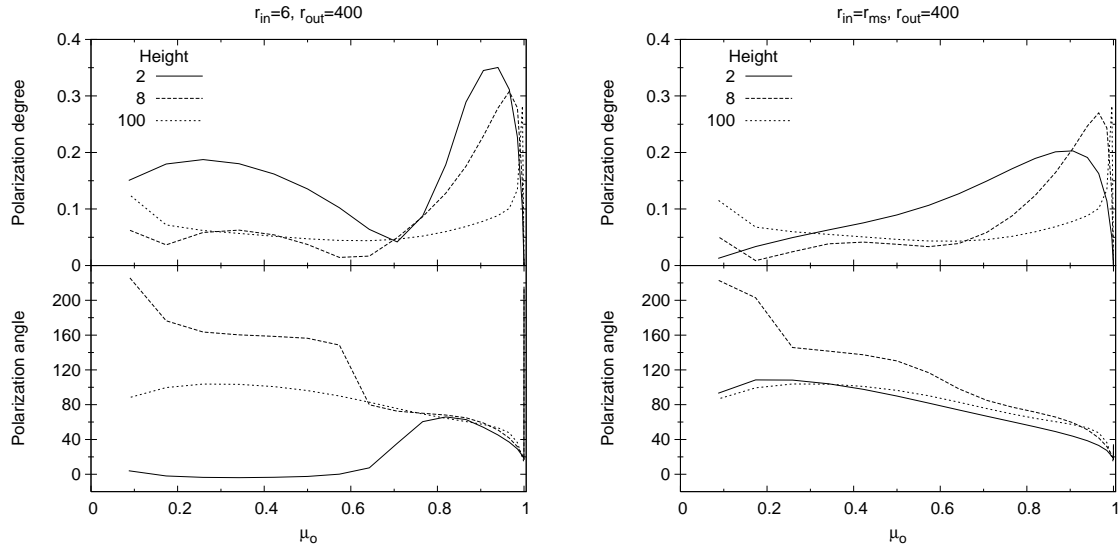


Figure 4.11: Polarization degree and angle as functions of  $\mu_o$  (cosine of observer inclination,  $\mu_o = 0$  corresponds to the edge-on view of the disc). The same model is shown as in the previous figure.

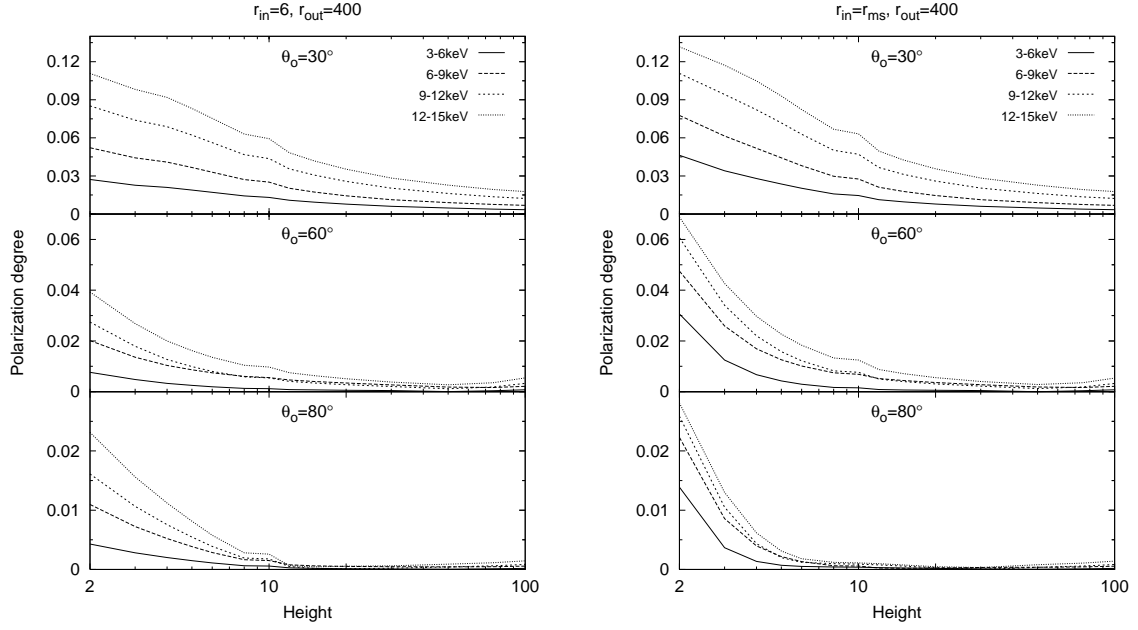


Figure 4.12: Net polarization degree of the total (primary plus reflected) signal as a function of  $h$ . Left panel:  $r_{\text{in}} = 6$ ; right panel:  $r_{\text{in}} = 1.20$ . The curves are parametrized by the corresponding energy range.

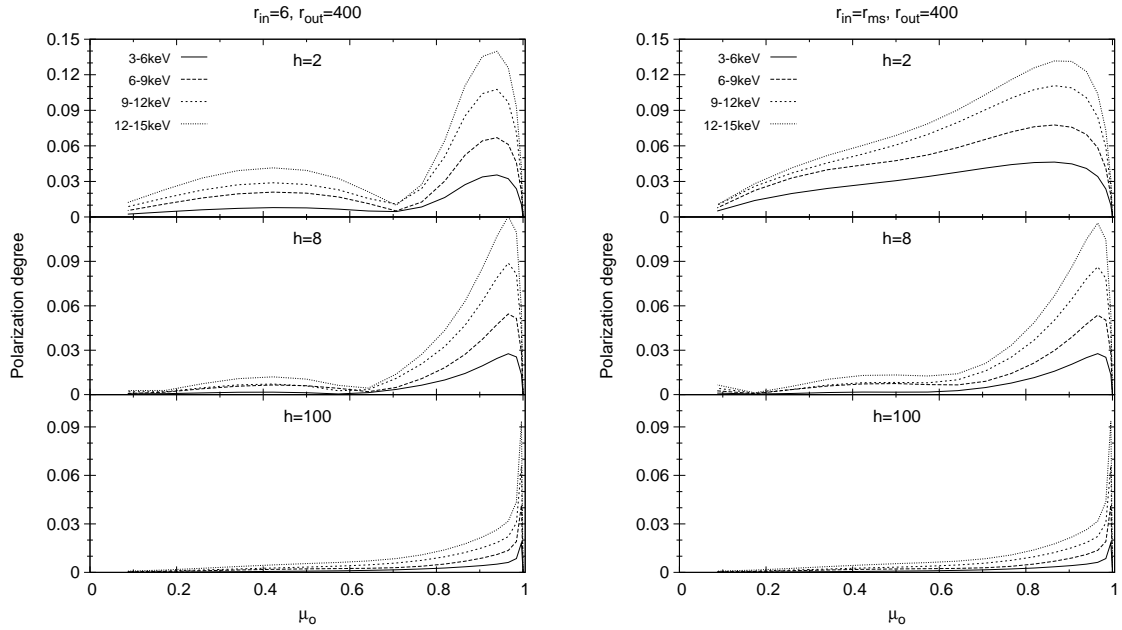


Figure 4.13: Net polarization degree of the total (primary plus reflected) signal as a function of  $\mu_o$ . The same model is shown as in the previous figure.

$\sim g_h^2(h, \theta_o) l_h(h, \theta_o)$ , where  $g_h = \sqrt{1 - 2h/(a^2 + h^2)}$  is the redshift of primary photons reaching directly the observer,  $l_h$  is the corresponding lensing factor. Here, the redshift is the dominant relativistic term, while lensing of primary photons is a few percent at most and it can be safely ignored. Anisotropy of primary radiation may further attenuate or amplify the polarization degree of the final signal, while the polarization angle is rather independent of this influence as long as the primary light is itself unpolarized.

The polarization of scattered light is also shown in Fig. 4.10, where we plot the polarization degree and the change of the polarization angle as functions of  $h$ . Notice that in the Newtonian case only polarization angles of  $0^\circ$  or  $90^\circ$  would be expected for reasons of symmetry. The change in angle is due to gravitation for which we assumed a rapidly rotating black hole. The two panels in the figure correspond to different locations of the inner disc edge:  $r_{\text{in}} = 6$  and  $r_{\text{in}} = 1.20$ , respectively. The curves are strongly sensitive to  $r_{\text{in}}$  and  $h$ , while the dependence on  $r_{\text{out}}$  is weak for a large disc (here  $r_{\text{out}} = 400$ ). Sensitivity to  $r_{\text{in}}$  is particularly appealing if one remembers the practical difficulties in estimating  $r_{\text{in}}$  by fitting spectra. The effect is clearly visible even for  $h \sim 20$ . Graphs corresponding to  $r_{\text{in}} = 6$  and  $a = 0.9987$ , resemble, in essence quite closely, the non-rotating case ( $a = 0$ ) because dragging effects are most prominent near the horizon.

Fig. 4.11 shows the polarization degree and angle as functions of the observer's inclination. Again, by comparing the two cases of different  $r_{\text{in}}$  one can clearly recognize that the polarization is sensitive to details of the flow near the inner disc boundary.

The dependence of the polarization degree of overall radiation (primary plus reflected) on the height of the primary source and the observer inclination in different energy ranges is shown in Figs. 4.12–4.13.

In this section we examined the polarimetric properties of X-ray illuminated accretion discs in the lamp-post model. From the figures shown it is clear that observed values of polarization angle and degree are rather sensitive to the model parameters. The approach adopted provides additional information with respect to traditional spectroscopy and so it has great potential for discriminating between different models. It offers an improved way of measuring rotation of the black hole because the radiation properties of the inner disc region most likely reflect the value of the black-hole angular momentum.

While our calculations have been performed assuming a stationary situation, in reality it is likely that the height of the illuminating source changes with time, and indeed such variations have been invoked by Miniutti *et al.* (2003) to explain the primary and reflected variability patterns of MCG–6-30-15. A complete time-resolved analysis (including all consequences of the light travel time in curved space-time) is beyond the scope of this section and we defer it to future work, assuming that the primary source varies on a time-scale longer than light-crossing time in the system. This is also a well-substantiated assumption from a practical point of view, since feasible techniques will anyway require sufficient integration time (i.e. order of several ksec). Once full temporal resolution is possible, the analysis described above can be readily extended. Here, it suffices to note that a variation of  $h$  implies a variation of the observed polarization angle of the reflected radiation. As it is hard to imagine a physical and/or geometrical effect giving rise to the same effect, time variability of the polarization angle can be considered (independently of the details) a very strong signature of strong-field general relativity effects at work.

New generation photoelectric polarimeters (Costa *et al.* 2001) in the focal plane of large area optics (such as those foreseen for *Xeus*) can probe the polarization degree of the order of one percent in bright AGNs, making polarimetry, along with timing and spectroscopy, a tool for exploring the properties of the accretion flows in the vicinity of black holes.

# Summary and future prospects

In this thesis we have developed a computational tool for modelling spectral features of X-ray sources in a strong gravitational field.

The following six transfer functions have been computed for light rays emitted from the equatorial plane of the Kerr black hole and received by an observer at infinity: the gravitational and Doppler shift, lensing, emission angle, relative time delay, change of the polarization angle and azimuthal emission angle. The values of these functions for different angular momenta of the black hole and inclination angles of the observer in Kerr ingoing coordinates have been stored in the form of tables in a FITS file. In computations, where parameters of the motion of the matter were needed, we have assumed a co-rotating Keplerian disc above the marginally stable orbit and freely falling matter below it. Graphical representations of the results have been made in the form of an atlas of contour figures of these functions.

For the modelling of the spectra of an accretion disc, several general relativistic codes have been developed. Some of them can be used inside a more general spectral fitting package XSPEC for routine fitting of the data measured by X-ray satellites. These are the models for the relativistic emission lines (KYGLINE, KYG1LINE and KYF1LL), Compton reflection (KYL1CR and KYH1REFL) and for the general use as a relativistic extension of existing models (the convolution models KYCONV and KYC1ONV). Other components of the tool have extended features for studying the non-stationary emission from accretion discs (KYGSPOT) and polarimetry (KYL1CR).

The newly developed codes have been employed in several applications. Firstly, we used our new KY models inside XSPEC and fitted the data from *XMM-Newton* observations of Seyfert galaxy MCG–6-30-15. Then we simulated emission from an X-ray illuminated spot orbiting near a black hole as an application on non-stationary emission from the disc. And finally, the polarization from an accretion disc illuminated by a primary source located above the black hole was computed.

There are several possibilities of how one can proceed further. We would like to:

- enhance the code so that it would be possible to investigate the self-irradiation of the disc,
- add more models to the KY package, first of all a model for the thermal emission,
- expand the code so that non-Keplerian discs can be studied as well,
- perform more polarization studies with the non-stationary lamp-post model,
- perform timing analysis of the emission from an orbiting spot in different energy bands,
- fit more data of X-ray sources acquired by X-ray satellites.

Further it would be possible to investigate applications of our code to quasi-periodic oscillations. Although our code is a two-dimensional one it might be interesting to compute how oscillations of the disc in the equatorial plane can affect the observed spectra at infinity.

# Appendix A

## Kerr space-time

In this Appendix as well as everywhere else in this thesis we use units where  $GM_{\bullet} = c = 1$  ( $M_{\bullet}$  is the mass of the central black hole) and we assume that the angular momentum  $a$  of the black hole is positive.

### A.1 Kerr metric

The Kerr metric in the Boyer-Lindquist coordinates  $(t, r, \theta, \varphi)$  is

$$g_{\mu\nu} = \begin{pmatrix} -(1 - \frac{2r}{\rho^2}) & 0 & 0 & -\frac{2ar \sin^2 \theta}{\rho^2} \\ 0 & \frac{\rho^2}{\Delta} & 0 & 0 \\ 0 & 0 & \rho^2 & 0 \\ -\frac{2ar \sin^2 \theta}{\rho^2} & 0 & 0 & \frac{\mathcal{A} \sin^2 \theta}{\rho^2} \end{pmatrix}, \quad (\text{A.1})$$

where  $\rho^2 \equiv r^2 + a^2 \cos^2 \theta$ ,  $\Delta \equiv r^2 - 2r + a^2$  and  $\mathcal{A} \equiv (r^2 + a^2)^2 - \Delta a^2 \sin^2 \theta$ .

Let's define special Kerr ingoing coordinates  $(\hat{t}, \hat{u}, \hat{\mu}, \hat{\varphi})$  by the following tetrad vectors

$$\begin{aligned} \frac{\partial}{\partial \hat{t}} &= \frac{\partial}{\partial t}, & d\hat{t} &= dt + \frac{r^2 + a^2}{\Delta} dr, \\ \frac{\partial}{\partial \hat{u}} &= -r^2 \frac{\partial}{\partial r} + r^2 \frac{r^2 + a^2}{\Delta} \left( \frac{\partial}{\partial t} + \Omega^H \frac{\partial}{\partial \varphi} \right), & d\hat{u} &= -\frac{1}{r^2} dr, \\ \frac{\partial}{\partial \hat{\mu}} &= -\frac{1}{\sin \theta} \frac{\partial}{\partial \theta}, & d\hat{\mu} &= -\sin \theta d\theta, \\ \frac{\partial}{\partial \hat{\varphi}} &= \frac{\partial}{\partial \varphi}, & d\hat{\varphi} &= d\varphi + \frac{a}{\Delta} dr, \end{aligned} \quad (\text{A.2})$$

with  $\Omega^H = \frac{a}{r^2 + a^2}$ .

The advantage of these coordinates, where  $\hat{u} \equiv r^{-1}$  and  $\hat{\mu} \equiv \cos \theta$ , is that the Kerr metric is not singular on the horizon of the black hole and spatial infinity ( $r \rightarrow \infty$ ) is brought to a finite value ( $\hat{u} \rightarrow 0$ ). Another advantage for numerical computations is that we get rid of the cosine function.

The relationship between the Boyer-Lindquist coordinate  $\varphi$  and the Kerr ingoing coordinate  $\varphi_K$ , for geodesics coming from infinity to the equatorial plane, can be expressed

in the following way:

$$\varphi = \varphi_K + \frac{a}{r_+ - r_-} \ln \frac{r - r_+}{r - r_-} \quad \text{for } a < 1, \quad (\text{A.3})$$

$$\varphi = \varphi_K - \frac{1}{r - 1} \quad \text{for } a = 1, \quad (\text{A.4})$$

with  $r_{\pm} = 1 \pm \sqrt{1 - a^2}$  being inner (−) and outer (+) horizon of the black hole.

Another useful way to express the transformation between the Boyer-Lindquist and special Kerr ingoing coordinates is by matrices of transformation

$$\frac{\partial x^\mu}{\partial \hat{x}^\nu} = \begin{pmatrix} 1 & \frac{r^2(r^2+a^2)}{\Delta} & 0 & 0 \\ 0 & -r^2 & 0 & 0 \\ 0 & 0 & -\frac{1}{\sin\theta} & 0 \\ 0 & \frac{r^2 a}{\Delta} & 0 & 1 \end{pmatrix} = \begin{pmatrix} 1 & \frac{(1+a^2\hat{u}^2)}{\hat{u}^2\tilde{\Delta}} & 0 & 0 \\ 0 & -\frac{1}{\hat{u}^2} & 0 & 0 \\ 0 & 0 & -\frac{1}{\sqrt{1-\hat{\mu}^2}} & 0 \\ 0 & \frac{a}{\tilde{\Delta}} & 0 & 1 \end{pmatrix}, \quad (\text{A.5})$$

$$\frac{\partial \hat{x}^\mu}{\partial x^\nu} = \begin{pmatrix} 1 & \frac{r^2+a^2}{\Delta} & 0 & 0 \\ 0 & -\frac{1}{r^2} & 0 & 0 \\ 0 & 0 & -\sin\theta & 0 \\ 0 & \frac{a}{\Delta} & 0 & 1 \end{pmatrix} = \begin{pmatrix} 1 & \frac{1+a^2\hat{u}^2}{\tilde{\Delta}} & 0 & 0 \\ 0 & -\hat{u}^2 & 0 & 0 \\ 0 & 0 & -\sqrt{1-\hat{\mu}^2} & 0 \\ 0 & \frac{a\hat{u}^2}{\tilde{\Delta}} & 0 & 1 \end{pmatrix}. \quad (\text{A.6})$$

The Kerr metric in special Kerr ingoing coordinates is

$$g_{\hat{\mu}\hat{\nu}} = \begin{pmatrix} -(1 - \frac{2\hat{u}}{\tilde{\rho}^2}) & -\frac{1}{\hat{u}^2} & 0 & -\frac{2a\hat{u}(1-\hat{\mu}^2)}{\tilde{\rho}^2} \\ -\frac{1}{\hat{u}^2} & 0 & 0 & \frac{a(1-\hat{\mu}^2)}{\hat{u}^2} \\ 0 & 0 & \frac{\tilde{\rho}^2}{\hat{u}^2(1-\hat{\mu}^2)} & 0 \\ -\frac{2a\hat{u}(1-\hat{\mu}^2)}{\tilde{\rho}^2} & \frac{a(1-\hat{\mu}^2)}{\hat{u}^2} & 0 & \frac{\tilde{\mathcal{A}}(1-\hat{\mu}^2)}{\hat{u}^2\tilde{\rho}^2} \end{pmatrix}, \quad (\text{A.7})$$

with  $\tilde{\rho}^2 \equiv \rho^2/r^2 = 1 + a^2\hat{u}^2\hat{\mu}^2$ ,  $\tilde{\Delta} \equiv \Delta/r^2 = 1 - 2\hat{u} + a^2\hat{u}^2$  and  $\tilde{\mathcal{A}} \equiv \mathcal{A}/r^4 = (1 + a^2\hat{u}^2)^2 - a^2\hat{u}^2\tilde{\Delta}(1 - \hat{\mu}^2)$ .

## A.2 Light rays in Kerr space-time

The four-momentum  $p^\mu \equiv \frac{dx^\mu}{d\lambda'}$  of photons travelling in Kerr space-time in the Boyer-Lindquist coordinates is (see e.g. Carter 1968 or Misner, Thorne & Wheeler 1973)

$$p^t \equiv \frac{dt}{d\lambda'} = [a(l - a\sin^2\theta) + (r^2 + a^2)(r^2 + a^2 - al)/\Delta]/\rho^2, \quad (\text{A.8})$$

$$p^r \equiv \frac{dr}{d\lambda'} = R_{\text{sgn}}\{(r^2 + a^2 - al)^2 - \Delta[(l - a)^2 + q^2]\}^{1/2}/\rho^2, \quad (\text{A.9})$$

$$p^\theta \equiv \frac{d\theta}{d\lambda'} = \Theta_{\text{sgn}}[q^2 - \cot^2\theta(l^2 - a^2\sin^2\theta)]^{1/2}/\rho^2, \quad (\text{A.10})$$

$$p^\varphi \equiv \frac{d\varphi}{d\lambda'} = [l/\sin^2\theta - a + a(r^2 + a^2 - al)/\Delta]/\rho^2, \quad (\text{A.11})$$

where  $l = \alpha(1 - \mu_o^2)^{1/2} = \alpha \sin \theta_o$  and  $q^2 = \beta^2 + \mu_o^2(\alpha^2 - a^2)$  are Carter's constants of motion with  $\alpha$  and  $\beta$  being impact parameters measured perpendicular and parallel, respectively, to the spin axis of the black hole projected onto the observer's sky. Here we define  $\alpha$  to be positive when a photon travels in the direction of the four-vector  $\frac{\partial}{\partial \varphi}$  at infinity, and  $\beta$  to be positive if it travels in the direction of  $-\frac{\partial}{\partial \theta}$  at infinity. The parameter  $\theta_o$  (and  $\mu_o = \cos \theta_o$ ) defines a point at infinity through which the light ray passes (we consider only light rays coming to or from the observer at infinity). Furthermore, we have denoted the sign of the radial component of the momentum by  $R_{\text{sgn}}$  and the sign of the  $\theta$ -component of the momentum by  $\Theta_{\text{sgn}}$ . We have chosen an affine parameter  $\lambda'$  along light geodesics in such a way that the conserved energy is normalized to  $-p_t = 1$ .

The four-momentum transformed into special Kerr ingoing coordinates is

$$p^{\hat{t}} \equiv \frac{d\hat{t}}{d\lambda'} = \frac{1}{\tilde{\rho}^2} \left[ 1 + a\hat{u}^2(l + a\hat{\mu}^2) - (1 + a^2\hat{u}^2) \frac{1 + 2\hat{u} - (l^2 + q^2)\hat{u}^2}{\hat{u}(2 - a\hat{u}l) + U_{\text{sgn}}\sqrt{U}} \right], \quad (\text{A.12})$$

$$p^{\hat{u}} \equiv \frac{d\hat{u}}{d\lambda'} = U_{\text{sgn}} \frac{\hat{u}^2 \sqrt{U}}{\tilde{\rho}^2}, \quad (\text{A.13})$$

$$p^{\hat{\mu}} \equiv \frac{d\hat{\mu}}{d\lambda'} = M_{\text{sgn}} \frac{\hat{u}^2 \sqrt{M}}{\tilde{\rho}^2}, \quad (\text{A.14})$$

$$p^{\hat{\varphi}} \equiv \frac{d\hat{\varphi}}{d\lambda'} = \frac{\hat{u}^2}{\tilde{\rho}^2} \left[ \frac{l}{1 - \hat{\mu}^2} - a \frac{1 + 2\hat{u} - (l^2 + q^2)\hat{u}^2}{\hat{u}(2 - a\hat{u}l) + U_{\text{sgn}}\sqrt{U}} \right], \quad (\text{A.15})$$

with  $U \equiv 1 + (a^2 - l^2 - q^2)\hat{u}^2 + 2[(a - l)^2 + q^2]\hat{u}^3 - a^2 q^2 \hat{u}^4$  and  $M \equiv q^2 + (a^2 - l^2 - q^2)\hat{\mu}^2 - a^2 \hat{\mu}^4$ . The sign of the  $\hat{u}$ - and  $\hat{\mu}$ -components of the four-momentum is denoted by  $U_{\text{sgn}}$  and  $M_{\text{sgn}}$ , respectively. Note that in these coordinates the four-momentum is not singular on the horizon as opposed to the expressions in the Boyer-Lindquist coordinates.

### A.3 Keplerian disc in Kerr space-time

Matter moves along free stable circular orbits with a rotational velocity (see e.g. Novikov & Thorne 1973)

$$\omega = \frac{d\varphi}{dt} = \frac{1}{r^{3/2} + a}. \quad (\text{A.16})$$

in a Keplerian disc. The disc resides in the equatorial plane of the black hole. Individual components of the four-velocity of the Keplerian disc in the Boyer-Lindquist coordinates are

$$U^t = \frac{r^2 + a\sqrt{r}}{r\sqrt{r^2 - 3r + 2a\sqrt{r}}}, \quad (\text{A.17})$$

$$U^r = 0, \quad (\text{A.18})$$

$$U^\theta = 0, \quad (\text{A.19})$$

$$U^\phi = \frac{1}{\sqrt{r(r^2 - 3r + 2a\sqrt{r})}}. \quad (\text{A.20})$$

There is no free stable circular orbit below the marginally stable orbit defined by

$$r_{\text{ms}} = 3 + Z_2 - \sqrt{(3 - Z_1)(3 + Z_1 + 2Z_2)} \quad (\text{A.21})$$

with  $Z_1 = 1 + (1 - a^2)^{1/3}[(1 + a)^{1/3} + (1 - a)^{1/3}]$  and  $Z_2 = \sqrt{3a^2 + Z_1^2}$ . We suppose that below this orbit the matter is in a free fall down to the horizon. Thus the matter conserves its specific energy  $-U_t$  and its specific angular momentum  $U_\phi$

$$-U_t(r < r_{\text{ms}}) \equiv E_{\text{ms}} \equiv -U_t(r_{\text{ms}}) = \frac{r_{\text{ms}}^2 - 2r_{\text{ms}} + a\sqrt{r_{\text{ms}}}}{r_{\text{ms}}\sqrt{r_{\text{ms}}^2 - 3r_{\text{ms}} + 2a\sqrt{r_{\text{ms}}}}}, \quad (\text{A.22})$$

$$U_\phi(r < r_{\text{ms}}) \equiv L_{\text{ms}} \equiv U_\phi(r_{\text{ms}}) = \frac{r_{\text{ms}}^2 + a^2 - 2a\sqrt{r_{\text{ms}}}}{\sqrt{r_{\text{ms}}(r_{\text{ms}}^2 - 3r_{\text{ms}} + 2a\sqrt{r_{\text{ms}}})}}. \quad (\text{A.23})$$

When we also consider the normalization condition for the four-velocity,  $U^\mu U_\mu = -1$ , then we get the following expressions for its contravariant components

$$U^t(r < r_{\text{ms}}) = \frac{1}{r\Delta} \{ [r(r^2 + a^2) + 2a^2]E_{\text{ms}} - 2aL_{\text{ms}} \}, \quad (\text{A.24})$$

$$U^r(r < r_{\text{ms}}) = -\frac{1}{r\sqrt{r}} \sqrt{[r(r^2 + a^2) + 2a^2]E_{\text{ms}}^2 - 4aE_{\text{ms}}L_{\text{ms}} - (r - 2)L_{\text{ms}}^2 - r\Delta}, \quad (\text{A.25})$$

$$U^\theta(r < r_{\text{ms}}) = 0, \quad (\text{A.26})$$

$$U^\varphi(r < r_{\text{ms}}) = \frac{1}{r\Delta} [2aE_{\text{ms}} + (r - 2)L_{\text{ms}}]. \quad (\text{A.27})$$

In our calculations we use the following local orthonormal tetrad connected with the matter in the disc

$$e_{(t)\mu} \equiv U_\mu, \quad (\text{A.28})$$

$$e_{(r)\mu} \equiv \frac{r}{\sqrt{\Delta(1 + U^r U_r)}} [U^r(U_t, U_r, 0, U_\varphi) + (0, 1, 0, 0)], \quad (\text{A.29})$$

$$e_{(\theta)\mu} \equiv (0, 0, r, 0), \quad (\text{A.30})$$

$$e_{(\varphi)\mu} \equiv \sqrt{\frac{\Delta}{1 + U^r U_r}} (-U^\varphi, 0, 0, U^t). \quad (\text{A.31})$$

## A.4 Initial conditions of integration

In this part of the Appendix we will sum up the initial conditions for integration of the equation of the geodesic

$$\frac{Dp^\mu}{d\lambda'} = \frac{dp^\mu}{d\lambda'} + \Gamma_{\sigma\tau}^\mu p^\sigma p^\tau, \quad \mu = \hat{t}, \hat{u}, \hat{\mu}, \hat{\varphi} \quad (\text{A.32})$$

and equation of the geodesic deviation

$$\frac{d^2 Y_j^\mu}{d\lambda'^2} + 2\Gamma_{\sigma\gamma}^\mu p^\sigma \frac{dY_j^\gamma}{d\lambda'} + \Gamma_{\sigma\tau,\gamma}^\mu p^\sigma p^\tau Y_j^\gamma = 0, \quad \mu = \hat{t}, \hat{u}, \hat{\mu}, \hat{\varphi}, \quad j = 1, 2 \quad (\text{A.33})$$

which we solve in order to compute transfer functions over the accretion disc (see Chapter 1 for details). Here  $p^\mu \equiv \frac{dx^\mu}{d\lambda'}$  is a four-momentum of light,  $\lambda'$  is an affine parameter for which the conserved energy  $-p_t = 1$ ,  $Y_j^\mu$  are two vectors characterizing the distance between nearby geodesics and  $\Gamma_{\mu\nu}^\sigma$  are Christoffel symbols for the Kerr metric. We solve these equations in special Kerr ingoing coordinates  $\hat{t}, \hat{u}, \hat{\mu}, \hat{\varphi}$  and we start integrating from the following initial point:

$$\hat{t}_i = 0, \quad \hat{u}_i = 10^{-11}, \quad \hat{\mu}_i = \mu_o = \cos \theta_o, \quad \hat{\varphi}_i = 0, \quad (\text{A.34})$$

where  $\theta_o$  is the inclination angle of the observer at infinity. The initial values of the four-momentum of light were defined by this point and eqs. (A.12)–(A.15) with  $U_{\text{sgn}} = +1$ ,  $M_{\text{sgn}} = 0$  for  $\beta = 0$  and  $M_{\text{sgn}} = \text{sign}(\beta)$  for  $\beta \neq 0$ .

Four-vectors  $Y_1^\mu$  and  $Y_2^\mu$  have the initial values

$$\begin{aligned} Y_{1i}^{\hat{t}} &= \beta \hat{u}_i, & Y_{2i}^{\hat{t}} &= \alpha \hat{u}_i, \\ Y_{1i}^{\hat{u}} &= -\beta \hat{u}_i^3, & Y_{2i}^{\hat{u}} &= -\alpha \hat{u}_i^3, \\ Y_{1i}^{\hat{\mu}} &= \hat{u}_i \sqrt{1 - \hat{\mu}_i^2}, & Y_{2i}^{\hat{\mu}} &= -\alpha \hat{u}_i^2 \hat{\mu}_i, \\ Y_{1i}^{\hat{\varphi}} &= \alpha \hat{u}_i^2 \hat{\mu}_i / (1 - \hat{\mu}_i^2), & Y_{2i}^{\hat{\varphi}} &= \hat{u}_i / \sqrt{1 - \hat{\mu}_i^2}, \end{aligned} \quad (\text{A.35})$$

and their derivatives have the initial values ( $dY_j^{\hat{\nu}}/d\lambda' = p^{\hat{\sigma}} \partial Y_j^{\hat{\nu}} / \partial x^{\hat{\sigma}}$ )

$$\begin{aligned} \frac{dY_{1i}^{\hat{t}}}{d\lambda'} &= \beta \hat{u}_i^2, & \frac{dY_{2i}^{\hat{t}}}{d\lambda'} &= \alpha \hat{u}_i^2, \\ \frac{dY_{1i}^{\hat{u}}}{d\lambda'} &= -3\beta \hat{u}_i^4, & \frac{dY_{2i}^{\hat{u}}}{d\lambda'} &= -3\alpha \hat{u}_i^4, \\ \frac{dY_{1i}^{\hat{\mu}}}{d\lambda'} &= \hat{u}_i^2 \sqrt{1 - \hat{\mu}_i^2}, & \frac{dY_{2i}^{\hat{\mu}}}{d\lambda'} &= -2\alpha \hat{u}_i^3 \hat{\mu}_i, \\ \frac{dY_{1i}^{\hat{\varphi}}}{d\lambda'} &= 2\alpha \hat{u}_i^3 \hat{\mu}_i / (1 - \hat{\mu}_i^2), & \frac{dY_{2i}^{\hat{\varphi}}}{d\lambda'} &= \hat{u}_i^2 / \sqrt{1 - \hat{\mu}_i^2}. \end{aligned} \quad (\text{A.36})$$

The initial vectors  $Y_{1i}^\mu$  and  $Y_{2i}^\mu$  were chosen in such a way that in the initial point, where we suppose the metric to be a flat-space Minkowski one, they are perpendicular to each other and to the four-momentum of light, are space-like and have unit length. We kept only the largest terms in  $\hat{u}_i$  in eqs. (A.35) and (A.36).

## A.5 Christoffel symbols

Here we show the Christoffel symbols and their first derivatives for the Kerr metric in special Kerr ingoing coordinates. They are needed for the numerical integration of the equation of the geodesic and geodesic deviation.

$$\begin{aligned} \Gamma_{\hat{t}\hat{t}}^{\hat{t}} &= \hat{u}^2(1 + a^2\hat{u}^2)(1 - a^2\hat{u}^2\hat{\mu}^2)/\tilde{\rho}^6 \\ \Gamma_{\hat{t}\hat{u}}^{\hat{t}} &= \Gamma_{\hat{u}\hat{t}}^{\hat{t}} = 0 \\ \Gamma_{\hat{t}\hat{\mu}}^{\hat{t}} &= \Gamma_{\hat{\mu}\hat{t}}^{\hat{t}} = 2a^2\hat{u}^3\hat{\mu}/\tilde{\rho}^4 \\ \Gamma_{\hat{t}\hat{\varphi}}^{\hat{t}} &= \Gamma_{\hat{\varphi}\hat{t}}^{\hat{t}} = -a(1 - \hat{\mu}^2)\Gamma_{\hat{t}\hat{t}}^{\hat{t}} \\ \Gamma_{\hat{u}\hat{u}}^{\hat{t}} &= 0 \\ \Gamma_{\hat{u}\hat{\mu}}^{\hat{t}} &= \Gamma_{\hat{\mu}\hat{u}}^{\hat{t}} = -a^2\hat{\mu}/\tilde{\rho}^2 \\ \Gamma_{\hat{u}\hat{\varphi}}^{\hat{t}} &= \Gamma_{\hat{\varphi}\hat{u}}^{\hat{t}} = -a(1 - \hat{\mu}^2)/(\hat{u}\tilde{\rho}^2) \\ \Gamma_{\hat{\mu}\hat{\mu}}^{\hat{t}} &= -(1 + a^2\hat{u}^2)/[\hat{u}(1 - \hat{\mu}^2)\tilde{\rho}^2] \\ \Gamma_{\hat{\mu}\hat{\varphi}}^{\hat{t}} &= \Gamma_{\hat{\varphi}\hat{\mu}}^{\hat{t}} = -a(1 - \hat{\mu}^2)\Gamma_{\hat{t}\hat{\mu}}^{\hat{t}} \end{aligned}$$

$$\begin{aligned}
\Gamma_{\hat{\varphi}\hat{\varphi}}^{\hat{t}} &= (1 - \hat{\mu}^2)(1 + a^2\hat{u}^2)[a^2\hat{u}^3(1 - \hat{\mu}^2)(1 - a^2\hat{u}^2\hat{\mu}^2) - \tilde{\rho}^4]/(\hat{u}\tilde{\rho}^6) \\
\Gamma_{\hat{t}\hat{t}}^{\hat{u}} &= -\hat{u}^4(1 - a^2\hat{u}^2\hat{\mu}^2)\tilde{\Delta}/\tilde{\rho}^6 \\
\Gamma_{\hat{t}\hat{u}}^{\hat{u}} &= \Gamma_{\hat{u}\hat{t}}^{\hat{u}} = -\hat{u}^2(1 - a^2\hat{u}^2\hat{\mu}^2)/\tilde{\rho}^4 \\
\Gamma_{\hat{t}\hat{\mu}}^{\hat{u}} &= \Gamma_{\hat{\mu}\hat{t}}^{\hat{u}} = 0 \\
\Gamma_{\hat{t}\hat{\varphi}}^{\hat{u}} &= \Gamma_{\hat{\varphi}\hat{t}}^{\hat{u}} = -a(1 - \hat{\mu}^2)\Gamma_{\hat{t}\hat{t}}^{\hat{u}} \\
\Gamma_{\hat{u}\hat{u}}^{\hat{u}} &= -2/\hat{u} \\
\Gamma_{\hat{u}\hat{\mu}}^{\hat{u}} &= \Gamma_{\hat{\mu}\hat{u}}^{\hat{u}} = a^2\hat{u}^2\hat{\mu}/\tilde{\rho}^2 \\
\Gamma_{\hat{u}\hat{\varphi}}^{\hat{u}} &= \Gamma_{\hat{\varphi}\hat{u}}^{\hat{u}} = a\hat{u}(1 - \hat{\mu}^2)[\hat{u}(1 - a^2\hat{u}^2\hat{\mu}^2) + \tilde{\rho}^2]/\tilde{\rho}^4 \\
\Gamma_{\hat{\mu}\hat{\mu}}^{\hat{u}} &= \hat{u}\tilde{\Delta}/[(1 - \hat{\mu}^2)\tilde{\rho}^2] \\
\Gamma_{\hat{\mu}\hat{\varphi}}^{\hat{u}} &= \Gamma_{\hat{\varphi}\hat{\mu}}^{\hat{u}} = 0 \\
\Gamma_{\hat{\varphi}\hat{\varphi}}^{\hat{u}} &= \hat{u}(1 - \hat{\mu}^2)\tilde{\Delta}[\tilde{\rho}^4 - a^2\hat{u}^3(1 - \hat{\mu}^2)(1 - a^2\hat{u}^2\hat{\mu}^2)]/\tilde{\rho}^6 \\
\Gamma_{\hat{t}\hat{t}}^{\hat{\mu}} &= 2a^2\hat{u}^5\hat{\mu}(1 - \hat{\mu}^2)/\tilde{\rho}^6 \\
\Gamma_{\hat{t}\hat{u}}^{\hat{\mu}} &= \Gamma_{\hat{u}\hat{t}}^{\hat{\mu}} = 0 \\
\Gamma_{\hat{t}\hat{\mu}}^{\hat{\mu}} &= \Gamma_{\hat{\mu}\hat{t}}^{\hat{\mu}} = 0 \\
\Gamma_{\hat{t}\hat{\varphi}}^{\hat{\mu}} &= \Gamma_{\hat{\varphi}\hat{t}}^{\hat{\mu}} = -2a\hat{u}^3\hat{\mu}(1 - \hat{\mu}^2)(1 + a^2\hat{u}^2)/\tilde{\rho}^6 \\
\Gamma_{\hat{u}\hat{u}}^{\hat{\mu}} &= 0 \\
\Gamma_{\hat{u}\hat{\mu}}^{\hat{\mu}} &= \Gamma_{\hat{\mu}\hat{u}}^{\hat{\mu}} = -1/(\hat{u}\tilde{\rho}^2) \\
\Gamma_{\hat{u}\hat{\varphi}}^{\hat{\mu}} &= \Gamma_{\hat{\varphi}\hat{u}}^{\hat{\mu}} = a\hat{\mu}(1 - \hat{\mu}^2)/\tilde{\rho}^2 \\
\Gamma_{\hat{\mu}\hat{\mu}}^{\hat{\mu}} &= \hat{\mu}(1 + a^2\hat{u}^2)/[(1 - \hat{\mu}^2)\tilde{\rho}^2] \\
\Gamma_{\hat{\mu}\hat{\varphi}}^{\hat{\mu}} &= \Gamma_{\hat{\varphi}\hat{\mu}}^{\hat{\mu}} = 0 \\
\Gamma_{\hat{\varphi}\hat{\varphi}}^{\hat{\mu}} &= \hat{\mu}(1 + a^2\hat{u}^2)(1 - \hat{\mu}^2)/\tilde{\rho}^2 + 2a^2\hat{u}^3\hat{\mu}(1 - \hat{\mu}^2)^2(1 + a^2\hat{u}^2 + \tilde{\rho}^2)/\tilde{\rho}^6 \\
\Gamma_{\hat{t}\hat{t}}^{\hat{\varphi}} &= a\hat{u}^4(1 - a^2\hat{u}^2\hat{\mu}^2)/\tilde{\rho}^6 \\
\Gamma_{\hat{t}\hat{u}}^{\hat{\varphi}} &= \Gamma_{\hat{u}\hat{t}}^{\hat{\varphi}} = 0 \\
\Gamma_{\hat{t}\hat{\mu}}^{\hat{\varphi}} &= \Gamma_{\hat{\mu}\hat{t}}^{\hat{\varphi}} = 2a\hat{u}^3\hat{\mu}/[(1 - \hat{\mu}^2)\tilde{\rho}^4] \\
\Gamma_{\hat{t}\hat{\varphi}}^{\hat{\varphi}} &= \Gamma_{\hat{\varphi}\hat{t}}^{\hat{\varphi}} = -a(1 - \hat{\mu}^2)\Gamma_{\hat{t}\hat{t}}^{\hat{\varphi}} \\
\Gamma_{\hat{u}\hat{u}}^{\hat{\varphi}} &= 0 \\
\Gamma_{\hat{u}\hat{\mu}}^{\hat{\varphi}} &= \Gamma_{\hat{\mu}\hat{u}}^{\hat{\varphi}} = -a\hat{\mu}/[(1 - \hat{\mu}^2)\tilde{\rho}^2] \\
\Gamma_{\hat{u}\hat{\varphi}}^{\hat{\varphi}} &= \Gamma_{\hat{\varphi}\hat{u}}^{\hat{\varphi}} = \Gamma_{\hat{u}\hat{\mu}}^{\hat{\mu}} \\
\Gamma_{\hat{\mu}\hat{\mu}}^{\hat{\varphi}} &= -a\hat{u}/[(1 - \hat{\mu}^2)\tilde{\rho}^2] \\
\Gamma_{\hat{\mu}\hat{\varphi}}^{\hat{\varphi}} &= \Gamma_{\hat{\varphi}\hat{\mu}}^{\hat{\varphi}} = -\hat{\mu}/(1 - \hat{\mu}^2) - 2a^2\hat{u}^3\hat{\mu}/\tilde{\rho}^4
\end{aligned}$$

$$\begin{aligned}
\Gamma_{\hat{\varphi}\hat{\varphi}}^{\hat{\varphi}} &= a\hat{u}(1-\hat{\mu}^2)[a^2\hat{u}^3(1-\hat{\mu}^2)(1-a^2\hat{u}^2\hat{\mu}^2)-\tilde{\rho}^4]/\tilde{\rho}^6 \\
\Gamma_{\hat{t}\hat{t},\hat{u}}^{\hat{t}} &= 2\hat{u}[\tilde{\rho}^4+2a^2\hat{u}^2(1-\hat{\mu}^2)-4a^2\hat{u}^2\hat{\mu}^2(1+a^2\hat{u}^2)]/\tilde{\rho}^8 \\
\Gamma_{\hat{t}\hat{u},\hat{u}}^{\hat{t}} &= \Gamma_{\hat{u}\hat{t},\hat{u}}^{\hat{t}} = 0 \\
\Gamma_{\hat{t}\hat{\mu},\hat{u}}^{\hat{t}} &= \Gamma_{\hat{\mu}\hat{t},\hat{u}}^{\hat{t}} = -2a^2\hat{u}^2\hat{\mu}(a^2\hat{u}^2\hat{\mu}^2-3)/\tilde{\rho}^6 \\
\Gamma_{\hat{t}\hat{\varphi},\hat{u}}^{\hat{t}} &= \Gamma_{\hat{\varphi}\hat{t},\hat{u}}^{\hat{t}} = -a(1-\hat{\mu}^2)\Gamma_{\hat{t}\hat{t},\hat{u}}^{\hat{t}} \\
\Gamma_{\hat{u}\hat{u},\hat{u}}^{\hat{t}} &= 0 \\
\Gamma_{\hat{u}\hat{\mu},\hat{u}}^{\hat{t}} &= \Gamma_{\hat{\mu}\hat{u},\hat{u}}^{\hat{t}} = 2a^4\hat{u}\hat{\mu}^3/\tilde{\rho}^4 \\
\Gamma_{\hat{u}\hat{\varphi},\hat{u}}^{\hat{t}} &= \Gamma_{\hat{\varphi}\hat{u},\hat{u}}^{\hat{t}} = a(1-\hat{\mu}^2)(1+3a^2\hat{u}^2\hat{\mu}^2)/(\hat{u}^2\tilde{\rho}^4) \\
\Gamma_{\hat{\mu}\hat{\mu},\hat{u}}^{\hat{t}} &= [1+3a^2\hat{u}^2\hat{\mu}^2-a^2\hat{u}^2(1-a^2\hat{u}^2\hat{\mu}^2)]/[\hat{u}^2(1-\hat{\mu}^2)\tilde{\rho}^4] \\
\Gamma_{\hat{\mu}\hat{\varphi},\hat{u}}^{\hat{t}} &= \Gamma_{\hat{\varphi}\hat{\mu},\hat{u}}^{\hat{t}} = -a(1-\hat{\mu}^2)\Gamma_{\hat{t}\hat{\mu},\hat{u}}^{\hat{t}} \\
\Gamma_{\hat{\varphi}\hat{\varphi},\hat{u}}^{\hat{t}} &= (1-\hat{\mu}^2)\{\tilde{\rho}^4[1+3a^2\hat{u}^2\hat{\mu}^2-a^2\hat{u}^2(1-a^2\hat{u}^2\hat{\mu}^2)] \\
&\quad +2a^2\hat{u}^3(1-\hat{\mu}^2)[\tilde{\rho}^4+2a^2\hat{u}^2(1-2a^2\hat{u}^2\hat{\mu}^2-3\hat{\mu}^2)]\}/(\hat{u}^2\tilde{\rho}^8) \\
\Gamma_{\hat{t}\hat{t},\hat{u}}^{\hat{u}} &= 2\hat{u}^3\{\hat{u}[6(1-a^2\hat{u}^2\hat{\mu}^2)-\tilde{\rho}^4]-2(1+a^2\hat{u}^2)(1-a^2\hat{u}^2\hat{\mu}^2) \\
&\quad +a^2\hat{u}^2[\tilde{\rho}^4-2(1-\hat{\mu}^2)]\}/\tilde{\rho}^8 \\
\Gamma_{\hat{t}\hat{u},\hat{u}}^{\hat{u}} &= \Gamma_{\hat{u}\hat{t},\hat{u}}^{\hat{u}} = -2\hat{u}(1-3a^2\hat{u}^2\hat{\mu}^2)/\tilde{\rho}^6 \\
\Gamma_{\hat{t}\hat{\mu},\hat{u}}^{\hat{u}} &= \Gamma_{\hat{\mu}\hat{t},\hat{u}}^{\hat{u}} = 0 \\
\Gamma_{\hat{t}\hat{\varphi},\hat{u}}^{\hat{u}} &= \Gamma_{\hat{\varphi}\hat{t},\hat{u}}^{\hat{u}} = -a(1-\hat{\mu}^2)\Gamma_{\hat{t}\hat{t},\hat{u}}^{\hat{u}} \\
\Gamma_{\hat{u}\hat{u},\hat{u}}^{\hat{u}} &= 2/\hat{u}^2 \\
\Gamma_{\hat{u}\hat{\mu},\hat{u}}^{\hat{u}} &= \Gamma_{\hat{\mu}\hat{u},\hat{u}}^{\hat{u}} = 2a^2\hat{u}\hat{\mu}/\tilde{\rho}^4 \\
\Gamma_{\hat{u}\hat{\varphi},\hat{u}}^{\hat{u}} &= \Gamma_{\hat{\varphi}\hat{u},\hat{u}}^{\hat{u}} = a(1-\hat{\mu}^2)[2\hat{u}(1-3a^2\hat{u}^2\hat{\mu}^2)+\tilde{\rho}^2(1-a^2\hat{u}^2\hat{\mu}^2)]/\tilde{\rho}^6 \\
\Gamma_{\hat{\mu}\hat{\mu},\hat{u}}^{\hat{u}} &= [2\tilde{\Delta}-\tilde{\rho}^2(1-a^2\hat{u}^2)]/[(1-\hat{\mu}^2)\tilde{\rho}^4] \\
\Gamma_{\hat{\mu}\hat{\varphi},\hat{u}}^{\hat{u}} &= \Gamma_{\hat{\varphi}\hat{\mu},\hat{u}}^{\hat{u}} = 0 \\
\Gamma_{\hat{\varphi}\hat{\varphi},\hat{u}}^{\hat{u}} &= -(1-\hat{\mu}^2)\{\tilde{\rho}^6(1-a^2\hat{u}^2)-2\tilde{\rho}^4(1+a^2\hat{u}^2)+2a^2\hat{u}^4(1-\hat{\mu}^2)[\tilde{\rho}^4-6(1-a^2\hat{u}^2\hat{\mu}^2)] \\
&\quad +2\hat{u}[\tilde{\rho}^4+(1+a^2\hat{u}^2)^2+a^4\hat{u}^4(1-\hat{\mu}^2)[5(1-\hat{\mu}^2)-\tilde{\rho}^2(3+a^2\hat{u}^2\hat{\mu}^2)]]\}/\tilde{\rho}^8 \\
\Gamma_{\hat{t}\hat{t},\hat{u}}^{\hat{\mu}} &= -2a^2\hat{u}^4\hat{\mu}(1-\hat{\mu}^2)(a^2\hat{u}^2\hat{\mu}^2-5)/\tilde{\rho}^8 \\
\Gamma_{\hat{t}\hat{u},\hat{u}}^{\hat{\mu}} &= \Gamma_{\hat{u}\hat{t},\hat{u}}^{\hat{\mu}} = 0 \\
\Gamma_{\hat{t}\hat{\mu},\hat{u}}^{\hat{\mu}} &= \Gamma_{\hat{\mu}\hat{t},\hat{u}}^{\hat{\mu}} = 0 \\
\Gamma_{\hat{t}\hat{\varphi},\hat{u}}^{\hat{\mu}} &= \Gamma_{\hat{\varphi}\hat{t},\hat{u}}^{\hat{\mu}} = 2a\hat{u}^2\hat{\mu}(1-\hat{\mu}^2)[a^2\hat{u}^2(a^2\hat{u}^2\hat{\mu}^2-5)-3(1-a^2\hat{u}^2\hat{\mu}^2)]/\tilde{\rho}^8 \\
\Gamma_{\hat{u}\hat{u},\hat{u}}^{\hat{\mu}} &= 0 \\
\Gamma_{\hat{u}\hat{\mu},\hat{u}}^{\hat{\mu}} &= \Gamma_{\hat{\mu}\hat{u},\hat{u}}^{\hat{\mu}} = (1+3a^2\hat{u}^2\hat{\mu}^2)/(\hat{u}^2\tilde{\rho}^4)
\end{aligned}$$

$$\begin{aligned}
\Gamma_{\hat{u}\hat{\varphi},\hat{u}}^{\hat{\mu}} &= \Gamma_{\hat{\varphi}\hat{u},\hat{u}}^{\hat{\mu}} = -2a^3\hat{u}\hat{\mu}^3(1-\hat{\mu}^2)/\tilde{\rho}^4 \\
\Gamma_{\hat{\mu}\hat{\mu},\hat{u}}^{\hat{\mu}} &= 2a^2\hat{u}\hat{\mu}/\tilde{\rho}^4 \\
\Gamma_{\hat{\mu}\hat{\varphi},\hat{u}}^{\hat{\mu}} &= \Gamma_{\hat{\varphi}\hat{\mu},\hat{u}}^{\hat{\mu}} = 0 \\
\Gamma_{\hat{\varphi}\hat{\varphi},\hat{u}}^{\hat{\mu}} &= 2a^2\hat{u}\hat{\mu}(1-\hat{\mu}^2)^2\{\tilde{\rho}^4 + \hat{u}[6(1+a^2\hat{u}^2) - a^2\hat{u}^2(1+\hat{\mu}^2)\tilde{\rho}^2]\}/\tilde{\rho}^8 \\
\Gamma_{\hat{t}\hat{t},\hat{u}}^{\hat{\varphi}} &= 4a\hat{u}^3(1-2a^2\hat{u}^2\hat{\mu}^2)/\tilde{\rho}^8 \\
\Gamma_{\hat{t}\hat{u},\hat{u}}^{\hat{\varphi}} &= \Gamma_{\hat{u}\hat{t},\hat{u}}^{\hat{\varphi}} = 0 \\
\Gamma_{\hat{t}\hat{\mu},\hat{u}}^{\hat{\varphi}} &= \Gamma_{\hat{\mu}\hat{t},\hat{u}}^{\hat{\varphi}} = -2a\hat{u}^2\hat{\mu}(a^2\hat{u}^2\hat{\mu}^2-3)/[(1-\hat{\mu}^2)\tilde{\rho}^6] \\
\Gamma_{\hat{t}\hat{\varphi},\hat{u}}^{\hat{\varphi}} &= \Gamma_{\hat{\varphi}\hat{t},\hat{u}}^{\hat{\varphi}} = -a(1-\hat{\mu}^2)\Gamma_{\hat{t}\hat{t},\hat{u}}^{\hat{\varphi}} \\
\Gamma_{\hat{u}\hat{u},\hat{u}}^{\hat{\varphi}} &= 0 \\
\Gamma_{\hat{u}\hat{\mu},\hat{u}}^{\hat{\varphi}} &= \Gamma_{\hat{\mu}\hat{u},\hat{u}}^{\hat{\varphi}} = 2a^3\hat{u}\hat{\mu}^3/[(1-\hat{\mu}^2)\tilde{\rho}^4] \\
\Gamma_{\hat{u}\hat{\varphi},\hat{u}}^{\hat{\varphi}} &= \Gamma_{\hat{\varphi}\hat{u},\hat{u}}^{\hat{\varphi}} = \Gamma_{\hat{u}\hat{\mu},\hat{u}}^{\hat{\mu}} \\
\Gamma_{\hat{\mu}\hat{\mu},\hat{u}}^{\hat{\varphi}} &= -a(1-a^2\hat{u}^2\hat{\mu}^2)/[(1-\hat{\mu}^2)\tilde{\rho}^4] \\
\Gamma_{\hat{\mu}\hat{\varphi},\hat{u}}^{\hat{\varphi}} &= \Gamma_{\hat{\varphi}\hat{\mu},\hat{u}}^{\hat{\varphi}} = 2a^2\hat{u}^2\hat{\mu}(a^2\hat{u}^2\hat{\mu}^2-3)/\tilde{\rho}^6 \\
\Gamma_{\hat{\varphi}\hat{\varphi},\hat{u}}^{\hat{\varphi}} &= a(1-\hat{\mu}^2)[\tilde{\rho}^4(a^2\hat{u}^2\hat{\mu}^2-1) + 4a^2\hat{u}^3(1-\hat{\mu}^2)(1-2a^2\hat{u}^2\hat{\mu}^2)]/\tilde{\rho}^8 \\
\Gamma_{\hat{t}\hat{t},\hat{\mu}}^{\hat{t}} &= 4a^2\hat{u}^4\hat{\mu}(1+a^2\hat{u}^2)(a^2\hat{u}^2\hat{\mu}^2-2)/\tilde{\rho}^8 \\
\Gamma_{\hat{t}\hat{u},\hat{\mu}}^{\hat{t}} &= \Gamma_{\hat{u}\hat{t},\hat{\mu}}^{\hat{t}} = 0 \\
\Gamma_{\hat{t}\hat{\mu},\hat{\mu}}^{\hat{t}} &= \Gamma_{\hat{\mu}\hat{t},\hat{\mu}}^{\hat{t}} = 2a^2\hat{u}^3(1-3a^2\hat{u}^2\hat{\mu}^2)/\tilde{\rho}^6 \\
\Gamma_{\hat{t}\hat{\varphi},\hat{\mu}}^{\hat{t}} &= \Gamma_{\hat{\varphi}\hat{t},\hat{\mu}}^{\hat{t}} = 2a\hat{\mu}\Gamma_{\hat{t}\hat{t}}^{\hat{t}} - a(1-\hat{\mu}^2)\Gamma_{\hat{t}\hat{t},\hat{\mu}}^{\hat{t}} \\
\Gamma_{\hat{u}\hat{u},\hat{\mu}}^{\hat{t}} &= 0 \\
\Gamma_{\hat{u}\hat{\mu},\hat{\mu}}^{\hat{t}} &= \Gamma_{\hat{\mu}\hat{u},\hat{\mu}}^{\hat{t}} = -a^2(1-a^2\hat{u}^2\hat{\mu}^2)/\tilde{\rho}^4 \\
\Gamma_{\hat{u}\hat{\varphi},\hat{\mu}}^{\hat{t}} &= \Gamma_{\hat{\varphi}\hat{u},\hat{\mu}}^{\hat{t}} = 2a\hat{\mu}(1+a^2\hat{u}^2)/(\hat{u}\tilde{\rho}^4) \\
\Gamma_{\hat{\mu}\hat{\mu},\hat{\mu}}^{\hat{t}} &= 2\hat{\mu}(1+a^2\hat{u}^2)[a^2\hat{u}^2(1-\hat{\mu}^2) - \tilde{\rho}^2]/[\hat{u}(1-\hat{\mu}^2)^2\tilde{\rho}^4] \\
\Gamma_{\hat{\mu}\hat{\varphi},\hat{\mu}}^{\hat{t}} &= \Gamma_{\hat{\varphi}\hat{\mu},\hat{\mu}}^{\hat{t}} = 2a\hat{\mu}\Gamma_{\hat{t}\hat{\mu}}^{\hat{t}} - a(1-\hat{\mu}^2)\Gamma_{\hat{t}\hat{\mu},\hat{\mu}}^{\hat{t}} \\
\Gamma_{\hat{\varphi}\hat{\varphi},\hat{\mu}}^{\hat{t}} &= -2\hat{\mu}(1+a^2\hat{u}^2)\{2a^2\hat{u}^3(1-\hat{\mu}^2)[(1+a^2\hat{u}^2)(1-a^2\hat{u}^2\hat{\mu}^2) + a^2\hat{u}^2(1-\hat{\mu}^2)] \\
&\quad - (1+a^2\hat{u}^2)\tilde{\rho}^4\}/(\hat{u}\tilde{\rho}^8) \\
\Gamma_{\hat{t}\hat{t},\hat{\mu}}^{\hat{u}} &= 4a^2\hat{u}^6\hat{\mu}\tilde{\Delta}(2-a^2\hat{u}^2\hat{\mu}^2)/\tilde{\rho}^8 \\
\Gamma_{\hat{t}\hat{u},\hat{\mu}}^{\hat{u}} &= \Gamma_{\hat{u}\hat{t},\hat{\mu}}^{\hat{u}} = -2a^2\hat{u}^4\hat{\mu}(a^2\hat{u}^2\hat{\mu}^2-3)/\tilde{\rho}^6 \\
\Gamma_{\hat{t}\hat{\mu},\hat{\mu}}^{\hat{u}} &= \Gamma_{\hat{\mu}\hat{t},\hat{\mu}}^{\hat{u}} = 0 \\
\Gamma_{\hat{t}\hat{\varphi},\hat{\mu}}^{\hat{u}} &= \Gamma_{\hat{\varphi}\hat{t},\hat{\mu}}^{\hat{u}} = 2a\hat{\mu}\Gamma_{\hat{t}\hat{t}}^{\hat{u}} - a(1-\hat{\mu}^2)\Gamma_{\hat{t}\hat{t},\hat{\mu}}^{\hat{u}}
\end{aligned}$$

$$\begin{aligned}
\Gamma_{\hat{u}\hat{u},\hat{\mu}}^{\hat{u}} &= 0 \\
\Gamma_{\hat{u}\hat{\mu},\hat{\mu}}^{\hat{u}} &= \Gamma_{\hat{\mu}\hat{u},\hat{\mu}}^{\hat{u}} = a^2\hat{u}^2(1 - a^2\hat{u}^2\hat{\mu}^2)/\tilde{\rho}^4 \\
\Gamma_{\hat{u}\hat{\phi},\hat{\mu}}^{\hat{u}} &= \Gamma_{\hat{\phi}\hat{u},\hat{\mu}}^{\hat{u}} = -2a\hat{u}\hat{\mu}\{\tilde{\rho}^2(1 + a^2\hat{u}^2) + \hat{u}[(1 + a^2\hat{u}^2)(1 - a^2\hat{u}^2\hat{\mu}^2) \\
&\quad + 2a^2\hat{u}^2(1 - \hat{\mu}^2)]\}/\tilde{\rho}^6 \\
\Gamma_{\hat{\mu}\hat{\mu},\hat{\mu}}^{\hat{u}} &= 2\hat{u}\hat{\mu}\tilde{\Delta}[\tilde{\rho}^2 - a^2\hat{u}^2(1 - \hat{\mu}^2)]/[(1 - \hat{\mu}^2)^2\tilde{\rho}^4] \\
\Gamma_{\hat{\mu}\hat{\phi},\hat{\mu}}^{\hat{u}} &= \Gamma_{\hat{\phi}\hat{\mu},\hat{\mu}}^{\hat{u}} = 0 \\
\Gamma_{\hat{\phi}\hat{\phi},\hat{\mu}}^{\hat{u}} &= 2\hat{u}\hat{\mu}\tilde{\Delta}\{-(1 + a^2\hat{u}^2)\tilde{\rho}^4 + 2a^2\hat{u}^3(1 - \hat{\mu}^2)[(1 + a^2\hat{u}^2)(1 - a^2\hat{u}^2\hat{\mu}^2) \\
&\quad + a^2\hat{u}^2(1 - \hat{\mu}^2)]\}/\tilde{\rho}^8 \\
\Gamma_{\hat{t}\hat{t},\hat{\mu}}^{\hat{\mu}} &= 2a^2\hat{u}^5[(1 - 3a^2\hat{u}^2\hat{\mu}^2)(1 - \hat{\mu}^2) - 2\hat{\mu}^2(1 + a^2\hat{u}^2)]/\tilde{\rho}^8 \\
\Gamma_{\hat{t}\hat{u},\hat{\mu}}^{\hat{\mu}} &= \Gamma_{\hat{u}\hat{t},\hat{\mu}}^{\hat{\mu}} = 0 \\
\Gamma_{\hat{t}\hat{\mu},\hat{\mu}}^{\hat{\mu}} &= \Gamma_{\hat{\mu}\hat{t},\hat{\mu}}^{\hat{\mu}} = 0 \\
\Gamma_{\hat{t}\hat{\phi},\hat{\mu}}^{\hat{\mu}} &= \Gamma_{\hat{\phi}\hat{t},\hat{\mu}}^{\hat{\mu}} = -2a\hat{u}^3(1 + a^2\hat{u}^2)[(1 - 3a^2\hat{u}^2\hat{\mu}^2)(1 - \hat{\mu}^2) - 2\hat{\mu}^2(1 + a^2\hat{u}^2)]/\tilde{\rho}^8 \\
\Gamma_{\hat{u}\hat{u},\hat{\mu}}^{\hat{\mu}} &= 0 \\
\Gamma_{\hat{u}\hat{\mu},\hat{\mu}}^{\hat{\mu}} &= \Gamma_{\hat{\mu}\hat{u},\hat{\mu}}^{\hat{\mu}} = 2a^2\hat{u}\hat{\mu}/\tilde{\rho}^4 \\
\Gamma_{\hat{u}\hat{\phi},\hat{\mu}}^{\hat{\mu}} &= \Gamma_{\hat{\phi}\hat{u},\hat{\mu}}^{\hat{\mu}} = a[\tilde{\rho}^2(1 - \hat{\mu}^2) - 2\hat{\mu}^2(1 + a^2\hat{u}^2)]/\tilde{\rho}^4 \\
\Gamma_{\hat{\mu}\hat{\mu},\hat{\mu}}^{\hat{\mu}} &= (1 + a^2\hat{u}^2)[(1 - 3a^2\hat{u}^2\hat{\mu}^2)(1 - \hat{\mu}^2) + 2\hat{\mu}^2(1 + a^2\hat{u}^2)]/[(1 - \hat{\mu}^2)^2\tilde{\rho}^4] \\
\Gamma_{\hat{\mu}\hat{\phi},\hat{\mu}}^{\hat{\mu}} &= \Gamma_{\hat{\phi}\hat{\mu},\hat{\mu}}^{\hat{\mu}} = 0 \\
\Gamma_{\hat{\phi}\hat{\phi},\hat{\mu}}^{\hat{\mu}} &= -1 + [(a^2\hat{u}^2 + 2)(1 - a^2\hat{u}^2\hat{\mu}^2) - \hat{\mu}^2(3 + a^2\hat{u}^2\hat{\mu}^2)]/\tilde{\rho}^4 \\
&\quad + 2a^2\hat{u}^3(1 - \hat{\mu}^2)\{(a^2\hat{u}^2 + 2)[6 - \tilde{\rho}^2(2\hat{\mu}^2 + 5)] - \hat{\mu}^2(6 - \tilde{\rho}^2 + \tilde{\rho}^4)\}/\tilde{\rho}^8 \\
\Gamma_{\hat{t}\hat{t},\hat{\mu}}^{\hat{\phi}} &= 4a^3\hat{u}^6\hat{\mu}(a^2\hat{u}^2\hat{\mu}^2 - 2)/\tilde{\rho}^8 \\
\Gamma_{\hat{t}\hat{u},\hat{\mu}}^{\hat{\phi}} &= \Gamma_{\hat{u}\hat{t},\hat{\mu}}^{\hat{\phi}} = 0 \\
\Gamma_{\hat{t}\hat{\mu},\hat{\mu}}^{\hat{\phi}} &= \Gamma_{\hat{\mu}\hat{t},\hat{\mu}}^{\hat{\phi}} = 2a\hat{u}^3[(1 - 3a^2\hat{u}^2\hat{\mu}^2)(1 - \hat{\mu}^2) + 2\hat{\mu}^2\tilde{\rho}^2]/[(1 - \hat{\mu}^2)^2\tilde{\rho}^6] \\
\Gamma_{\hat{t}\hat{\phi},\hat{\mu}}^{\hat{\phi}} &= \Gamma_{\hat{\phi}\hat{t},\hat{\mu}}^{\hat{\phi}} = 2a\hat{\mu}\Gamma_{\hat{t}\hat{t}}^{\hat{\phi}} - a(1 - \hat{\mu}^2)\Gamma_{\hat{t}\hat{t},\hat{\mu}}^{\hat{\phi}} \\
\Gamma_{\hat{u}\hat{u},\hat{\mu}}^{\hat{\phi}} &= 0 \\
\Gamma_{\hat{u}\hat{\mu},\hat{\mu}}^{\hat{\phi}} &= \Gamma_{\hat{\mu}\hat{u},\hat{\mu}}^{\hat{\phi}} = -a[(1 - a^2\hat{u}^2\hat{\mu}^2)(1 - \hat{\mu}^2) + 2\hat{\mu}^2\tilde{\rho}^2]/[(1 - \hat{\mu}^2)^2\tilde{\rho}^4] \\
\Gamma_{\hat{u}\hat{\phi},\hat{\mu}}^{\hat{\phi}} &= \Gamma_{\hat{\phi}\hat{u},\hat{\mu}}^{\hat{\phi}} = \Gamma_{\hat{u}\hat{\mu},\hat{\mu}}^{\hat{\mu}} \\
\Gamma_{\hat{\mu}\hat{\mu},\hat{\mu}}^{\hat{\phi}} &= -2a\hat{u}\hat{\mu}[\tilde{\rho}^2 - a^2\hat{u}^2(1 - \hat{\mu}^2)]/[(1 - \hat{\mu}^2)^2\tilde{\rho}^4] \\
\Gamma_{\hat{\mu}\hat{\phi},\hat{\mu}}^{\hat{\phi}} &= \Gamma_{\hat{\phi}\hat{\mu},\hat{\mu}}^{\hat{\phi}} = -(1 + \hat{\mu}^2)/(1 - \hat{\mu}^2)^2 - 2a^2\hat{u}^3(1 - 3a^2\hat{u}^2\hat{\mu}^2)/\tilde{\rho}^6] \\
\Gamma_{\hat{\phi}\hat{\phi},\hat{\mu}}^{\hat{\phi}} &= 2a\hat{u}\hat{\mu}\{\tilde{\rho}^4(1 + a^2\hat{u}^2) - 2a^2\hat{u}^3(1 - \hat{\mu}^2)[a^2\hat{u}^2(1 - \hat{\mu}^2) \\
&\quad + (1 + a^2\hat{u}^2)(1 - a^2\hat{u}^2\hat{\mu}^2)]\}/\tilde{\rho}^8
\end{aligned}$$

# Appendix B

## Description of FITS files

### B.1 Transfer functions in **KBHtablesNN.fits**

The transfer functions are stored in the file **KBHtablesNN.fits** as binary extensions and parametrized by the value of the observer inclination angle  $\theta_o$  and the horizon of the black hole  $r_h$ . We found parametrization by  $r_h$  more convenient than using the rotational parameter  $a$ , although the latter choice may be more common. Each extension provides values of a particular transfer function for different radii, which are given in terms of  $r - r_h$ , and for the Kerr ingoing axial coordinates  $\varphi_K$ . Values of the horizon  $r_h$ , inclination  $\theta_o$ , radius  $r - r_h$  and angle  $\varphi_K$ , at which the functions are evaluated, are defined as vectors at the beginning of the FITS file.

The definition of the file **KBHtablesNN.fits**:

0. All of the extensions defined below are binary.
1. The first extension contains six integers defining which of the functions is present in the tables. The integers correspond to the delay,  $g$ -factor, cosine of the local emission angle, lensing, change of the polarization angle and azimuthal emission angle, respectively. Value 0 means that the function is not present in the tables, value 1 means it is.
2. The second extension contains a vector of the horizon values in  $GM/c^2$  ( $1.00 \leq r_h \leq 2.00$ ).
3. The third extension contains a vector of the values of the observer's inclination angle  $\theta_o$  in degrees ( $0^\circ \leq \theta_o \leq 90^\circ$ ,  $0^\circ$  – axis,  $90^\circ$  – equatorial plane).
4. The fourth extension contains a vector of the values of the radius relative to the horizon  $r - r_h$  in  $GM/c^2$ .
5. The fifth extension contains a vector of the values of the azimuthal angle  $\varphi_K$  in radians ( $0 \leq \varphi_K \leq 2\pi$ ). Note that  $\varphi_K$  is a Kerr ingoing axial coordinate, not the Boyer-Lindquist one!
6. All the previous vectors have to have values sorted in an increasing order.
7. In the following extensions the transfer functions are defined, each extension is for a particular value of  $r_h$  and  $\theta_o$ . The values of  $r_h$  and  $\theta_o$  are changing with each extension in the following order:

$$\begin{aligned}
& r_h[1] \times \theta_o[1], \\
& r_h[1] \times \theta_o[2], \\
& r_h[1] \times \theta_o[3], \\
& \dots \\
& \dots \\
& r_h[2] \times \theta_o[1], \\
& r_h[2] \times \theta_o[2], \\
& r_h[2] \times \theta_o[3], \\
& \dots \\
& \dots
\end{aligned}$$

8. Each of these extensions has the same number of columns (up to six). In each column, a particular transfer function is stored – the delay,  $g$ -factor, cosine of the local emission angle, lensing, change of the polarization angle and azimuthal emission angle, respectively. The order of the functions is important but some of the functions may be missing as defined in the first extension (see 1. above). The functions are:

delay – the Boyer-Lindquist time in  $GM/c^3$  that elapses between the emission of a photon from the disc and absorption of the photon by the observer’s eye at infinity plus a constant,

$g$ -factor – the ratio of the energy of a photon received by the observer at infinity to the local energy of the same photon when emitted from an accretion disc,

cosine of the emission angle – the cosine of the local emission angle between the emitted light ray and local disc normal,

lensing – the ratio of the area at infinity perpendicular to the light rays through which photons come to the proper area at the disc perpendicular to the light rays and corresponding to the same flux tube,

change of the polarization angle in radians – if the light emitted from the disc is linearly polarized then the direction of polarization will be changed by this angle at infinity – counter-clockwise if positive, clockwise if negative (we are looking towards the coming emitted beam); on the disc we measure the angle of polarization with respect to the “up” direction perpendicular to the disc with respect to the local rest frame; at infinity we also measure the angle of polarization with respect to the “up” direction perpendicular to the disc – the change of polarization angle is the difference between these two angles,

azimuthal emission angle in radians – the angle between the projection of the three-momentum of an emitted photon into the disc (in the local rest frame co-moving with the disc) and the radial tetrad vector.

For mathematical formulae defining the functions see eqs. (1.5)–(1.7), (1.10)–(1.12) and (1.18) in Chapter 1.

9. Each row corresponds to a particular value of  $r - r_h$  (see 4. above).  
 10. Each element corresponding to a particular column and row is a vector. Each element of this vector corresponds to a particular value of  $\varphi_K$  (see 5. above).

We have pre-calculated three sets of tables – `KBHtables00.fits`, `KBHtables50.fits` and `KBHtables99.fits`. All of these tables were computed for an accretion disc near a Kerr black hole with no disc corona present. Therefore, ray-tracing in the vacuum Kerr space-time could be used for calculating the transfer functions. When computing the transfer functions, it was supposed that the matter in the disc rotates on stable circular (free) orbits above the marginally stable orbit. The matter below this orbit is freely falling

and has the same energy and angular momentum as the matter which is on the marginally stable orbit.

The observer is placed in the direction  $\varphi = \pi/2$ . The black hole rotates counter-clockwise. All six functions are present in these tables.

Tables are calculated for these values of the black-hole horizon:

- `KBHtables00.fits`: 1.00, 1.05, 1.10, 1.15, ..., 1.90, 1.95, 2.00 (21 elements),
- `KBHtables50.fits`: 1.00, 1.10, 1.20, ..., 1.90, 2.00 (11 elements),
- `KBHtables99.fits`: 1.05 (1 element),

and for these values of the observer's inclination:

- `KBHtables00.fits`: 0.1, 1, 5, 10, 15, 20, ..., 80, 85, 89 (20 elements),
- `KBHtables50.fits`: 0.1, 1, 10, 20, ..., 80, 89 (11 elements),
- `KBHtables99.fits`: 0.1, 1, 5, 10, 15, 20, ..., 80, 85, 89 (20 elements).

The radii and azimuths at which the functions are evaluated are same for all three tables:

- radii  $r - r_h$  are exponentially increasing from 0 to 999 (150 elements),
- values of the azimuthal angle  $\varphi_K$  are equidistantly spread from 0 to  $2\pi$  radians with a much denser cover “behind” the black hole, i.e. near  $\varphi_K = 1.5\pi$  (because some of the functions are changing heavily in this area for higher inclination angles,  $\theta_o > 70^\circ$ ) (200 elements).

## B.2 Tables in `KBHlineNN.fits`

Pre-calculated functions  $dF(g) \equiv dg F(g)$  defined in the eq. (2.16) are stored in FITS files `KBHlineNN.fits`. These functions are used by all axisymmetric models. They are stored as binary extensions and they are parametrized by the value of the observer inclination angle  $\theta_o$  and the horizon of the black hole  $r_h$ . Each extension provides values for different radii, which are given in terms of  $r - r_h$ , and for different  $g$ -factors. Values of the  $g$ -factor, radius  $r - r_h$ , horizon  $r_h$ , and inclination  $\theta_o$ , at which the functions are evaluated, are defined as vectors at the beginning of the FITS file.

The definition of the file `KBHlineNN.fits`:

0. All of the extensions defined below are binary.
1. The first extension contains one row with three columns that define bins in the  $g$ -factor:
  - integer in the first column defines the width of the bins (0 – constant, 1 – exponentially growing),
  - real number in the second column defines the lower boundary of the first bin (minimum of the  $g$ -factor),
  - real number in the third column defines the upper boundary of the last bin (maximum of the  $g$ -factor).
2. The second extension contains a vector of the values of the radius relative to the horizon  $r - r_h$  in  $GM/c^2$ .
3. The third extension contains a vector of the horizon values in  $GM/c^2$  ( $1.00 \leq r_h \leq 2.00$ ).
4. The fourth extension contains a vector of the values of the observer's inclination angle  $\theta_o$  in degrees ( $0^\circ \leq \theta_o \leq 90^\circ$ ,  $0^\circ$  – axis,  $90^\circ$  – equatorial plane).
5. All the previous vectors have to have values sorted in an increasing order.

6. In the following extensions the functions  $dF(g)$  are defined, each extension is for a particular value of  $r_h$  and  $\theta_o$ . The values of  $r_h$  and  $\theta_o$  are changing with each extension in the same order as in tables in the `KBHtablesNN.fits` file (see the previous section, point 7.). Each extension has one column.
7. Each row corresponds to a particular value of  $r - r_h$  (see 2. above).
8. Each element corresponding to a particular column and row is a vector. Each element of this vector corresponds to a value of the function for a particular bin in the  $g$ -factor. This bin can be calculated from number of elements of the vector and data from the first extension (see 1. above).

We have pre-calculated several sets of tables for different limb darkening/brightening laws and with different resolutions. All of them were calculated from tables in the `KBHtables00.fits` file (see the previous section for details) and therefore these tables are calculated for the same values of the black-hole horizon and observer's inclination. All of these tables have equidistant bins in the  $g$ -factor which fall in the interval  $\langle 0.001, 1.7 \rangle$ . Several sets of tables are available:

- `KBHline00.fits` for isotropic emission, see eq. (3.5),
- `KBHline01.fits` for Laor's limb darkening, see eq. (3.6),
- `KBHline02.fits` for Haardt's limb brightening, see eq. (3.7).

All of these tables have 300 bins in the  $g$ -factor and 500 values of the radius  $r - r_h$  which are exponentially increasing from 0 to 999. We have produced also tables with a lower resolution – `KBHline50.fits`, `KBHline51.fits`, and `KBHline52.fits` with 200 bins in the  $g$ -factor and 300 values of the radius.

### B.3 Lamp-post tables in `lamp.fits`

This file contains pre-calculated values of the functions needed for the lamp-post model. It is supposed that a primary source of emission is placed on the axis at a height  $h$  above the Kerr black hole. The matter in the disc rotates on stable circular (free) orbits above the marginally stable orbit and it is freely falling below this orbit where it has the same energy and angular momentum as the matter which is on the marginally stable orbit. It is assumed that the corona between the source and the disc is optically thin, therefore ray-tracing in the vacuum Kerr space-time could be used for computing the functions.

There are five functions stored in the `lamp.fits` file as binary extensions. They are parametrized by the value of the horizon of the black hole  $r_h$ , and height  $h$ , which are defined as vectors at the beginning of the FITS file. Currently only tables for  $r_h = 1.05$  (i.e.  $a \doteq 0.9987492$ ) and  $h = 2, 3, 4, 5, 6, 8, 10, 12, 15, 20, 30, 50, 75$  and 100 are available. The functions included are:

- angle of emission in degrees – the angle under which a photon is emitted from a primary source placed at a height  $h$  on the axis above the black hole measured by a local stationary observer ( $0^\circ$  – a photon is emitted downwards,  $180^\circ$  – a photon is emitted upwards),
- radius – the radius in  $GM/c^2$  at which a photon strikes the disc,
- $g$ -factor – the ratio of the energy of a photon hitting the disc to the energy of the same photon when emitted from a primary source,
- cosine of the incident angle – an absolute value of the cosine of the local incident angle between the incident light ray and local disc normal,

- azimuthal incident angle in radians – the angle between the projection of the three-momentum of the incident photon into the disc (in the local rest frame co-moving with the disc) and the radial tetrad vector.

For mathematical formulae defining the functions see eqs. (2.29)–(2.31) in Section 2.4.

The definition of the file `lamp.fits`:

0. All of the extensions defined below are binary.
1. The first extension contains a vector of the horizon values in  $GM/c^2$ , though currently only FITS files with tables for one value of the black-hole horizon are accepted ( $1.00 \leq r_h \leq 2.00$ ).
2. The second extension contains a vector of the values of heights  $h$  of a primary source in  $GM/c^2$ .
3. In the following extensions the functions are defined, each extension is for a particular value of  $r_h$  and  $h$ . The values of  $r_h$  and  $h$  are changing with each extension in the following order:

$$\begin{aligned}
 & r_h[1] \times h[1], \\
 & r_h[1] \times h[2], \\
 & r_h[1] \times h[3], \\
 & \dots \\
 & \dots \\
 & r_h[2] \times h[1], \\
 & r_h[2] \times h[2], \\
 & r_h[2] \times h[3], \\
 & \dots \\
 & \dots
 \end{aligned}$$

4. Each of these extensions has five columns. In each column, a particular function is stored – the angle of emission, radius,  $g$ -factor, cosine of the local incident angle and azimuthal incident angle, respectively. The extensions may have a different number of rows.

## B.4 Coefficient of reflection in `fluorescent_line.fits`

Values of the coefficient of reflection  $f(\mu_i, \mu_e)$  for a fluorescent line are stored for different incident and reflection angles in this file. For details on the model of scattering used for computations see Matt, Perola & Piro (1991). It is assumed that the incident radiation is a power law with the photon index  $\Gamma = 1.7$ . The coefficient does not change its angular dependences for other photon indices, only its normalization changes (see Fig. 14 in George & Fabian 1991). The FITS file consists of three binary extensions:

- the first extension contains absolute values of the cosine of incident angles,
- the second extension contains values of the cosine of reflection angles,
- the third extension contains one column with vector elements, here values of the coefficient of reflection are stored for different incident angles (rows) and for different reflection angles (elements of a vector).

## B.5 Tables in `refspectra.fits`

The function  $f(E_l; \mu_i, \mu_e)$  which gives dependence of a locally emitted spectrum on the angle of incidence and angle of emission is stored in this FITS file. The emission is induced by a power-law incident radiation. Values of this function were computed by the Monte Carlo simulations of Compton scattering, for details see Matt, Perola & Piro (1991). The reflected radiation depends on the photon index  $\Gamma$  of the incident radiation. There are several binary extensions in this fits file:

- the first extension contains energy values in keV where the function  $f(E_l; \mu_i, \mu_e)$  is computed, currently the interval from 2 to 300 keV is covered,
- the second extension contains the absolute values of the cosine of the incident angles,
- the third extension contains the values of the cosine of the emission angles,
- the fourth extension contains the values of the photon indices  $\Gamma$  of the incident power law, currently tables for  $\Gamma = 1.5, 1.6, \dots, 2.9$  and 3.0 are computed,
- in the following extensions the function  $f(E_l; \mu_i, \mu_e)$  is defined, each extension is for a particular value of  $\Gamma$ ; here values of the function are stored as a vector for different incident angles (rows) and for different angles of emission (columns), each element of this vector corresponds to a value of the function for a certain value of energy.

# Appendix C

## Description of the integration routines

Here we describe the technical details about the integration routines, which act as a common driver performing the ray-tracing for various models of the local emission. The description of non-axisymmetric and axisymmetric versions are both provided. An appropriate choice depends on the form of intrinsic emissivity. Obviously, non-axisymmetric tasks are computationally more demanding.

### C.1 Non-axisymmetric integration routine **ide**

This subroutine integrates the local emission and local Stokes parameters for (partially) polarized emission of the accretion disc near a rotating (Kerr) black hole (characterized by the angular momentum  $a$ ) for an observer with an inclination angle  $\theta_o$ . The subroutine has to be called with ten parameters:

`ide(ear,ne,nt,far,qar,uar,var,ide_param,emissivity,ne_loc)`

**ear** – real array of energy bins (same as **ear** for local models in XSPEC),  
**ne** – integer, number of energy bins (same as **ne** for local models in XSPEC),  
**nt** – integer, number of grid points in time (**nt** = 1 means stationary model),  
**far(ne,nt)** – real array of photon flux per bin (same as **photar** for local models in XSPEC but with the time resolution),  
**qar(ne,nt)** – real array of the Stokes parameter Q divided by the energy,  
**uar(ne,nt)** – real array of the Stokes parameter U divided by the energy,  
**var(ne,nt)** – real array of the Stokes parameter V divided by the energy,  
**ide\_param** – twenty more parameters needed for the integration (explained below),  
**emissivity** – name of the external emissivity subroutine, where the local emission of the disc is defined (explained in detail below),  
**ne\_loc** – number of points (in energies) where local photon flux (per keV) in the emissivity subroutine is defined.

The description of the **ide\_param** parameters follows:

**ide\_param(1)** –  $a/M$  – the black-hole angular momentum ( $0 \leq a/M \leq 1$ ),

`ide_param(2)` – `theta_o` – the observer inclination in degrees ( $0^\circ$  – pole,  $90^\circ$  – equatorial plane),  
`ide_param(3)` – `rin-rh` – the inner edge of the non-zero disc emissivity relative to the black-hole horizon (in  $GM/c^2$ ),  
`ide_param(4)` – `ms` – determines whether we also integrate emission below the marginally stable orbit; if its value is set to zero and the inner radius of the disc is below the marginally stable orbit then the emission below this orbit is taken into account, if set to unity it is not,  
`ide_param(5)` – `rout-rh` – the outer edge of the non-zero disc emissivity relative to the black-hole horizon (in  $GM/c^2$ ),  
`ide_param(6)` – `phi` – the position angle of the axial sector of the disc with non-zero emissivity in degrees,  
`ide_param(7)` – `dphi` – the inner angle of the axial sector of the disc with non-zero emissivity in degrees ( $dphi \leq 360^\circ$ ),  
`ide_param(8)` – `nrad` – the radial resolution of the grid,  
`ide_param(9)` – `division` – the switch for the spacing of the radial grid (0 – equidistant, 1 – exponential),  
`ide_param(10)` – `nphi` – the axial resolution of the grid,  
`ide_param(11)` – `smooth` – the switch for performing simple smoothing (0 – no, 1 – yes),  
`ide_param(12)` – `normal` – the switch for normalizing of the final spectrum,  
     if = 0 – total flux is unity (usually used for the line),  
     if > 0 – flux is unity at the energy = `normal` keV (usually used for the continuum),  
     if < 0 – final spectrum is not normalized,  
`ide_param(13)` – `zshift` – the overall redshift of the object,  
`ide_param(14)` – `ntable` – tables to be used, it defines a double-digit number NN in the name of the FITS file `KBHtablesNN.fits` containing the tables ( $0 \leq ntable \leq 99$ ),  
`ide_param(15)` – `edivision` – the switch for spacing the grid in local energies (0 – equidistant, 1 – exponential),  
`ide_param(16)` – `periodic` – if set to unity then local emissivity is periodic if set to zero it is not (need not to be set if `nt` = 1),  
`ide_param(17)` – `dt` – the time step (need not to be set if `nt` = 1),  
`ide_param(18)` – `polar` – whether the change of the polarization angle and/or azimuthal emission angle will be read from FITS tables (0 – no, 1 – yes),  
`ide_param(19)` – `r0-rh` and  
`ide_param(20)` – `phi0` – in dynamical computations the initial time will be set to the time when photons emitted from the point [`r0`, `phi0`] on the disc (in the Boyer-Lindquist coordinates) reach the observer.

The subroutine `ide` needs an external emissivity subroutine in which the local emission and local Stokes parameters are defined. This subroutine has twelve parameters:

```
emissivity(ear_loc, ne_loc, nt, far_loc, qar_loc, uar_loc, var_loc, r, phi, cosine,
           phiphoton, first_emis)
```

`ear_loc(0:ne_loc)` – real array of the local energies where the local photon flux `far_loc` is defined, with special meaning of `ear_loc(0)` – if its value is larger than zero then

the local emissivity consists of two energy regions where the flux is non-zero; the flux between these regions is zero and `ear_loc(0)` defines the number of points in local energies with the zero local flux,

- `ne_loc` – integer, the number of points (in energies) where the local photon flux (per keV) is defined,
- `nt` – integer, the number of grid points in time (`nt = 1` means stationary model),
- `far_loc(0:ne_loc,nt)` – real array of the local photon flux (per keV) – if the local emissivity consists of two separate non-zero regions (i.e. `ear_loc(0) > 0`) then `far_loc(0,it)` is the index of the last point of the first non-zero local energy region,
- `qar_loc(ne_loc,nt)` – real array of the local Stokes parameter Q divided by the local energy,
- `uar_loc(ne_loc,nt)` – real array of the local Stokes parameter U divided by the local energy,
- `var_loc(ne_loc,nt)` – real array of the local Stokes parameter V divided by the local energy,
- `r` – the radius in  $GM/c^2$  where the local photon flux `far_loc` at the local energies `ear_loc` is wanted
- `phi` – the azimuth (the Boyer-Lindquist coordinate  $\varphi$ ) where the local photon flux `far_loc` at the local energies `ear_loc` is wanted,
- `cosine` – the cosine of the local angle between the emitted ray and local disc normal,
- `phiphoton` – the angle between the emitted ray projected onto the plane of the disc (in the local frame of the moving disc) and the radial component of the local tetrad (in radians),
- `first_emis` – boolean, TRUE if we enter the emissivity subroutine from the subroutine `ide` for the first time, FALSE if we have already been in this subroutine (this is convenient if we want to calculate some initial values when we are in the emissivity subroutine for the first time, e.g. trajectory of the falling spot).

## C.2 Axisymmetric integration routine `idre`

This subroutine integrates the local axisymmetric emission of an accretion disc near a rotating (Kerr) black hole (characterized by the angular momentum  $a$ ) for an observer with an inclination angle  $\theta_o$ . The subroutine has to be called with eight parameters:

`idre(ear,ne,photar,idre_param,cmodel,ne_loc,ear_loc,far_loc)`

- `ear` – real array of energy bins (same as `ear` for local models in XSPEC),
- `ne` – integer, the number of energy bins (same as `ne` for local models in XSPEC),
- `photar` – real array of the photon flux per bin (same as `photar` for local models in XSPEC),
- `idre_param` – ten more parameters needed for the integration (explained below),
- `cmodel` – 32-byte string with a base name of a FITS file with tables for axisymmetric emission (e.g. “KBHline” for `KBHlineNN.fits`),
- `ne_loc` – the number of points (in energies) where the local photon flux (per keV) is defined in the emissivity subroutine,
- `ear_loc` – array of the local energies where the local photon flux `far_loc` is defined,

`far_loc` – array of the local photon flux (per keV).

The description of the `idre_param` parameters follows:

- `idre_param(1)` – `a/M` – the black-hole angular momentum ( $0 \leq a/M \leq 1$ ),
- `idre_param(2)` – `theta_o` – the observer inclination in degrees ( $0^\circ$  – pole,  $90^\circ$  – equatorial plane),
- `idre_param(3)` – `rin-rh` – the inner edge of the non-zero disc emissivity relative to the black-hole horizon (in  $GM/c^2$ ),
- `idre_param(4)` – `ms` – determines whether we also integrate emission below the marginally stable orbit; if its value is set to zero and the inner radius of the disc is below the marginally stable orbit then the emission below this orbit is taken into account, if set to unity it is not,
- `idre_param(5)` – `rout-rh` – the outer edge of the non-zero disc emissivity relative to the black-hole horizon (in  $GM/c^2$ ),
- `idre_param(6)` – `smooth` – the switch for performing simple smoothing (0 – no, 1 – yes),
- `idre_param(7)` – `normal` – the switch for normalizing the final spectrum,
  - if = 0 – total flux is unity (usually used for the line),
  - if > 0 – flux is unity at the energy = `normal` keV (usually used for the continuum),
  - if < 0 – final spectrum is not normalized,
- `idre_param(8)` – `zshift` – the overall redshift of the object,
- `idre_param(9)` – `ntable` – tables to be used, it defines a double-digit number NN in the name of the FITS file (e.g. in `KBHlineNN.fits`) containing the tables ( $0 \leq ntable \leq 99$ ),
- `idre_param(10)` – `alpha` – the radial power-law index.

The subroutine `idre` does not need any external emissivity subroutine.

## Appendix D

# Atlas of transfer functions

In this Appendix we provide a graphical representation of the transfer functions that are needed for computations of relativistic spectral profiles. For a mathematical definition of these functions and details of the adopted notation see Chapter 1. Although graphical representation is not necessary in the process of computations and actual data fitting, we find it extremely useful and practical for quick order-of-magnitude estimates. Often, expected values of various quantities can be seen almost instantly. For example, the magnitude and the range of the energy shift, the effect of gravitational lensing, the importance of the relative time delay etc. can be estimated from these graphs, assuming only basic parameters of the light emitting region.

The following contour graphs of the functions represent a top view of the equatorial plane for three different observer's inclination angles ( $\theta_o = 0.1^\circ$ ,  $45^\circ$  and  $85^\circ$ ) in four different spatial scales (three columns in Figs. D.1–D.21 and the coarsest scale in Figs. D.22–D.23). In the finest scale (the first column) we define the radial coordinate in a different way to that in the other columns. Specifically, we use  $r'^2 \equiv x'^2 + y'^2 = (r - r_h)^2$ . The use of  $r'$  brings the horizon  $r_h$  to the origin so that the region just outside the black hole is well resolved in these plots. We show figures for two values of an angular momentum  $a$  of the black hole (rows in Figs. D.1–D.21), particularly for the Schwarzschild black hole ( $a = 0$ , the horizon is at  $r_h = 2$  and the marginally stable orbit is at  $r_{ms} = 6$ ) and for an almost extreme Kerr black hole ( $a \doteq 0.9987$ , the horizon is at  $r_h = 1.05$  and the marginally stable orbit is at  $r_{ms} \doteq 1.198$ ). The clock-wise distortion of the contours visible in the second row is due to the frame-dragging near a rapidly rotating Kerr black hole, which is clearly visible in the Boyer-Lindquist coordinates. This effect is largely eliminated by the transformation from the Boyer-Lindquist to the Kerr ingoing coordinates (the last row of panels in Figs. D.1–D.21).

An observer is located to the top of the graphs. The black hole rotates counter-clockwise. The values of the functions are encoded by a colour scale, as indicated above each panel. The marginally stable orbit is also shown (drawn as a circle) where relevant.

The atlas shown here is only a part of a larger set that contains figures for more values of the observer's inclination and angular momentum of the black hole (including an extreme Kerr black hole). An interested reader can ask for the whole atlas by contacting the author at `dovciak@mbbox.troja.mff.cuni.cz`.

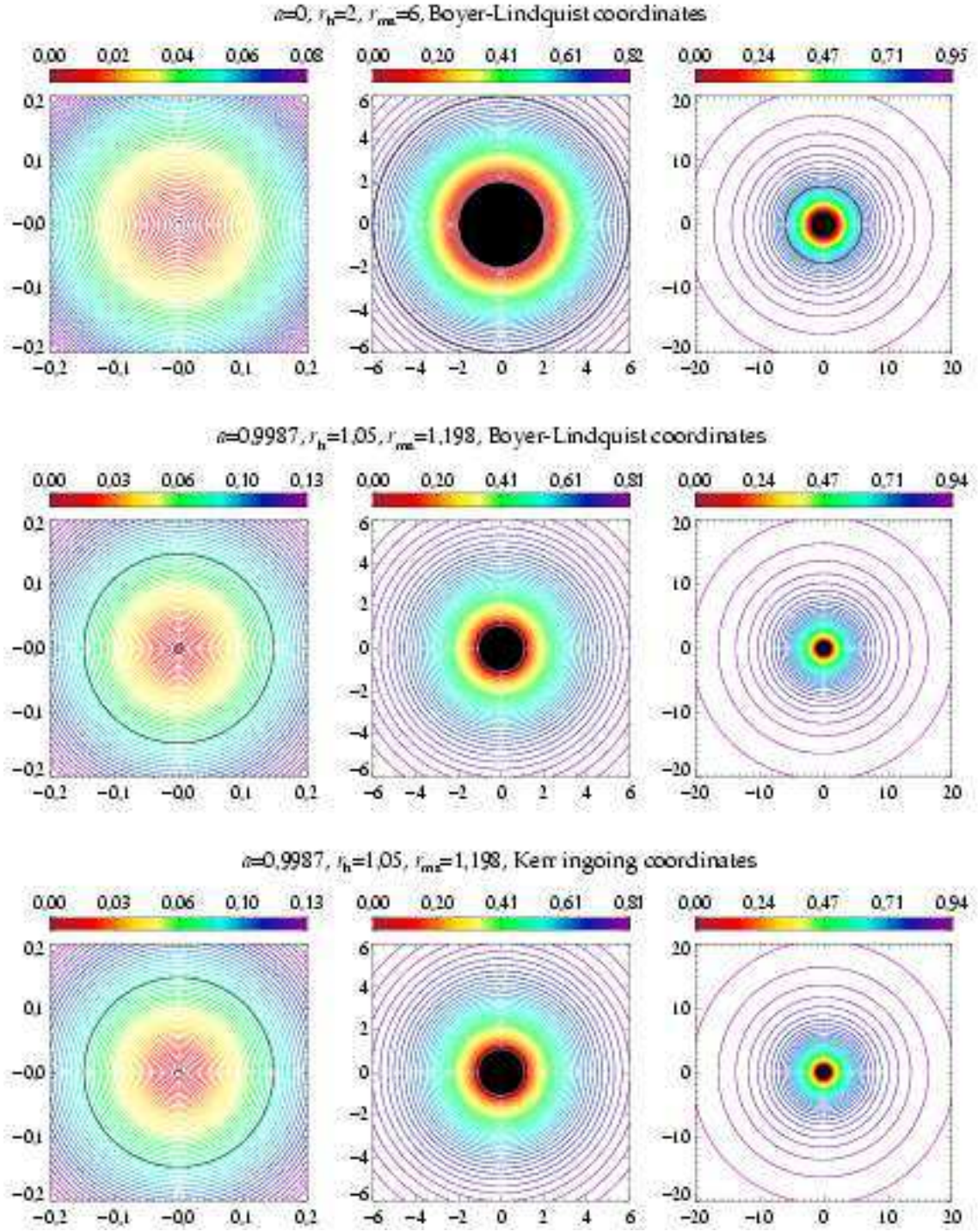
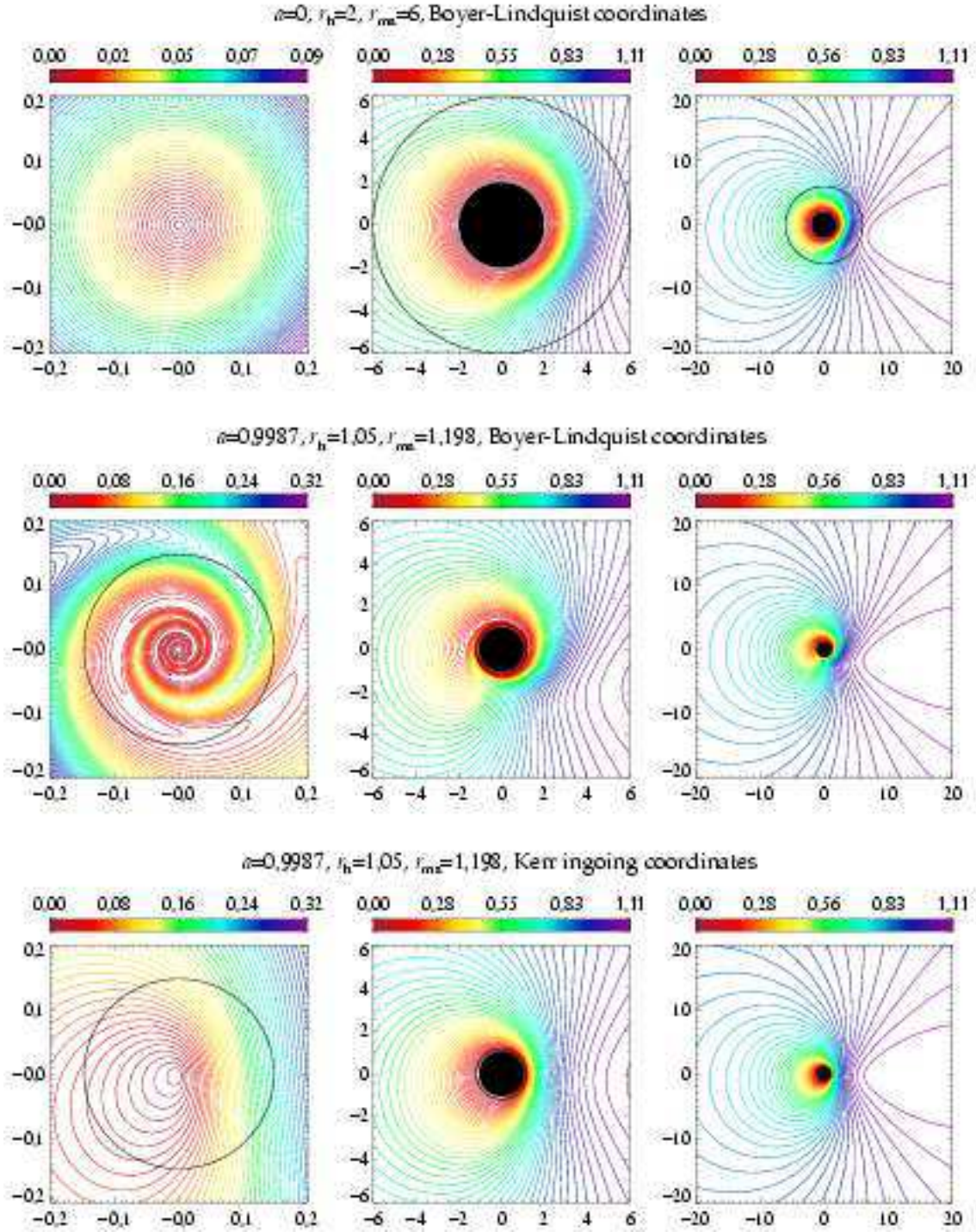


Figure D.1:  $g$ -factor for the inclination  $\theta_o = 0.1^\circ$ .

Figure D.2:  $g$ -factor for the inclination  $\theta_o = 45^\circ$ .

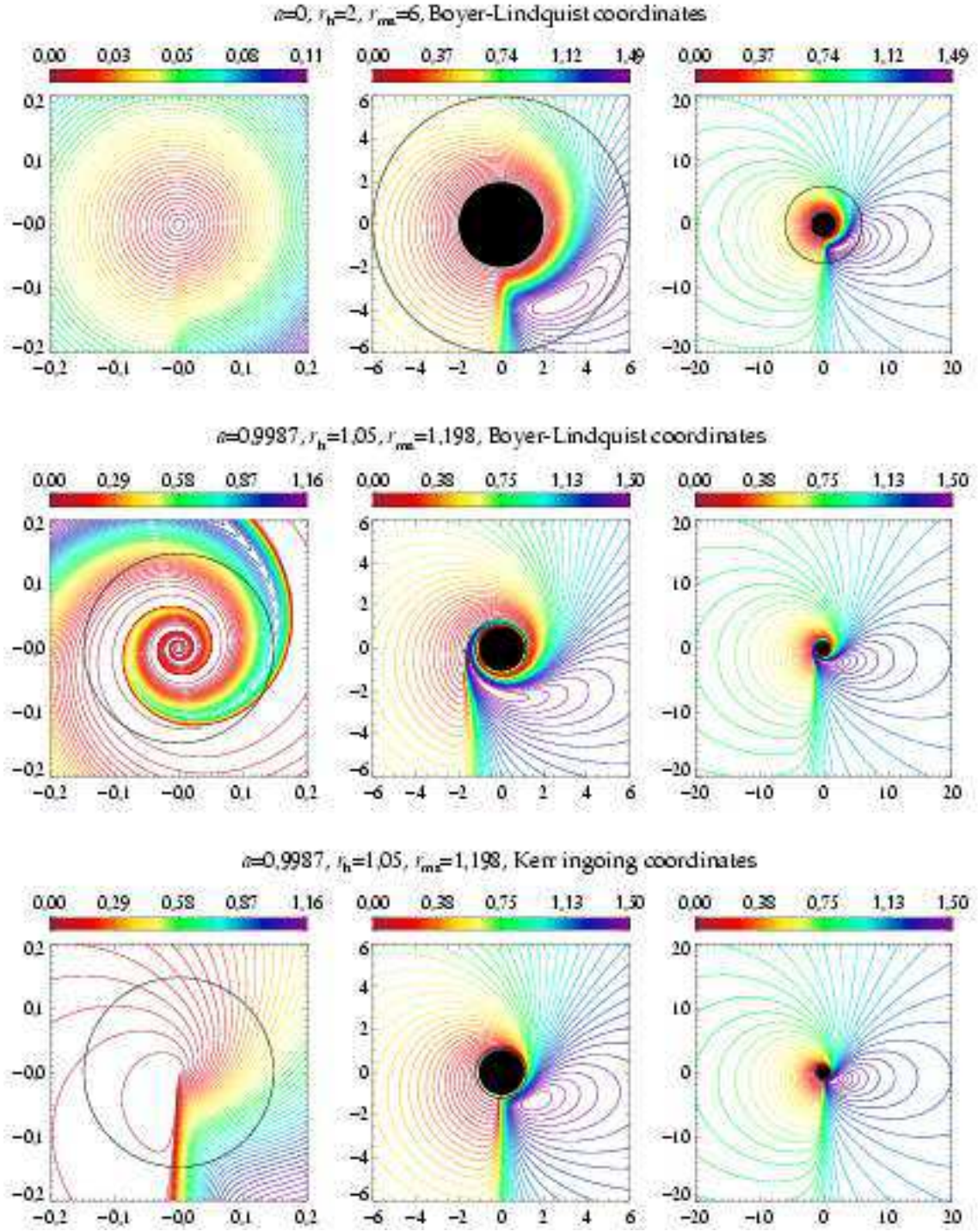
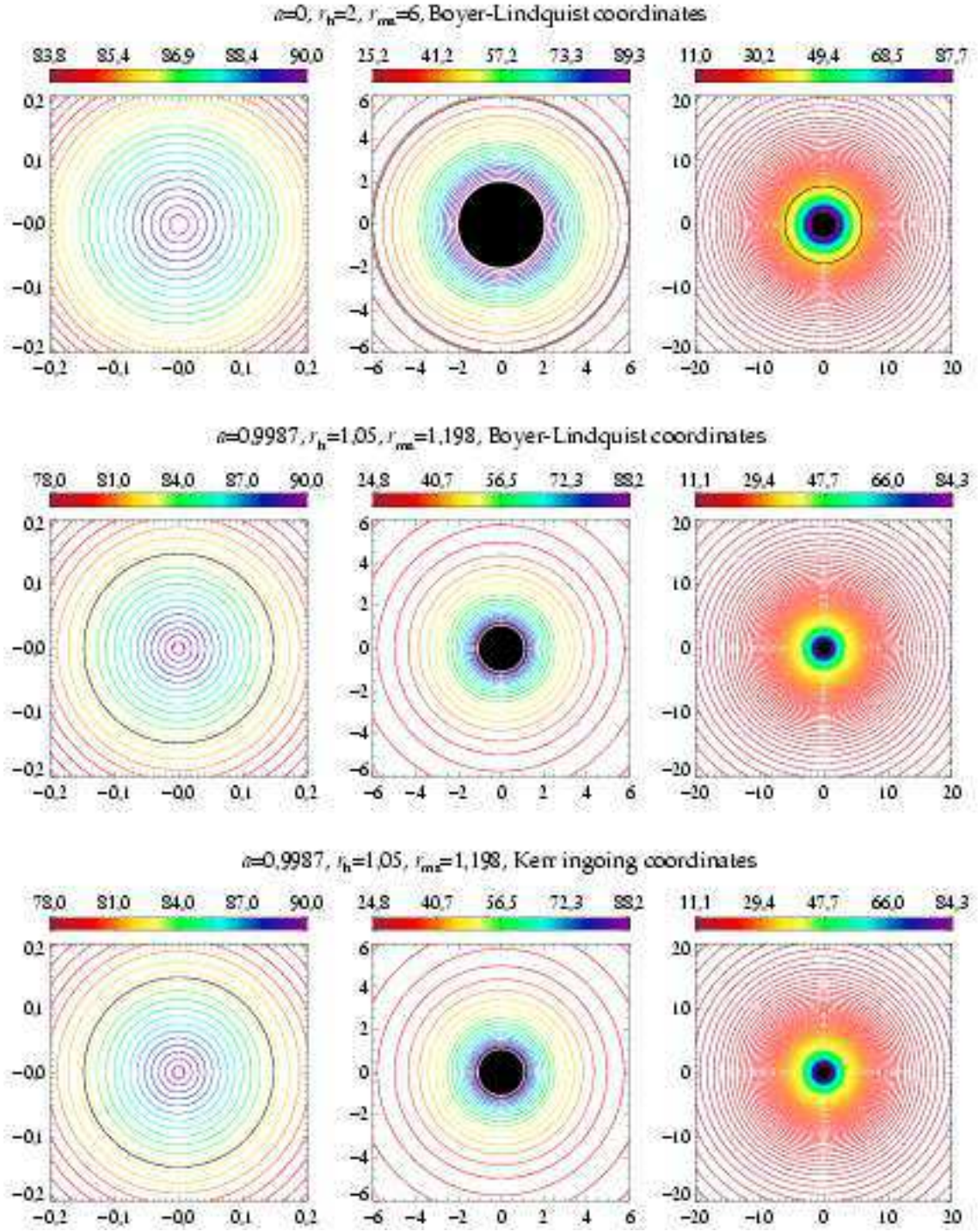


Figure D.3:  $g$ -factor for the inclination  $\theta_o = 85^\circ$ .

Figure D.4: Emission angle for the inclination  $\theta_o = 0.1^\circ$ .

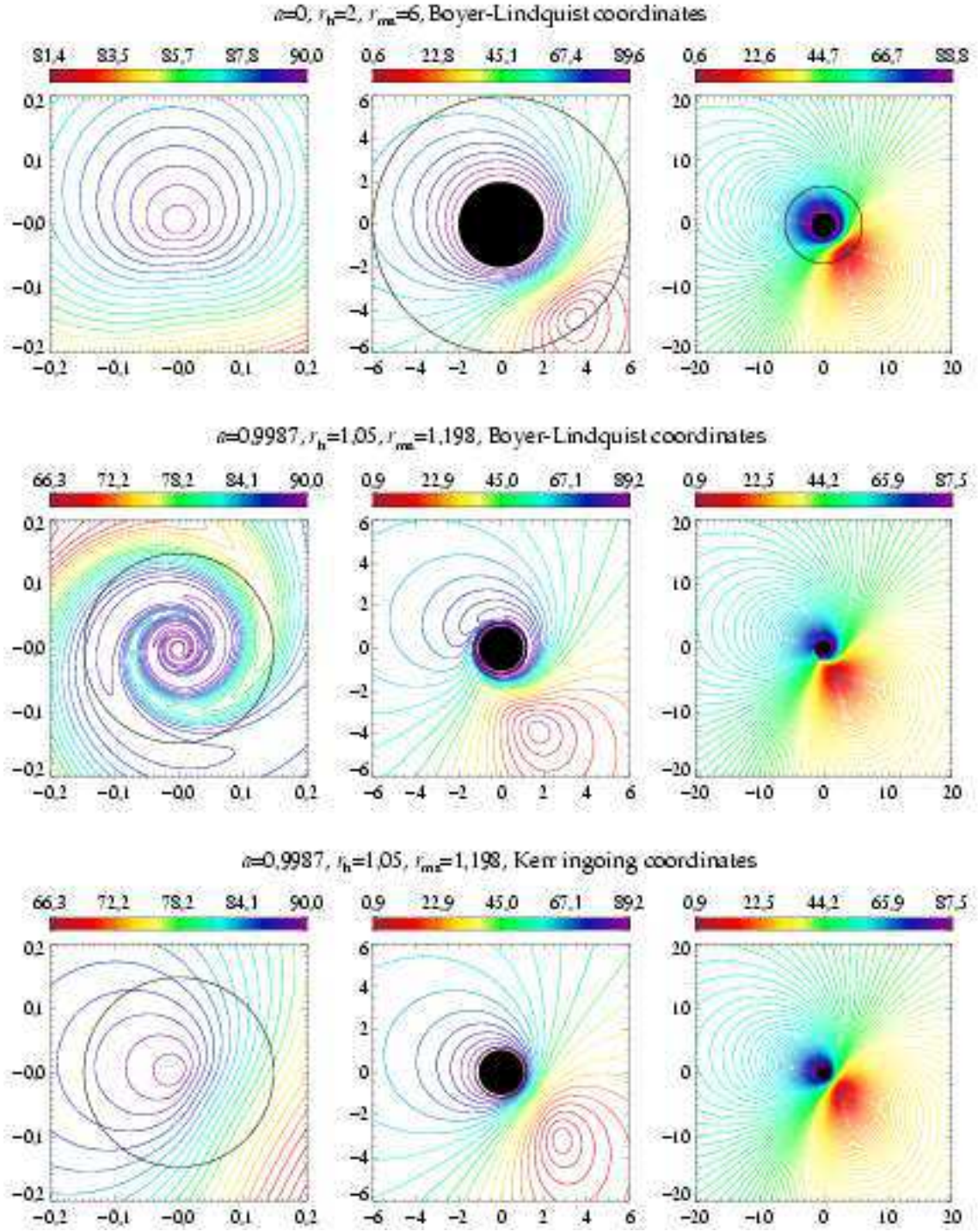
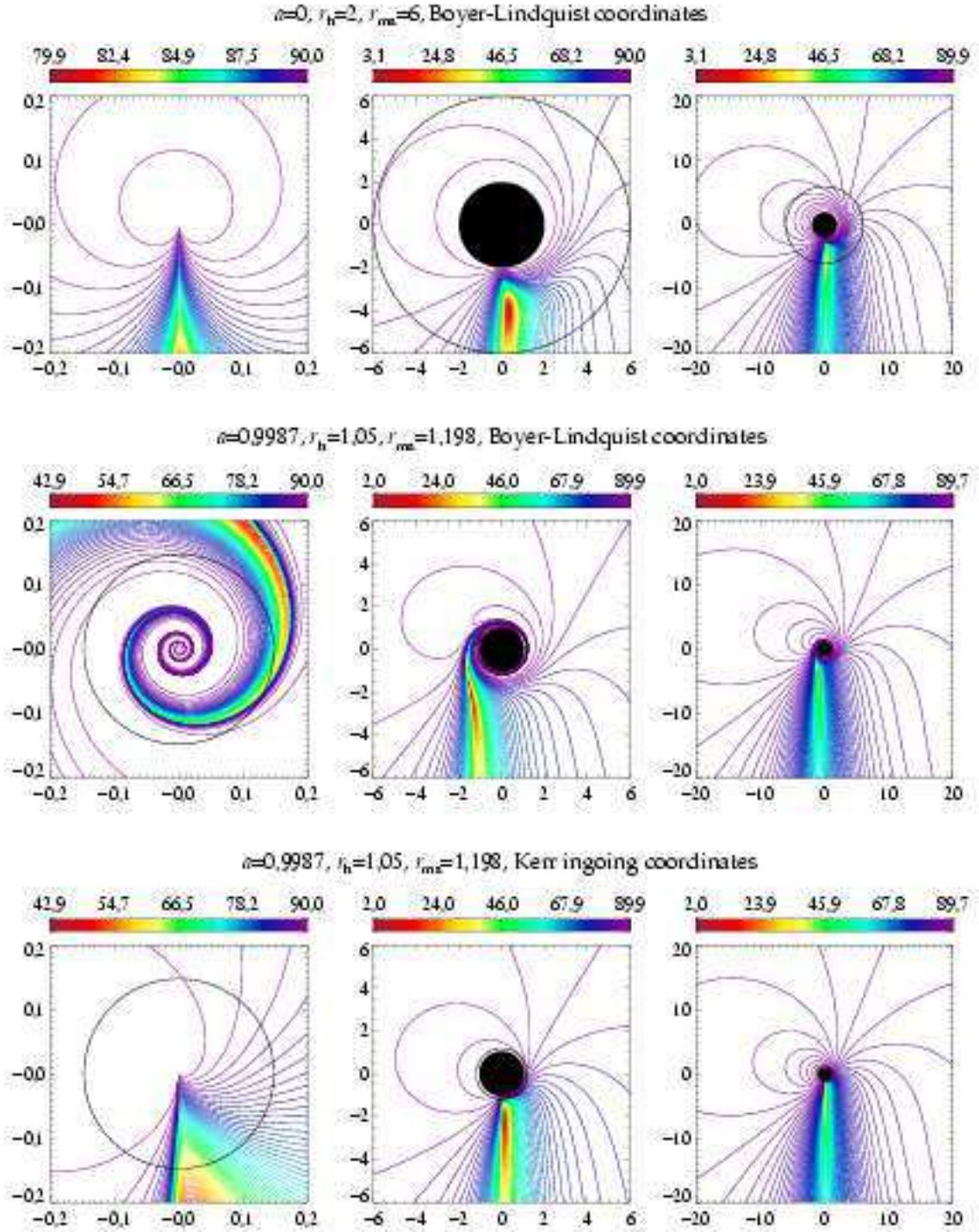


Figure D.5: Emission angle for the inclination  $\theta_o = 45^\circ$ .

Figure D.6: Emission angle for the inclination  $\theta_o = 85^\circ$ .

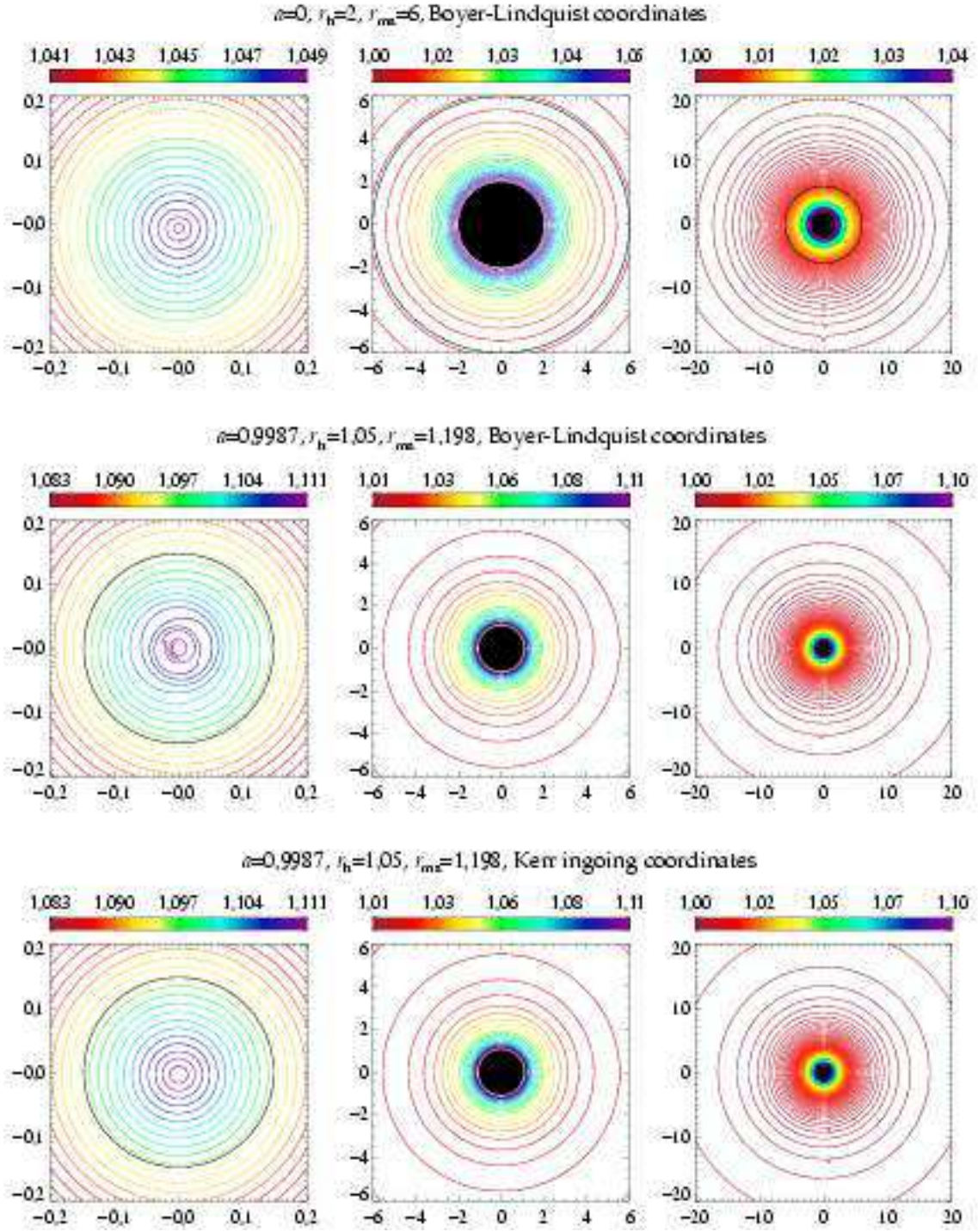
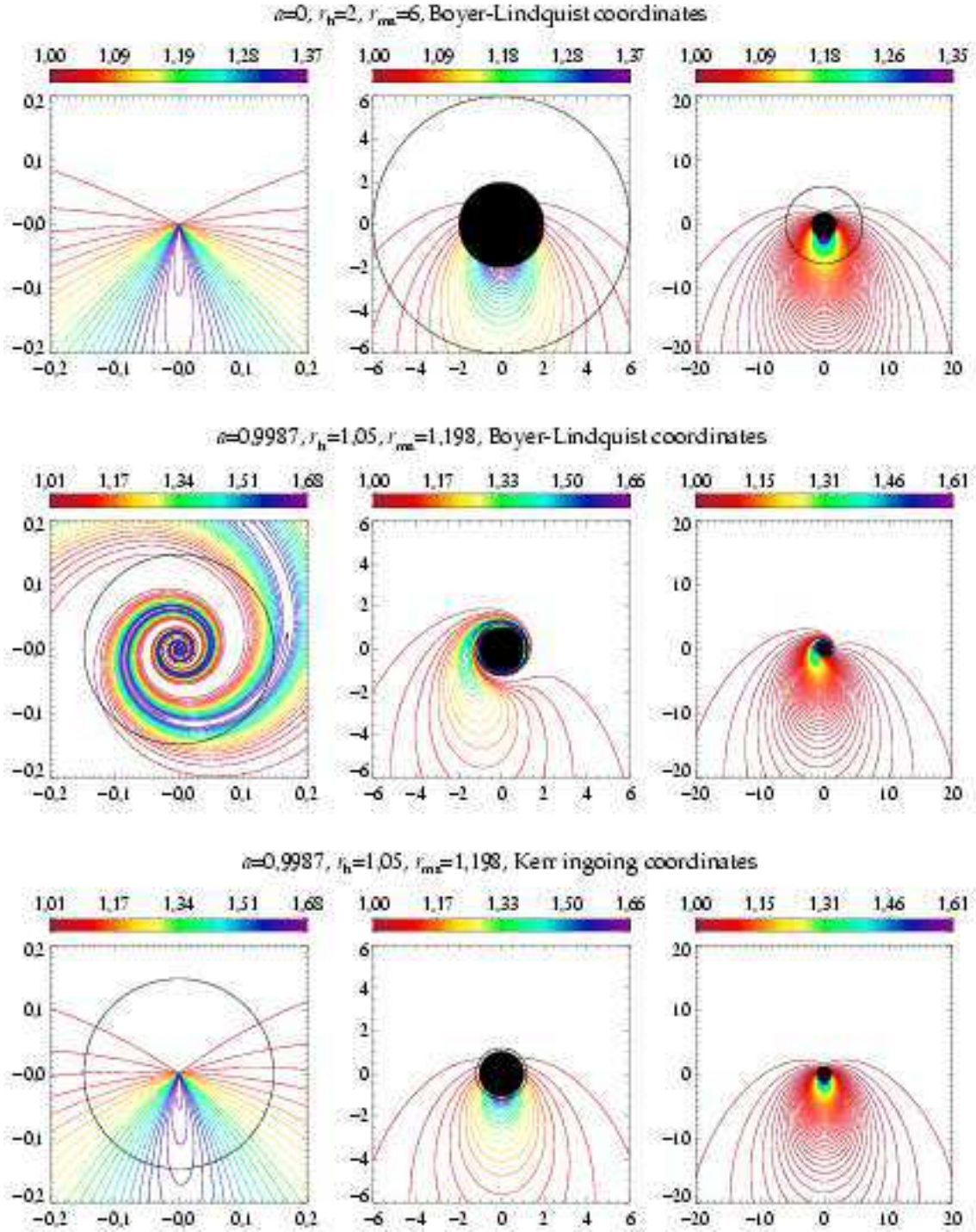


Figure D.7: Lensing for the inclination  $\theta_o = 0.1^\circ$ .

Figure D.8: Lensing for the inclination  $\theta_o = 45^\circ$ .

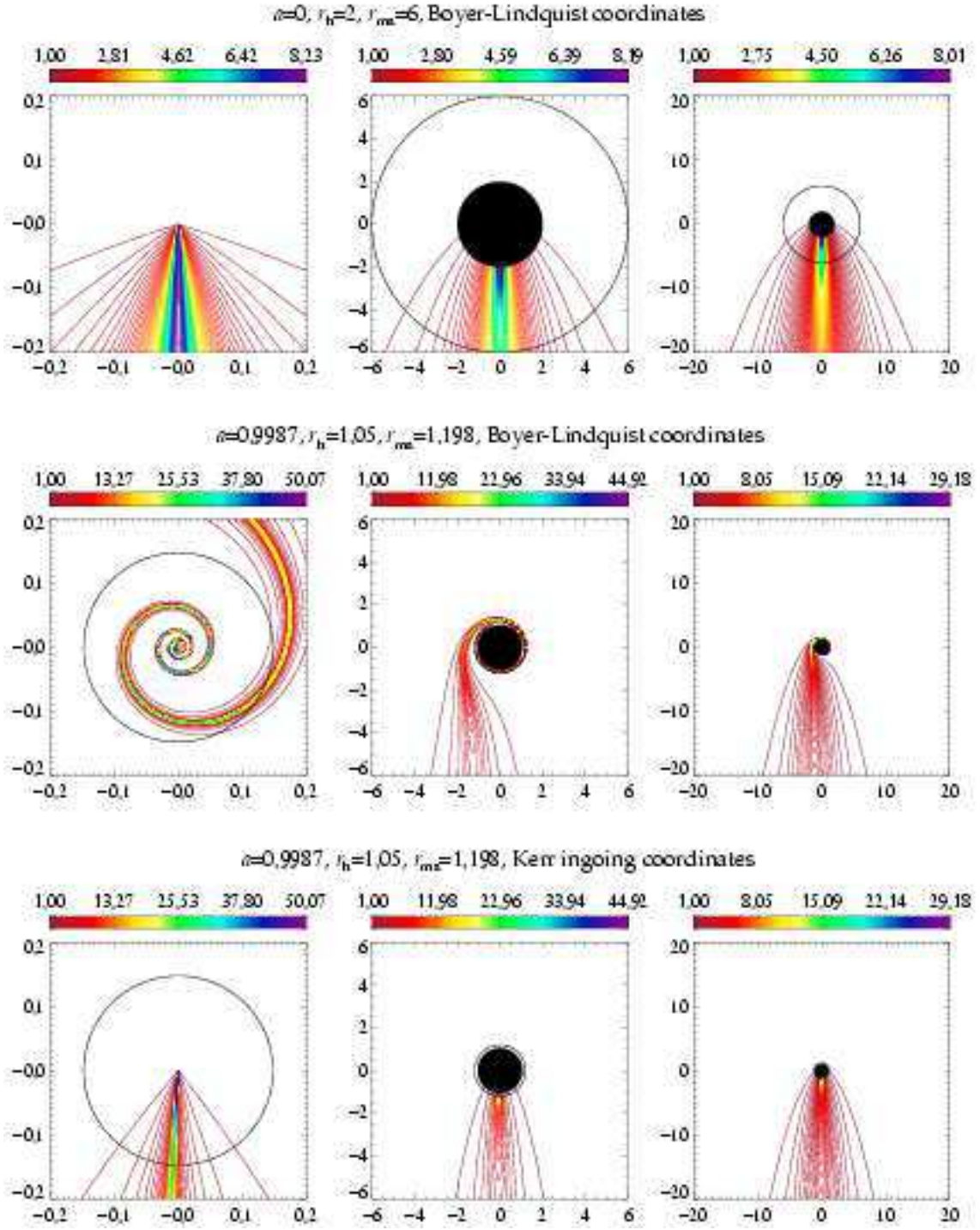
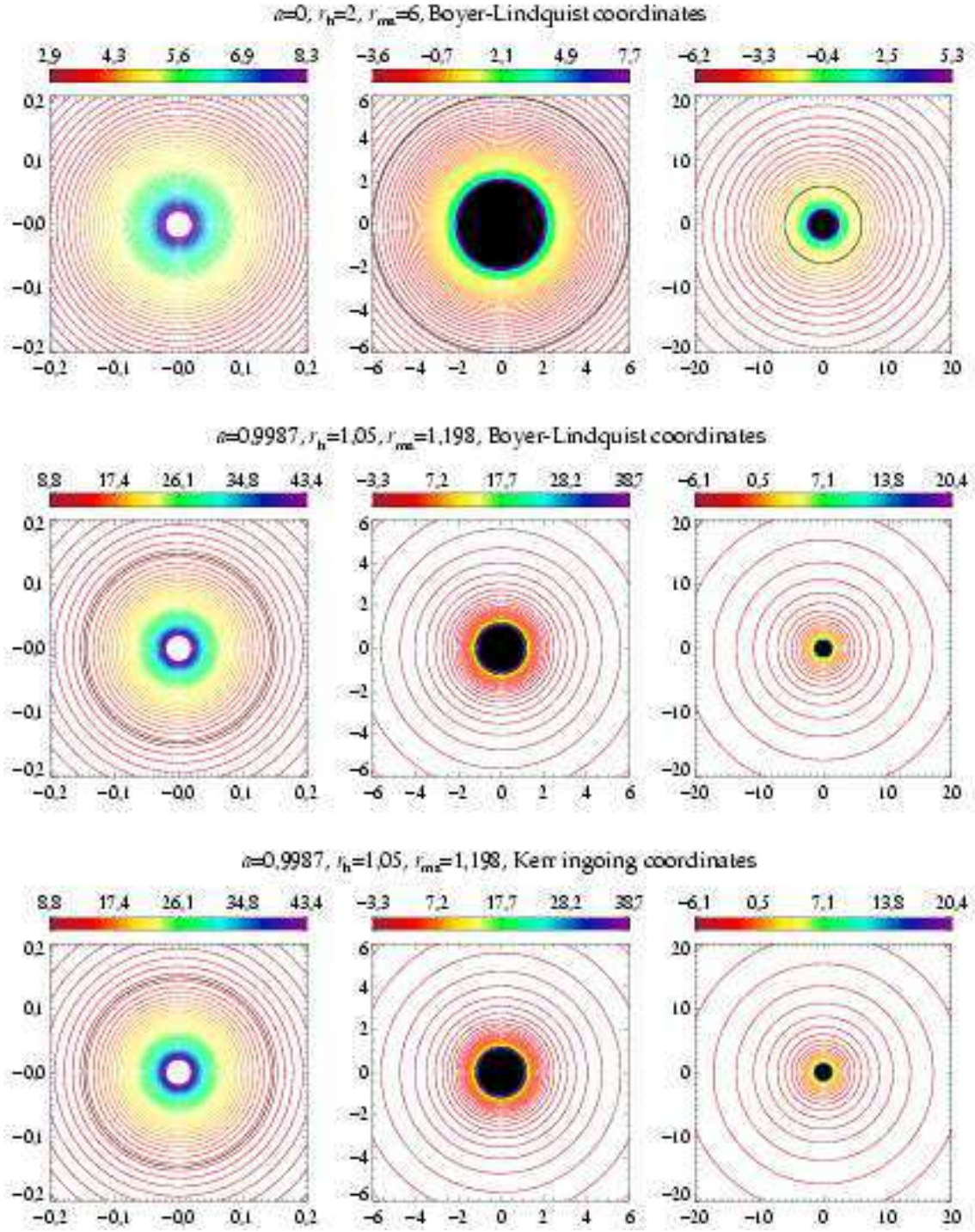


Figure D.9: Lensing for the inclination  $\theta_o = 85^\circ$ .

Figure D.10: Relative time delay for the inclination  $\theta_o = 0.1^\circ$ .

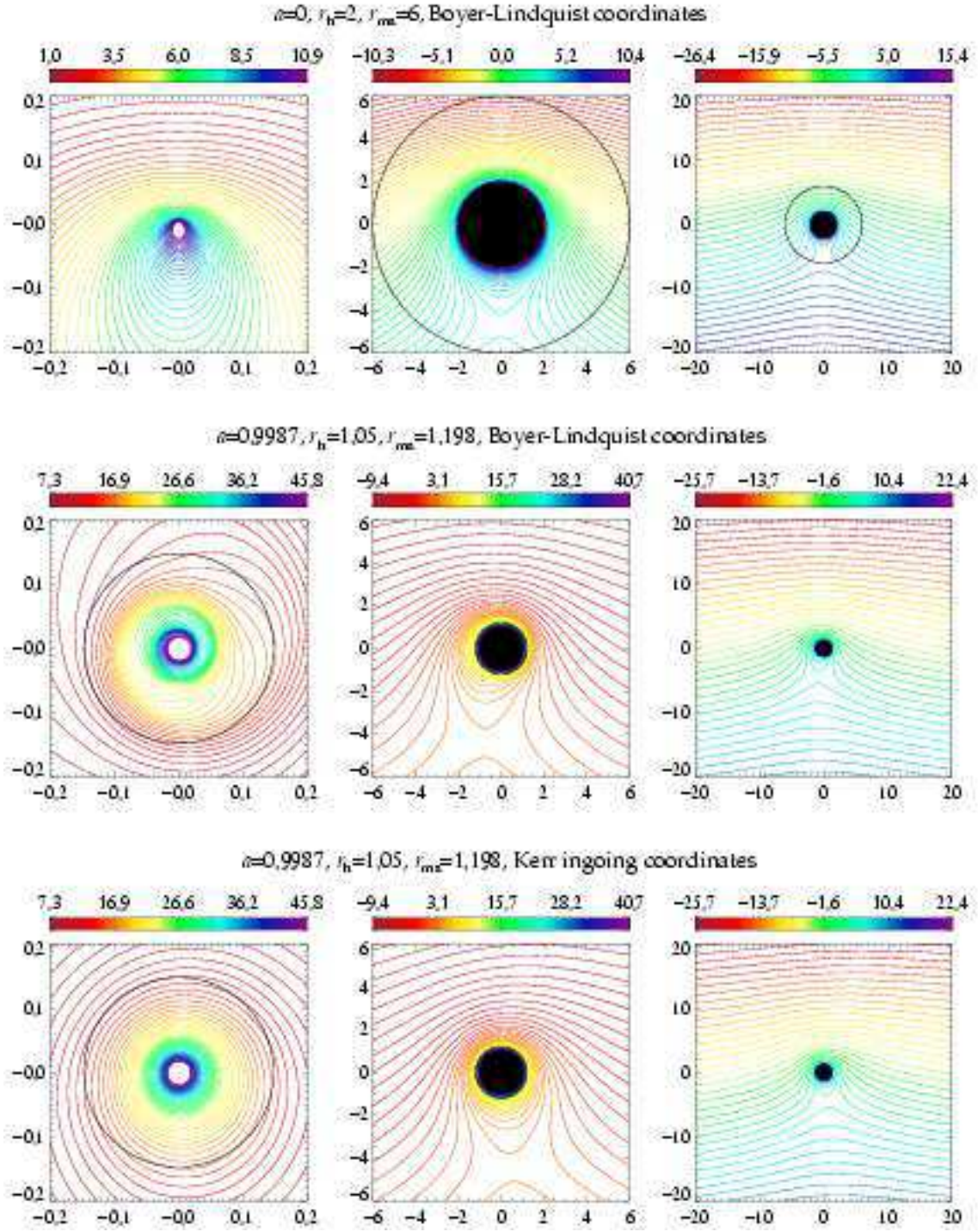
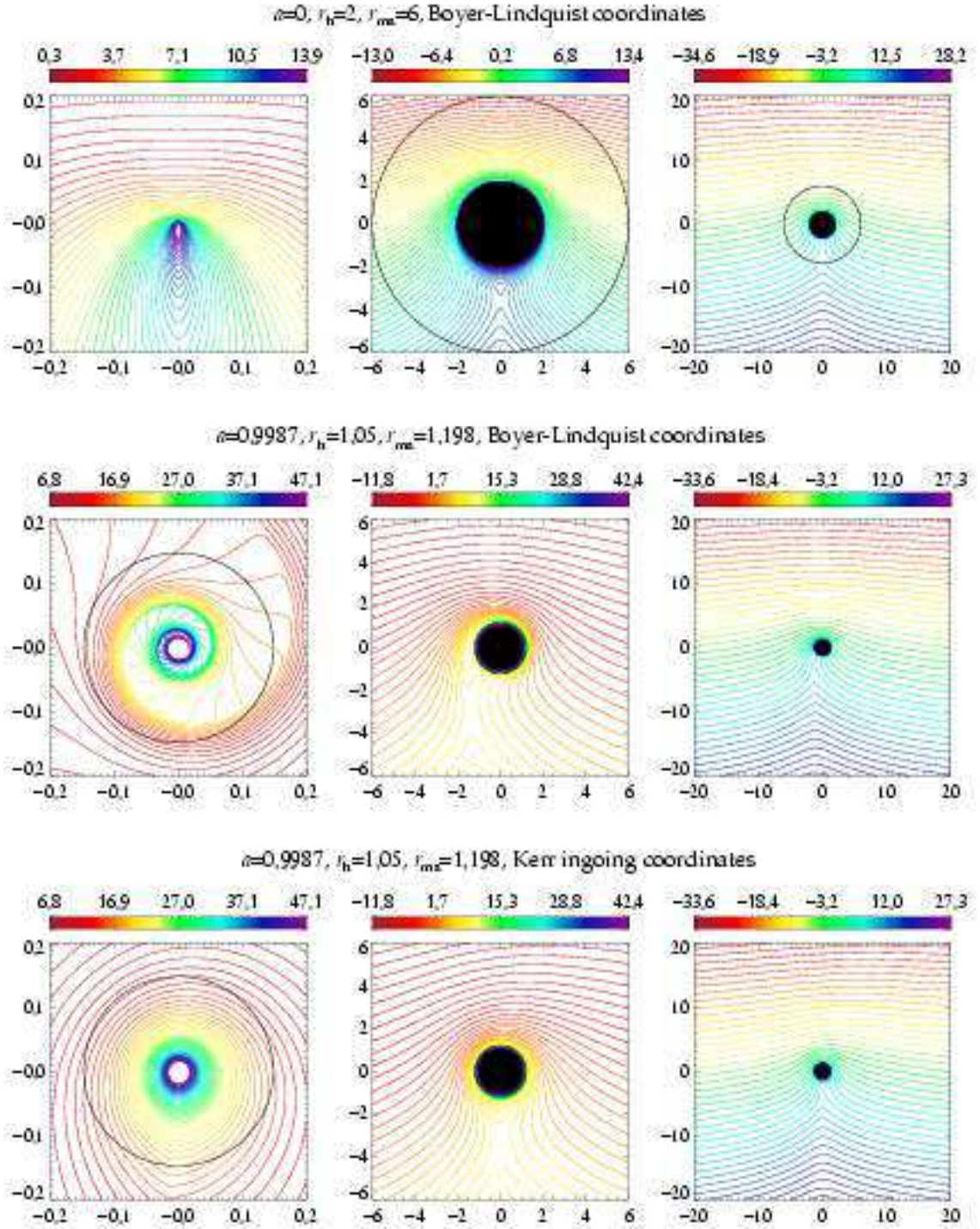


Figure D.11: Relative time delay for the inclination  $\theta_o = 45^\circ$ .

Figure D.12: Relative time delay for the inclination  $\theta_o = 85^\circ$ .

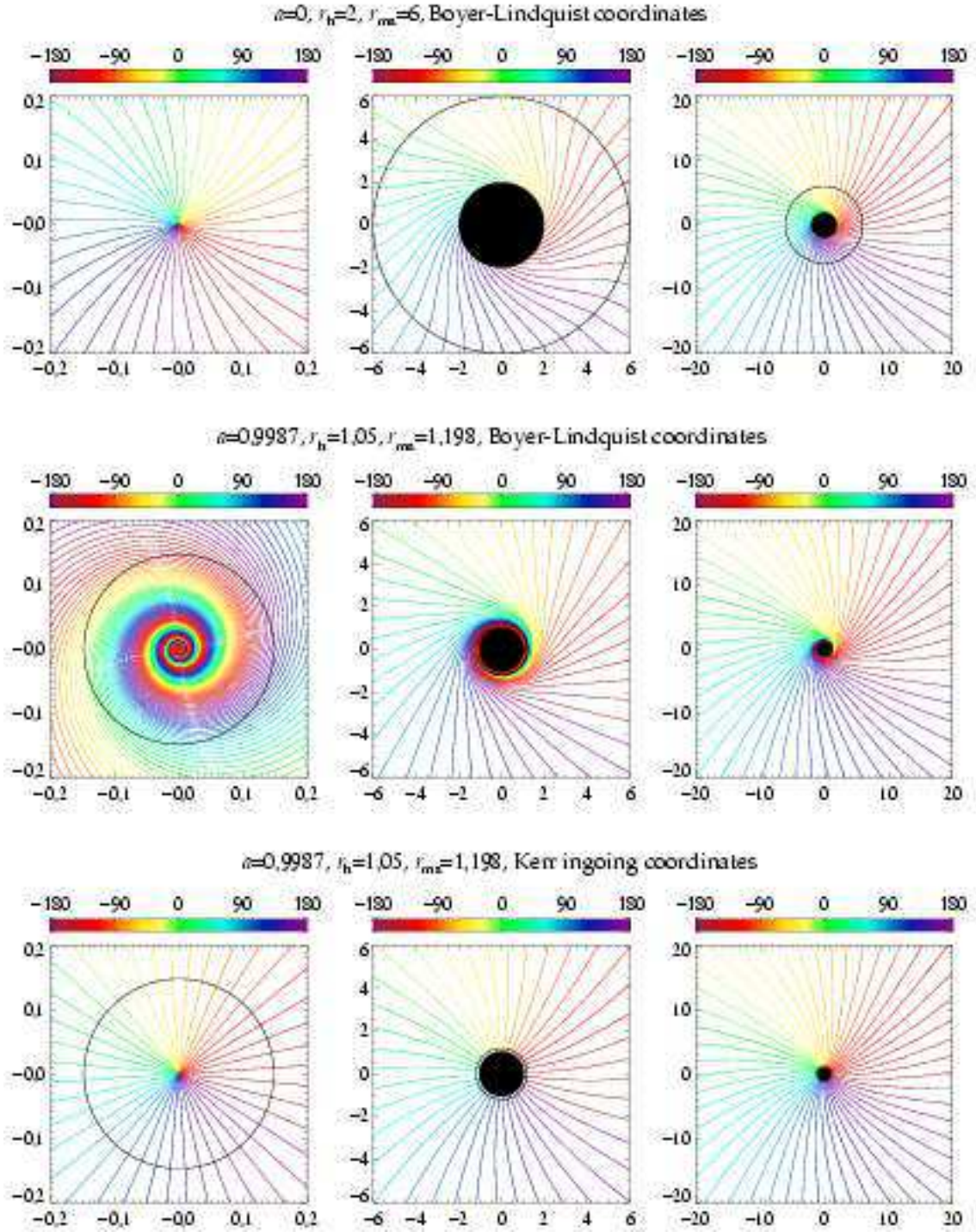


Figure D.13: Change of the polarization angle for the inclination  $\theta_o = 0.1^\circ$ .

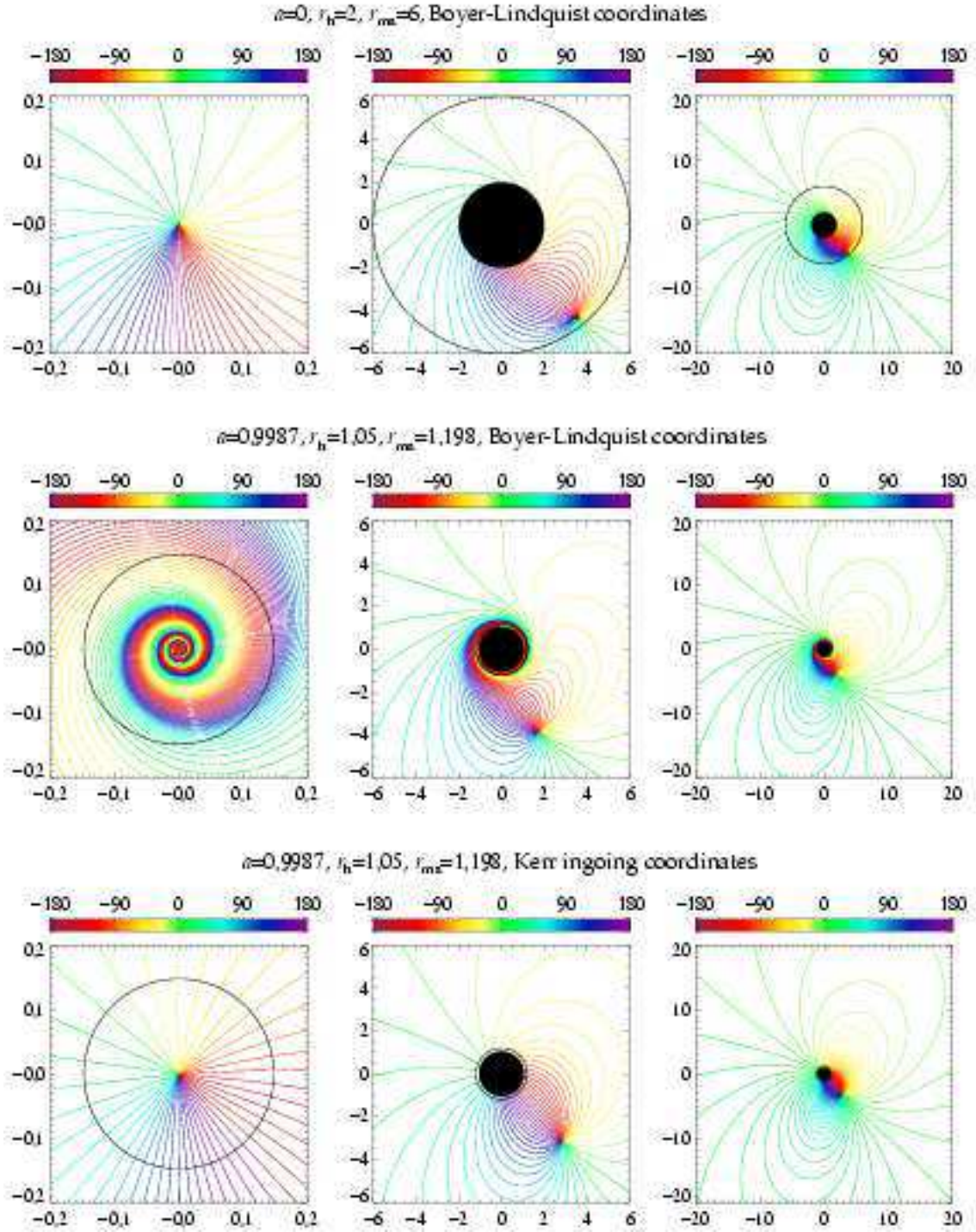


Figure D.14: Change of the polarization angle for the inclination  $\theta_o = 45^\circ$ .

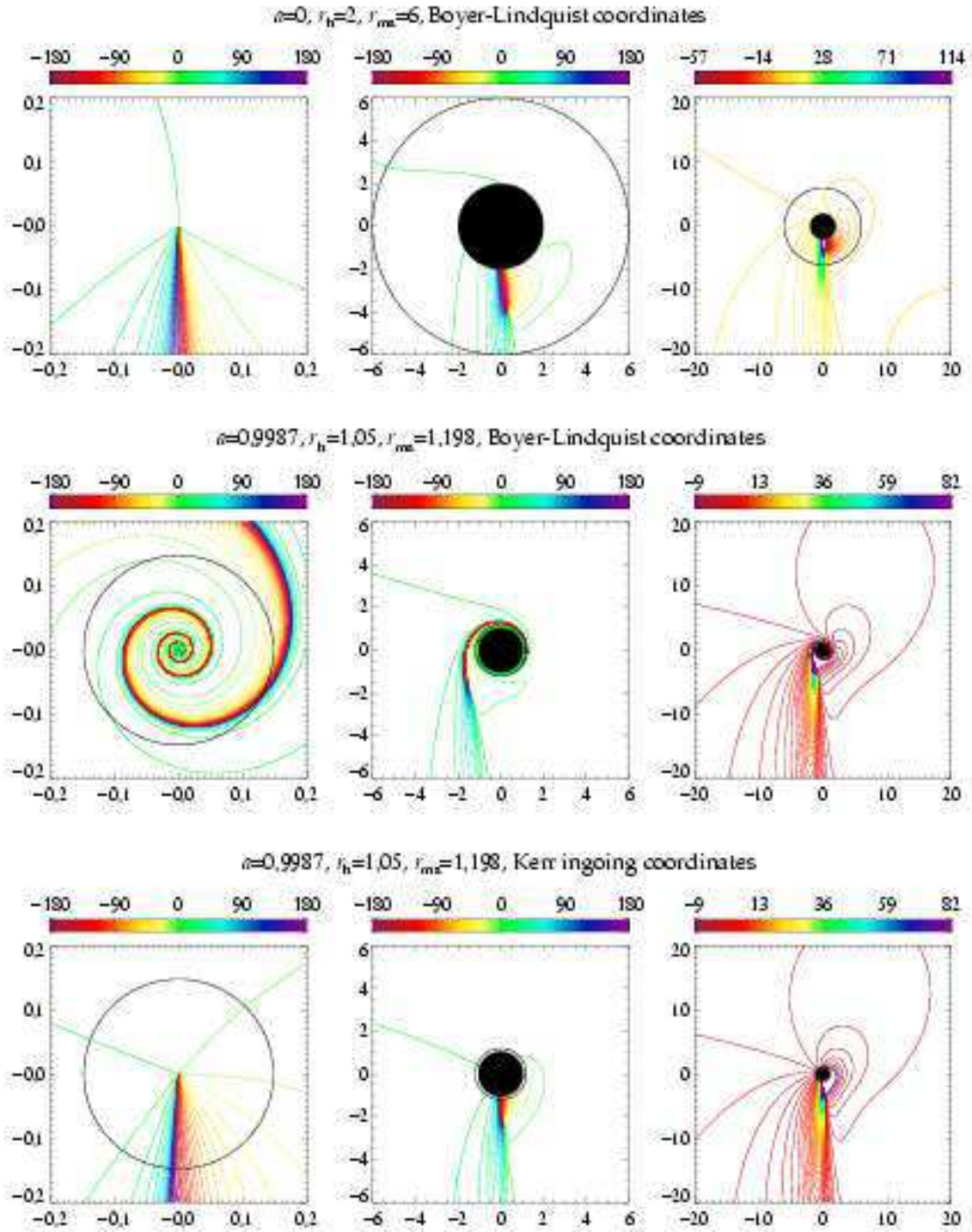
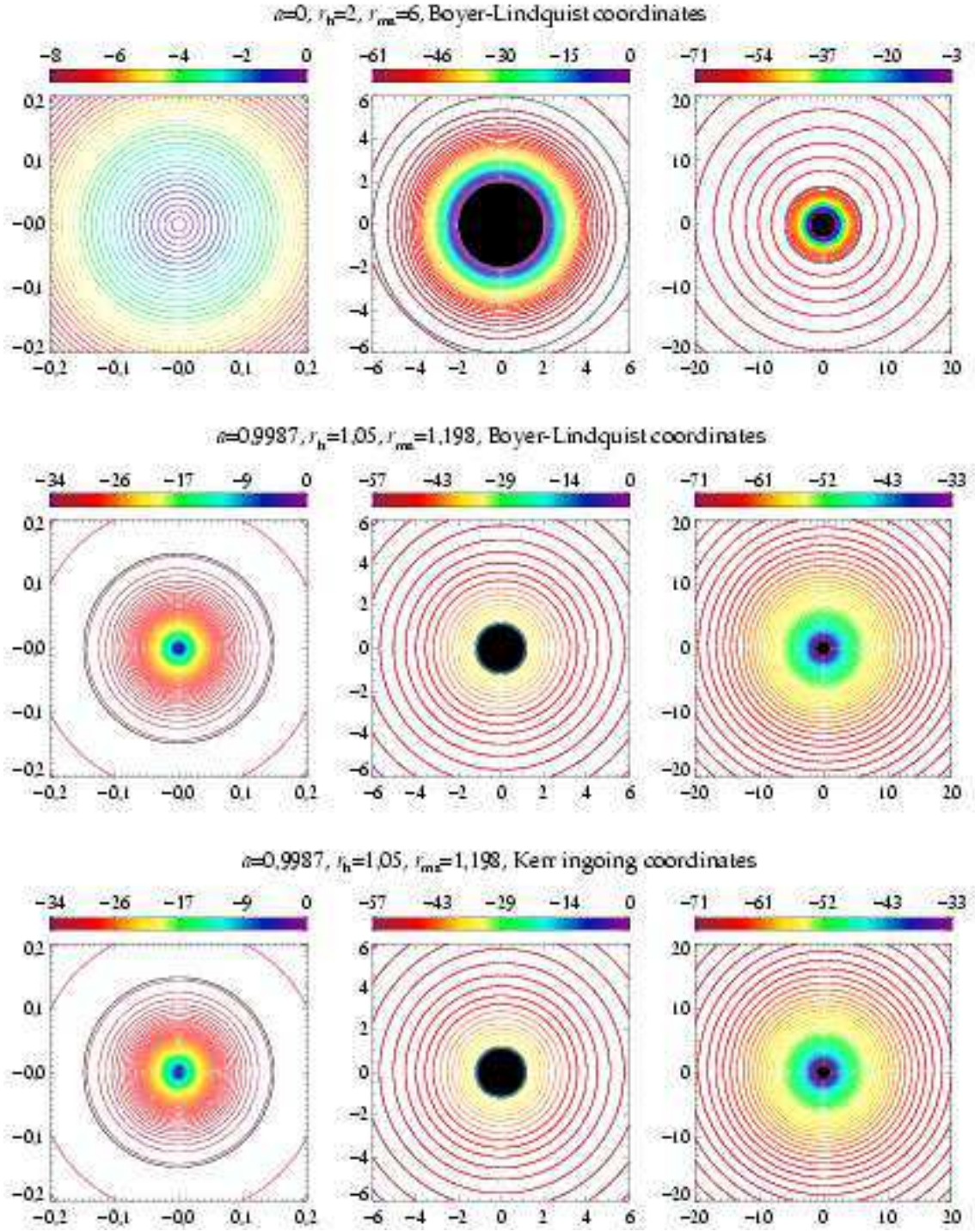


Figure D.15: Change of the polarization angle for the inclination  $\theta_o = 85^\circ$ .

Figure D.16: Azimuthal emission angle for the inclination  $\theta_o = 0.1^\circ$ .

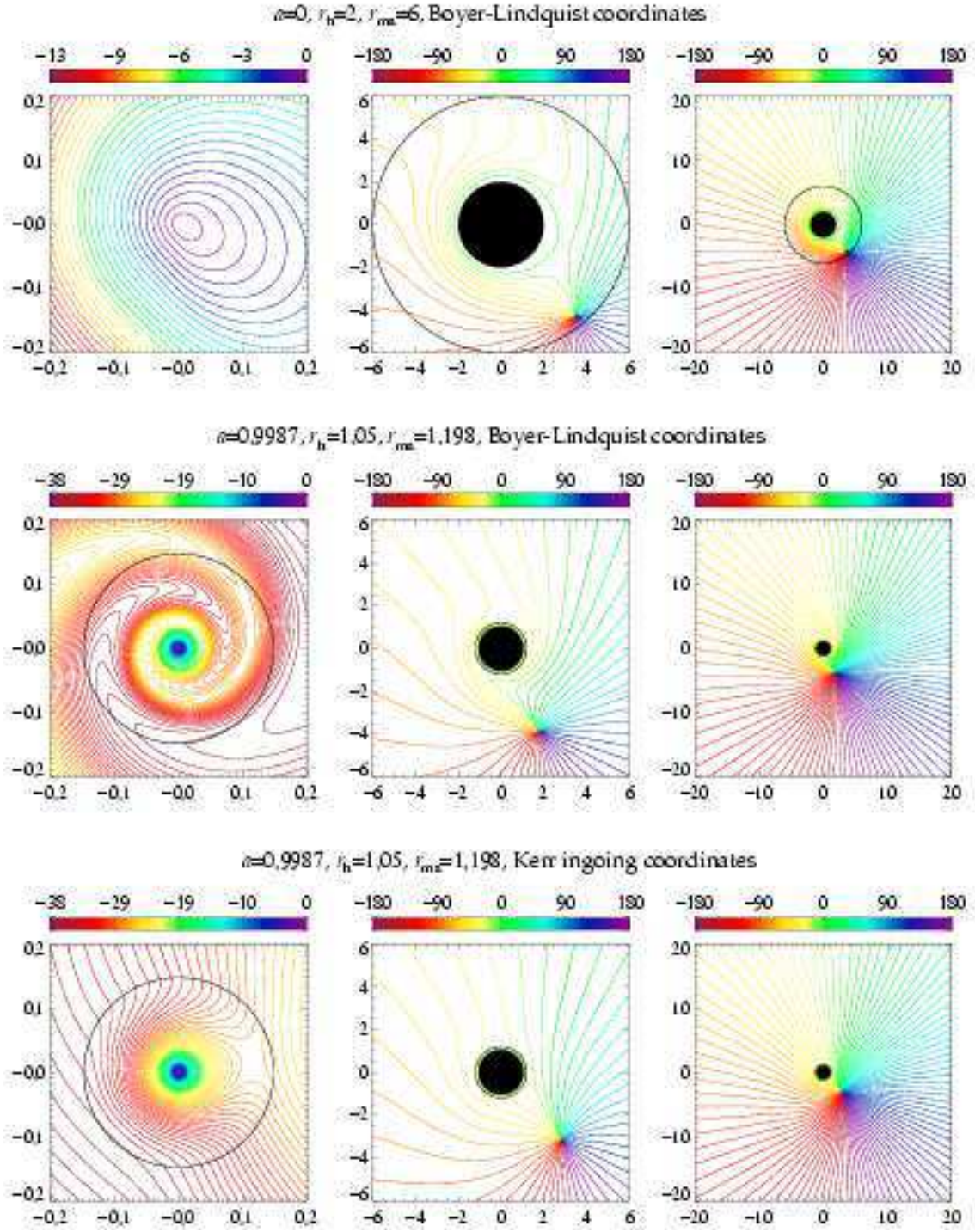


Figure D.17: Azimuthal emission angle for the inclination  $\theta_o = 45^\circ$ .

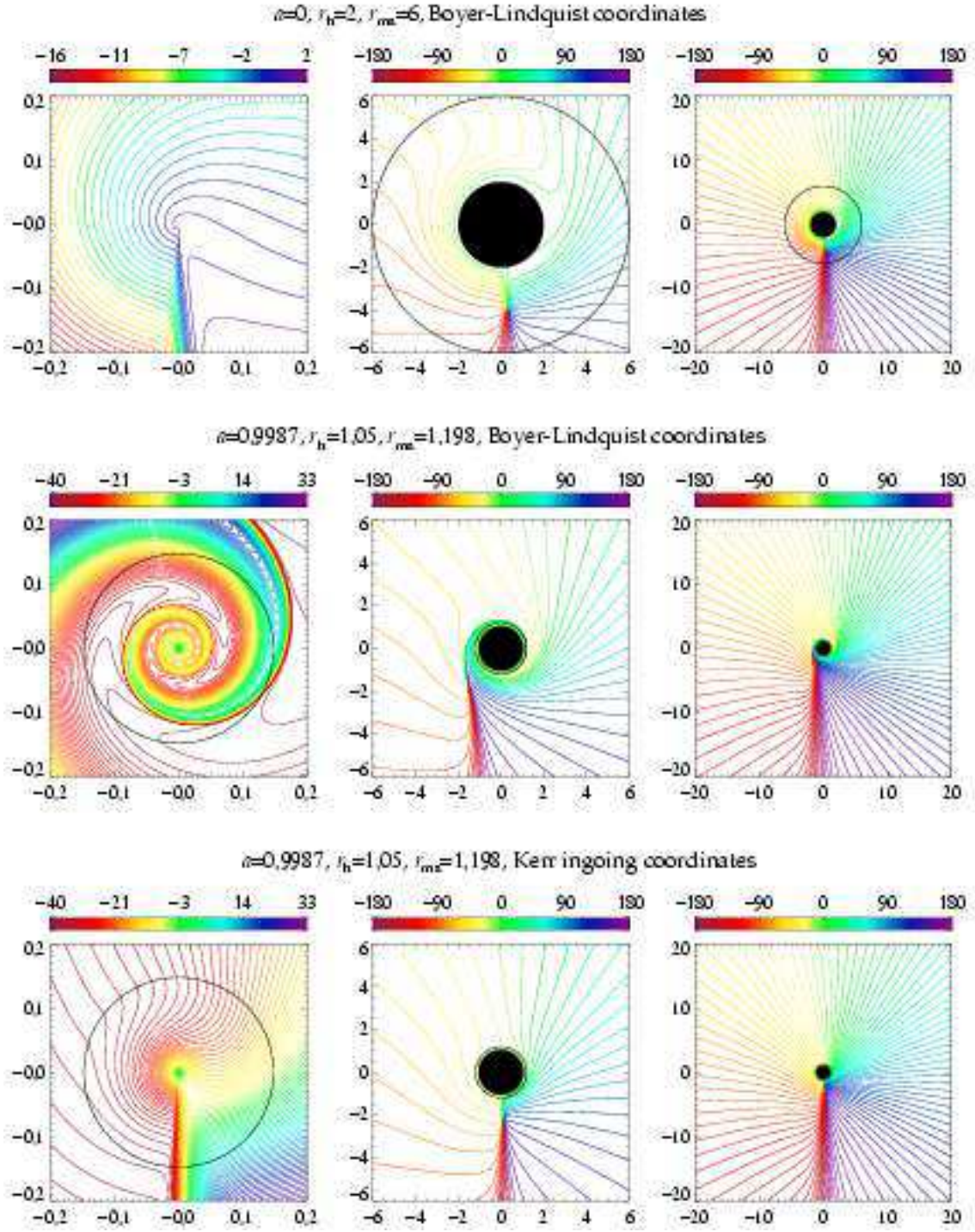


Figure D.18: Azimuthal emission angle for the inclination  $\theta_o = 85^\circ$ .

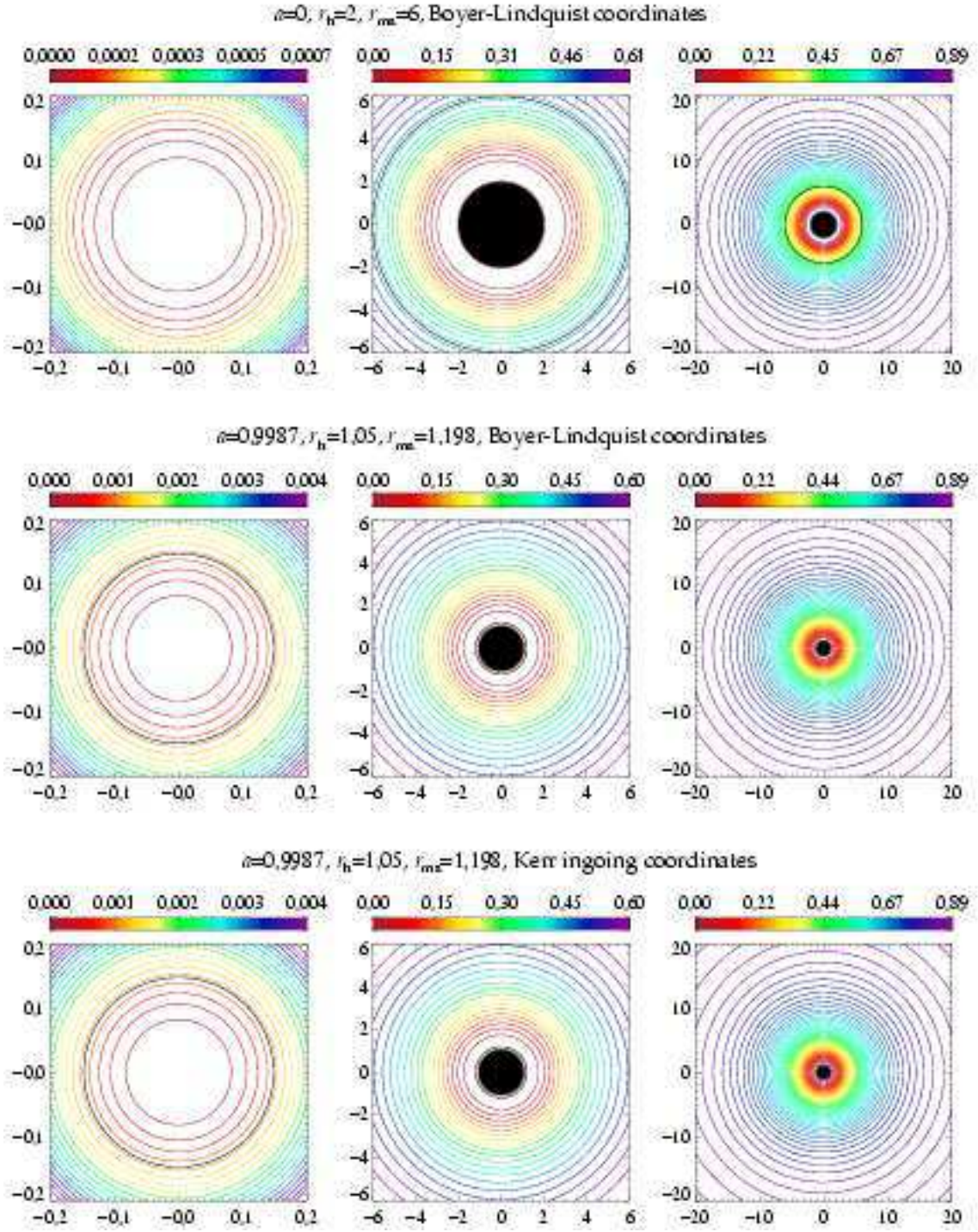
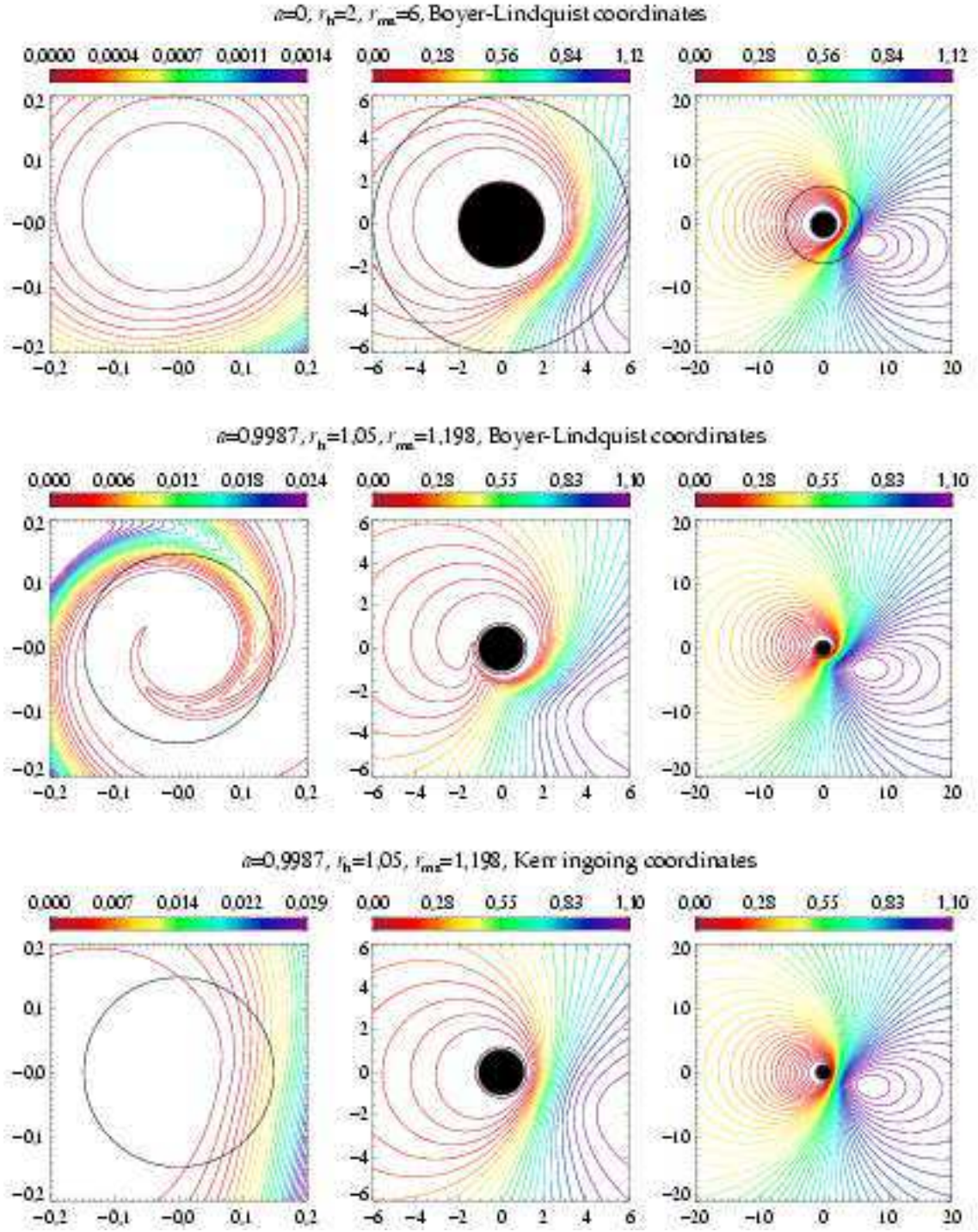


Figure D.19: Overall transfer function for the inclination  $\theta_o = 0.1^\circ$ .

Figure D.20: Overall transfer function for the inclination  $\theta_o = 45^\circ$ .

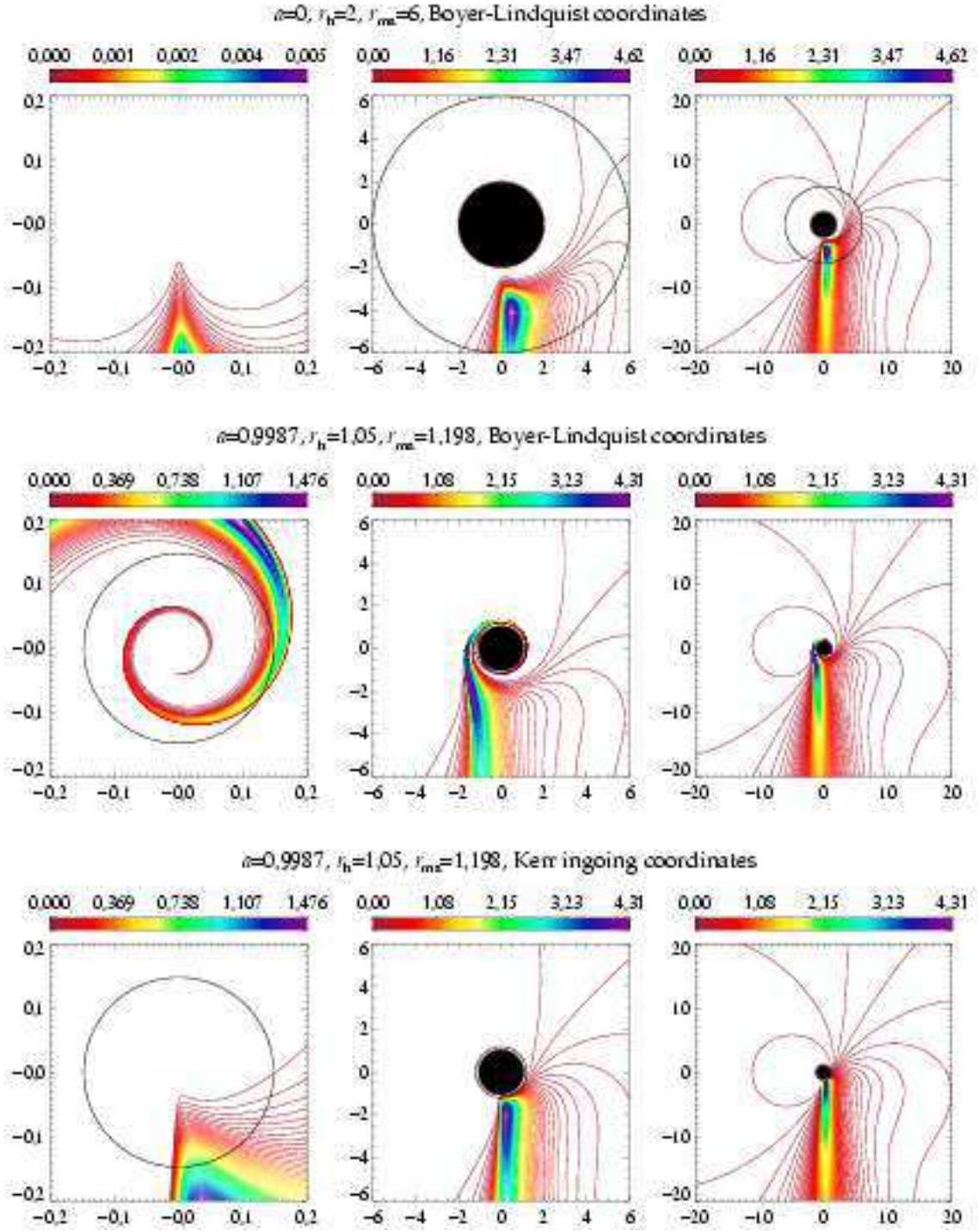


Figure D.21: Overall transfer function for the inclination  $\theta_o = 85^\circ$ .

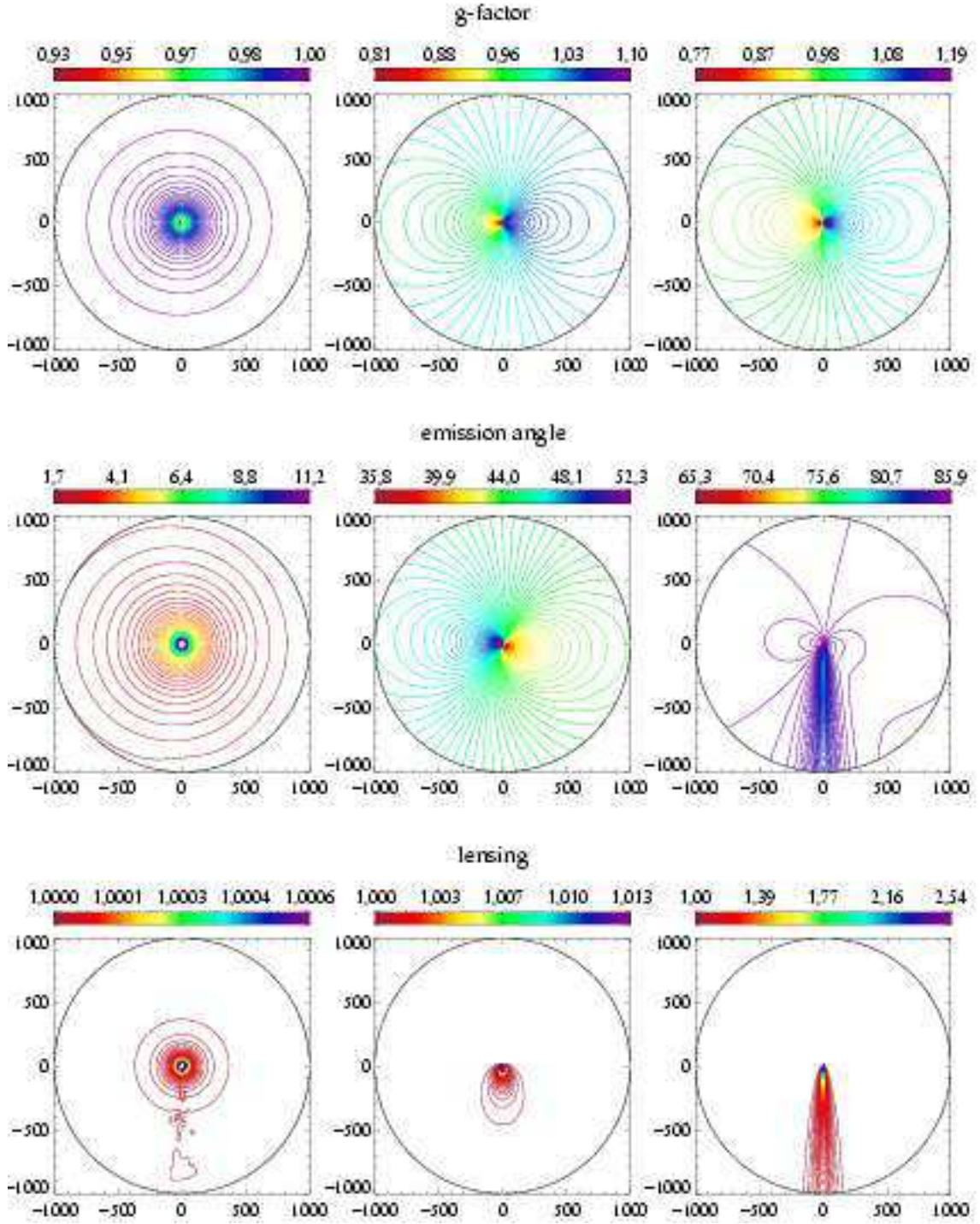


Figure D.22:  $g$ -factor, emission angle and lensing for the inclinations  $\theta_o = 0.1^\circ, 45^\circ$  and  $85^\circ$  (from left to right). The strange features in the graph for lensing with the observer inclination  $0.1^\circ$  are due to numerical errors which arise when integrating geodesics passing close to the axis in spherical coordinates. Notice, though, that the errors are not significantly large.

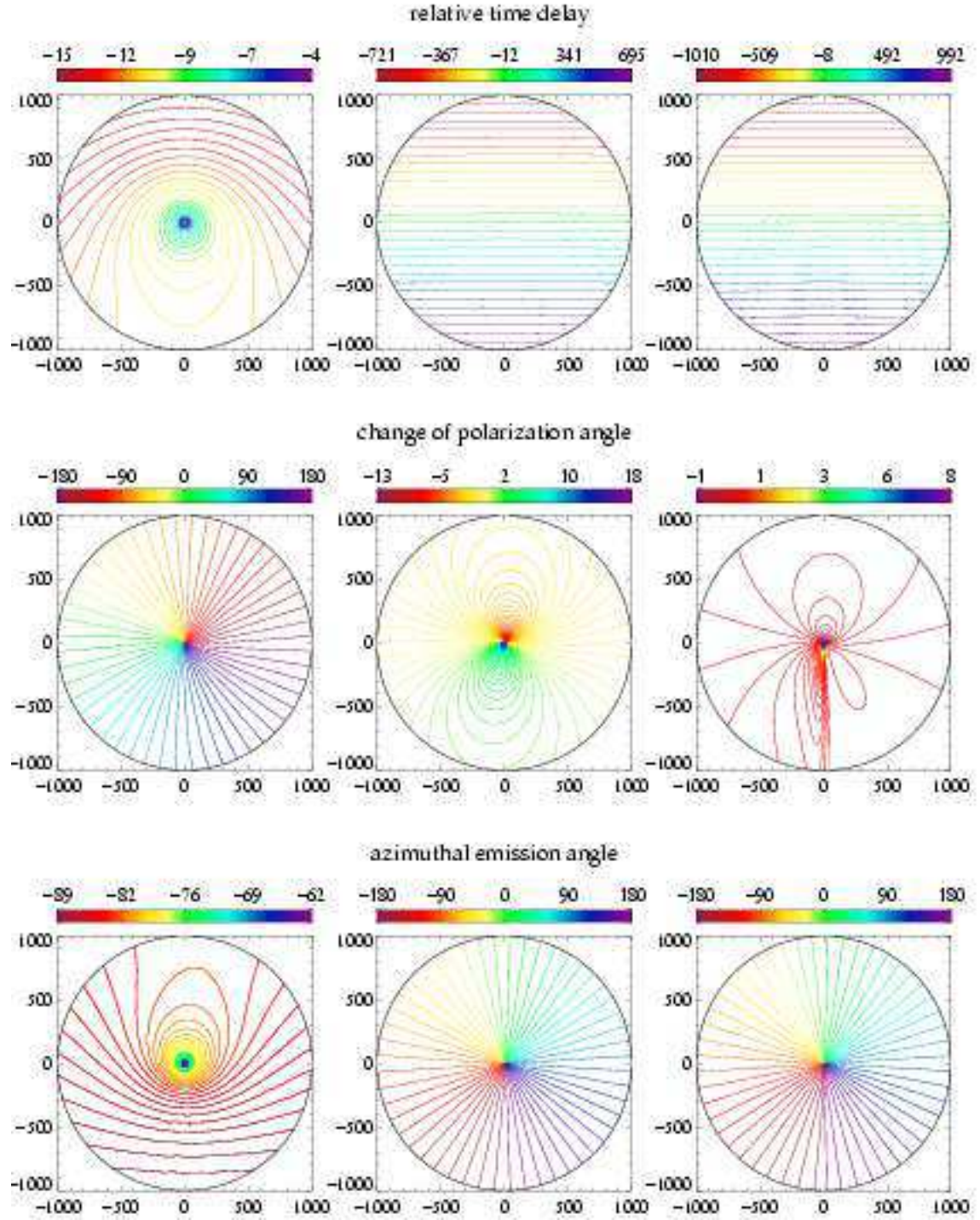


Figure D.23: Relative time delay, change of the polarization angle and azimuthal emission angle for the inclinations  $\theta_o = 0.1^\circ$ ,  $45^\circ$  and  $85^\circ$  (from left to right).

# Bibliography

- Abramowicz M. A., Bao G., Lanza A. & Zhang X.-H. (1991). X-ray variability power spectra of active galactic nuclei. *A&A*, **245**, 454. ADS. [7]
- Abramowicz M. A., Beloborodov A. M., Chen X.-M. & Igumenshchev I. V. (1996). Special relativity and the pseudo-Newtonian potential. *A&A*, **313**, 334. ADS. [59]
- Agol E. (1997). The effects of magnetic fields, absorption, and relativity on the polarization of accretion disks around supermassive black holes. *Ph.D. Thesis*. ADS. [7, 62]
- Arnaud K. A. (1996). XSPEC: The first ten years. In *Astronomical data analysis software and systems V*, volume 101, page 17. Jacoby G. & Barnes J., ASP Conf. Series. ADS. [16, 44, 45]
- Artemova I. V., Björnsson G. & Novikov I. D. (1996). Modified Newtonian potentials for the description of relativistic effects in accretion disks around black holes. *ApJ*, **461**, 565. ADS. [59]
- Asaoka I. (1989). X-ray spectra at infinity from a relativistic accretion disk around a Kerr black hole. *PASJ*, **41**, 763. ADS. [7]
- Ballantyne D. R., Ross R. R. & Fabian A. C. (2001). X-ray reflection by photoionized accretion discs. *MNRAS*, **327**, 10. ADS. [52]
- Ballantyne D. R., Vaughan S. & Fabian A. C. (2003). A two-component ionized reflection model of MCG-6-30-15. *MNRAS*, **342**, 239. ADS. [52]
- Bao G., Hadrava P. & Østgaard E. (1994). Emission-line profiles from a relativistic accretion disk and the role of its multiple images. *ApJ*, **435**, 55. ADS. [7]
- Bao G., Hadrava P., Wiita P. & Xiong Y. (1997). Polarization variability of active galactic nuclei and X-ray binaries. *ApJ*, **487**, 142. ADS. [7, 16]
- Bao G., Wiita P. J. & Hadrava P. (1996). Energy-dependent polarization variability as a black hole signature. *Phys. Rev. Lett.*, **77**, 12. ADS. [62]
- Bardeen J. M. (1973). Rapidly rotating stars, disks, and black holes. In *Black holes*, page 241. C. de Witt and B. S. de Witt, Gordon & Breach, New York. [3]
- Bardeen J. M., Press W. H. & Teukolsky S. A. (1972). Rotating black holes: locally nonrotating frames, energy extraction, and scalar synchrotron radiation. *ApJ*, **178**, 347. ADS. [54]
- Beckwith K. & Done C. (2004). Iron line profiles in strong gravity. *MNRAS*. In press. [astro-ph/0402199]. [7, 44, 45]
- Bianchi S., Matt G., Balestra I., Guainazzi M. & Perola G. C. (2004). X-ray reprocessing in Seyfert galaxies: simultaneous XMM-Newton/BeppoSAX observations. *A&A*. Submitted. [astro-ph/0404308]. [62]
- Bičák J., Semerák O. & Hadrava P. (1993). Collimation effects of the Kerr field. *MNRAS*, **263**, 545. ADS. [3]

- Blandford R. D. & Znajek R. L. (1977). Electromagnetic extraction of energy from Kerr black holes. *MNRAS*, **179**, 433. ADS. [2]
- Boller T., Keil R., Trümper J., O'Brien P. T., Reeves J. & Page M. (2001). Detection of an X-ray periodicity in the narrow-line Seyfert 1 galaxy Mrk 766 with XMM-Newton. *A&A*, **365**, L146. ADS. [53]
- Bondi H. & Hoyle F. (1944). On the mechanism of accretion by stars. *MNRAS*, **104**, 273. ADS. [3]
- Bowyer S., Byram E. T., Chubb T. A. & Friedman H. (1965). Cosmic X-ray sources. *Science*, **147**, 394. ADS. [4]
- Bromley B. C., Chen K. & Miller W. A. (1997). Line emission from an accretion disk around a rotating black hole: toward a measurement of frame dragging. *ApJ*, **475**, 57. ADS. [7]
- Čadež A., Calvani M. & Fanton C. (2003). X-ray iron line profiles from warped accretion discs. *Memorie della Societa Astronomica Italiana*, **74**, 446. ADS. [7]
- Carter B. (1968). Global structure of the Kerr family of gravitational fields. *Phys. Rev.*, **174**, 1559. ADS. [8, 22, 70]
- Chandrasekhar S. (1931). The maximum mass of ideal white dwarfs. *ApJ*, **74**, 81. ADS. [2]
- Chandrasekhar S. (1960). *Radiative transfer*. Dover publications, New York. ADS. [21, 36, 63]
- Chandrasekhar S. (1983). *The mathematical theory of black holes*. Clarendon Press/Oxford University Press (International Series of Monographs on Physics. Volume 69), p. 663. ADS. [3]
- Chen K. & Eardley D. M. (1991). Polarization properties of emission lines from relativistic accretion disks. *ApJ*, **382**, 125. ADS. [7]
- Connors P. A., Piran T. & Stark R. F. (1980). Polarization features of X-ray radiation emitted near black holes. *ApJ*, **235**, 224. ADS. [7, 13, 16, 62]
- Connors P. A. & Stark R. F. (1977). Observable gravitational effects on polarised radiation coming from near a black hole. *Nature*, **269**, 128. ADS. [13]
- Costa E., Soffitta P., Bellazzini R., Brez A., Lumb N. & Spandre G. (2001). An efficient photoelectric X-ray polarimeter for the study of black holes and neutron stars. *Nature*, **411**, 662. ADS. [62, 67]
- Cunningham C. T. (1975). The effects of redshifts and focusing on the spectrum of an accretion disk around a Kerr black hole. *ApJ*, **202**, 788. ADS. [6, 8]
- Cunningham C. T. (1976). Returning radiation in accretion disks around black holes. *ApJ*, **208**, 534. ADS. [6]
- Curtis H. D. (1918). *Publications of Lick Observatory*, **13**, 11. ADS. [3]
- Czerny B., Róžańska A., Dovčiak M., Karas V. & Dumont A.-M. (2004). The structure and radiation spectra of illuminated accretion disks in AGN. II. Flare/spot model of X-ray variability. *A&A*, **420**, 1. ADS. [5, 45, 61]
- Dabrowski Y., Fabian A. C., Iwasawa K., Lasenby A. N. & Reynolds C. S. (1997). The profile and equivalent width of the X-ray iron emission line from a disc around a Kerr black hole. *MNRAS*, **288**, L11. ADS. [50]
- Damour T. (1980). Mechanical, electrodynamical and thermodynamical properties of black holes. In *Gravitational Radiation, Collapsed Objects, and Exact Solutions*, page 454.

- ADS. [2]
- Damour T., Ruffini R., Hani R. S. & Wilson J. R. (1978). Regions of magnetic support of a plasma around a black hole. *Phys. Rev. D*, **17**, 1518. ADS. [2]
- Dovčiak M., Bianchi S., Guainazzi M., Karas V. & Matt G. (2004a). Relativistic spectral features from X-ray-illuminated spots and the measure of the black hole mass in active galactic nuclei. *MNRAS*, **350**, 745. ADS. [5, 62]
- Dovčiak M., Karas V., Martocchia A., Matt G. & Yaqoob T. (2004b). XSPEC model to explore spectral features from black hole sources. In *Proc. of the workshop on processes in the vicinity of black holes and neutron stars*. S. Hledík & Z. Stuchlík, Opava. In press. ADS. [5, 16]
- Dovčiak M., Karas V. & Matt G. (2004). Polarization signatures of strong gravity in AGN accretion discs. *MNRAS*. In press. ADS. [5]
- Dovčiak M., Karas V. & Yaqoob T. (2004). An extended scheme for fitting X-ray data with accretion disk spectra in the strong gravity regime. *ApJS*, **153**, 205. ADS. [5, 37]
- Einstein A. (1916). Die Grundlage der allgemeinen Relativitätstheorie. *Ann. Phys. (Leipzig)*, **49**, 769. [2]
- Fabian A. C., Iwasawa K., Reynolds C. S. & Young A. J. (2000). Broad iron lines in active galactic nuclei. *PASP*, **112**, 1145. ADS. [15, 54, 62]
- Fabian A. C., Rees M. J., Stella L. & White N. E. (1989). X-ray fluorescence from the inner disc in Cygnus X-1. *MNRAS*, **238**, 729. ADS. [7, 16]
- Fabian A. C. & Vaughan S. (2003). The iron line in MCG-6-30-15 from XMM-Newton: evidence for gravitational light bending? *MNRAS*, **340**, L28. ADS. [47]
- Fabian A. C., Vaughan S., Nandra K., Iwasawa K., Ballantyne D. R., Lee J. C., de Rosa A., Turner A. & Young A. J. (2002). A long hard look at MCG-6-30-15 with XMM-Newton. *MNRAS*, **335**, L1. ADS. [47, 48, 50, 52, 53, 62]
- de Felice F., Nobili L. & Calvani M. (1974). Blackhole physics. *A&A*, **30**, 111. ADS. [6]
- Fishbone L. G. & Moncrief V. (1976). Relativistic fluid disks in orbit around Kerr black holes. *ApJ*, **207**, 962. ADS. [3]
- Frank J., King A. & Raine D. J. (2002). *Accretion Power in Astrophysics: Third Edition*. Cambridge University Press. ADS. [3]
- George I. M. & Fabian A. C. (1991). X-ray reflection from cold matter in active galactic nuclei and X-ray binaries. *MNRAS*, **249**, 352. ADS. [45, 82]
- Gerbal D. & Pelat D. (1981). Profile of a line emitted by an accretion disk – influence of the geometry upon its shape parameters. *A&A*, **95**, 18. ADS. [7]
- Ghisellini G., Haardt F. & Matt G. (1994). The contribution of the obscuring torus to the X-ray spectrum of Seyfert galaxies – a test for the unification model. *MNRAS*, **267**, 743. ADS. [28]
- Giacconi R., Gursky H., Paolini F. R. & Rossi B. B. (1962). Evidence for X-rays from sources outside the Solar system. *Phys. Rev. Lett.*, **9**, 439. ADS. [4]
- Gierliński M., Maciolek-Niedźwiecki A. & Ebisawa K. (2001). Application of a relativistic accretion disc model to X-ray spectra of LMC X-1 and GRO J1655-40. *MNRAS*, **325**, 1253. ADS. [44]
- Goyder R. & Lasenby A. N. (2004). Inferring the coronal flaring patterns in AGN from reverberation maps. *MNRAS*. In press. [astro-ph/0309518]. [16]
- Guainazzi M. (2003). The history of the iron K $\alpha$  line profile in the Piccinotti AGN ESO

- 198-G24. *A&A*, **401**, 903. ADS. [8, 53]
- Guainazzi M., Matt G., Molendi S., Orr A., Fiore F., Grandi P., Matteuzzi A., Mineo T., Perola G. C., Parmar A. N. & Piro L. (1999). BeppoSAX confirms extreme relativistic effects in the X-ray spectrum of MCG-6-30-15. *A&A*, **341**, L27. ADS. [47]
- Haardt F. (1993). Anisotropic Comptonization in thermal plasmas – spectral distribution in plane-parallel geometry. *ApJ*, **413**, 680. ADS. [28]
- Haardt F. & Maraschi L. (1993). X-ray spectra from two-phase accretion disks. *ApJ*, **413**, 507. ADS. [3]
- Haardt F., Maraschi L. & Ghisellini G. (1994). A model for the X-ray and ultraviolet emission from Seyfert galaxies and galactic black holes. *ApJ*, **432**, L95. ADS. [61]
- Hameury J.-M., Marck J.-A. & Pelat D. (1994).  $e^+ - e^-$  annihilation lines from accretion discs around Kerr black holes. *A&A*, **287**, 795. ADS. [7]
- Hanisch R. J., Farris A., Greisen E. W., Pence W. D., Schlesinger B. M., Teuben P. J., Thompson R. W. & Warnock A. (2001). Definition of the flexible image transport system (FITS). *A&A*, **376**, 359. ADS. [7]
- Hawking S. W. (1971). Gravitationally collapsed objects of very low mass. *MNRAS*, **152**, 75. ADS. [3]
- Hawking S. W. (1975a). Particle creation by black holes. *Commun. Math. Phys.*, **43**, 199. See also in Hawking (1975b). [3]
- Hawking S. W. (1975b). Particle creation by black holes. In *Quantum gravity; Proceedings of the Oxford Symposium, Harwell, Berks., England, February 15, 16, 1974*, page 219. Oxford, Clarendon Press. ADS. [115]
- Hawking S. W. & Ellis G. F. R. (1973). *The large scale structure of space-time*. Cambridge Monographs on Mathematical Physics, London: Cambridge University Press. ADS. [116]
- Hawley J. F., Gammie C. F. & Balbus S. A. (1995). Local three-dimensional magnetohydrodynamic simulations of accretion disks. *ApJ*, **440**, 742. ADS. [3]
- Iwasawa K., Fabian A. C., Brandt W. N., Kunieda H., Misaki K., Terashima Y. & Reynolds C. S. (1998). Detection of an X-ray periodicity in the Seyfert galaxy IRAS 18325-5926. *MNRAS*, **295**, L20. ADS. [53]
- Iwasawa K., Fabian A. C., Reynolds C. S., Nandra K., Otani C., Inoue H., Hayashida K., Brandt W. N., Dotani T., Kunieda H., Matsuoka M. & Tanaka Y. (1996). The variable iron K emission line in MCG-6-30-15. *MNRAS*, **282**, 1038. ADS. [15, 47]
- Karas V. (1996). Light curve of a source orbiting a black hole: a fitting formula. *ApJ*, **470**, 743. ADS. [60]
- Karas V., Huré J.-M. & Semerák O. (2004). Topical review: gravitating discs around black holes. *Classical and Quantum Gravity*, **21**, 1. ADS. [3]
- Karas V., Lanza A. & Vokrouhlický D. (1995). Emission-line profiles from self-gravitating thin disks. *ApJ*, **440**, 108. ADS. [3, 7]
- Karas V. & Vokrouhlický D. (1991). Dynamics of charged particles near a black hole in a magnetic field. *Journal de Physique I*, **1**, 1005. ADS. [2]
- Karas V., Vokrouhlický D. & Polnarev A. G. (1992). In the vicinity of a rotating black hole – a fast numerical code for computing observational effects. *MNRAS*, **259**, 569. ADS. [7]
- Kato S., Fukue J. & Mineshige S. (1998). *Black-hole accretion disks*. Kyoto, Japan: Kyoto

- University Press. ADS. [3]
- Kerr R. P. (1963). Gravitational field of a spinning mass as an example of algebraically special metrics. *Phys. Rev. Lett.*, **11**, 237. ADS. [2]
- Kojima Y. (1991). The effects of black hole rotation on line profiles from accretion discs. *MNRAS*, **250**, 629. ADS. [7, 30]
- Kormendy J. & Richstone D. (1995). Inward bound – the search for supermassive black holes in galactic nuclei. *ARA&A*, **33**, 581. ADS. [2]
- Krolik J. & Hawley J. F. (2002). Where is the inner edge of an accretion disk around a black hole? *ApJ*, **573**, 754. ADS. [15]
- Laor A. (1991). Line profiles from a disc around a rotating black hole. *ApJ*, **376**, 90. ADS. [7, 16, 24, 28, 30, 44]
- Laor A., Netzer H. & Piran T. (1990). Massive thin accretion discs. II. Polarization. *MNRAS*, **242**, 560. ADS. [7, 28]
- Laplace P. S. (1796). *Le Système du Monde Vol. II. Des Mouvements Réels des Corps Célestes* (Paris: Duprat). [2]
- Laplace P. S. (1799). Beweis des Satzes, dass die anziehende Kraft bey einem Weltkörper so gross seyn könne, dass das Licht davon nicht ausströmen kann. *Allgemeine Geographische Ephemeriden* (Weimar), 4(1). Engl. trans. in Hawking & Ellis (1973) or Stephani (2003). [2]
- Lee J. C., Fabian A. C., Reynolds C. S., Brandt W. N. & Iwasawa K. (2000). The X-ray variability of the Seyfert 1 galaxy MCG–6-30-15 from long ASCA and RXTE observations. *MNRAS*, **318**, 857. ADS. [53]
- Lee J. C., Ogle P. M., Canizares C. R., Marshall H. L., Schulz N. S., Morales R., Fabian A. C. & Iwasawa K. (2001). Revealing the dusty warm absorber in MCG–6-30-15 with the Chandra high-energy transmission grating. *ApJ*, **554**, L13. ADS. [15]
- Lynden-Bell D. (1969). Galactic nuclei as collapsed old quasars. *Nature*, **223**, 690. ADS. [3]
- Madejski G. M., Done C., Turner T. J., Mushotzky R. F., Serlemitsos P., Fiore F., Sikora M. & Begelman M. C. (1993). Solving the mystery of the X-ray periodicity in the Seyfert galaxy NGC 6814. *Nature*, **365**, 626. ADS. [53]
- Magdziarz P. & Zdziarski A. A. (1995). Angle-dependent Compton reflection of X-rays and gamma-rays. *MNRAS*, **273**, 837. ADS. [45]
- Martocchia A., Karas V. & Matt G. (2000). Effects of Kerr space-time on spectral features from X-ray illuminated accretion discs. *MNRAS*, **312**, 817. ADS. [7, 16, 24, 44, 46, 50]
- Martocchia A. & Matt G. (1996). Iron  $K\alpha$  line intensity from accretion discs around rotating black holes. *MNRAS*, **282**, L53. ADS. [62]
- Martocchia A., Matt G. & Karas V. (2002). On the origin of the broad, relativistic iron line of MCG–6-30-15 observed by XMM-Newton. *A&A*, **383**, L23. ADS. [15]
- Martocchia A., Matt G., Karas V., Belloni T. & Feroci M. (2002). Evidence for a relativistic iron line in GRS 1915+105. *A&A*, **387**, 215. ADS. [15]
- Mason K. O., Branduardi-Raymont G., Ogle P. M., Page M. J., Puchnarewicz E. M., Behar E., Córdova F. A., Davis S., Maraschi L., McHardy I. M., O’Brien P. T., Friedhorsky W. C. & Sasseen T. P. (2003). The X-ray spectrum of the Seyfert I galaxy Markarian 766: dusty warm absorber or relativistic emission lines? *ApJ*, **582**, 95. ADS. [15]

- Matt G. (1993). X-ray polarization properties of a centrally illuminated accretion disc. *MNRAS*, **260**, 663. ADS. [7, 63]
- Matt G., Fabian A. C. & Ross R. R. (1993). X-ray photoionized accretion discs – ultraviolet and X-ray continuum spectra and polarization. *MNRAS*, **264**, 839. ADS. [7, 16]
- Matt G. & Perola G. C. (1992). The iron  $K\alpha$  response in an X-ray illuminated relativistic disc and a black hole mass estimate. *MNRAS*, **259**, 433. ADS. [53]
- Matt G., Perola G. C. & Piro L. (1991). The iron line and high energy bump as X-ray signatures of cold matter in Seyfert 1 galaxies. *A&A*, **247**, 25. ADS. [33, 34, 63, 82, 83]
- Matt G., Perola G. C., Piro L. & Stella L. (1992). Iron  $K\alpha$  line from X-ray illuminated relativistic discs. *A&A*, **257**, 63. Ibid. (1992), **263**, 453. ADS. [24, 60]
- Matt G., Perola G. C. & Stella L. (1993). Multiple-peaked line profiles from relativistic disks at high inclination angles. *A&A*, **267**, 643. ADS. [60]
- Matthews T. A., Bolton J. G., Greenstein J. L., Münch G. & Sandage A. R. (1960). 107th Meeting Amer. Astr. Soc., Dec. 31, 1960 (unpublished). **21**, 148. See *Sky and Tel.* (1961). [4]
- Matthews T. A. & Sandage A. (1962). 3C 196 as a second radio star. *PASP*, **74**, 406. ADS. [4]
- McClintock J. E. & Remillard R. A. (2003). Black hole binaries. In *Compact stellar X-ray sources*. W. H. G. Lewin & M. van der Klis, Cambridge University Press. [astro-ph/0306213]. [15]
- Merloni A. & Fabian A. C. (2001). Thunderclouds and accretion discs: a model for the spectral and temporal variability of Seyfert 1 galaxies. *MNRAS*, **328**, 958. ADS. [61]
- Michell J. (1784). On the means of discovering the distance, magnitude, etc. of the fixed stars, in consequence of the Diminution of the Velocity of their Light, in case such a Diminution should be found to take place in any of them, and such other Data should be procured from Observations, as would be farther necessary for that Purpose. *Philosophical Transactions of the Royal Society of London*, **74**, 35. [2]
- Miller J. M., Fabian A. C., Wijnands R., Remillard R. A., Wojdowski P., Schulz N. S., Di Matteo T., Marshall H. L., Canizares C. R., Pooley D. & Lewin W. H. G. (2002). Resolving the composite Fe  $K\alpha$  emission line in the Galactic black hole Cygnus X-1 with Chandra. *ApJ*, **578**, 348. ADS. [15]
- Miller J. M., Fabian A. C., in't Zand J. J. M., Reynolds C. S., Wijnands R., Nowak M. A. & Lewin W. H. G. (2002). A relativistic Fe  $K\alpha$  emission line in the intermediate-luminosity *BeppoSAX* spectrum of the Galactic microquasar V4641 Sgr. *ApJ*, **577**, L15. ADS. [15]
- Miniutti G., Fabian A. C., Goyder R. & Lasenby A. N. (2003). The lack of variability of the iron line in MCG-6-30-15: general relativistic effects. *MNRAS*, **344**, L22. ADS. [53, 62, 67]
- Miniutti G., Fabian A. C. & Miller J. M. (2004). The relativistic Fe emission line in XTE J1650-500 with *BeppoSAX*: evidence for black hole spin and light-bending effects? *MNRAS*, **351**, 466. ADS. [15]
- Misner C. W., Thorne K. S. & Wheeler J. A. (1973). *Gravitation*. W. H. Freeman & Co., San Fransisco. ADS. [8, 22, 54, 70]
- Nandra K., George I. M., Mushotzky R. F., Turner T. J. & Yaqoob T. (1997). ASCA

- observations of Seyfert 1 galaxies. II. Relativistic iron  $K\alpha$  emission. *ApJ*, **477**, 602. ADS. [47]
- Nayakshin S. & Kazanas D. (2002). On time-dependent X-ray reflection by photoionized accretion disks: implications for Fe  $K\alpha$  line reverberation studies of active galactic nuclei. *ApJ*, **567**, 85. ADS. [52]
- Newman E. T., Couch R., Chinnapared K., Exton A., Prakash A. & Torrence R. (1965). Metric of a rotating, charged mass. *J. Math. Phys.*, **6**, 918. [2]
- Nishikawa K.-I., Koide S., Shibata K., Kudoh T., Sol H. & Hughes J. P. (2001). 3-D general relativistic MHD simulations of generating jets. *Bulletin of the American Astronomical Society*, **33**, 1498. ADS. [3]
- Nordström G. (1918). On the energy of the gravitational field in Einstein's theory. *Proc. Kon. Ned. Akad. Wet.*, **20**, 1238. [2]
- Novikov I. D. & Thorne K. S. (1973). Astrophysics of black holes. In *Black holes*, page 343. C. de Witt and B. S. de Witt, Gordon & Breach, New York. [3, 71]
- Ogura J., Ohuo N. & Kojima Y. (2000). Profiles and polarization properties of emission lines from relativistic disks. *PASJ*, **52**, 841. ADS. [7]
- Oppenheimer J. R. & Volkoff G. M. (1939). On massive neutron cores. *Phys. Rev.*, **55**, 374. ADS. [2]
- Ostriker J. (1964). The equilibrium of self-gravitating rings. *ApJ*, **140**, 1067. ADS. [3]
- Paczynski B. (1978a). A model of self-gravitating accretion disk. *Acta Astronomica*, **28**, 91. ADS. [3]
- Paczynski B. (1978b). A model of self-gravitating accretion disk with a hot corona. *Acta Astronomica*, **28**, 241. ADS. [3]
- Pariev V. I. & Bromley B. C. (1998). Line emission from an accretion disk around a black hole: effects of disk structure. *ApJ*, **508**, 590. ADS. [44]
- Pariev V. I., Bromley B. C. & Miller W. A. (2001). Estimation of relativistic accretion disk parameters from iron line emission. *ApJ*, **547**, 649. ADS. [8]
- Penrose R. & Floyd G. R. (1971). Black holes – extraction of rotational energy. *Nature Physical Science*, **229**, 177. ADS. [2]
- Petrucci P. O. & Henri G. (1997). Anisotropic illumination of AGN's accretion disk by a non thermal source. II. General relativistic effects. *A&A*, **326**, 99. ADS. [62]
- Phillips K. C. & Mészáros P. (1986). Polarization and beaming of accretion disc radiation. *ApJ*, **310**, 284. ADS. [28]
- Poutanen J. & Fabian A. C. (1999). Spectral evolution of magnetic flares and time lags in accreting black hole sources. *MNRAS*, **306**, L31. ADS. [61]
- Pozdnyakov L. A., Sobol' I. M. & Sunyaev R. A. (1979). The profile evolution of X-ray spectral lines due to Comptonization – Monte Carlo computations. *A&A*, **75**, 214. ADS. [62]
- Price R. H. & Thorne K. S. (1986). Membrane viewpoint on black holes: properties and evolution of the stretched horizon. *Phys. Rev. D*, **33**, 915. ADS. [2]
- Pringle J. E. & Rees M. J. (1972). Accretion disc models for compact X-ray sources. *A&A*, **21**, 1. ADS. [3]
- Rauch K. P. & Blandford R. D. (1994). Optical caustics in a Kerr space-time and the origin of rapid X-ray variability in active galactic nuclei. *ApJ*, **421**, 46. ADS. [7]

- Rees M. J. (1975). Expected polarization properties of binary X-ray sources. *MNRAS*, **171**, 457. ADS. [62]
- Reissner H. (1916). Über die Eigengravitation des elektrischen Feldes nach Einsteinschen Theorie. *Ann. Phys. (Leipzig)*, **59**, 106. [2]
- Reynolds C. S. & Begelman M. C. (1997). Iron fluorescence from within the innermost stable orbit of black hole accretion disks. *ApJ*, **488**, 109. ADS. [15]
- Reynolds C. S. & Nowak M. A. (2003). Fluorescent iron lines as a probe of astrophysical black hole systems. *Phys. Rep.*, **377**, 389. ADS. [15, 54, 62]
- Reynolds C. S., Young A. J., Begelman M. C. & Fabian A. C. (1999). X-ray iron line reverberation from black hole accretion disks. *ApJ*, **514**, 164. ADS. [16]
- Rhoades C. E. & Ruffini R. (1974). Maximum mass of a neutron star. *Phys. Rev. Lett.*, **32**, 324. ADS. [2]
- Róžańska A., Dumont A.-M., Czerny B. & Collin S. (2002). The structure and radiation spectra of illuminated accretion discs in active galactic nuclei. I. Moderate illumination. *MNRAS*, **332**, 799. ADS. [52]
- Ruszkowski M. (2000). X-ray iron line variability for the model of an orbiting flare above a black hole accretion disc. *MNRAS*, **315**, 1. ADS. [16]
- Salpeter E. E. (1964). Accretion of interstellar matter by massive objects. *ApJ*, **140**, 796. ADS. [4]
- Schmidt M. (1963). 3C 273: a star-like object with large red-shift. *Nature*, **197**, 1040. ADS. [4]
- Schneider P., Ehlers J. & Falco E. E. (1992). *Gravitational lenses*. Springer-Verlag Berlin Heidelberg New York. ADS. [11, 19]
- Schnittman J. D. & Bertschinger E. (2004). The harmonic structure of high-frequency quasi-periodic oscillations in accreting black holes. *ApJ*, **606**, 1098. ADS. [7, 44]
- Schwarzschild K. (1916). From the observatory. *PASP*, **28**, 269. ADS. [2]
- Semerák O. & Karas V. (1999). Pseudo-Newtonian models of a rotating black hole field. *A&A*, **343**, 325. ADS. [59]
- Seyfert C. K. (1943). Nuclear emission in spiral nebulae. *ApJ*, **97**, 28. ADS. [3]
- Shakura N. I. & Sunyaev R. A. (1973). Black holes in binary systems. Observational appearance. *A&A*, **24**, 337. ADS. [3]
- Shapiro S. L., Lightman A. P. & Eardley D. M. (1976). A two-temperature accretion disk model for Cygnus X-1 – structure and spectrum. *ApJ*, **204**, 187. ADS. [3]
- Sharp N. A. (1979). Geodesics in black hole space-times. *General Relativity and Gravitation*, **10**, 659. ADS. [3]
- Speith R., Riffert H. & Ruder H. (1995). The photon transfer function for accretion disks around a Kerr black hole. *Computer Physics Communications*, **88**, 109. ADS. [7]
- Stella L. (1990). Measuring black hole mass through variable line profiles from accretion disks. *Nature*, **344**, 747. ADS. [16, 53]
- Stephani H. (2003). Laplace, Weimar, Schiller and the birth of black hole theory. *ArXiv General Relativity and Quantum Cosmology e-prints*. [gr-qc/0304087]. [116]
- Sunyaev R. A. & Titarchuk L. G. (1985). Comptonization of low-frequency radiation in accretion disks. Angular distribution and polarization of hard radiation. *A&A*, **143**, 374. ADS. [63]

- Tanaka Y., Nandra K., Fabian A. C., Inoue H., Otani C., Dotani T., Hayashida K., Iwasawa K., Kii T., Kunieda H., Makino F. & Matsuoka M. (1995). Gravitationally redshifted emission implying an accretion disk and massive black hole in the active galaxy MCG–6-30-15. *Nature*, **375**, 659. ADS. [47]
- Thorne K. S. (1974). Disk-accretion onto a black hole. II. Evolution of the hole. *ApJ*, **191**, 507. ADS. [54]
- Thorne K. S., Price R. H. & MacDonald D. A. (1986). *Black holes: the membrane paradigm*. New Haven: Yale University Press. ADS. [2]
- Turner T. J., Kraemer S. B. & Reeves J. N. (2004). Transient relativistically shifted lines as a probe of black hole systems. *ApJ*, **603**, 62. ADS. [53]
- Turner T. J., Mushotzky R. F., Yaqoob T., George I. M., Snowden S. L., Netzer H., Kraemer S. B., Nandra K. & Chelouche D. (2002). Narrow components within the Fe K $\alpha$  profile of NGC 3516: evidence of the importance of general relativistic effects? *ApJ*, **574**, L123. ADS. [8, 53]
- Usui F., Nishida S. & Eriguchi Y. (1998). Emission-line profiles from self-gravitating toroids around black holes. *MNRAS*, **301**, 721. ADS. [7]
- Viergutz S. U. (1993). Image generation in Kerr geometry. I. Analytical investigations on the stationary emitter-observer problem. *A&A*, **272**, 355. ADS. [7]
- de Villiers J. & Hawley J. F. (2003). Global general relativistic magnetohydrodynamic simulations of accretion tori. *ApJ*, **592**, 1060. ADS. [3]
- Wald R. M. (1974). Black hole in a uniform magnetic field. *Phys. Rev. D*, **10**, 1680. ADS. [2]
- Wald R. M. (1998). *Black holes and relativistic stars*. Chicago: University of Chicago Press. ADS. [2]
- Walker M. & Penrose R. (1970). On quadratic first integrals of the geodesic equations for type {22} space-times. *Commun. Math. Phys.*, **18**, 265. [13]
- Wilms J., Reynolds C. S., Begelman M. C., Reeves J., Molendi S., Staubert R. & Kendziorra E. (2001). XMM-EPIC observation of MCG–6-30-15: direct evidence for the extraction of energy from a spinning black hole? *MNRAS*, **328**, L27. ADS. [15, 50]
- Yaqoob T., George I. M., Kallman T. R., Padmanabhan U., Weaver K. A. & Turner T. J. (2003). Fe XXV and Fe XXVI diagnostics of the black hole and accretion disk in active galaxies: Chandra time-resolved grating spectroscopy of NGC 7314. *ApJ*, **596**, 85. ADS. [8, 53, 62]
- Yaqoob T. & Padmanabhan U. (2004). The cores of the Fe K lines in Seyfert 1 galaxies observed by the Chandra high energy grating. *ApJ*, **604**, 63. ADS. [15]
- Zakharov A. F. (1994). On the hotspot near a Kerr black-hole – Monte-Carlo simulations. *MNRAS*, **269**, 283. ADS. [7]
- Zeldovich Y. B. & Novikov I. D. (1964). *Dokl. Acad. Nauk. SSSR*, **158**, 811. [4]
- Życki P. & Czerny B. (1994). The iron K $\alpha$  line from a partially ionized reflecting medium in an active galactic nucleus. *MNRAS*, **266**, 653. ADS. [45]